

**NOVEL APPLICATIONS OF ORGANIC  
FLUOROPHORES: WHITE LIGHT EMISSION,  
CHEMOSENSOR AND AMBIENT MICRODROPLET  
SYNTHESIS**

**NORFATIRAH MUHAMAD SARIH**

**FACULTY OF SCIENCE  
UNIVERSITI MALAYA  
KUALA LUMPUR**

**2021**

**NOVEL APPLICATIONS OF ORGANIC  
FLUOROPHORES: WHITE LIGHT EMISSION,  
CHEMOSENSOR AND AMBIENT MICRODROPLET  
SYNTHESIS**

**NORFATIRAH MUHAMAD SARIH**

**THESIS SUBMITTED IN FULFILMENT OF THE  
REQUIREMENTS FOR THE DEGREE OF DOCTOR  
PHILOSOPHY**

**DEPARTMENT OF CHEMISTRY  
FACULTY OF SCIENCE  
UNIVERSITI MALAYA  
KUALA LUMPUR**

**2021**

**UNIVERSITI MALAYA**  
**ORIGINAL LITERARY WORK DECLARATION**

Name of Candidate: **NORFATIRAH BINTI MUHAMAD SARIH**

Matric No: **SHC150029**

Name of Degree: **DOCTOR OF PHILOSOPHY (SCIENCE)**

Title of Project Thesis:

**NOVEL APPLICATIONS OF ORGANIC FLUOROPHORES: WHITE  
LIGHT EMISSION, CHEMOSENSOR AND AMBIENT  
MICRODROPLET SYNTHESIS**

Field of Study: **PHYSICAL ORGANIC CHEMISTRY**

I do solemnly and sincerely declare that:

- (1) I am the sole author/writer of this Work;
- (2) This Work is original;
- (3) Any use of any work in which copyright exists was done by way of fair dealing and for permitted purposes and any excerpt or extract from, or reference to or reproduction of any copyright work has been disclosed expressly and sufficiently and the title of the Work and its authorship have been acknowledged in this Work;
- (4) I do not have any actual knowledge nor do I ought reasonably to know that the making of this work constitutes an infringement of any copyright work;
- (5) I hereby assign all and every rights in the copyright to this Work to the University of Malaya ("UM"), who henceforth shall be owner of the copyright in this Work and that any reproduction or use in any form or by any means whatsoever is prohibited without the written consent of UM having been first had and obtained;
- (6) I am fully aware that if in the course of making this Work I have infringed any copyright whether intentionally or otherwise, I may be subject to legal action or any other action as may be determined by UM.

Candidate's Signature

Date: 9/7/2021

Subscribed and solemnly declared before,

Witness's Signature

Date:

Name:

Designation

# NOVEL APPLICATIONS OF ORGANIC FLUOROPHORES: WHITE LIGHT EMISSION, CHEMOSENSOR AND AMBIENT MICRODROPLET SYNTHESIS

## ABSTRACT

This thesis has focused on the applications of organic fluorophore for producing white light emission, developing a fluorescence-based sensor of  $\text{Fe}^{3+}$  and a new method for the accelerated synthesis of dansyl aniline (DA). The first work in this research relates to a novel means to generate white light emission (WLE) by mixing three fluorescent organic compounds; furocoumarin (FC), DA, and 7-hydroxycoumarin-3-carboxylic acid (CC). This novel mixture is immobilised in silica aerogel and applied as a coating to a UV LED to demonstrate its applicability as a low-cost, organic coating for WLE via simultaneous emission. Kept in an ethanol solution while immobilised in silica aerogel, the mixture exhibits a Commission Internationale d'Eclairage (CIE) chromaticity index of (0.27, 0.33). It was observed that a broadband and simultaneous emission involving CC, FC and DA played a vital role in obtaining a CIE index close to that of pure white light. The next application uses coumarin derivatives to develop a novel chemosensor for the sensitive and selective detection of  $\text{Fe}^{3+}$ . Furocoumarin (furo[3,2-c]coumarin) derivatives have been synthesised from a single step, high yielding (82-92%) chemistry involving a 4-hydroxycoumarin [4+1] cycloaddition reaction. They were characterised by FTIR,  $^1\text{H-NMR}$ , and, for the first time, a comprehensive UV-Vis and fluorescence spectroscopy study was carried out to determine if such compounds can serve as useful sensors. Based on the fluorescence data, the most promising furocoumarin derivative (2-(cyclohexylamino)-3-phenyl-4H-furo[3,2-c]chromen-4-one, FH), exhibits strong fluorescence ( $\Phi_f = 0.48$ ) with long fluorescence lifetime (5.6 ns) and large Stokes' shift, suggesting FH could be used as a novel fluorescent chemosensor. FH exhibits a highly selective, sensitive, and instant turn-off fluorescence response to  $\text{Fe}^{3+}$  over other metal ions which is attributed to a charge transfer mechanism. Selectivity is demonstrated

against 13 other competing metal ions ( $\text{Na}^+$ ,  $\text{K}^+$ ,  $\text{Mg}^{2+}$ ,  $\text{Ca}^{2+}$ ,  $\text{Mn}^{2+}$ ,  $\text{Fe}^{2+}$ ,  $\text{Al}^{3+}$ ,  $\text{Ni}^{2+}$ ,  $\text{Cu}^{2+}$ ,  $\text{Zn}^{2+}$ ,  $\text{Co}^{2+}$ ,  $\text{Pb}^{2+}$  and  $\text{Ru}^{3+}$ ) and aqueous compatibility is demonstrated in a 10% MeOH- $\text{H}_2\text{O}$  solution. This novel sensor has a limit of detection of  $1.93 \mu\text{M}$ , below that of the US environmental protection agency guidelines ( $5.37 \mu\text{M}$ ), with a linear dynamic range of  $\sim 28$  ( $\sim 2\text{--}30 \mu\text{M}$ ) and an  $R_2$  value of 0.9975. As an exemplar application, the potential of this sensor was demonstrated for the rapid measurement of  $\text{Fe}^{3+}$  in mineral and tap water samples, establishing the real-world application of FH as a “turn off” fluorescence sensor. Lastly, the research is expanded to discover the nucleophilic substitution reactions of dansyl aniline by reactive paper spray ionisation-mass spectrometry (PSI-MS). PSI-MS is an emerging tool for ambient reaction monitoring via micro droplet reaction acceleration. PSI was used to accelerate and monitor the time course of the reaction of dansyl chloride with aniline, in acetonitrile, to produce dansyl aniline. Three distinct PSI arrangements were explored in this study to represent three types of sample loading and interactions, the conventional single tip as well as two novel setups, dual tip, and a co-axial setup. The effect on product yield was investigated using these different types of paper tips for a range of geometric considerations, including distance of microdroplet travel. It was observed that product yield is increased at a given distance and decreases thereafter for all PSI configurations. Amongst the variety of sample loading methods, the novel dual tip arrangement showed increased product yield which also exhibited the largest microdroplet density. In general, the reaction monitoring by PSI-MS with a dual tip configuration shows much promise and was further utilised for the successful synthesis of a silyl-alkylated dansyl aniline compound demonstrating a rapid and simple optimisation procedure based on ratio concentration adjustments.

**Keywords:** Organic Fluorophores, White Light Emission, Chemosensor, Ambient Microdroplet Synthesis, PSI-MS.

# **APLIKASI NOVEL PNDARFLUOR ORGANIK: PANCARAN CAHAYA PUTIH, PENDERIAAN KIMIA DAN SINTESIS TITISAN MIKRO SECARA AMBIEN**

## **ABSTRAK**

Tesis ini memfokus kepada aplikasi bahan pendarfluor organik untuk menghasilkan pancaran cahaya putih, menghasilkan penderia  $\text{Fe}^{3+}$  berdasarkan pendarfluor, dan memantau serta mempercepatkan reaksi sintesis dansil anilina. Projek pertama dalam penyelidikan ini adalah untuk menghasilkan pancaran cahaya putih dengan mencampurkan tiga sebatian organik pendarfluor; furokumarin (FC), dansil anilina (DA), dan 7-hidroksikumarin-3-asid karbosilat (CC). Campuran novel ini tidak bergerak dalam aerogel silika dan digunakan sebagai lapisan pada LED UV bagi menunjukkan kegunaannya sebagai lapisan organik berkost rendah bagi menghasilkan pancaran cahaya putih melalui pancaran serentak. Campuran pendarfluor di dalam larutan etanol diperangkapkan di dalam silika aerogel telah menunjukkan indeks kekromaian *Commission Internationale d'Eclairage* (CIE) (0.27, 0.33). Berdasarkan penemuan dalam kajian ini, pancaran jalur lebar dan serentak melibatkan asid karbosilat kumarin, furokumarin dan dansil anilina memainkan peranan penting dalam memperoleh indeks CIE yang hampir dengan cahaya putih. Aplikasi seterusnya adalah dengan menggunakan terbitan kumarin sebagai penderiaan kimia dan berkongsi penemuan baru mengenai furokumarin sebagai penderia kimia untuk  $\text{Fe}^{3+}$ . Terbitan furokumarin (furo [3,2-c] kumarin) telah disintesis secara satu langkah, dengan peratus penghasilan yang tinggi (82-92%), melibatkan tindak balas penambahan siklo 4-hidroksikumarin [4+1]. Sebatian ini dicirikan dengan FTIR,  $^1\text{H-NMR}$ , dan untuk pertama kalinya, kajian spektroskopi UV-Vis dan pendarfluoran yang komprehensif telah dilakukan untuk menentukan sama ada sebatian ini dapat berfungsi sebagai penderia yang berguna. Berdasarkan data pendarfluorannya yang diperolehi, terbitan furokumarin yang paling baik adalah (2-(sikloheksilamino)-3-fenil-4H-furo [3,2-c] kromen-4-on, (FH). Sebatian ini

menunjukkan pendarfluor yang kuat ( $\Phi_f = 0.48$ ) dengan jangka hayat pendarfluoran yang panjang (5.6 ns) dan peralihan Stokes yang besar. Justeru itu ia menunjukkan bahawa FH dapat digunakan sebagai penderiaan kimia pendarfluor yang baru. FH menunjukkan tindak balas pendarfluor yang pantas, terpilih, sensitif, dan responsif terhadap  $\text{Fe}^{3+}$  berbanding dengan ion logam yang lain, ianya dikaitkan dengan mekanisme pemindahan caj. Keterpilihan telah ditunjukkan terhadap 13 ion logam lain yang bersaing ( $\text{Na}^+$ ,  $\text{K}^+$ ,  $\text{Mg}^{2+}$ ,  $\text{Ca}^{2+}$ ,  $\text{Mn}^{2+}$ ,  $\text{Fe}^{2+}$ ,  $\text{Al}^{3+}$ ,  $\text{Ni}^{2+}$ ,  $\text{Cu}^{2+}$ ,  $\text{Zn}^{2+}$ ,  $\text{Co}^{2+}$ ,  $\text{Pb}^{2+}$  and  $\text{Ru}^{3+}$ ) dan keterlarutan dalam air telah ditunjukkan dalam larutan 10% MeOH-H<sub>2</sub>O. Penderia FH mengkoordinasikan  $\text{Fe}^{3+}$  dalam stoikiometri 1:2 dengan pemalar mengikat,  $K_a = 5.25 \times 10^3 \text{ M}^{-1}$ . Penderia baru ini mempunyai had pengesanan pada  $1.93 \mu\text{M}$ , di bawah nilai dalam garis panduan agensi perlindungan alam sekitar AS ( $5.37 \mu\text{M}$ ), dengan julat dinamik linear  $\sim 28$  ( $\sim 2\text{--}30 \mu\text{M}$ ) dan nilai  $R^2 = 0.9975$ . Dari segi aplikasi, potensi penderia ini telah ditunjukkan untuk mengukur  $\text{Fe}^{3+}$  dengan cepat di dalam sampel air mineral dan air paip, menjadikan aplikasi FH sebagai penderia pemadaman pendarfluor. Bagi projek terakhir, penyelidikan dilakukan untuk mengkaji tindak balas penukargantian nukleofilik dansil anilina dengan kaedah Kertas Penyemburan Pengionan-jisim Spektrometri (PSI-MS) yang reaktif. PSI-MS adalah alat yang diguna untuk pemantauan tindak balas persekitaran melalui pecutan tindak balas titisan mikro. PSI digunakan untuk memecut dan memantau jangka masa tindak balas dansil klorida dengan anilina, dalam asetonitril, untuk menghasilkan dansil anilina. Tiga konfigurasi berbeza PSI telah di kaji dalam kajian ini untuk mewakili tiga jenis pemuatan dan interaksi sampel, iaitu hujung tunggal konvensional serta dua persediaan baru, dwi hujung, dan pemasangan sepaksi. Kesan terhadap produk hasil di kaji menggunakan pelbagai jenis kertas dengan pelbagai pertimbangan geometri, termasuk jarak perjalanan titisan mikro. Kajian mendapati hasil meningkat pada jarak tertentu dan menurun selepas itu bagi semua konfigurasi PSI. Daripada pelbagai kaedah pemuatan sampel, dwi hujung

telah menunjukkan peningkatan hasil yang juga menunjukkan kepadatan titisan mikro terbesar. Pemantauan tindak balas oleh PSI-MS dengan konfigurasi dwi hujung menunjukkan peningkatan hasil dan berpotensi untuk digunakan dalam menyediakan sebatian pengalkilan silil dansil anilina seperti yang telah ditunjukkan mengikut prosedur optimum mudah dan pantas berdasarkan pelarasan nisbah kepekatan.

**Kata kunci:** Pendarfluor Organik, Pancaran Cahaya Putih, Penderiaan Kimia Dan Sintesis Titisan Mikro Secara Ambien, PSI-MS.

Universiti Malaya

## ACKNOWLEDGEMENTS

Throughout this PhD journey, I have received a great deal of support and assistance by all those around me. I would first like to abundantly thank my main supervisors, Dr. Hairul Anuar Tajuddin, Prof. Dr. Zanariah Abdullah, and Dr. Simon Maher for the continuous support of my PhD study and research, for their patience, motivation, enthusiasm, and immense knowledge. Their guidance has helped me in all my time spent on the research and writing of this thesis. I could not have imagined having better advisors and mentors for my PhD study. Their invaluable expertise aided in the formulation of the research topic, methodology and all other aspects of this work. I would also like to acknowledge my co-supervisor Dr. Anna Grace Slater, for their advice. My appreciation also extends to my fellow lab mates from the Blue Organic Lab at University of Malaya; Nordiana Nordin, Hasna Nadiah Johari, Nurul Faeizin, Bayhaki Sadidarto, Mohd Shamim, Phoebe Suzanna and Nur Idayu and also to my colleagues at University of Liverpool; Monrawat, Dave Perez, Barry Smith, Dr. Behnam Bastani, Cedric Boisdon, for the stimulating discussions, excellent cooperation and for all the fun we have had in the last four years with all the opportunities I had the privilege to conduct my research and further my dissertation at both universities. Further thanks to my collaborators, Prof. Peter Meyers, Dr. Alex Ciupa, Dr. Ben Slater, and Dr. Abraham Badu-Tawiah (from the Ohio state University) for their valuable guidance and wonderful collaboration. You provided me with the tools that I needed to choose the right direction and successfully complete my journal publications.

Foremost, I would like to greatly thank my beloved husband, Abu Dzar Mohd Isa, and my wonderful children, Ayra Alesya, Saif Salahuddin and Muhammad Al-Fateh for their enduring love, spiritual support, understanding, cooperation, and for all their sacrifices throughout this journey, and also my deepest thanks to my beloved mom, Kamariah Hamzah, late father, Muhamad Sarih, parents in law, Rosfaridah Mohd Suan and Mohd

Isa Nik, and siblings for supporting me in everything, particularly your wise guidance and concerns. You are always there for me, and this PhD journey would not have been possible without the support of my beloved family.

Finally, I want to acknowledge the University of Malaya and Malaysia's Ministry of Education for supporting my study financially and providing me with a monthly stipend for me to survive this PhD journey.

Universiti Malaya

## TABLE OF CONTENTS

<b>ABSTRACT</b> .....	<b>iii</b>
<b>ABSTRAK</b> .....	<b>v</b>
<b>ACKNOWLEDGEMENTS</b> .....	<b>viii</b>
<b>TABLE OF CONTENTS</b> .....	<b>x</b>
<b>LIST OF FIGURES</b> .....	<b>xiii</b>
<b>LIST OF TABLES</b> .....	<b>xxiii</b>
<b>LIST OF SYMBOLS AND ABBREVIATIONS</b> .....	<b>xxiv</b>
<b>LIST OF APPENDICES</b> .....	<b>xxvii</b>
<b>CHAPTER 1: INTRODUCTION</b> .....	<b>1</b>
1.1 Introduction to Fluorescence .....	1
1.2 Organic Fluorophores .....	4
1.3 Problem Statement and Overview of the Research .....	8
1.4 Objectives of the Research .....	9
1.5 Thesis Outlines .....	9
<b>CHAPTER 2: WHITE ORGANIC LIGHT EMISSION</b> .....	<b>11</b>
2.1 Background and Introduction To White Organic Light Emission.....	11
2.2 White Organic Light Emissive Materials Reviews .....	14
2.3 White Light Emission from a Simple Mixture of Fluorescent Organic Compounds .....	43
2.4 Materials And Methods .....	44
2.4.1 Synthesis Of Furo[3,2-C]Coumarin (Fc) .....	44
2.4.2 Synthesis Of Dansyl Aniline (Da) .....	45
2.5 Results And Discussion .....	46

2.6	Conclusion .....	53
<b>CHAPTER 3: COUMARINS AS FLUORESCENT CHEMOSENSORS.....</b>		<b>55</b>
3.1	Introduction.....	59
3.2	Coumarin Derivatives as Chemosensors for Fe <sup>3+</sup> .....	59
3.3	Furo[3,2-c]coumarin-derived Fe <sup>3+</sup> Selective Fluorescence Sensor: Synthesis, Fluorescence Study And Application To Water Analysis.....	74
3.3.1	Materials and Methods .....	74
3.3.2	Results and discussion .....	77
3.4	Conclusion .....	88
<b>CHAPTER 4: RAPID SCREENING AND REACTION MONITORING VIA DUAL-TIP PAPER SPRAY IONISATION .....</b>		<b>89</b>
4.1	Introduction.....	89
4.2	Chemical Reaction and Reaction Monitoring by Reactive PS-MS .....	92
4.3	Accelerated Nucleophilic Substitution Reactions of Dansyl Chloride with Aniline Under Ambient Conditions via Dual-Tip Reactive Paper Spray.....	102
4.4	Materials And Methods.....	103
4.4.1	The paper spray tip configurations. ....	104
4.4.2	The procedure for the dansyl aniline synthesis by ESI-MS.....	105
4.4.3	The procedure for the dansyl aniline synthesis under reactive paper spray conditions.....	105
4.4.4	The procedure for the silyl-alkylated dansyl aniline synthesis by reactive paper spray with dual-tip configuration.....	105
4.4.5	Observations of reactive paper spray for the fluorescent product using UV-light .....	105
4.4.6	Characterising the droplet distribution. ....	106
4.5	Results and Discussion .....	106
4.6	Conclusion .....	114

<b>CHAPTER 5: CONCLUSIONS AND FUTURE WORK .....</b>	<b>116</b>
<b>REFERENCES.....</b>	<b>119</b>
<b>LIST OF PUBLICATIONS AND PAPERS PRESENTED .....</b>	<b>145</b>
<b>APPENDIX .....</b>	<b>149</b>

Universiti Malaya

## LIST OF FIGURES

Figure 1.1	: (1) The fluorophore absorbs light energy at a certain wavelength. (2) Light absorption occurs to elevate fluorophore to electronically excited state. (3) The fluorophore releases the absorbed light energy at a longer wavelength. The electrons then return to their ground state.....	1
Figure 1.2	: Jablonski Diagram: (i) Absorption of a photon causes the electron to jump from the ground state ( $S_0$ ) to an excited state, (ii) Internal conversion to $S_1$ , (iii) Fluorescence happens releasing energy, (iv) Nonradiative decay, (v) Intersystem crossing from singlet excited state to triplet state, $T_1$ , (vi) Phosphorescence, (vii) Nonradiative decay.....	2
Figure 1.3	: Some common organic dyes.....	5
Figure 2.1	: A typical CIE (1931) plot showing the coordinates of pure white light (0.33, 0.33).....	12
Figure 2.2	: (a) The normalised PL spectra of <b>PF</b> toluene solution (blue line), <b>PS-b-P4VP/R110</b> micellar solution (green line), and <b>PS-b-P4VP/S101</b> micellar solution (red line). (b) PL spectra of white light emitting solution and (c) white light emitting solid film of <b>PS-b-P4VP/PF/R110/S101</b> , at 380 nm excitation wavelength.....	15
Figure 2.3	: Top. Schematic illustration for the unenhanced (left) and enhanced (right) white light from a single layer of diblock copolymer micelles. Bottom. The spectra of both enhanced white light emitting thin film <b>PS-b-P4VP/PF/C343-R110/C343-S101</b> (black solid line) and unenhanced white light emitting thin film <b>PS-b-P4VP/PF/R110/S101</b> (black dotted line) under excitation light of 380 nm.....	16
Figure 2.4	: (a) Illustration of the preparation of solvent-free white-emitting liquid composite. b) Emission spectrum of <b>OPV</b> ( $\lambda_{ex}$ =360 nm) supported on quartz plate; inset shows the image of the white emission from <b>OPV</b> . c) Fluorescence matrix scan of composite material.....	17
Figure 2.5	: The blend of liquid OPVs with emissive solid dopants on a glass surface as paint and on LED generating white illumination.....	17
Figure 2.6	: Top. Chemical structures of OF (1-4) = Oligofluorene derivatives, <b>DCM</b> = 4-(dicyanomethylene)-2-methyl-6-(4-	

	dimethylamino-styryl)-4H-pyran and <b>DCM2</b> = 4-(4-diethylaminostyryl)-N-methylpyridinium iodide.....	18
Figure 2.6	: Bottom. (a) Photographs of <b>OF3</b> nanoparticles containing (1) 0 mol%, (2) 0.8 mol% and (3) 4 mol% of <b>D1</b> (encapsulated) under 365 nm UV light. (b) CIE coordinate diagram of the emission colours obtained for <b>OF3</b> nanoparticles alone (yellow circle), containing 0.8 mol% of <b>D1</b> (black star) and <b>DCM2</b> (yellow diamond).....	19
Figure 2.7	: Top. Chemical structures of <b>OF</b> and <b>DCM</b> . Photographs of the nanoparticle dispersion in aq. medium with different concentrations of <b>DCM</b> ( $\lambda_{ex} = 365$ nm) and (bottom) the FL microscopic images ( $\lambda_{ex} = 330-380$ nm).....	20
Figure 2.8	: Top. Chemical Structures of <b>Q</b> , <b>R</b> , and <b>RhB</b> , Photograph of each solution under UV Light irradiation excited at 365 nm; (d) Normalised Fluorescence Spectra of <b>Q</b> , <b>R</b> , and <b>RhB</b> in their solution. (a) Fluorescence spectra of W- gel having molar ratio <b>Q:M:R:RhB</b> 100:100:0.5:0.02 for excitation at 360 nm, Bottom. (b) Photograph of W-gel under UV light at 365 nm, and (c) CIE coordinate for W-gel (0.31, 0.36).....	21
Figure 2.9	: RhB-containing silica core-shell nanoparticles showed white light emissions under UV (365 nm).....	22
Figure 2.10	: (a) Absorption spectra, (b) PL spectra under excitation at 532 nm, (c) PL spectra under excitation at 365 nm, and (d) photographs under excitation at 365 nm of pristine PMMA and its composite films with CB-RhB/SNP in different concentrations.....	23
Figure 2.11	: Chemical structures of stilbenes ( <b>D1-D3</b> ) and perylenes ( <b>A1-A3</b> ) derivatives. ....	24
Figure 2.12	: UV-Vis absorption spectra of white light emitting solutions of different pair of donors and acceptors: (a) <b>D2-A1</b> (b) <b>D2-A3</b> (c) <b>D2-A2</b> (d) <b>D3-A1</b> (e) <b>D3-A3</b> (f) <b>D3-A2</b> (g) <b>D1-A1</b> (h) White light emitting solutions exposed to the UV lamp at 365 nm.....	25
Figure 2.13	: Photographs of commercially available UV-LED coated with white light emitting solutions: (a) <b>D1-A1</b> (b) <b>D2-A1</b> (c) <b>D2-A2</b> .....	25
Figure 2.14	: Top. Chemical structures of <b>B-OPV</b> , <b>M-OPV</b> , and <b>oligomers</b> . (a) Fluorescence emission spectrum of a decane gel of <b>1</b> ( $3.2 \times 10^{-4}$ M) in presence of 2.1 mol % of <b>3</b> ( $\lambda_{ex} = 380$ nm, $l = 1$ mm). Inset shows the white light emission of the gel under UV light at 365 nm. (b) The corresponding 1931 CIE	

	coordinate diagram of the white light emission ( $x=0.31$ , $y=0.35$ ).....	26
Figure 2.15	: (a) Chemical structures of <b>Peptide 1</b> and <b>Peptide 2</b> ; the UV absorption spectrum of (b) <b>Peptide 1</b> (c) <b>Peptide 2</b> (d) the white light emitting solution in ODCB. Inset shows the white light emission of the gel under UV light at 365nm.....	27
Figure 2.16	: The chemical structures of <b>B</b> , <b>G</b> , <b>Red</b> , <b>H<sub>2</sub>B</b> and the white light emitting nanofibers made up from <b>B</b> , <b>G</b> and <b>Red</b> .....	28
Figure 2.17	: Top. The chemical structures of ( <b>CN-DPASDB</b> ) and <b>TDPVBi</b> . Bottom. The layers of WOLED comprises of AIEE materials.....	29
Figure 2.18	: Top: Photoluminescence spectra of <b>1</b> (left) and <b>2</b> (right) in the crystalline state at ex. = 370 nm and in $5 \times 10^{-5}$ M DMF solution (ex. = 315 nm for <b>1</b> and 320 nm for <b>2</b> ). Middle: Chemical structures of <b>1</b> and <b>2</b> . Bottom: CIE coordinates and photographs (inset) for crystalline samples of <b>1</b> and <b>2</b> under excitation at 370 nm. Red dots show the CIE coordinates for ideal white light, (0.33, 0.33).....	30
Figure 2.19	: Photographs of a commercially available 5 mm 365–370 nm UV LED illuminating purple blue light (a: turn on); the UV LED coated with a thin layer of sample <b>1</b> in the PMMA matrix (b: turn off; c: turn on); the UV LED coated with a thin layer of sample <b>2</b> in the PMMA matrix (d: turn off; e: turn on).....	30
Figure 2.20	: Top. Chemical Structures of (a) Anthocyanins and (b) Curcumin. Bottom. UV-Visible spectra (black) and fluorescence spectra. (a) Pom extract (blue line), [anthocyanin] = 85 $\mu$ M and (b) Tur extract (green line), where [Curcumin] = 9.85 $\mu$ M with their fluorescent images under UV lamp, in 1% HCl ethanol at ex. = 380 nm).....	31
Figure 2.21	: Figure 2.21 White light emission in PVA film. (a) Emission spectrum of white light emission combined with PVA film, inset displays excellent white photograph of PVA film under UV excitation (380 nm) and (b) CIE coordinate plot white light emitting PVA film (0.32, 0.25).....	32
Figure 2.22	: Chemical structure of <b>NI</b> .....	32
Figure 2.23	: Fluorescence spectra showing excitation wavelengths allows the <b>NI</b> dyes to display blue, green or white light emission based on the excitation wavelength.....	33

Figure 2.24	: pH dependent systems in <b>SNAFR-1</b> (left) and emission of <b>SNAFR-1</b> based on different excitation wavelengths in DMSO with 0.25% phosphate buffer (50 mM, pH 7).....	34
Figure 2.25	: Illustration of tautomer compound <b>3</b> and its deprotonation. Inset photograph of <b>3</b> in DMSO solution (ex. = 360 nm).....	34
Figure 2.26	: Top. Chemical structures of diazine rings (pyrazine (3), quinoxaline (4,5,7) and pyrimidine (1,2,6) derivatives). Bottom. Schematic illustration of development of white emission and fluorescence quenching compounds.....	35
Figure 2.27	: Top. Normalised fluorescence spectra of <b>diphenylbutadiynes</b> at different ratios of acetonitrile-water system. Bottom. Fluorescence spectrum of <b>diphenylbutadiynes</b> in acetonitrile. Inset photograph of the <b>diphenylbutadiynes</b> in acetonitrile under UV light at ex. 370 nm.....	36
Figure 2.28	: Fluorescence spectra from the combination of a single fluorescent Lewis basic dye by adding different concentrations of Lewis acid achieved a white-light emission. Inset photograph of the dye and Lewis acid in toluene solution under UV lamp at $\lambda_{ex} = 365$ nm.....	37
Figure 2.29	: Photographs of a solution of the dye and $B(C_6F_5)_3$ in toluene under a UV lamp, excitation at 365 nm) (left); CIE of a solution of <b>6</b> with 0–100 equiv of $B(C_6F_5)_3$ (right).....	37
Figure 2.30	: Chemical structures of <b>TPE-Pys 2</b> and <b>TPE-Pys 4</b> .....	38
Figure 2.31	: Chemical structures of white light emitting organic molecules ( <b>NP4C</b> and <b>NP6C</b> ) (b) the schematic cartoon illustration of single-molecule white light emitters and its fluorescence spectrum.....	39
Figure 2.32	: (a) Some emission colour coordinates for <b>NP4C</b> plotted in the CIE 1931 chromaticity diagram consistent to the PL emission for multifarious control strategies. (b) Several fluorescence photographs of <b>NP4C</b> solutions in combination with several conditions including temperature, solvent polarity and host-guest interaction, at concentration 25 $\mu$ M.....	40
Figure 2.33	: Chemical structure, absorption, and emission spectra of a) <b>DPPZ</b> in THF solution under 298 and 78 K. The inset is the	

	photo of the steady-state emission of <b>DPPZ</b> . The excitation wavelength for DPPZ is 390 nm.....	41
Figure 2.34	: Schematic illustrations of encapsulated dye liquid-filled capsules plotted in the CIE 1931 chromaticity diagram consistent to different thermal responses.....	42
Figure 2.35	: Chemical Structure of <b>1H</b> .....	42
Figure 2.36	: Solid state emission spectra with the CIE coordinates of <b>1H</b> in its normal form. Inset pictures indicate the colours under irradiation at 365 nm.....	43
Figure 2.37	: Chemical structures of (a) FC, (b) DA and (c) CC.....	44
Figure 2.38	: Synthesis of furo[3,2-c]coumarin derivatives.....	45
Figure 2.39	: Synthesis of dansyl aniline.....	46
Figure 2.40	: (a) Absorption spectra for each of the compounds (CC = $2.2 \times 10^{-3}$ M, FC = $1.6 \times 10^{-3}$ M and DA = $1.6 \times 10^{-3}$ M) in ethanol. (b) Fluorescence spectra for each of the compounds (CC = $2.2 \times 10^{-3}$ M, FC = $1.6 \times 10^{-3}$ M and DA = $1.6 \times 10^{-3}$ M) in ethanol. Inset: Photograph taken under UV light (390 nm) for each of the compounds (CC, FC and DA) in ethanol.....	47
Figure 2.41	: CIE-1931 diagram. Chromaticity plot for colour coordinates of CC ( $\blacktriangle$ ), FC ( $\blacksquare$ ) and DA ( $\bullet$ ).....	48
Figure 2.42	: CIE-1931 diagram. Chromaticity plot for colour coordinates of CC ( $\blacktriangle$ ), FC ( $\blacksquare$ ), DA ( $\bullet$ ) and for the mixture, CFD ( $\blacklozenge$ ) corresponding to a ratio of 1.375:1:7 CC:FC:DA, in ethanol solution.....	49
Figure 2.43	: (a) Fluorescence spectrum for a mixture, CFD, of CC:FC:DA (1.375:1:7) in ethanol at 390 nm. Inset: (i) Colour spectrum and (ii) photograph of the CFD solution in ethanol under UV light (390 nm). (b) Shows overlay of both fluorescence spectrum from a mixture (CFD, where CC:FC:DA = 1.375:1:7) and the fluorescence spectra of the three components individually (FC, CC, DA) in ethanol at 390 nm.....	51
Figure 2.44	: White light emission aerogel. (a) Emission spectrum of mixture incorporated into aerogel for white light emission. Inset (i) Colour spectrum of the modified aerogel and (ii) photograph of the modified aerogel under UV illumination (390 nm). (b) CIE plot for colour coordinate of white light emitting aerogel (0.27,0.33).....	52

Figure 2.45	: Side-by-side image for the same UV LED. In each image the left-hand side is the uncoated UV LED and the right-hand side LED is coated with aerogel to produce white light emission. Both images are taken of the same experimental setup: (a) is a side view and (b) is a top view.....	53
Figure 3.1	: Structural formula of coumarin. ....	56
Figure 3.2	: a) UV–Vis and (b) Fluorescence spectra of <b>L</b> (10 $\mu$ M) in the absence and presence of 1 eq. of different metal ions in methanol.....	60
Figure 3.3	: Structures of <b>L</b> and <b>L'</b> and approach of metal ions toward the coordination sites of both isomers.....	60
Figure 3.4	: Proposed mechanism and binding of <b>DC-Fe<sup>3+</sup></b> .....	61
Figure 3.5	: (a) Chemical structure <b>DAT-1</b> . (b) Fluorescent (bottom) and color (top) responses of <b>DAT-1</b> (20 $\mu$ M) in Na <sub>2</sub> HPO <sub>4</sub> –citric acid buffer solutions (0.2 M) upon the addition of (100 equiv.) metal ions in water.....	62
Figure 3.6	: Possible binding mode of <b>CN</b> with Fe <sup>3+</sup> .....	63
Figure 3.7	: The chemical structure of 7-oxy-3-(3,4,5-trimethoxyphenyl)coumarin substituted phthalonitrile derivative ( <b>OCP</b> ).....	63
Figure 3.8	: The fluorescence emission responses of the <b>OCP</b> to different metal ions under UV lamp.....	64
Figure 3.9	: Molecular structures of (S)-(1-((7-hydroxy-2-oxo-2H-chromen-4-yl) methyl)-1H-1,2,3-triazol-4-yl)methyl 2-(tert-butoxycabonylamino)-3-phenylpropanoate, <b>A</b> and (S)-(1-((7-hydroxy-2-oxo-2H-chromen-4-yl)methyl)-1H-1,2,3-triazol-4-yl) methyl 2-(benzyloxycabonylamino)-3-phenylpropanoate, <b>B</b> .....	64
Figure 3.10	: Proposed structure of <b>A-Fe<sup>3+</sup></b> and <b>B-Fe<sup>3+</sup></b> complexes.....	65
Figure 3.11	: Proposed mechanism for detection of Fe <sup>3+</sup> and inset photograph under UV irradiation at ex. 475 nm.....	65
Figure 3.12	: Fe <sup>3+</sup> -induced FRET OFF–ON and PET ON–OFF.....	66
Figure 3.13	: Proposed binding site for <b>APC-Fe<sup>3+</sup></b> and <b>APC –Cu<sup>2+</sup></b> complexes.....	67
Figure 3.14	: Column diagrams of the relative fluorescence intensity of <b>APC</b> with different, metal ions at 480 nm. Black bars	

	represent the addition of various metal ions to the blank solution and grey bars represent the subsequent addition of (a) Fe <sup>3+</sup> (5 eq.) and (B) Cu <sup>2+</sup> (5 eq.) into the solutions.....	67
Figure 3.15	: The proposed binding modes for compound <b>PC1</b> and <b>PC2</b> with Fe <sup>3+</sup> .....	68
Figure 3.16	: The proposed mechanism for PO <sub>4</sub> <sup>3-</sup> detection by <b>PICA</b> -Fe <sup>3+</sup> complex.....	69
Figure 3.17	: Proposed complexation mechanism for sensing of Ca <sup>2+</sup> and Fe <sup>3+</sup> ions by <b>TC</b> . ....	69
Figure 3.18	: <b>Probe 1</b> showed a decrease in fluorescence intensity upon complexation with Fe <sup>3+</sup> and shows potential to be used as an intracellular chemosensor for Fe <sup>3+</sup> .....	70
Figure 3.19	: (a) Changes in the emission spectra of <b>FB</b> in the presence of different metal ions in HEPES buffer (DMSO:H <sub>2</sub> O = 3:7, 20 mM, pH = 7.2); (b) Fluorescence response of <b>FB</b> to Fe <sup>3+</sup> in the presence of other common metal ions.....	71
Figure 3.20	: The proposed mechanism for PPI detection by <b>FB</b> -Fe <sup>3+</sup> complex.....	71
Figure 3.21	: The fluorescence emission responses of the <b>APICP</b> to different metal ions and proposed binding mechanism of <b>APICP</b> -Fe <sup>3+</sup> /Hg <sup>2+</sup> complexes.....	72
Figure 3.22	: Synthesis of furo[3,2-c]coumarin derivative.....	76
Figure 3.23	: Fluorescence Spectra of Furocoumarin derivatives ( <b>FC</b> , <b>FH</b> , <b>FNO<sub>2</sub></b> ) in ethanol. Inset: Photograph image of furocoumarin in ethanol under UV lamp illumination.....	78
Figure 3.24	: Possible mechanisms whereby chloro- substituent (R=Cl) donates electron density through aromatic ring compared with nitro- substituent (R=NO <sub>2</sub> ).....	78
Figure 3.25	: Fluorescence spectra of <b>FH</b> (0.5 μM) in the presence of different metal ions (100 equiv.) in methanol.....	79
Figure 3.26	: Fluorescence emission spectra of <b>FH</b> (0.5 μM) was titrated with Fe <sup>3+</sup> (0 – 100 equiv.) in methanol.....	81
Figure 3.27	: Calibration curve based on <b>FH</b> titration with Fe <sup>3+</sup> in methanol.....	81
Figure 3.28	: Job's plot for determining the stoichiometry for <b>FH</b> and Fe <sup>3+</sup> in methanol. Total concentration= 2x10 <sup>-5</sup> M.....	82

Figure 3.29	: Benesi–Hildebrand plot of <b>FH</b> sensor with $\text{Fe}^{3+}$ .....	82
Figure 3.30	: Competitive experiments in the <b>FH</b> + $\text{Fe}^{3+}$ system with potential interfering metal ions. <b>FH</b> (0.5 $\mu\text{M}$ ), $\text{Fe}^{3+}$ (50 $\mu\text{M}$ ), and other metals (50 $\mu\text{M}$ ). Excited at 374 nm and emission measured at 511 nm.....	83
Figure 3.31	: Proposed binding mode of <b>FH</b> with $\text{Fe}^{3+}$ .....	84
Figure 3.32	: Fluorescence spectra of <b>FH</b> (5 $\mu\text{M}$ ) in the presence of different metal ions (10 equiv.) in water/methanol (9:1, v/v).....	86
Figure 3.33	: Fluorescence emission spectra of <b>FH</b> (5 $\mu\text{M}$ ) was titrated with $\text{Fe}^{3+}$ (0.2–equiv.) in water/methanol (9:1, v/v).....	86
Figure 3.34	: Competitive experiments in the <b>FH</b> + $\text{Fe}^{3+}$ system with interfering metal ions. <b>FH</b> (5 $\mu\text{M}$ ), $\text{Fe}^{3+}$ (50 $\mu\text{M}$ ) and other metals (50 $\mu\text{M}$ ) in water/methanol (9:1, v/v). Excited at 374 nm and emission measured at 511 nm.....	87
Figure 4.1	: Schematic diagrams of the PS-MS.....	91
Figure 4.2	: Katritzky reaction monitoring between 2,4,6-triphenyl pyrylium cation and mono-, di-amines monitored by reactive PS mass spectrometry.....	93
Figure 4.3	: Time-resolved mass spectra displaying the Katritzky reaction between the pyrylium cation ( $m/z$ 309) and p-methoxyaniline to produce the pyridinium cation ( $m/z$ 414). a) using reactive PS-MS (as dwell time shown in each spectrum) and b) under bulk solution-phase conditions. R.A. = relative abundance.....	94
Figure 4.4	: PS mass spectra recorded after 2 minutes plasma-based dehydrogenation reaction involving (a) <b>THQ</b> (MW 133) and (b) 6-methoxy-THQ (MW 163) to produce the corresponding quinolines at $m/z$ 130 and 160, respectively...	95
Figure 4.5	: PSI of a reaction mixture (6-hydroxy-1-indanone and para-substituted benzaldehyde) being sprayed from a paper spray substrate toward the MS inlet.....	96
Figure 4.6	: Online paper spray reaction (from spotted starting reagents) collected on a TLC plate (left); Chromatographic separation on TLC plate (right).....	96

Figure 4.7	: (a) Ion chromatogram produced when paper spray ionisation is performed on the reaction mixture. Negative ion mass spectra are shown in (b) spray mode 1 and (c) spray mode 2.	97
Figure 4.8	: Schematic illustration of the nanocatalyst-embedded paper for the reactive paper spray methods.....	98
Figure 4.9	: Schematic diagrams of the steps for photocatalysis degradation process of the Methylene Blue dye with photolytic reactions and subsequent PS-MS analysis.....	99
Figure 4.10	: Synthesis of Carboxylic Acids from Alcohols in Microdroplets.....	99
Figure 4.11	: Setup of single-tip paper spray for microdroplet oxidation of 4-methoxybenzyl alcohol with NaOCl. ....	100
Figure 4.12	: Schematic of the experimental setup of LAPSI-MS. A green diode laser was pointed at the tip of the paper with a continuous supply of analyte through a syringe with fused silica capillary.....	100
Figure 4.13	: LAPSI-MS spectra of PAHs: (A) naphthalene, (B) pyrene, and (C) benzanthracene in positive ion mode. Isotope distributions of the species are shown.....	101
Figure 4.14	: Synthesis of dansyl aniline.....	103
Figure 4.15	: Photograph of the three paper spray arrangements: (a) single tip, (b) dual tip, and (c) co-axial.....	103
Figure 4.16	: Dimensions of the three different paper spray configurations: (a) single tip, (b) dual tip, (c) co-axial.....	104
Figure 4.17	: (a) Experimental set-up for the droplet distribution (e.g., dual tips). (b) Typical Image Processing steps.....	106
Figure 4.18	: Time-resolved mass spectra showing the synthesis of dansyl aniline (protonated molecular product ion at $m/z$ 327), from the reaction between [aniline+H] <sup>+</sup> at $m/z$ 94 and [dansyl chloride+H] <sup>+</sup> at $m/z$ 270. (a) Using single tip (conventional) PSI-MS and (b) by ESI-MS.....	108
Figure 4.19	: Absolute abundance of product ion ( $m/z$ 327) from each paper arrangement loaded at different distances. The error bars indicate the standard deviation from 3 replicas.....	109
Figure 4.20	: Image of paper substrate collection surface (i.e., target) whereby 0.1 M of dansyl chloride and 0.1 M aniline solution were sprayed from: single tip, dual tip and co-axial tip	

	arrangements at a distance of 2 cm (as labelled in the image).....	110
Figure 4.21	: Reactive paper showed reagents were spraying by dual tip paper arrangement.....	111
Figure 4.22	: Droplet distribution analysis by spraying 0.001 mM of dansyl chloride and aniline solution from: (a) single tip, (b) dual-tips and (c) co-axial tip arrangement at a distance of 5 mm to an ITO glass slide (as the target/collection surface). Imaging area: 18.13 mm x 13.60 mm (horizontal x vertical), with microscope magnification (x40 lens).....	111
Figure 4.23	: Droplet distribution for the three paper loading types. Each was sprayed on to an ITO coated glass slide at a distance of 5 mm and the central region of the slide was examined in each case to obtain the droplet distribution.....	111
Figure 4.24	: Flow of spraying observation under UV light from each of the paper tips: single tip (ST), dual-tip (DT) and coaxial (CA).....	112
Figure 4.25	: Synthesis of silyl-functionalized dansyl aniline.....	113
Figure 4.26	: Mass spectrum showing the synthesis of silyl alkylated dansyl aniline (protonated molecular product ion at $m/z$ 489), from the reaction between [dansyl aniline+H] <sup>+</sup> at $m/z$ 327 and [(3-bromopropyl)trimethoxysilane +H] <sup>+</sup> at $m/z$ 244 (very little appearance in the full spectrum) in 1:2 ratio (v/v) by using dual tip PSI-MS.....	114

## LIST OF TABLES

Table 1.1	: Organic Fluorophores Surveys.....	7
Table 2.1	: Various ratio combinations of dansyl aniline (DA) with furocoumarin (FC) and carboxylic coumarin (CC).....	48
Table 3.1	: Summary of the literature surveyed that selectively recognise Fe <sup>3+</sup> only and other metals.....	73
Table 3.2	: Concentration [M], Absorbance (Abs), fluorescence lifetimes ( $\tau$ ) and quantum yield ( $\Phi_f$ ) for fluorescence properties of furocoumarin derivatives in ethanol solution. nd = not determined.....	78
Table 3.3	: Analytical results of <b>FH</b> -Fe <sup>3+</sup> in water samples.....	88

## LIST OF SYMBOLS AND ABBREVIATIONS

<b>Abs</b>	:	<b>Absorbance</b>
$\tau$	:	fluorescence lifetimes ( $\tau$ )
<b>quantum yield (<math>\Phi_f</math>)</b>	:	quantum yield ( $\Phi_f$ )
$\lambda_{em}$	:	emission wavelength
$\lambda_{ex}$	:	excitation wavelength
<b>1</b>	:	1-(4-acetylphenyl)-1,2,3-triazole
<b>2</b>	:	1-(4-carboxyphenyl)-1,2,3-triazole
<b>3</b>	:	4-hydroxy-1,3-thiazoles
<b>Alq3</b>	:	tris(8-hydroxyquinolino)aluminium
<b>1H</b>	:	1-(1H-phenanthro[9,10-d]imidazol-2-yl)naphthalen-2-ol
<b>A</b>	:	(S)-(1-((7-hydroxy-2-oxo-2H-chromen-4-yl) methyl)-1H-1,2,3-triazol-4-yl)methyl 2-(tert-butoxycarbonylamino)-3-phenylpropanoate
<b>A1, A2, A3</b>	:	perylene derivatives (acceptor)
<b>AIE</b>	:	Aggregation-Induced Emission
<b>AIEE</b>	:	Aggregation-Induced Enhanced Emission
<b>APC</b>	:	(S)-4-((4-((3-amino-2-oxo-4-phenylbutoxy)methyl)-1H-1,2,3-triazol-1-yl)methyl)-7-hydroxy-2H-chromen-2-one
<b>APICP</b>	:	2-amino-4-phenyl-6-(isocoumarin-3-yl)-3-cyanopyridine
<b>B</b>	:	(S)-(1-((7-hydroxy-2-oxo-2H-chromen-4-yl)methyl)-1H-1,2,3-triazol-4-yl) methyl 2-(benzyloxycarbonylamino)-3-phenylpropanoate
<b>BLUE</b>	:	2,3-didecyloxy-anthracene
<b>B-OPV</b>	:	bischolesterol-OPV
<b>C343</b>	:	coumarin 343
<b>CA</b>	:	coaxial
<b>CB</b>	:	covalently-bonded
<b>CC</b>	:	7-carboxylic acid-coumarin
<b>CIE</b>	:	Commission Internationale d'Eclairage
<b>CN</b>	:	Coumarin-naphthalimide conjugate
<b>CN-DPASDB</b>	:	1,4-bis(a-cyano-4-diphenylaminostyryl)-2,5-diphenylbenzene
<b>CR</b>	:	Coumarin-rhodamine derivative
<b>CWA</b>	:	Chemical warfare agent
<b>Cy-NC</b>	:	Cyclohexyl isocyanide
<b>D1, D2, D3</b>	:	stilbenes derivatives (donor)
<b>DCM2</b>	:	4-(4-diethylaminostyryl)-N-methylpyridinium iodide.
<b>DA</b>	:	Dansyl aniline
<b>DAT-1</b>	:	2-amino-2-(hydroxymethyl)-1,3-propanediol (tris)
<b>DBSs</b>	:	dried blood samples

<b>DC</b>	:	Diaza-18-crown-6 ether, joined with dual coumarin (7-amino-4-trifluoromethylcoumarins) compounds
<b>DC</b>	:	Dansyl chloride
<b>DCM</b>	:	4-(dicyanomethylene)-2-methyl-6-(4-dimethylaminostyryl)-4H-pyran
<b>DFT</b>	:	Density-functional theory
<b>DPPZ</b>	:	dibenzo[a,c]phenazine
<b>DT</b>	:	dual-tip
<b>eq.</b>	:	equivalent
<b>ESI-MS</b>	:	Electrospray Ionisation Mass Spectrometry
<b>FB</b>	:	Fluorescent probe coumarin based
<b>FC</b>	:	furocoumarin
<b>FCI</b>	:	2-(cyclohexylamino)-3-(4-chlorophenyl)-4H-furo[3,2-c]chromen-4-one
<b>FH</b>	:	2-(cyclohexylamino)-3-phenyl-4H-furo[3,2-c]chromen-4-one
<b>FNO2</b>	:	2-(cyclohexylamino)-3-(4-nitrophenyl)-4H-furo[3,2-c]chromen-4-one
<b>FRET</b>	:	Fluorescence Resonance Energy Transfer
<b>G</b>	:	2,3-dihexadecyloxy-5,12-diphenyl-tetracene
<b>ICT</b>	:	intramolecular charge transfer
<b>IR</b>	:	Infra-red
<b>L</b>	:	coumarin Schiff base compound
<b>LCD</b>	:	Liquid-Crystal Display
<b>LE</b>	:	locally excited
<b>M</b>	:	melamine
<b>m/z</b>	:	Mass to charge ratio
<b>M-OPV</b>	:	monocholesterol-OPV
<b>MW</b>	:	Molecular weight
<b>NI</b>	:	N-aryl-2,3-naphthalimides derivatives
<b>NP4C and NP6C</b>	:	Coumarin derivatives
<b>OCP</b>	:	7-oxy-3-(3,4,5-trimethoxyphenyl)coumarin substituted phthalonitrile derivatives
<b>ODCB</b>	:	o-dichlorobenzene
<b>OF</b>	:	oligofluorene derivative
<b>OF1, OF2, OF3, OF4</b>	:	oligofluorene-based nanoparticles
<b>OLED</b>	:	Organic Light-Emitting Diodes
<b>OPV</b>	:	oligo(p-phenylenevinylene)
<b>PA</b>	:	physically-adsorbed
<b>PC1</b>	:	Phenanthro[9,10-d]imidazole-coumarin derivative (1)
<b>PC2</b>	:	Phenanthro[9,10-d]imidazole-coumarin derivative (2)
<b>PDI</b>	:	perylene diimide
<b>PF</b>	:	Polyfluorene
<b>PICA</b>	:	N-(3-(1H-phenanthro[9,10-d]yridine-2-yl)phenyl)-2-((4-methyl-2-oxo-2H-chromen-7-yl)oxy)acetamide
<b>PL</b>	:	photoluminescent
<b>PMMA</b>	:	poly(methylmethacrylate)
<b>PN</b>	:	pyridinium-naphthalene

<b>PPi</b>	:	pyrophosphate
<b>Probe 1</b>	:	7-hydroxy-2-oxo-N-(yridine-2-ylmethyl)chromene-3-carboxamide
<b>PSI</b>	:	Paper Spray Ionisation
<b>PSI-MS</b>	:	Paper Spray Ionisation Mass Spectrometry
<b>Q</b>	:	6,7-dimethoxy-2,4[1H, 3H]-quinazolinedione
<b>R</b>	:	riboflavin
<b>R110</b>	:	Rhodamine 110 chloride
<b>RC</b>	:	Rhodamine 6G and coumarin conjugate
<b>RED</b>	:	2,3-dihexadecyloxy-5,6,11,12-tetraphenyl-tetracene
<b>RGB</b>	:	Red Green Blue
<b>RhB</b>	:	Rhodamine B
<b>S101</b>	:	sulforhodamine 101
<b>SNAFR-1</b>	:	seminaphtho[a]fluorine
<b>SNP</b>	:	silica nanoparticle
<b>ST</b>	:	single tip
<b>TC</b>	:	Triazole-coumarin derivative
<b>TDPVBi</b>	:	2,5,20,50-tetrakis(2,2-diphenylvinyl) biphenyl
<b>TFA</b>	:	trifluoroacetic acid
<b>TPE-Pys</b>	:	tetraphenylethylene-substituted pyrenes
<b>UV</b>	:	Ultraviolet
<b>VIBGYOR</b>	:	Violet Indigo Blue Green Yellow Orange Red
<b>WOLEDs</b>	:	White Organic Light-Emitting Diodes

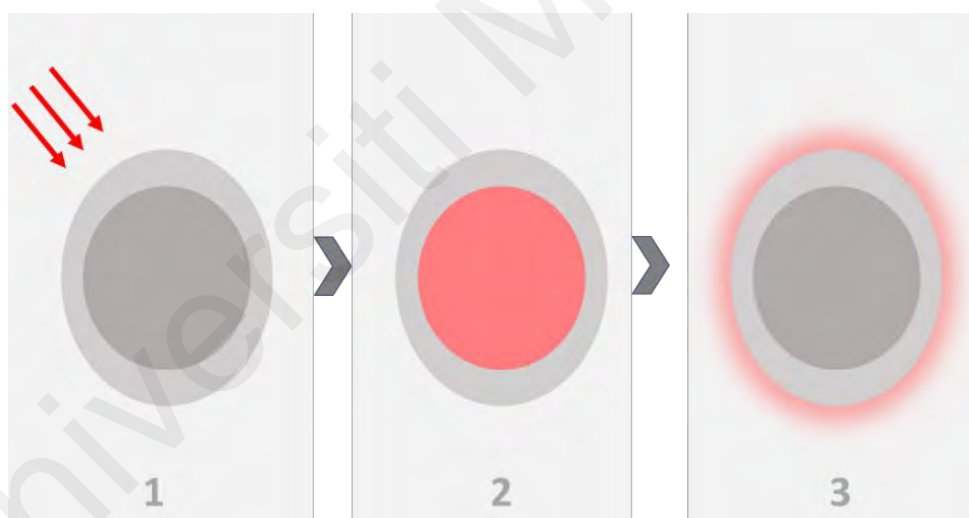
## LIST OF APPENDICES

Figure A1	: Absorbance spectra for all the ratios tested in ethanol (A-E). A-E entries correspond with the description given in Table 2.1.....	149
Figure A2	: Fluorescence spectra for three different ratio mixtures: (a) 1.375:1:5 (series C, Table 2.1), (b) 1.375:1:6 (Series D, Table 2.1) and (c) 1.375:1:7 (Series E, Table 2.1).....	150
Figure A3	: UV-Vis Spectra of Furocoumarin derivatives (FC, FH, FNO <sub>2</sub> ) in ethanol.....	151
Figure A4	: Photograph of FH on its own and mixed with various metal ions (as labelled) under UV light illumination (380 nm).....	151
Figure A5	: Mass spectra of (a) FH in acetonitrile and (b) FH mixed with Iron Nitrite.....	152
Figure A6	: Job's plot for determining the stoichiometry for FH and Fe <sup>3+</sup> in water/methanol (9:1, v/v). Total concentration = 2x10 <sup>-5</sup> M.	153
Figure A7	: IR spectra of FH (a) before and (b) after the addition of Fe <sup>3+</sup> .	153
Figure A8	: <sup>1</sup> H NMR spectrum of FH.....	154
Figure A9	: <sup>1</sup> H NMR spectrum of FC1.....	155
Figure A10	: <sup>1</sup> H NMR spectrum of FNO <sub>2</sub> .....	156
Figure A11	: <sup>1</sup> H NMR spectrum of DA.....	157
Figure A12	: Total droplet count from each of the paper types (obtained from the data of Figure 4.22).....	158

## CHAPTER 1: INTRODUCTION

### 1.1 Introduction to Fluorescence

The fluorescence phenomenon is deemed to be an important research tool in the scientific fields of chemistry, biology, materials science, biomedical science, and their interfaces due to its high sensitivity and wide applicability. Fluorescence happens when a substance that absorbs light or other electromagnetic radiation causes its electrons move to higher energy levels, then later relaxes to ground state by releasing light at a longer wavelength. The materials that are fluorescent, known as fluorophores, immediately stop to glow when the source of radiation is turned off, but different for phosphorescent materials, which remain to emit light for some time after. Figure 1.1 illustrates the phenomenon of the excitation and emission of fluorophores.



**Figure 1.1: (1) The fluorophore absorbs light energy at a certain wavelength. (2) Light absorption occurs to elevate fluorophore to electronically excited states. (3) The fluorophore releases the absorbed light energy at a longer wavelength. The electrons then return to their ground state.**

Since fluorophores shine when their atoms or molecules get excited, then later relax to their ground state, they are known to be in a conjugated system. Their energy is dependent on their molecular makeup; therefore, the highest level of excitation and emission depends on the molecule or atom. This means that the energy depends on how strongly two or more atoms are held together. In this way, the total energy of the molecule is the

sum of the energies holding the nuclei together as well as the energy of the chemical bonds holding the molecule together. The fluorescence process can be illustrated in the Jablonski diagram as shown in Figure 1.2. The process starts once a molecule in a singlet electronic ground state ( $S_0$ ) absorbs a photon of energy in the form of light. This stimulates the molecule electron to higher energy orbitals, then relaxes promptly to the first singlet excited state ( $S_1$ ). The decay of the excited state can cause either the emission of a photon called fluorescence or undergo nonradiative decay. The nonradiative “quenching” of fluorophores can happen for a number of reasons, for example, bond rotation or vibration, molecular collision or photoinduced electron transfer (PeT) (Lavis & Raines, 2008). The excited state can also go from intersystem crossing (ITC) to the triplet excited state ( $T_1$ ) and the resultant relaxation is either by photon emission (called “phosphorescence”) or “nonradiative decay”.

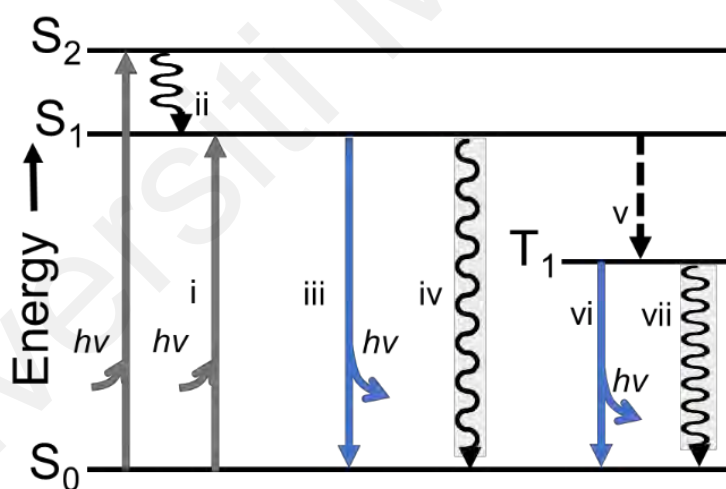


**Figure 1.2: Jablonski Diagram: (i) Absorption of a photon causes the electron to jump from the ground state ( $S_0$ ) to an excited state, (ii) Internal conversion to  $S_1$ , (iii) Fluorescence happens releasing energy, (iv) Nonradiative decay, (v) Intersystem crossing from singlet excited state to triplet state,  $T_1$ , (vi) Phosphorescence, (vii) Nonradiative decay.**

Some useful photophysical properties of fluorophores are given that are used throughout this thesis:

a) Fluorescence excitation spectrum: The graph is plotted based on the number of fluorescence photons generated by a fluorophore (Y, vertical axis) versus the excitation wavelength (X, abscissa).

b) Absorption spectrum: The graph is plotted as the absorbency of a fluorophore (Y) versus the wavelength (X). For a first estimation, the absorption spectrum of a fluorophore corresponds to the fluorescence excitation spectrum. Therefore, the absorption spectrum can be used as a substitute for the fluorescence excitation spectrum.

c) Fluorescence emission spectrum: The graph is plotted based on the number of fluorescence photons generated by a fluorophore (Y) against the emission wavelength (X).

d) Molar extinction coefficient: The ability of a substance to absorb light at a specific wavelength. The fluorescence output for each fluorophore is relative to the extinction coefficient of the product (at the relevant excitation wavelength) and the fluorescence quantum yield.

e) Quantum yield ( $\Phi_f$ ): Number of fluorescence photons emitted for each excitation photon absorbed.

f) Fluorescence quenching: Loss or decrease of fluorescence signal due to short-range interactions between the fluorophore and the local molecular environment, including other fluorophores (self-quenching).

## 1.2 Organic Fluorophores

According to A. Jain, et al., fluorescent chemical compounds known as fluorophores, or fluorochromes, contain a combination of aromatic groups, “planar or cyclic molecules with several  $\pi$  bonds” (A. Jain, Blum, & Subramaniam, 2009). They are hardly used on their own. For example, fluorophores are used as tracers in fluids, as dyes for staining certain structures, as substrates for enzymes, and as probes or indicators. However, they are commonly covalently bonded to macromolecules, which serve as markers. A marker can be a dye, or tag, for affinity or bioactive reagents; for example, antibodies, peptides, and nucleic acids. In general, they are mainly used to stain tissues, cells, or other materials in a variety of analytical methods, such as fluorescent imaging and spectroscopy.

Fluorophores can be divided in to three groups:

- Firstly, there are organic fluorophores, some of which are commonly known as organic dyes, for example anthracene, naphthalimide, pyrene, BODIPY, fluorescein, rhodamine, resorufin, coumarin and cyanine (Figure 1.3) (Jiao, Zhu, Chen, & Duan, 2015). For example fluorescein, is famously applied in biological research for cells labeling and tracking especially in fluorescence microscopy application (J. Liu, Fraire, De Smedt, Xiong, & Braeckmans, 2020). In fact, the derivatives of fluorescein have been chemically blended with the aim to improve their photostability and solubility. Süel (2011) opined that the fluorescent dyes provide higher photostability and brightness than fluorescent proteins (Süel, 2011). Today, there is a wide range of dyes which acquire excitation or emission spectra with optimal quantum yields and excitation coefficients. They are mostly commercially available for any wavelength of fluorescence emission.

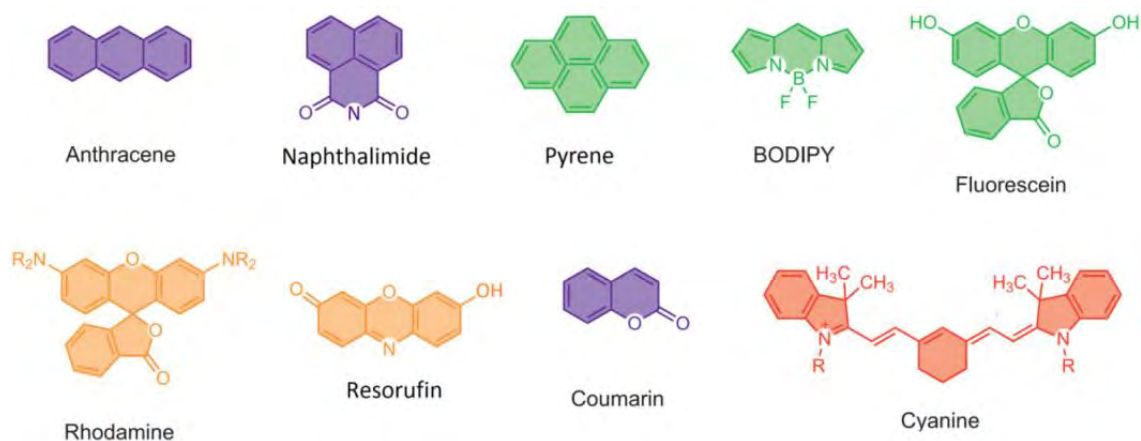


**Figure 1.3 Some common organic dyes.(Jiao et al., 2015)**

- The second group comprises of biological fluorophores. One example of a biological fluorophore is the green fluorescent protein (GFP). GFP was first isolated from jellyfish called *Aequorea Victoria* ("Chapter 1 - Tools of the Cell Biologist," 2008; E. Liu, Vega, Treiser, Sung, & Moghe, 2011), and has been used as a gene expression reporter. Other than GFP, phycobiliproteins are also known as highly fluorescent protein including allophycocyanin, phycocyanin, phycoerythrin, and phycoerythrocyanin compounds, which have been utilised in biological expression systems and are very common in today's biological research (Udayan, Arumugam, & Pandey, 2017).

- The final group is referred to as quantum dots, which include nanocrystals that acquire unique chemical properties. They give strict control over the spectral characteristics of the fluorescence.

Each fluorophore has different characteristics. These characteristics should be known prior to selecting which fluorophore to use for a given application or experimental system. Organic fluorophores are widely utilised as optoelectronic devices (Y. L. Chang et al., 2013; D'Andrade & Forrest, 2004; Youjun Yang, Lowry, Schowalter, Fakayode, Escobedo, Xu, Zhang, Jensen, Fronczek, Warner, et al., 2006; N.-N. Zhang et al., 2017), chemosensors (J. Chen, Cao, Wang, Wu, & Wang, 2009; J. Fan, Hu, Zhan, & Peng, 2013; J. Huang et al., 2014; Luo, Liu, Li, & Luo, 2018; Qin, Yang, Wang, & Li, 2015),

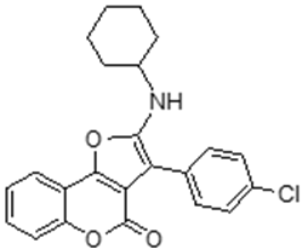
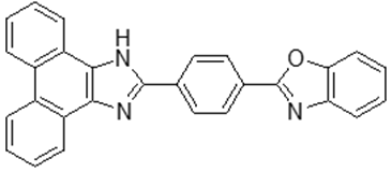
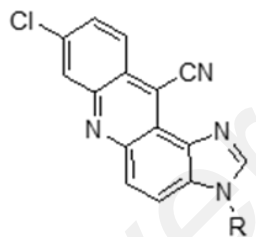
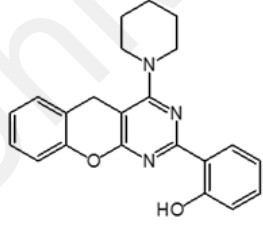
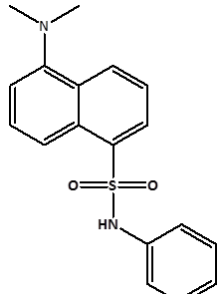
biosensors (Ayranci, Kirbay, Demirkol, Ak, & Timur, 2018; Ming et al., 2017; P. Zhang et al., 2016) and for bioimaging devices (Courtis et al., 2014; Gabe, Urano, Kikuchi, Kojima, & Nagano, 2004; Santra, Zhang, Wang, Tapeç, & Tan, 2001). However, the undesirable photophysical properties of fluorophores limit the potential of their applications. For example, some organic fluorophores typically have the disadvantage of possessing small Stokes shifts (less than  $25 \text{ cm}^{-1}$ ), which can lead to self-quenching and fluorescence detection faults due to excitation backscattering effects. Therefore, there is a need to thoroughly investigate these fluorophores in order to properly determine which organic fluorophore suits the required application. This will also help eliminate or reduce the undesirable photophysical properties of the materials. In the following chapters, an examination is carried out on how each of the photophysical properties of the selected organic fluorophores was applied for the development of white emission light, fluorescent chemosensing and reaction monitoring.

As the first step of this research, a database of organic fluorophores that can give promising fluorescence properties was compiled to select those compounds which can produce broadband or white light emission after mixing. Then, a short-list of candidate compounds was drawn up that can exhibit similar excitation wavelengths but produce different emission wavelengths in order to produce a wide and broadband range of emission wavelengths without overlapping the excitation wavelength, as detailed in Table 1.1.

From initial experiments, furo[3,2-c]coumarin performed well as part of this PhD project. The substance exhibits high fluorescent intensity emitted at 480 nm upon excitation at 375 nm. Furo[3,2-c]coumarin has been a guideline for selection of another heteroaromatic with either a shorter or longer wavelength emission at 480 nm. Then, another preferred synthesised organic fluorophore candidate in this research is dansyl aniline and a purchased chemical namely, carboxylic coumarin. These compounds have

been investigated and found to comprise of excitation wavelengths in a similar range, 340-375 nm. Therefore, based on the expected finding, a broad emission will be produced by mixing of these organic fluorescent candidates due to contain of similar range of excitation wavelengths but emitted at different wavelengths.

**Table 1.1: Organic Fluorophores Surveys**

Compounds	$\lambda_{ex}$ (nm)	$\lambda_{em}$ (nm)	$\Phi_f$	Ref.
	375	480	-	(V. Nair, R. S. Menon, A. U. Vinod, & S. Viji, 2002b)
	374	461 (I = ~150 a.u.)	-	(Y.-F. Sun, Huang, Lu, & Cui, 2009)
 R = alkyl	380	488	0.86-0.92	(Sahraei, Pordel, Behmadi, & Razavi, 2013)
	350	450	0.75	(Shaikh et al., 2014)
	360	530	-	(J. Huang et al., 2014)

### 1.3 Problem Statement and Overview of the Research

Inorganic luminescence has long been established to produce different light emitting materials with all ranges of primary colours. However, most of them are not environmentally friendly due to high energy consumption. Furthermore, the process usually involves, liberates, or contains highly toxic chemicals like arsenic and cyanides. It is also quite expensive because of the high cost involved in the mining operation and the limited amount of raw materials.

Organic fluorophore materials are an alternative to develop the material replacements due to their similar characteristics. Searching for effective organic fluorophores materials that perform similarly is considerably challenging because the energy conversion is still below the expected performance. Besides, synthesising organic fluorophores would be an additional benefit to produce a different condensed environment.

The expected outcome of this research, firstly, is an opportunity to produce broader emission intensities to white light emission and also tunable emission wavelengths by introducing different amounts of compounds to the substrate. Secondly, to produce a novel furocoumarin fluorescence based-sensor and thirdly, to introduce an accelerated synthesis screening method of dansyl aniline for the reaction, performed and monitored by using Paper Spray Ionisation-Mass Spectrometry (PSI-MS).

#### **1.4 Objectives of the research**

The main target of the research is to develop a mixture of fluorophores from varying heterocyclics in order to produce a multiband, or broader emission wavelengths. The target can be achieved by the following objectives:

1. To synthesise and characterise a few organic fluorophores that comprise of an excitation wavelength in the range of 350-375 nm and fluoresce at different wavelengths above 400 nm.
2. To develop white light emission from synthesised organic fluorophores.
3. To produce a fluorescence-based sensor from synthesised furocoumarin.
4. To investigate the accelerated synthesis reaction of dansyl aniline by using a novel form of PSI-MS.

#### **1.5 Thesis outlines**

The overall focus of this dissertation will be on the organic fluorophores and their application in (i) developing white light emissions, (ii) producing fluorescence-based sensors and (iii) investigating the accelerated synthesis reaction of an organic fluorescent by using a novel mass spectrometric setup.

Chapter 2 will mainly focus on the development of white light emission from organic materials. Firstly, this chapter will include an introduction and general findings from previous studies regarding white light emission. There are a few examples of white light emission development from different criteria of organic compounds including simple molecules, macromolecules, oligomers, and self-assembly molecules. At the end of this chapter, white light emission is demonstrated from a mixture of simple molecules in both solution and solid (aerogel) forms. This finding has been published in Nature Scientific Reports.

Chapter 3 will report on the application of coumarin derivatives as fluorescent chemosensors for the detection of the metallic ion,  $\text{Fe}^{3+}$ . Coumarin is a well-known organic fluorophore that mainly emits around 430 nm and produces a blue emission light; its derivatives have been applied as chemosensors for varying types of metal ions; including furo[3,2]-coumarin. This chapter will include our finding about furo[3,2]-coumarin as the fluorescent chemosensor for  $\text{Fe}^{3+}$  and its potential to test with real water samples, which include untreated mineral and tap water samples. This finding also has been published in Nature Scientific Reports.

Chapter 4 will focus on the ambient ionisation method, PSI and its application to accelerate, screen and monitor the synthesis reaction. In this part of the work, the dansyl aniline synthesis reaction was examined by using a modified paper substrate into a dual tip arrangement. Dansyl aniline is an organic fluorophore that allows the reaction between reagents on the paper to be visualised (under UV light illumination) to gain a better understanding of where the reaction takes place (on the paper substrate or in the microdroplet/gas phase). The synthesis monitoring has also been extended to the silyl-alkylated dansyl aniline compound which demonstrates a rapid and simple optimisation procedure based on ratio concentration adjustments.

Finally, Chapter 5 draws conclusions from the research presented in the thesis. It also provides directions for further research and future applications.

## CHAPTER 2: WHITE ORGANIC LIGHT EMISSION

In this chapter it is discovered that white organic light can be emitted from a simple mixture of organic fluorophores. The synthesis of organic fluorophores; furocoumarin and dansyl aniline as well as a purchased chemical (carboxylic coumarin), have been utilised in this research for the generation of white organic light. To start, this chapter will discuss the introduction of white organic light emission, followed by a review of the recent status in the design and development of white organic light emissive materials from single molecules, as well as the combination of molecules including polymeric and self-assembled systems. Then, the chapter describes the main works of this research: “White Light Emission from a Simple Mixture of Fluorescent Organic Compounds” significant parts of which have been published in the scientific peer-reviewed literature (Muhamad Sarih et al., 2019).

### 2.1 Background and Introduction to White Organic Light Emission

Our eyesight is biologically fixed for perceiving the visible spectra within the region ~390-700 nm; this range includes colours: violet, indigo, blue, green, yellow, orange and red (VIBGYOR). White light illumination is required in order to observe, or differentiate, any set of colours, or colour mixtures, within this region (Mukherjee & Thilagar, 2014). The human eyes are familiar to white light illumination due to the common presence of white light derived from both natural and artificial light. Scientifically, white light comes from the composition of three primary colours namely, red (R), green (G), and blue (B). Despite, the human eyes see white light as not has any particular spectral distribution of lights and can be obtained from infinite different compositions of primary colours (Wyszecki & Stiles, 1982). By the year 1931, a standard colourimetric system that has since become widely known by its abbreviation, CIE 1931, was established by the Commission Internationale d’Éclairage (CIE) (Cie, 1932; l’Éclairage, 1924). To date, this system is the preferred standard. Based on the CIE plot, all colours from the visible

spectra are positioned by two coordinates, namely  $x$  and  $y$ . They are called the colour coordinates and CIE regulation stipulates that the colour coordinates for equal energy point of white light are (0.33, 0.33) as shown in Figure 2.1. As aforementioned, the white light is initiated by adjusting the compositions of three primary colours. It also may be initiated by combining any two paired colour of lights with certain amounts only if the link line of their colour coordinates can connect in the white light region (Mukherjee & Thilagar, 2014).

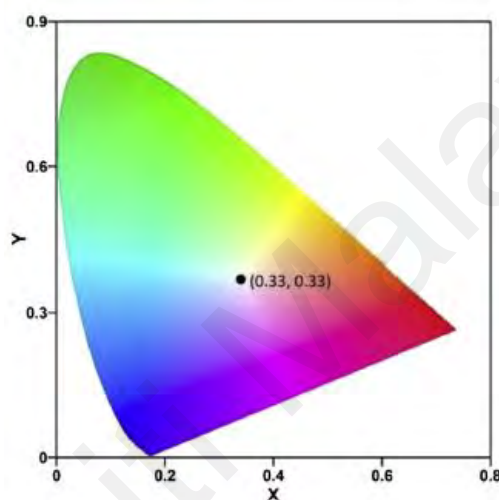


**Figure 2.1: A typical CIE (1931) plot showing the coordinates of pure white light (0.33, 0.33).**

As display and lighting technology develops, efficient and environmentally friendly methods of producing coloured and white light are in increasing demand. Inorganic luminescence has long been established as a means to produce light with a range of colour profiles. However, most inorganic light-emitters are not environmentally friendly due to their high energy consumption and the process usually involving, liberating, or containing scarce metals or highly toxic chemicals like arsenic and cyanides. Organic fluorescent materials show excellent potential as a low-cost, green and sustainable alternative (Klauck, 2006),(V. Singh & Mishra, 2015). The most common application of organic fluorescence is for lighting purposes and there is much research surrounding other applications such as fluorescent labelling for bio-imaging (Galas et al., 2018; Han, Li, Qiu, Zhang, & Zhang,

2017; Kolemen & Akkaya, 2017; McCann et al., 2011; Sozmen et al., 2014) and chemosensors (Atilgan, Ozdemir, & Akkaya, 2010; Bozdemir et al., 2010; Coskun, Deniz, & Akkaya, 2007; Yi Liu et al., 2016; S. Maher et al., 2016; D. Wu et al., 2017). Organic fluorescent materials have contributed significant advancements in the field of artificial lighting for which global energy savings of ~20% are predicted (Mukherjee & Thilagar, 2014). In particular, light emitting devices based on organic materials such as organic light-emitting diodes (OLEDs) and liquid crystal displays (LCDs) have received extensive attention in recent years (Hawken, Lovins, & Lovins, 2013; E. Jang et al., 2010). More recently, the commercialisation of OLED technologies have led to an increased demand for white organic light-emitting diodes (WOLEDs). (Y. L. Chang et al., 2013; D'Andrade & Forrest, 2004; Gaynor et al., 2013; Kamtekar, Monkman, & Bryce, 2010; Shang, Li, & Lin, 2014; Tang et al., 2013)

Several photo-physical principles have been used for achieving white light emission (Mukherjee & Thilagar, 2014; V. Singh & Mishra, 2016b), these include inter- and intramolecular charge transfer (Park et al., 2015), Forster resonance energy transfer (FRET) (Maiti, Bhattacharjee, Datta, & Banerjee, 2013; Sanju, Neelakandan, & Ramaiah, 2011; V. Singh & Mishra, 2015; V. Singh & Mishra, 2016a), excited state intramolecular proton transfer (ESIPT) (Benelhadj et al., 2014; Maity, Ali, Agarwalla, Anothumakkool, & Das, 2015), hydrogen bonding mediated J-aggregation (Molla & Ghosh, 2012) and the mixing of monomer and excimer fluorescence (Yu Liu, Nishiura, Wang, & Hou, 2006). Multi-component white light emission comprises a mixture of different molecules that allow the colour temperature to be tuned by simply adjusting the composition, compared to using a single molecule (N.-N. Zhang et al., 2017). Not surprisingly, there is significant recent interest for generation of mixed emitter white light emission. Such systems comprise of inorganic, organic and hybrid systems including polymers (Nicolai, Hof, & Blom, 2012), metal-organic frameworks (C.-Y. Sun et al., 2013; Q.-Y. Yang et al., 2014),

metal complexes (Sessolo, Tordera, & Bolink, 2013) and lanthanide doped systems (Ledemi et al., 2014). Several examples of strategies employing mixtures of organic fluorophores have been reported, including a mixture of three emitting dyes covering the RGB region (Sanju & Ramaiah, 2013), donor-acceptor conjugated pairs (Maiti et al., 2013) and self-assembly based compounds (Abbel et al., 2009; Giansante et al., 2011; Giansante, Schäfer, Raffy, & Del Guerzo, 2012; Vijayakumar, Sugiyasu, & Takeuchi, 2011; X. Wang, Yan, Zhou, & Pei, 2010). Others have mixed a range of oligomers that rely on intramolecular fluorescence energy transfer processes like FRET to produce tuneable white light emission (Balan, Vijayakumar, Ogi, & Takeuchi, 2012; Melucci et al., 2010; Vijayakumar et al., 2011). In the following sections, different types of organic white-light emissive materials are discussed with their design strategies and emission properties.

## 2.2 White Organic Light Emissive Materials Reviews

Ideally, the white light emitter requires concurrent emission of the three primary colours with nearly similar distribution of intensities covering the entire region of the visible spectrum. However, the production of white-light emitters is not an easy process because of the negative effects of intermolecular interactions and energy transfer processes causing the failure of mixing several emitters. A vast range of research has widely considered this issue which has led to reasonable progress of organic white-light emitters. Moreover, the designs produced have sufficiently helped a large area of the chemistry including energy transfer, simple protonation, designed self-assembly, and the simple mixing of materials. Wang et al, 2009, revealed that white light emission is achieved by simultaneous emission from a single layer of diblock copolymer micelles containing green (Rhodamine 110 chloride (**R110**)) and red-light-emitting dyes (sulforhodamine 101 (**S101**)) in the separate micellar cores and blue-light-emitting polymer (Polyfluorene (**PF**)) around their periphery, as illustrated in Figure 2.2 (Ruobing

Wang, Peng, Qiu, Yang, & Xie, 2009). The FRET between fluorophores is inhibited owing to micelle isolation, causing simultaneous emission of these three species. To produce simultaneous emission, **PF** toluene, **R110**-loaded micellar, and **S101**-loaded micellar were mixed with a certain ratio and then spin-coated at 2000 rpm for 60 s or solvent-cast onto quartz or silicon substrates.

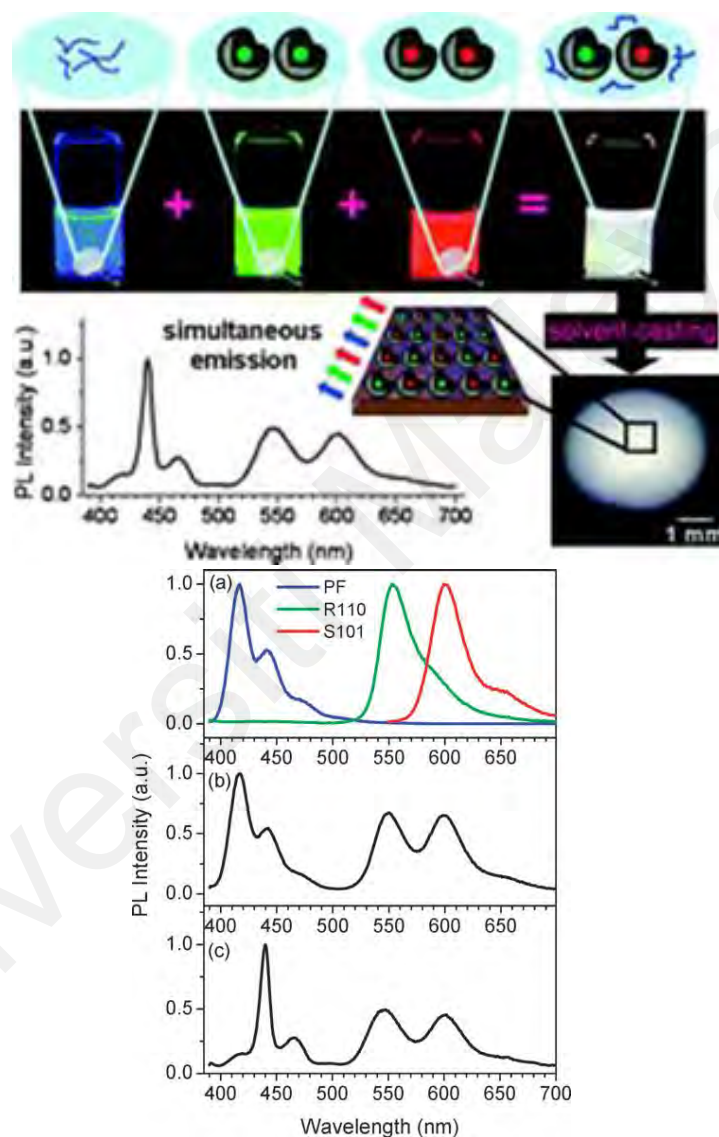


**Figure 2.2:** (a) The normalised PL spectra of PF toluene solution (blue line), PS-b-P4VP/R110 micellar solution (green line), and PS-b-P4VP/S101 micellar solution (red line). (b) PL spectra of white light emitting solution and (c) white light emitting solid film of PS-b-P4VP/PF/R110/S101, at 380 nm excitation wavelength (Ruobing Wang et al., 2009).

Enhancement of the research by Wang et al., has been attained by adding Coumarin 343 (C343) as the light-collecting donor which could be encapsulated in the micellar cores together with the light-emitting acceptor R110, or S101, because the emission spectrum of C343 overlaps well with the absorption spectra of R110 and S101, as shown in Figure 2.3 (Ruobing Wang, Peng, Qiu, & Yang, 2011). FRET was permitted between a donor and an acceptor in cores but was blocked among these three light-emitting species by micellar coronas, which was caused in their enhanced simultaneous emissions.

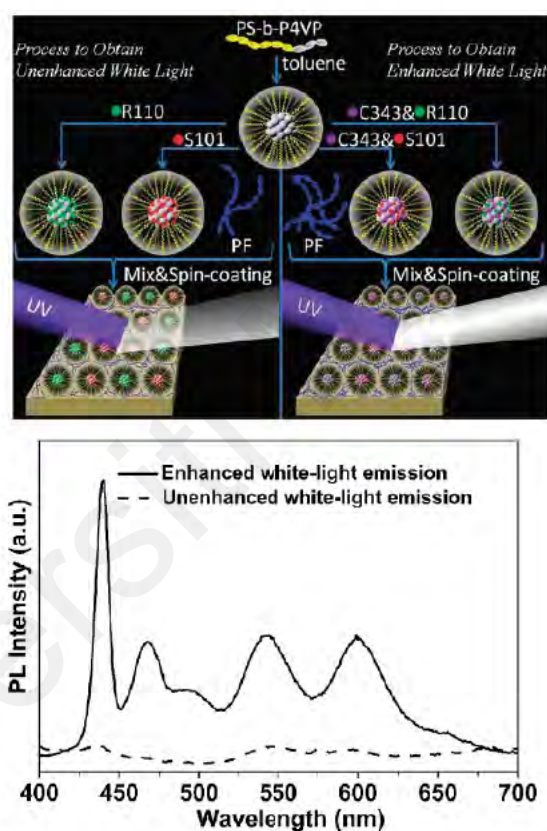


**Figure 2.3:** Top. Schematic illustration for the unenhanced (left) and enhanced (right) white light from a single layer of diblock copolymer micelles. Bottom. The spectra of both enhanced white light emitting thin film PS-b-P4VP/PF/C343–R110/C343–S101 (black solid line) and unenhanced white light emitting thin film PS-b-P4VP/PF/R110/S101 (black dotted line) under excitation light of 380 nm (R. Wang et al., 2011).

Babu et al., have generated solvent-free luminescent white light emitting organic liquids by combining the green emitting (tris(8-hydroxyquinolinato)aluminium) (Alq3) and orange/red emitting (rubrene) components with blue emitting Oligo(p-

phenylenevinylene) (**OPV**) in the required molar ratio. The mixtures were blended by using a spatula in a watch glass, as illustrated in Figure 2.4 (Santhosh Babu et al., 2012). Figure 2.5 shows the solvent-free white-light emitting dye liquids, which can be applied onto several surfaces and also onto LEDs that are made by blending of liquid **OPVs** with emissive solid dopants.

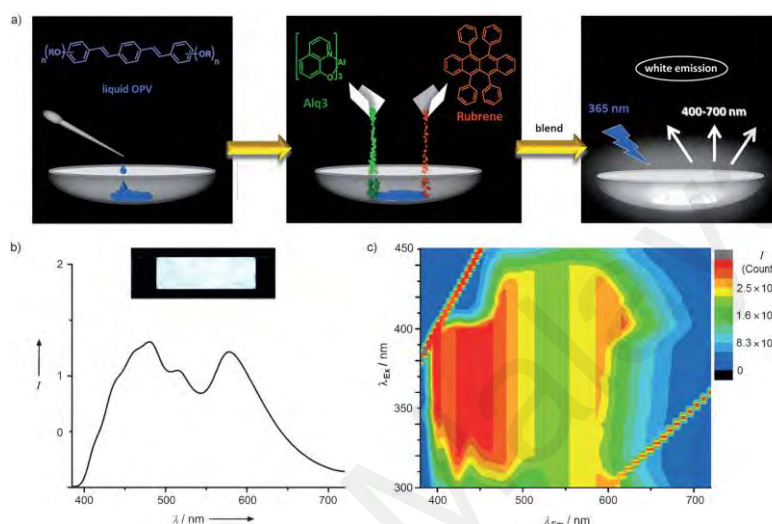


**Figure 2.4:** (a) Illustration of the preparation of solvent-free white-emitting liquid composite. (b) Emission spectrum of OPV ( $\lambda_{ex}=360$  nm) supported on quartz plate; inset shows the image of the white emission from OPV. (c) Fluorescence matrix scan of composite material (Santhosh Babu et al., 2012).

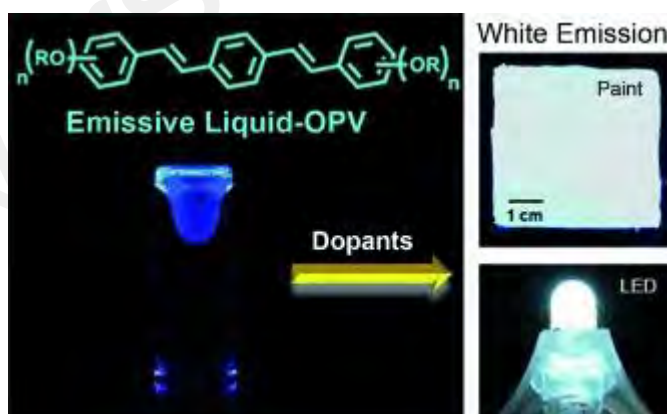


**Figure 2.5:** The blend of liquid OPVs with emissive solid dopants on a glass surface as paint and on LED generating white illumination (Santhosh Babu et al., 2012).

Other than that, oligofluorene-based nanoparticles can also achieve colour tuneable emission including white, for example, fluorene-based linear p-conjugated oligomers with different end functional groups having zero- (**OF1**), one- (**OF2**), two- (**OF3**) and three-point (**OF4**) hydrogen bonding sites (chemical structures are given in Figure 2.6,

Top) (Balan et al., 2012). The white emission was achieved by using a re-precipitation method in which self-assembled nanoparticles were prepared in aqueous medium. The fluorescence quenching pointedly rises from **OF1** to **OF4** designating enhanced interaction between chromophores with increasing number of hydrogen bonding sites in the molecules. As shown in Figure 2.6 Bottom (b), the **OF3** nanoparticles were used as a donor scaffold for FRET by encapsulating varying amounts of an orange-red emitting neutral dye, 4-(dicyanomethylene)-2-methyl-6-(4-dimethylamino-styryl)-4H-pyran (**DCM**), thereby achieving colour tuneable emission including white. The FRET efficiency with both dyes showed direct correlation with the number of H-bonding sites. Therefore, it showed the hydrogen bond assisted modulation of functional properties and colour tuneable FRET emission towards the oligofluorene-based nanoparticles in aqueous medium.

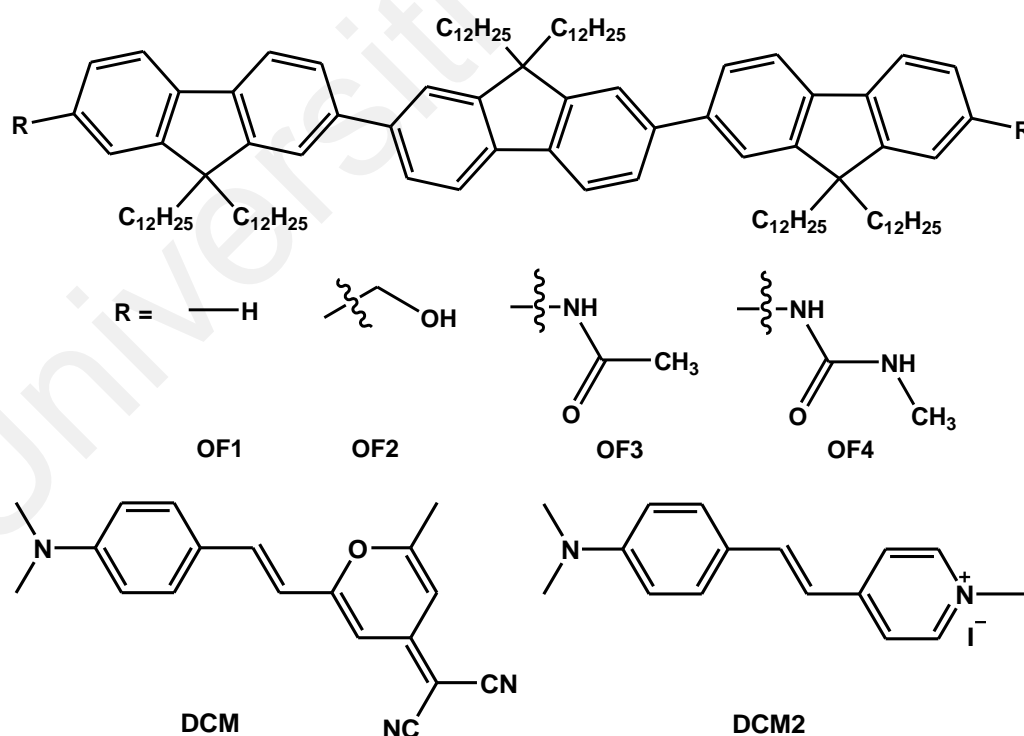


**Figure 2.6: Top. Chemical structures of OF (1-4) = Oligofluorene derivatives, DCM = 4-(dicyanomethylene)-2-methyl-6-(4-dimethylamino-styryl)-4H-pyran and DCM2 = 4-(4-diethylaminostyryl)-N-methylpyridinium iodide.**

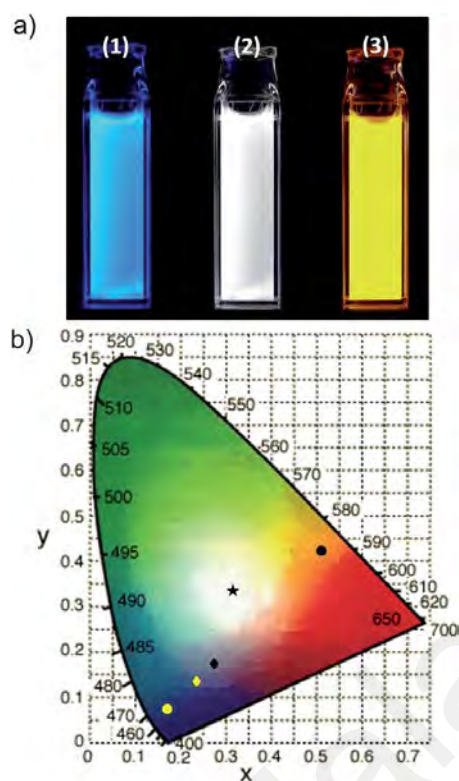


**Figure 2.6: Bottom (a) Photographs of OF3 nanoparticles containing (1) 0 mol%, (2) 0.8 mol% and (3) 4 mol% of DCM (encapsulated) under 365 nm UV light. (b) CIE coordinate diagram of the emission colours obtained for OF3 nanoparticles alone (yellow circle), containing 0.8 mol% of DCM (black star) and DCM2 (yellow diamond) (Balan et al., 2012).**

Another example of using oligofluorene nanoparticles for producing white light emission utilises self-assembled, surfactant-free organic nanoparticles of an oligofluorene derivative (**OF**) in aqueous medium that encapsulate with an orange–red emitting dye, 4-(Dicyanomethylene)-2-methyl-6-(4-dimethylaminostyryl)-4H-pyran (**DCM**) as illustrated in Figure 2.7 (Vijayakumar et al., 2011). The blue emission of the **OF** nanoparticles was tuned to white through FRET by encapsulating **DCM** (1 mol%) within the **OF** nanoparticle scaffold.

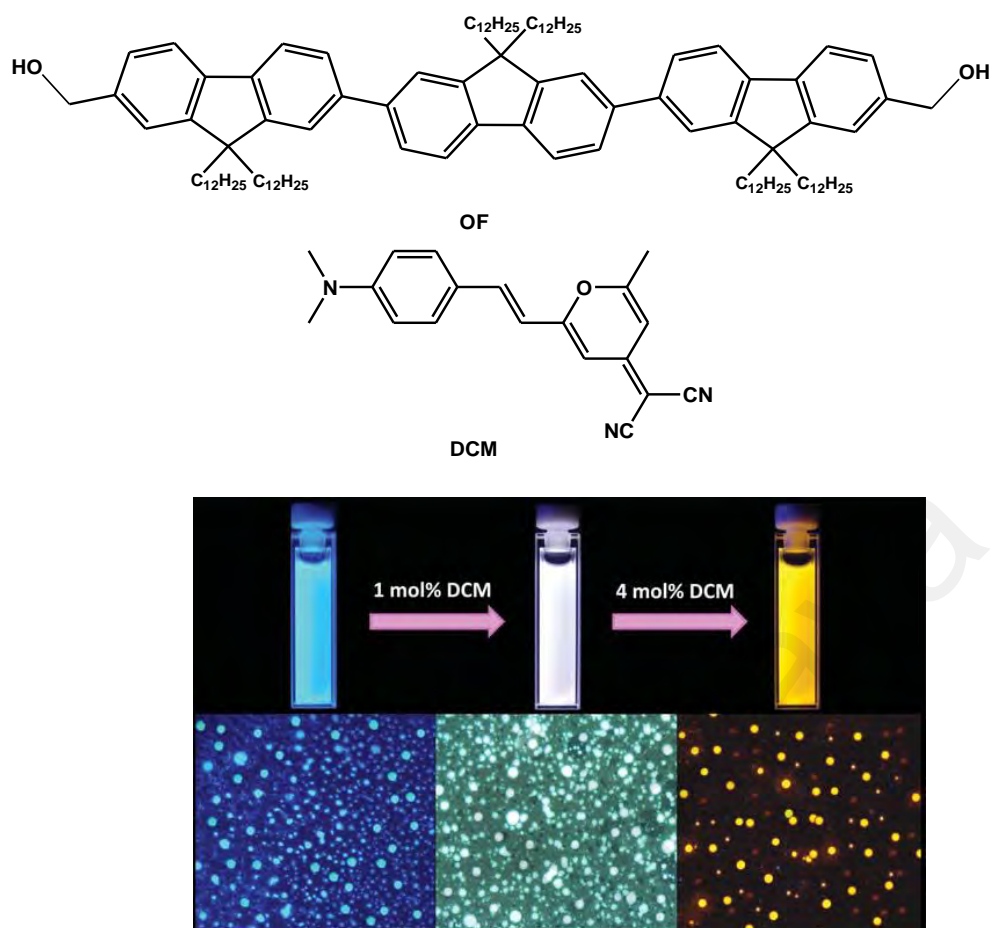


**Figure 2.7:** (Top) Chemical structures of OF and DCM. Photographs of the nanoparticle dispersion in aq. medium with different concentrations of DCM ( $\lambda_{\text{ex}} = 365 \text{ nm}$ ) and (bottom) the FL microscopic images ( $\lambda_{\text{ex}} = 330\text{--}380 \text{ nm}$ ) (Vijayakumar et al., 2011).

Besides, a co-assembled light-harvesting melamine (**M**) hydrogel, 6,7-dimethoxy-2,4[1H, 3H]-quinazolinedione as blue (**Q**) with riboflavin as green (**R**), can also be used to produce an organic white light emitting hydrogel (W-gel) by mixing with the dye rhodamine B as orange (**RhB**) in a required proportion, as shown in Figure 2.8. (Top) (Bairi, Roy, Chakraborty, & Nandi, 2013). By varying the **RhB** and **R** concentration in a constant molar ratio of **Q** and **R**, at 1:1 **MQ** gel white light emission is observed for the W-gel composition having molar ratio of **M:Q:R:RhB** = 100:100:0.5:0.02 with CIE coordinates of (0.31, 0.36) for excitation at 360 nm, as illustrated in Figure 2.8, Bottom.

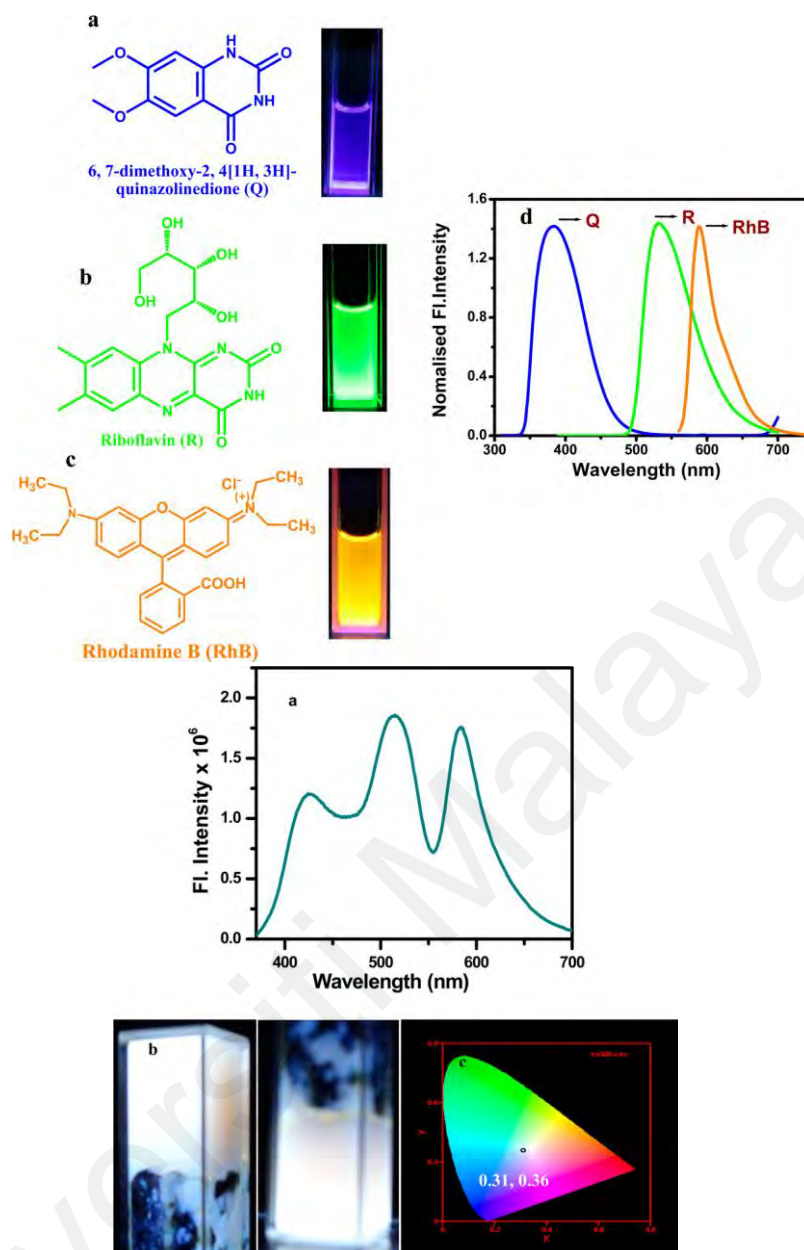


**Figure 2.8: Top. Chemical Structures of Q, R, and RhB, Photograph of each solution under UV Light irradiation excited at 365 nm; (d) Normalised Fluorescence Spectra of Q, R, and RhB in their solution. (a) Fluorescence spectra of W- gel having molar ratio Q:M:R:RhB 100:100:0.5:0.02 for excitation at 360 nm, Bottom. (b) Photograph of W-gel under UV light at 365 nm, and (c) CIE coordinate for W-gel (0.31, 0.36) (Bairi et al., 2013).**

Another study reports white light photoluminescent (PL) silica nanoparticles and their applications to produce PL polymer films and nanofibers. The photoluminescent used is Rhodamine B (**RhB**) which physically adsorbs or chemically bonds to silica nanoparticle (**SNP**) surfaces, which results in **RhB**- modified **SNPs** (Figure 2.9) (Hsu & Liu, 2010). The **RhB**-modified **SNPs** display white light PL emissions when excited at 365 nm,

which is different from the characteristic **RhB** emission (yellow light emission). The physically adsorbed (PA) **RhB** to **SNPs** (**PA-RhB/SNP**) show stimuli-responsive properties, but in solution, the **RhB** molecules were released from **SNPs**, so the PL emission turned from white light to yellow emission. Alternatively, covalently bonded (CB)-**RhB** molecules with **SNPs** (**CA-RhB/SNP**) are effective to produce white light PL polymer composites; poly(methylmethacrylate) (PMMA) films (from casting process) and nanofibers (from electrospinning process), as shown in Figure 2.10.

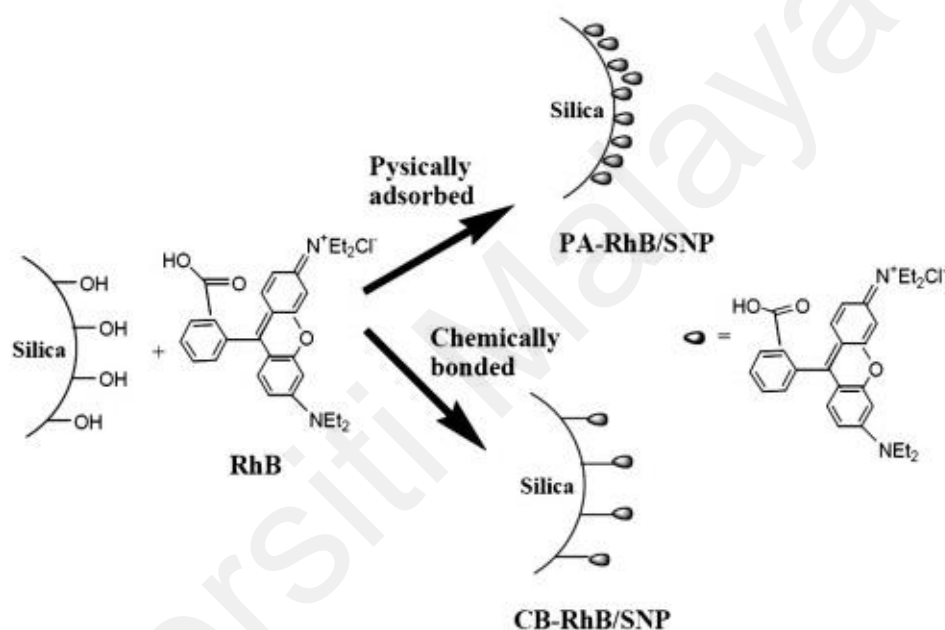


**Figure 2.9: RhB-containing silica core-shell nanoparticles showed white light emissions under UV (365 nm) (Hsu & Liu, 2010).**

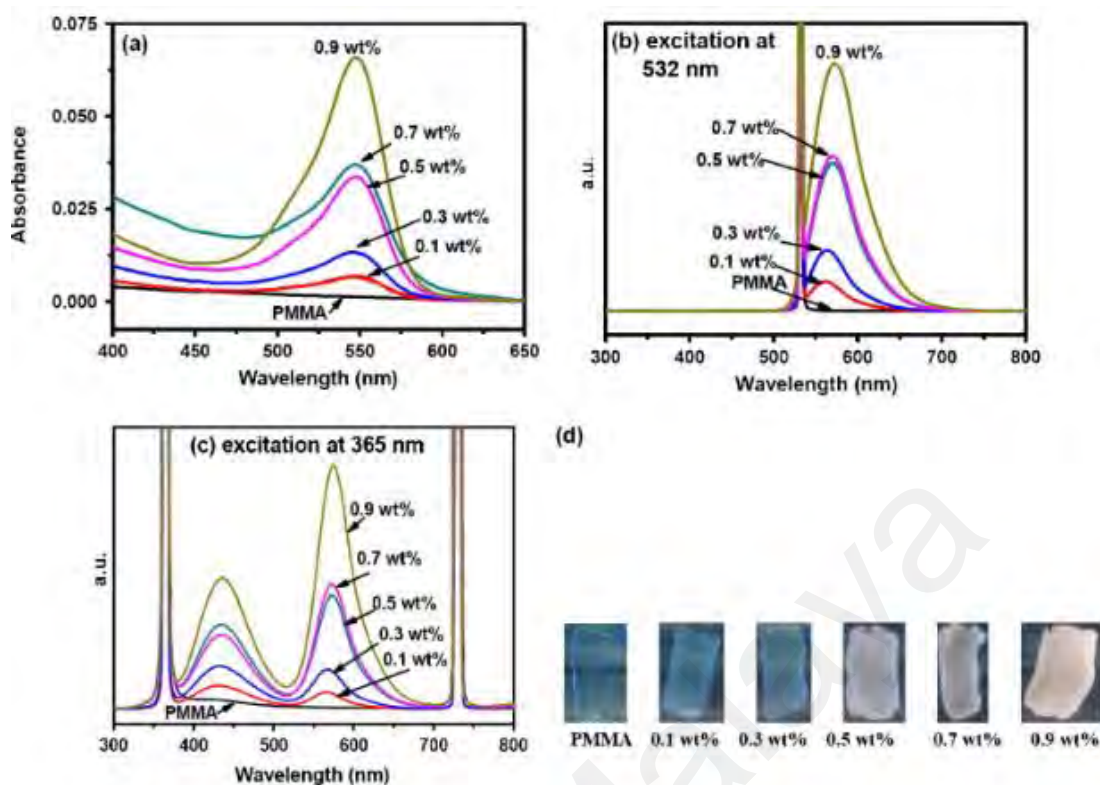


**Figure 2.10: (a) Absorption spectra, (b) PL spectra under excitation at 532 nm, (c) PL spectra under excitation at 365 nm, and (d) photographs under excitation at 365 nm of pristine PMMA and its composite films with CB-RhB/SNP in different concentrations (Hsu & Liu, 2010).**

An interesting study uses donor-acceptor molecules for modulation of FRET to produce white light emission from a sequence of stilbene moiety (**D1-D3**) having donor molecules (blue emitters) and a series of perylene moiety (**A1-A3**) comprising acceptor molecules (orange emitters) that were blended together in chlorobenzene (highly toxic) solution, the chemical structures are shown in Figure 2.11 (Maiti et al., 2013). The compounds have been selected for donor-acceptor sets in FRET in order to relate energy transfer efficiency with the white light emission. It revealed that commonly good energy transfer efficiency leads to white light emission, while poor efficiency of energy transfer displays no significant white light emission. Figure 2.12 shows the UV-vis absorption spectra of white light emitting solutions from different pairs of donors and acceptors and Figure 2.13 shows the photograph of the white light emitting solutions coated onto the LED.

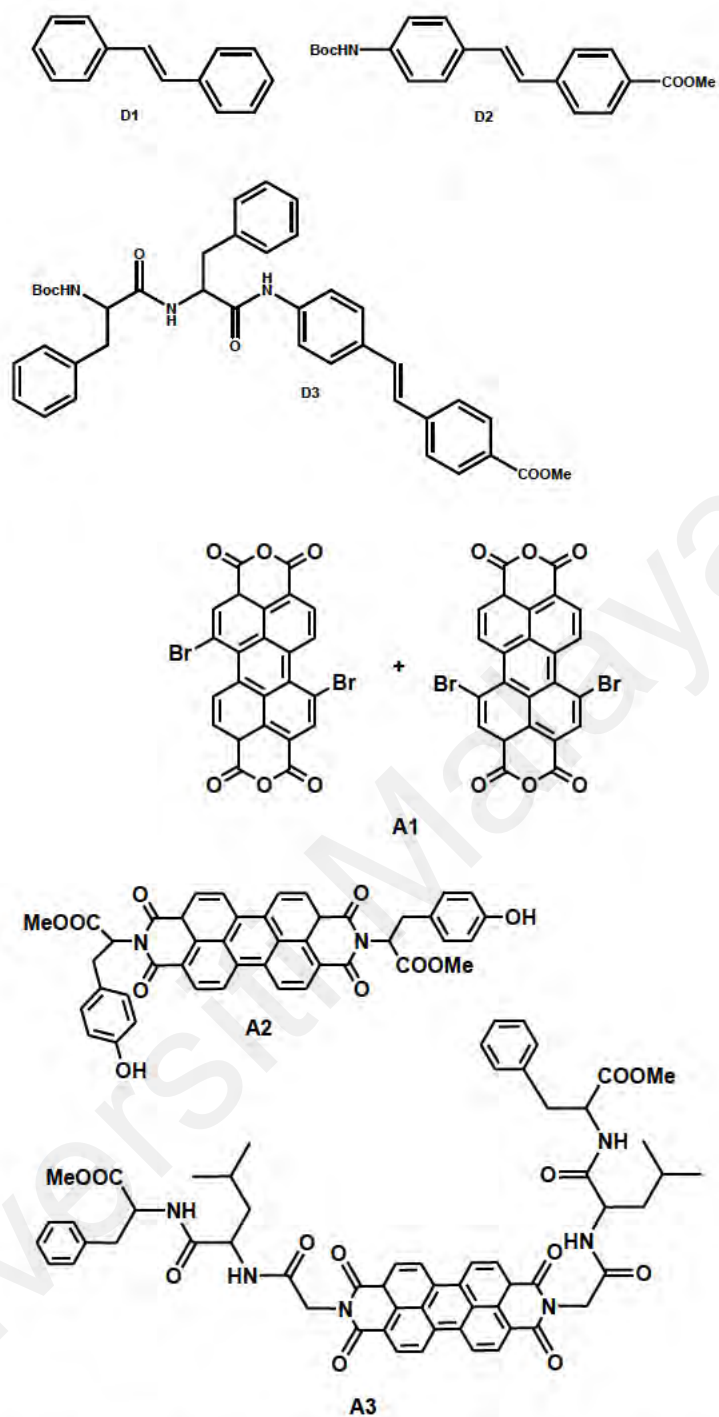


**Figure 2.11: Chemical structures of stilbenes (D1-D3) and perylenes (A1-A3) derivatives.**

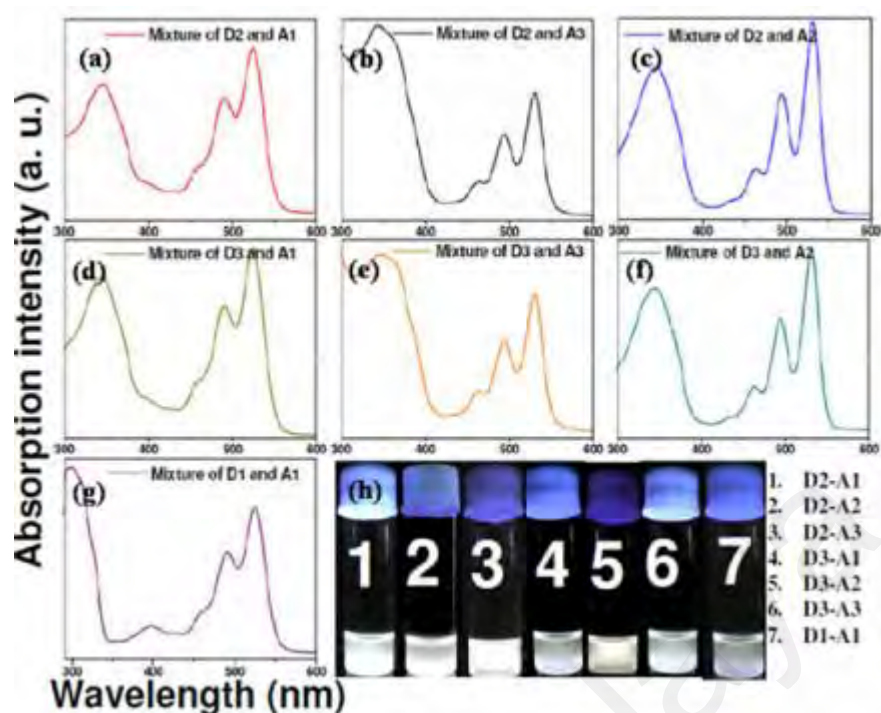


**Figure 2.12:** UV-vis absorption spectra of white light emitting solutions of different pair of donors and acceptors: (a) D2-A1 (b) D2-A3 (c) D2-A2 (d) D3-A1 (e) D3-A3 (f) D3-A2 (g) D1-A1 (h) White light emitting solutions exposed to the UV lamp at 365 nm (Maiti et al., 2013).



**Figure 2.13:** Photographs of commercially available UV-LED coated with white light emitting solutions: (a) D1-A1 (b) D2-A1 (c) D2-A2 (Maiti et al., 2013).

A white light emitting organogel has been produced and reported that employs RGB emission to control donor self-assembly and excitation energy transfer modulation (Vijayakumar, Praveen, & Ajayaghosh, 2009). There are two donors, bischolesterol-OPV (**B-OPV**) and monocholesterol-OPV (**M-OPV**) for which the chromophores are packed as pseudo-J-type aggregates and an acceptor. Conjugated **oligomers** produce red-light-emission for producing the organogels (Figure 2.14, Top image). Energy transfer studies between donor and acceptor were carried out by mixing appropriate volumes to a decane solution. The concentration of the donor **B-OPV** is maintained at  $3.2 \times 10^{-4} \text{M}$  while the amount of acceptor varied from 0 to 2 mol%. The mixture was then heated to  $80^\circ\text{C}$  to

form a homogeneous solution, and slowly cooled to room temperature, to form co-assembled gels for producing white light emitting organogels, as illustrated in Figure 2.14 (a) and (b).

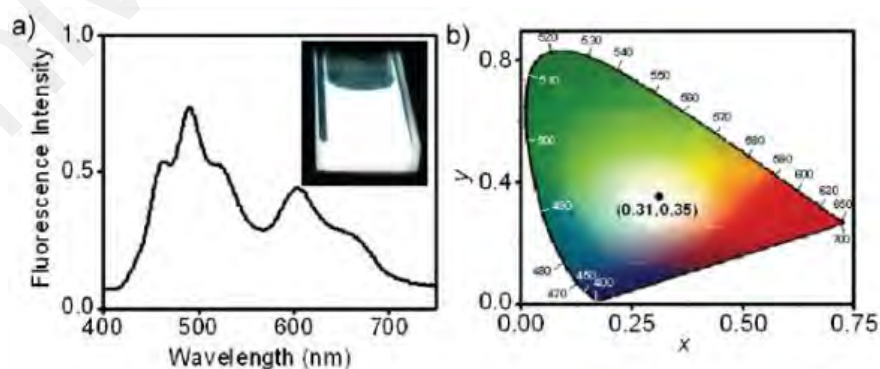
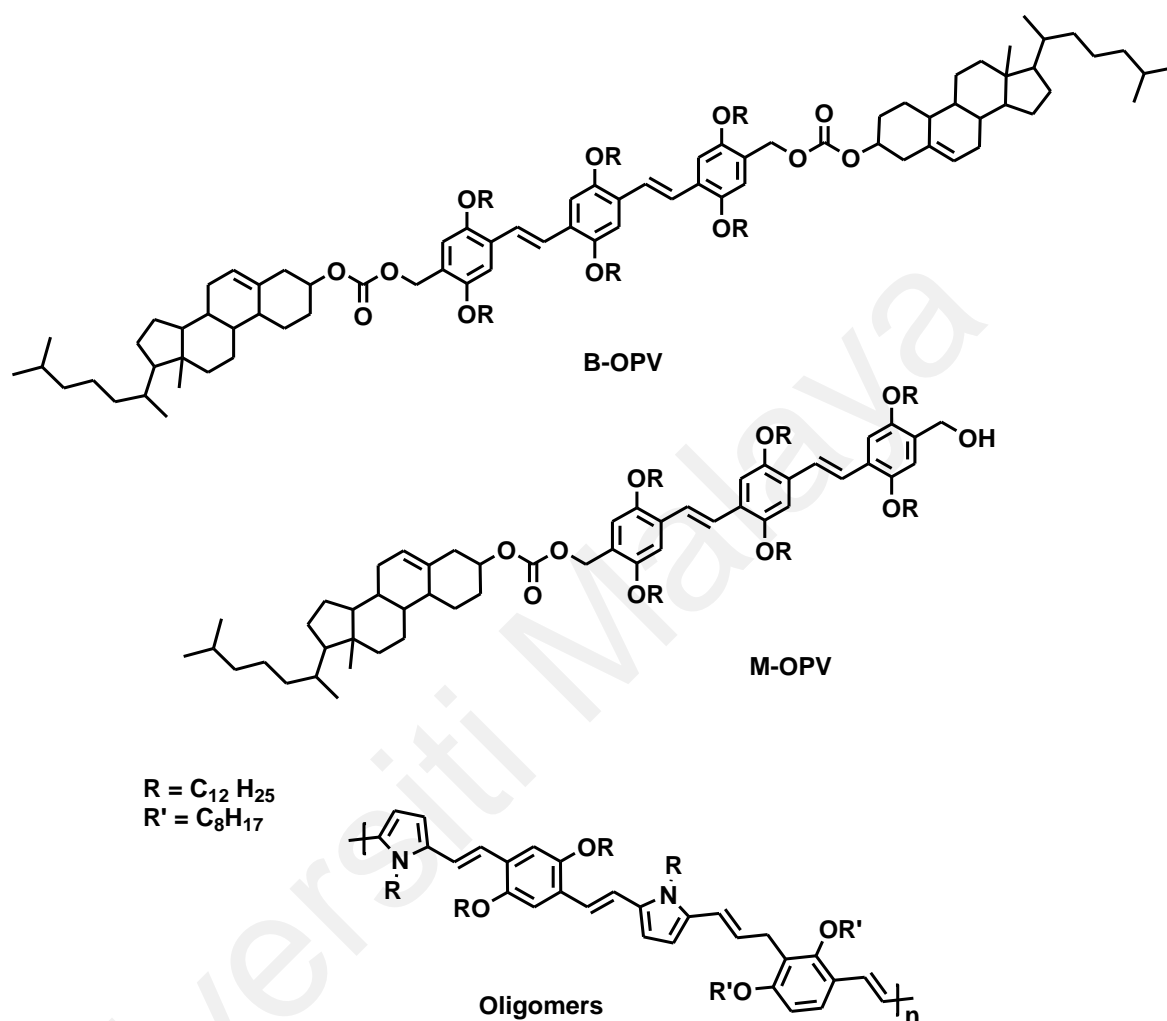


**Figure 2.14: Top. Chemical structures of B-OPV, M-OPV, and oligomers. (a) Fluorescence emission spectrum of a decane gel of 1 ( $3.2 \times 10^{-4} M$ ) in presence of 2.1 mol % of 3 (ex. = 380 nm). Inset shows the white light emission of the gel under UV light at 365nm. (b) The corresponding 1931 CIE coordinate diagram of the white light emission ( $x = 0.31$ ,  $y = 0.35$ ) (Vijayakumar et al., 2009).**

Maiti and Banerjee reported a white light emitting system from a peptide based on two components (Maiti & Banerjee, 2013). It was established on the basis of a co-assembly of a perylene diimide (PDI) that contains a peptide system as an acceptor and a stilbene as a donor in organic solvents, chemical structures are shown in Figure 2.15 (a). **Peptide 1** contains a stilbene moiety, as a blue emission, while **peptide 2** is made-up of PDI and peptide compound as an orange fluorescence emission. Both are excited at 365 nm as illustrated in Figure 2.15 (b) and (c). In Figure 2.15 (d) the white light emission has been produced by mixing equimolar of **Peptide 1** and **Peptide 2** in o-dichlorobenzene (ODCB).

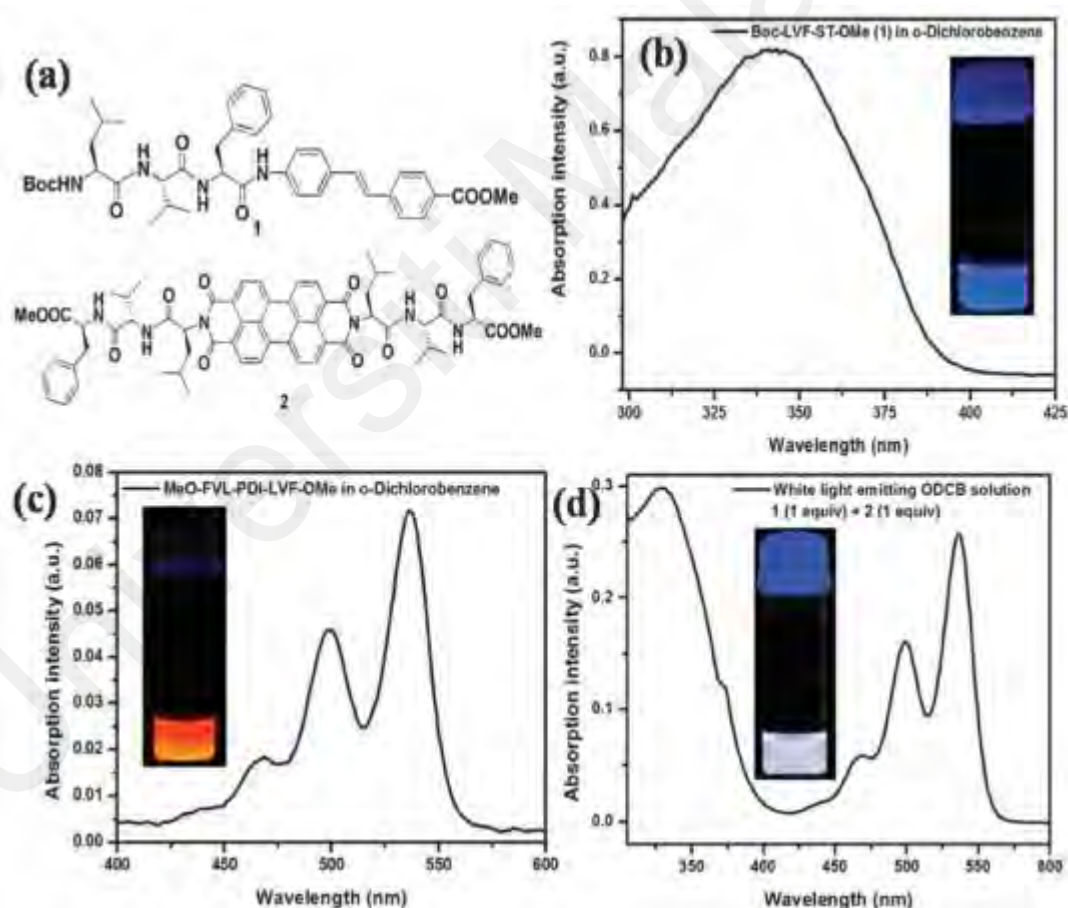


**Figure 2.15:** (a) Chemical structures of Peptide 1 and Peptide 2; the UV absorption spectrum of (b) Peptide 1 (c) Peptide 2 (d) the white light emitting solution in ODCB. Inset shows the white light emission of the gel under UV light at 365nm (Maiti & Banerjee, 2013).

There are three components of self-assembled nanofibers which have been discovered by a direct and cascade energy transfer to yield colour-tuneable and white light emission. (Giansante, Schäfer, Raffy, & Del Guerzo, 2012) The co-self-assembly of a blue-light emitting organogelator (2,3-didecyloxy-anthracene (**BLUE**)), 2,3-dihexadecyloxy-5,12-diphenyl-tetracene (**G**) as green emitting, and red emitting from 2,3-dihexadecyloxy-5,6,11,12-tetraphenyl-tetracene (**RED**) hosts yield light harvesting nanofibers with tuneable emissive properties (Figure 2.16). White light emission is achieved in organogels under near-UV excitation, and their establishing nanofibers as identified by confocal fluorescence micro-spectroscopy.

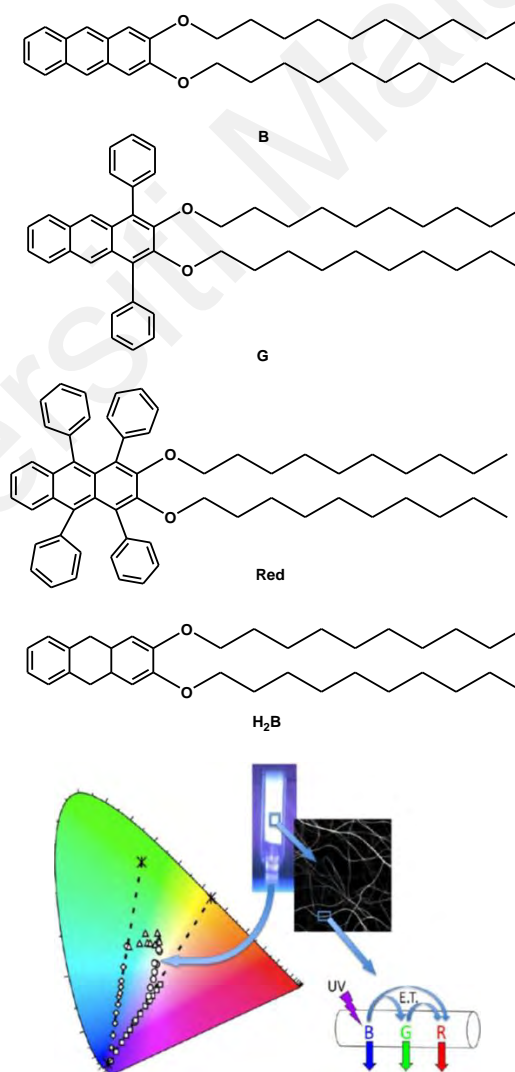


**Figure 2.16: The chemical structures of B, G, Red, H<sub>2</sub>B and the white light emitting nanofibers made up from B, G and Red (Giansante, Schäfer, et al., 2012).**

Liu et al., established the first aggregation-induced enhanced emission (AIEE) materials for producing white organic light-emitting diodes (WOLEDs) (S. Liu, Li, Diao, & Ma, 2010). The construction of WOLED by combining both, orange AIEE material (1,4-bis(a-cyano-4-diphenylaminostyryl)-2,5-diphenylbenzene (**CN-DPASDB**) and blue AIEE molecules, 2,5,20,50-tetrakis(2,2-diphenylvinyl) biphenyl (**TDPVBi**) leads to simplification in device fabrication and excellent colour stability, which is perhaps the most impressive fluorescent WOLED reported, as shown in Figure 2.17.

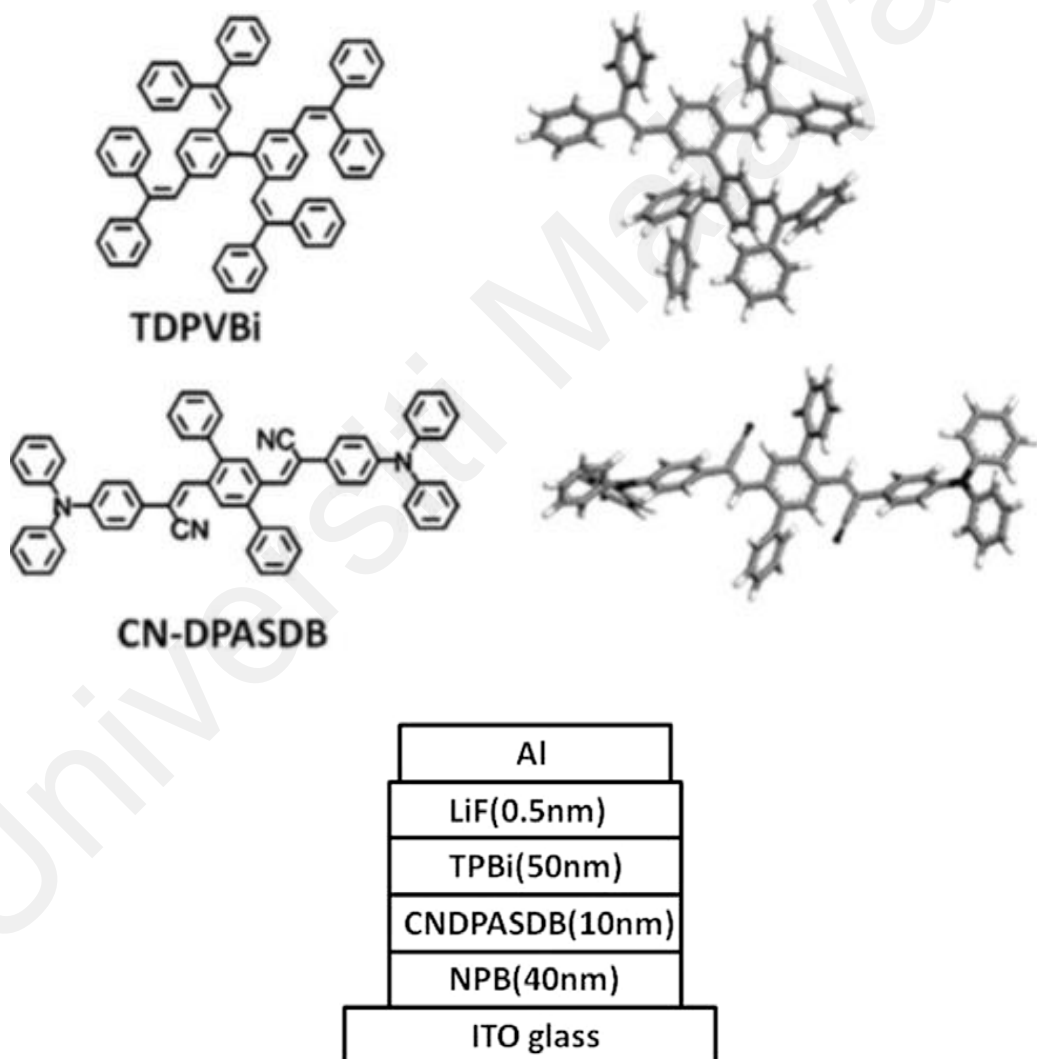


**Figure 2.17: Top. The chemical structures of (CN-DPASDB) and TDPVBi. Bottom, The layers of WOLED comprises of AIEE materials (S. Liu et al., 2010).**

Remarkably, Zhang et al., reported white light emission from single-component small organic triazole molecules, between 1-(4-acetylphenyl)-1,2,3-triazole (**1**) and 1-(4-carboxyphenyl)-1,2,3-triazole (**2**) in the solid form for the first time (Figure 2.18) (N.-N. Zhang et al., 2017). This unusual characteristic of broadband emission can be tuned by adjusting the degree of electron delocalisation and intermolecular interaction intensities. Figure 2.19 shows the photographs of a UV LED with and without coats of samples **1** and **2** in the PMMA matrix.

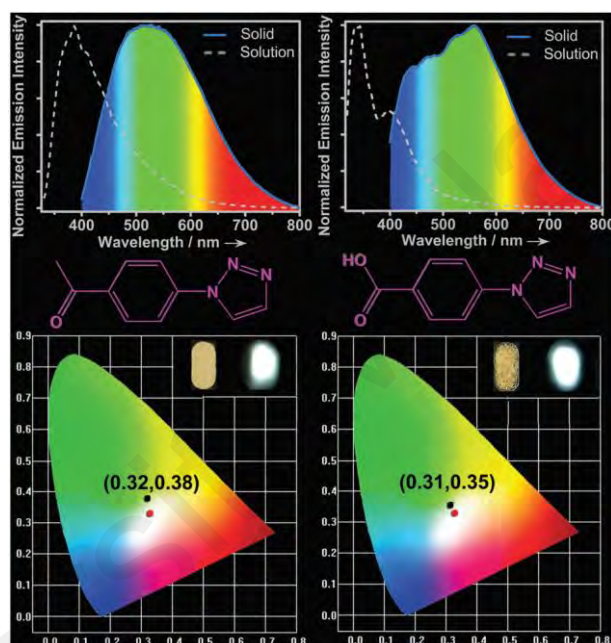


**Figure 2.18:** Top. Photoluminescence spectra of **1** (left) and **2** (right) in the crystalline state at ex. = 370 nm and in  $5 \times 10^{-5}$  M DMF solution (ex. = 315 nm for **1** and 320 nm for **2**). Middle. Chemical structures of **1** and **2**. Bottom. CIE coordinates and photographs (inset) for crystalline samples of **1** and **2** under excitation at 370 nm. Red dots show the CIE coordinates for ideal white light, (0.33, 0.33) (N.-N. Zhang et al., 2017).

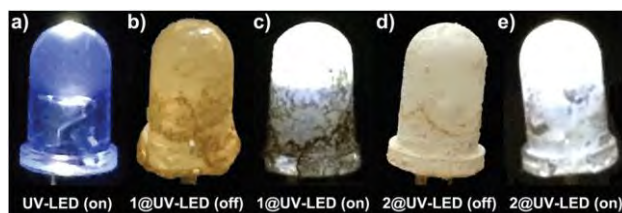


**Figure 2.19:** Photographs of a commercially available 5 mm 365–370 nm UV LED illuminating purple blue light (a: turn on); the UV LED coated with a thin layer of sample **1** in the PMMA matrix (b: turn off; c: turn on); the UV LED coated with a thin layer of sample **2** in the PMMA matrix (d: turn off; e: turn on) (N.-N. Zhang et al., 2017).

**Anthocyanins** and **curcumin** mixture extracted from red pomegranate and turmeric produced almost pure white light emission when photoexcited at 380 nm, with CIE chromaticity index (0.35, 0.33) in acidic ethanol (V. Singh & Mishra, 2015). Figure 2.20 shows the chemical structures of **anthocyanins** and **curcumin** and their emission colours. White light emission was also observed in polyvinyl alcohol film (0.32, 0.25), and in gelatin gel (0.26, 0.33) using the same extract mixture (as shown in Figure 2.21). It was perceived that a cascade of FRET involving polyphenolics, curcumin and anthocyanins contributed a vital role in gaining a CIE index near to pure white light.

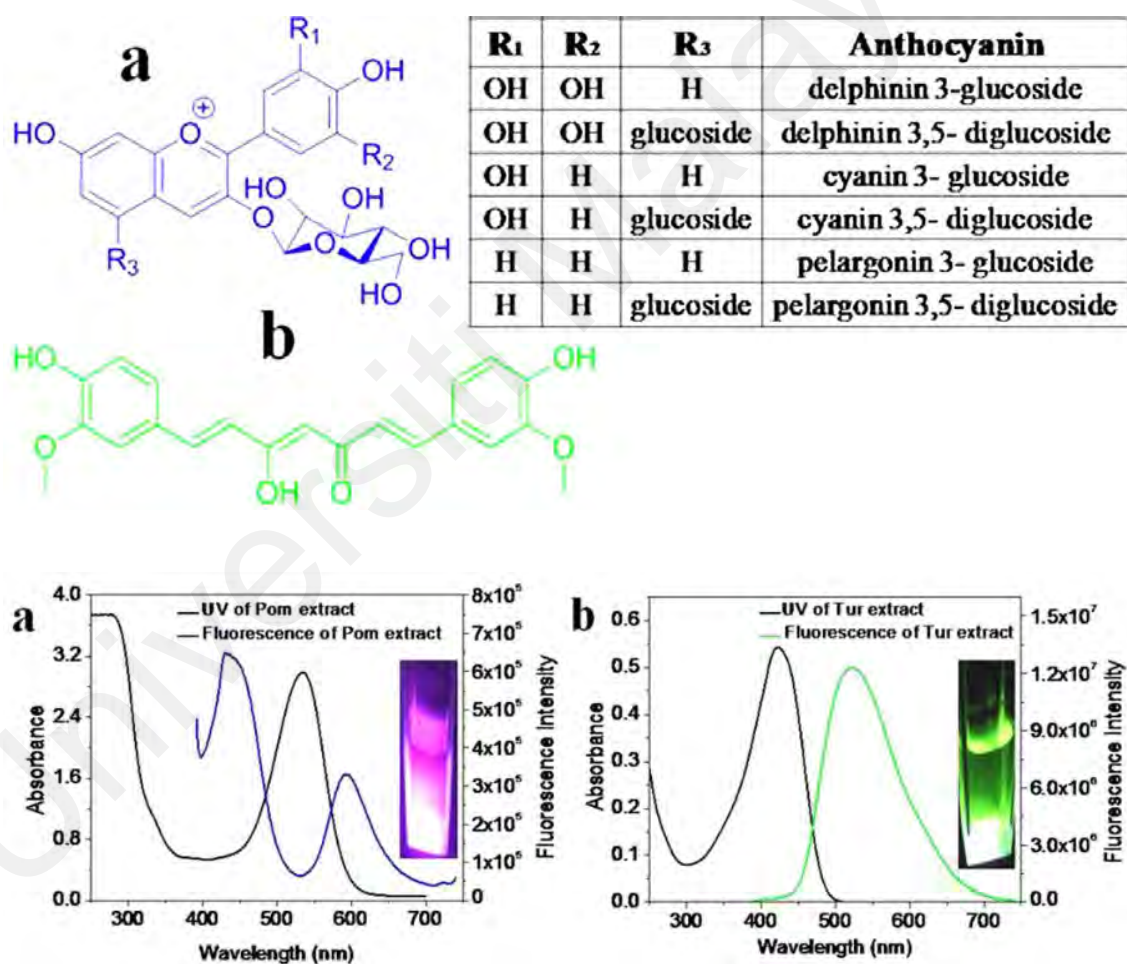


**Figure 2.20:** Top. Chemical Structures of (a) Anthocyanins and (b) Curcumin. Bottom. UV-Visible spectra (black) and fluorescence spectra. (a) Pom extract (blue line), [anthocyanin] = 85  $\mu\text{M}$  and (b) Tur extract (green line), where [Curcumin] = 9.85  $\mu\text{M}$  with their fluorescent images under UV lamp, in 1% HCl ethanol at ex. = 380 nm (V. Singh & Mishra, 2015).

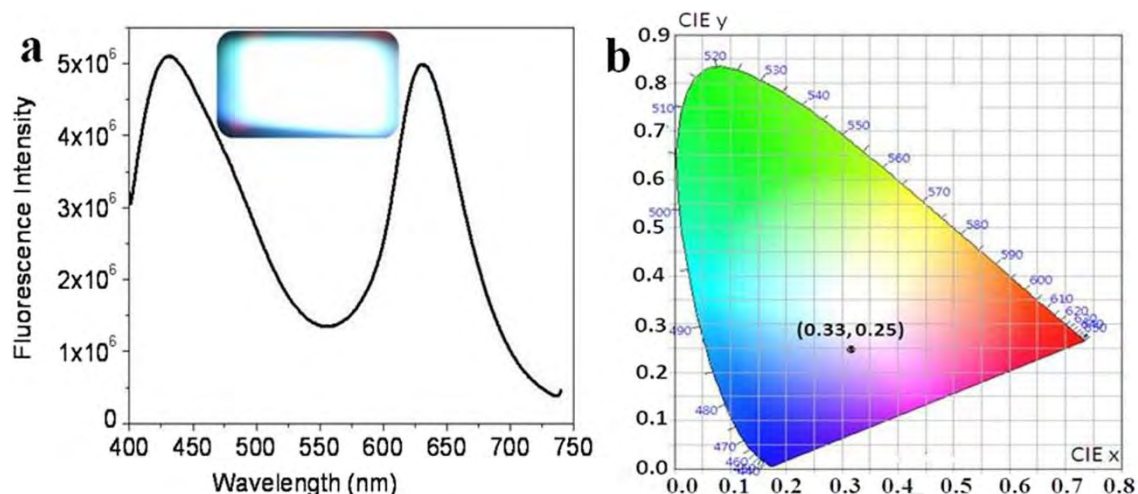


**Figure 2.21: White light emission in PVA film. (a) Emission spectrum of white light emission combined with PVA film, inset displays excellent white photograph of PVA film under UV excitation (380 nm) and (b) CIE coordinate plot white light emitting PVA film (0.32, 0.25) (V. Singh & Mishra, 2015).**

White light from panchromatic emission molecules is hardly perceived in literary works. Usually, the molecules exist in more than one form (e.g. tautomers) and the overall emission profiles can be recognised as a combination of several separate emission processes. (Mukherjee & Thilagar, 2014) Heagy and Nandhikonda revealed a new white light fluorophore from N-aryl-2,3-naphthalimides derivatives (NI) (chemical structure as shown in Figure 2.22) by the optimisation of excitation wavelengths (Nandhikonda & Heagy, 2010). Figure 2.23 shows NI excited at 340 nm, presenting an intense shorter-wavelength emission which produces blue emission, at 380 nm, and displays stronger green light emission and then, at 360 nm which conversely shows as a relatively balanced emission from the individual states producing pure white light emission.

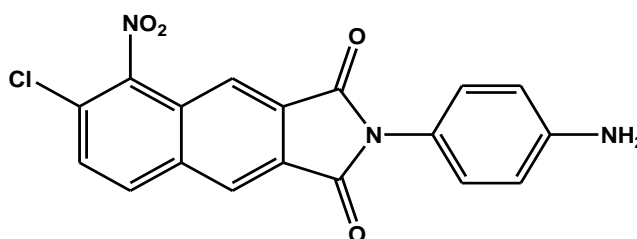


**Figure 2.22: Chemical structure of NI.**

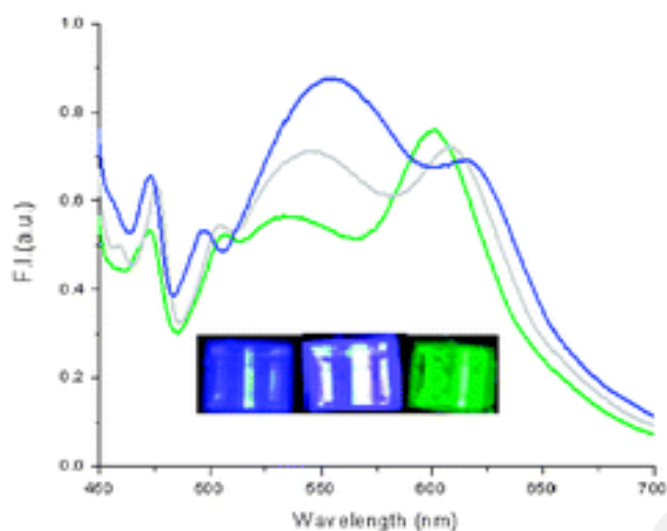


**Figure 2.23: Fluorescence spectra showing excitation wavelengths allows the NI dyes to display blue, green or white light emission based on the excitation wavelength (Nandhikonda & Heagy, 2010).**

Halochromic white light emission has also been discovered in simpler and smaller organic compounds. In 2006, Yang and his team produced halochromic white light emission from benzo-[a]xanthene, seminaphtho[a]fluorine (**SNAFR-1**). **SNAFR-1**, is a pH-insensitive compound that displays bluish violet emission around 390 nm in various solvents, due to the emission from the naphthyl unit (Youjun Yang, Lowry, Schowalter, Fakayode, Escobedo, Xu, Zhang, Jensen, Fronczek, Warner, et al., 2006). Aside from the blue emission, **SNAFR-1** also displays two emission bands; one at ~560 nm produces green light (in neutral) and another that exhibits red emission light at ~670 nm (in anionic form). The colour luminance of **SNAFR-1** is highly sensitive to excitation energies which can be obtained from a variety of colours (from yellow to red) based on an appropriate choice of excitation wavelength (Figure 2.24). Later, Gorls and his team studied the photophysical properties of 4-hydroxy-1,3-thiazoles (**3**), and they also revealed that, even a simple compound can be employed for the generation of bright white emission light in pure DMSO solution (excitation at 360 nm) which can be attributed to combined emission from the keto-enol tautomers and protonated as well as deprotonated states (Figure 2.25) (Täuscher et al., 2011).

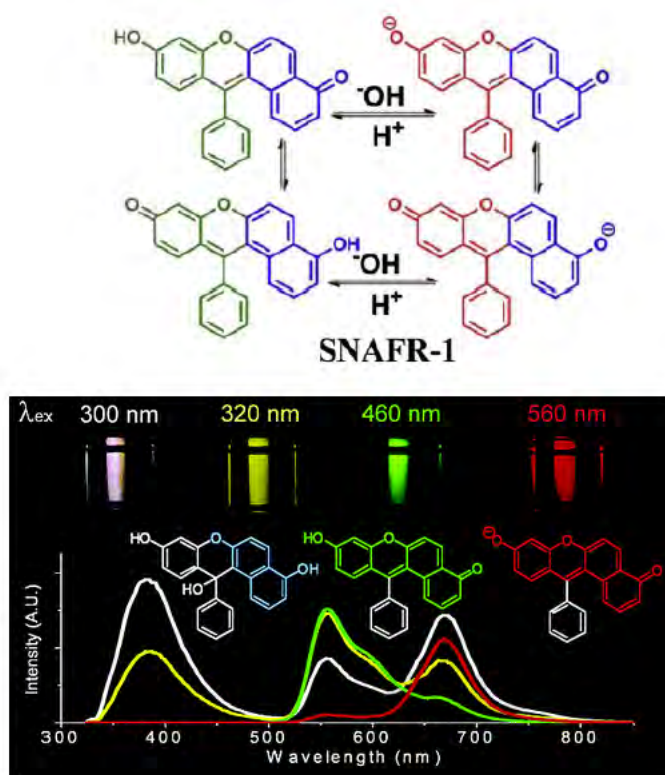


**Figure 2.24:** pH dependent systems in SNAFR-1 (left) and emission of SNAFR-1 based on different excitation wavelengths in DMSO with 0.25% phosphate buffer (50 mM, pH 7) (Youjun Yang, Lowry, Schowalter, Fakayode, Escobedo, Xu, Zhang, Jensen, Fronczek, Warner, et al., 2006).

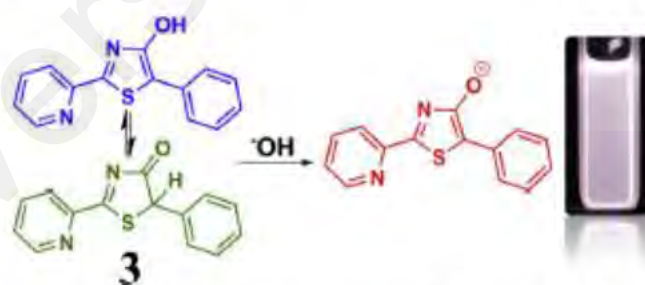


**Figure 2.25:** Illustration of tautomer compound 3 and its deprotonation. Inset photograph of 3 in DMSO solution (ex. = 360 nm) (Täuscher et al., 2011).

In 2017, Achelle et al., pronounced the fluorescent performance upon protonation of a series of D- $\pi$ -A push-pull molecules based on a methoxyphenyl, or methoxynaphthyl as a donor unit and a diazine as an acceptor unit with altered  $\pi$ -bridges, chemical structures as shown in Figure 2.26, (Top) (Achelle, Rodríguez-López, Katan, & Robin-le Guen, 2016). The effect of protonation on the emission properties depends on the nature of the diazine ring which includes pyrazine, quinoxaline and pyrimidine derivatives. The

addition of trifluoroacetic acid (TFA) to pyrazine and quinoxaline derivatives led to a quenching of the fluorescence but pyrimidine derivatives controlled protonation of blue-emission leading to white emission by formation of an orange emissive acidified form, as illustrated in Figure 2.26, Bottom. This occurrence allows WOLEDs development based on push-pull pyrimidine derivatives so it permits the opportunity of developing these materials to produce WOLEDs.

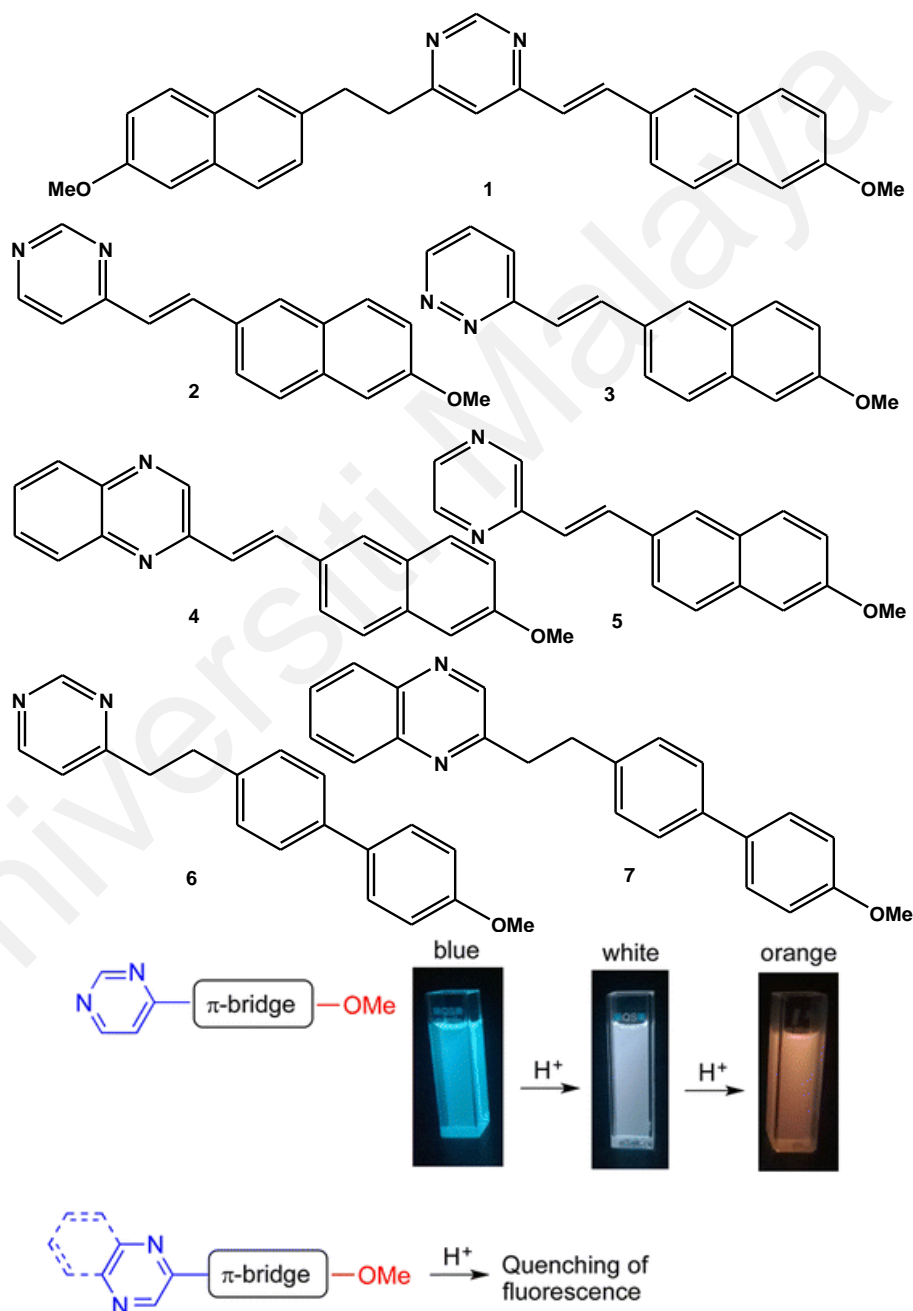


**Figure 2.26: Top. Chemical structures of diazine rings (pyrazine (3), quinoxaline (4,5,7) and pyrimidine (1,2,6) derivatives). Bottom. Schematic illustration of development of white emission and fluorescence quenching compounds (Achelle et al., 2016).**

Mishra and co-workers reported that, **diphenylbutadiynes** derivatives show locally excited (LE) and excimer emissions in water, multiple emissions from the LE, excimer, and intramolecular charge transfer (ICT) states in acetonitrile–water solvent systems. Whereas in 100% acetonitrile, the excimer emission disappears and the LE and ICT emissions dominate, as shown in Figure 2.27 (Pati, Jana, Gharpure, & Mishra, 2016). For the system of the push ( $-NMe_2$ )–pull ( $-CN$ ) diphenylbutadiyne, the intensity of the ICT emission rises with the increase of fluorophore concentration. This suggests that the ICT emission accompanies intermolecular CT emission which is of exciplex type. Because of the intensities of LE and exciplex emissions of the push–pull diphenylbutadiyne, when properly balanced both broadly cover the visible region (400–700 nm) in acetonitrile, therefore pure white light emission is obtained.

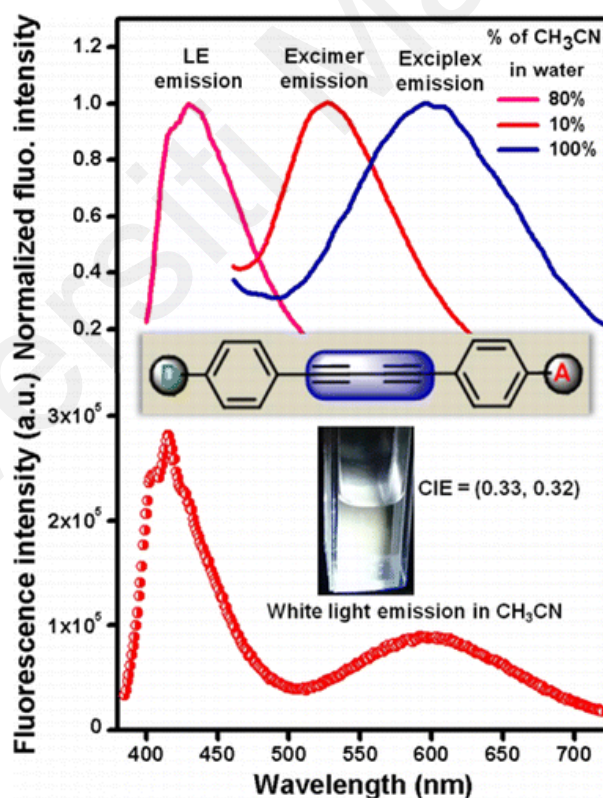


**Figure 2.27:** Top. Normalised fluorescence spectra of diphenylbutadiynes at different ratios of acetonitrile-water system. Bottom. Fluorescence spectrum of diphenylbutadiynes in acetonitrile. Inset photograph of the diphenylbutadiynes in acetonitrile under UV light at ex. 370 nm (Pati et al., 2016).

**5-N-arylaminothiazoles** is a Lewis Basis dye that consists of pyridyl groups displayed as clear halochromism and halofluorism after adding of Brønsted and Lewis acids, as shown in Figure 2.28 (Yamaguchi, Murai, Guo, Sasamori, & Tokitoh, 2016). The emission of white light was produced from a single fluorescent dye by tuning the ratio of the dye and tris(pentafluorophenyl)borane,  $B(C_6F_5)_3$ , whereby the CIE coordinates showed a linear change from blue, white to orange emission light, as shown in Figure 2.29.

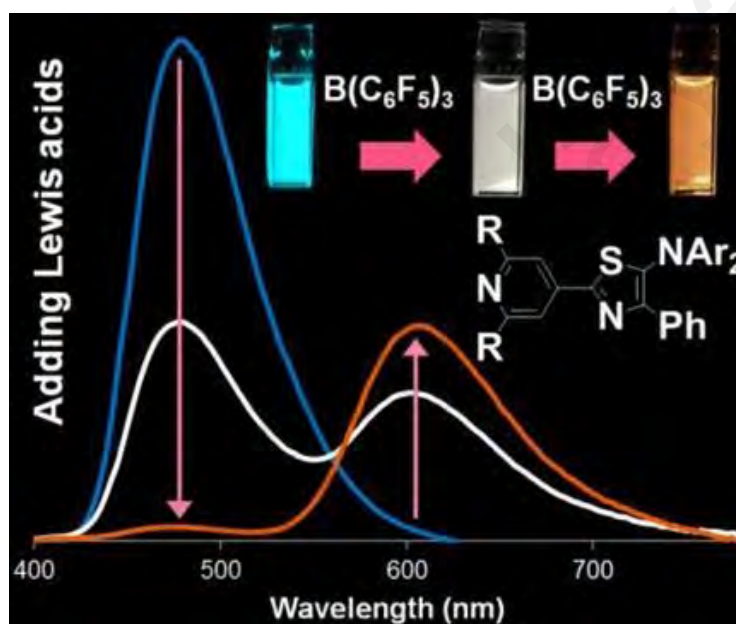


**Figure 2.28:** Fluorescence spectra from the combination of a single fluorescent Lewis basic dye by adding different concentrations of Lewis acid achieved a white-light emission. Inset photograph of the dye and Lewis acid in toluene solution under UV lamp at  $\lambda_{ex}=365$  nm (Yamaguchi et al., 2016).

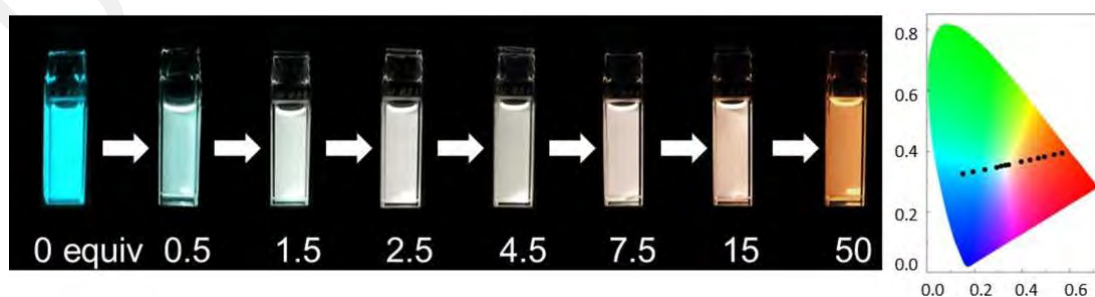


**Figure 2.29:** Photographs of a solution of the dye and  $B(C_6F_5)_3$  in toluene under a UV lamp, excitation at 365 nm (left); CIE of a solution of 6 with 0–100 equivalent of  $B(C_6F_5)_3$  (right) (Yamaguchi et al., 2016).

This finding introduced a new strategy to attain white light emission from single tetraphenylethylene-substituted pyrenes (**TPE-Pys**) with aggregation-induced emission (AIE) features (Feng et al., 2018). **TPE-Pys** showed multi-colour emissions from blue (474 nm) to yellow (531 nm) by presenting different substituents on the phenyl rings of TPE both in solution and in solid form. When TPE units are introduced into pyrene, the compounds show AIE characteristics with high thermal stability, strong fluorescence, and high quantum yield in the solid state. Especially, **TPE-Pys 2** and **TPE-Pys 4** (chemical structure as shown in Figure 2.30) which exhibit white light emission in THF/water solution. Therefore, both compounds can produce white light emission from a single AIE-active molecule through the aggregated state by adjusting the composition of the solvent mixture.

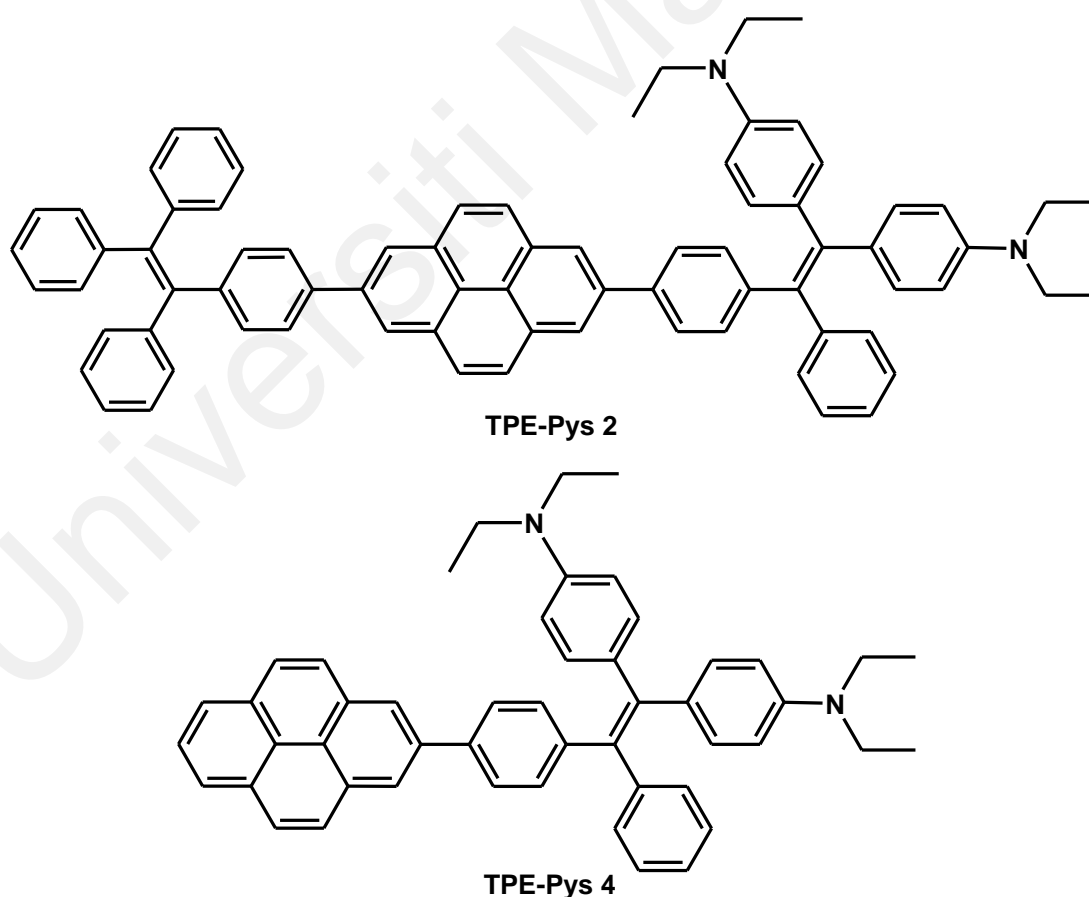


**Figure 2.30: Chemical structures of TPE-Pys 2 and TPE-Pys 4.**

Tian and his team designed and synthesised single molecules to produce white light emission from pyridinium-naphthalene (PN) core and coumarin groups (**NP4C** and **NP6C**), as new bi-functional organic molecules with a symmetric donor–acceptor–donor (D–A–D) type structure in aqueous solution (Figure 2.31) (D. Li et al., 2018). The molecules have folding behaviour that is attributed to hydrophobic effects,  $\pi$ – $\pi$  stacking and donor–acceptor interactions, which could intensely boost the efficiency of ICT together with significant charge transfer (CT) emission. Due to this phenomenon, multi-colour fluorescence, including white light emission, can be fine-tuned in different conditions (e.g. excitation wavelength, solvent polarity, temperature, and host–guest interactions). Figure 2.32 shows **NP4C** emission colour coordinates plotted in a CIE 1931 chromaticity diagram consistent with the PL emission for multifarious control strategies and fluorescence photographs of **NP4C** solutions at concentration 25  $\mu$ M. In this study they also prepared a white light emission hydrogel by dispersing one of the compounds in a commercial agarose gelator.

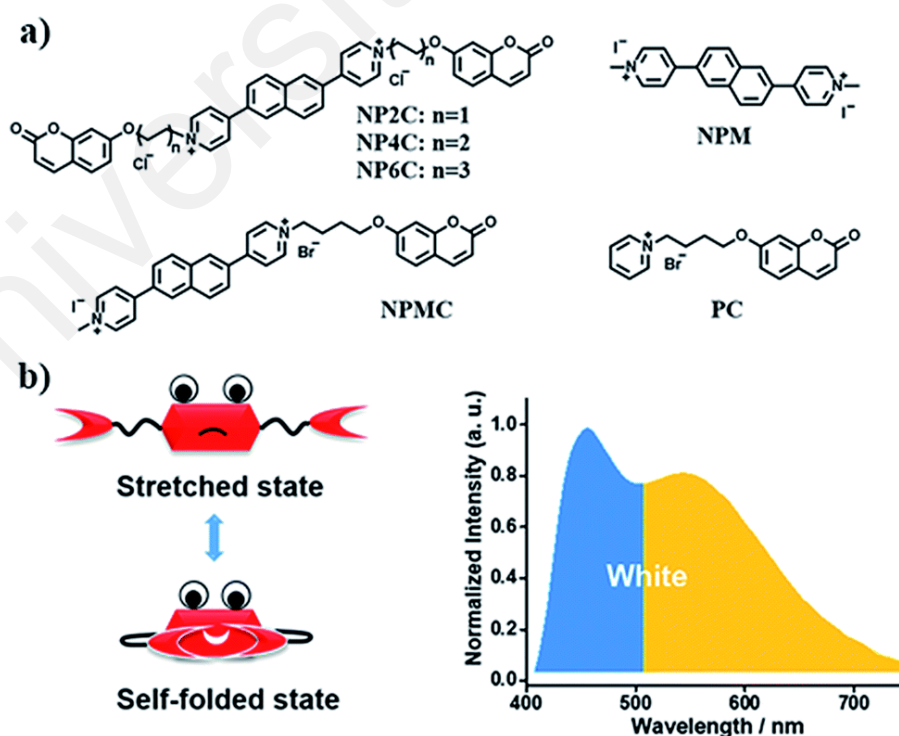


**Figure 2.31: Chemical structures of white light emitting organic molecules (NP4C and NP6C) (b) the schematic cartoon illustration of single-molecule white light emitters and its fluorescence spectrum (D. Li et al., 2018).**

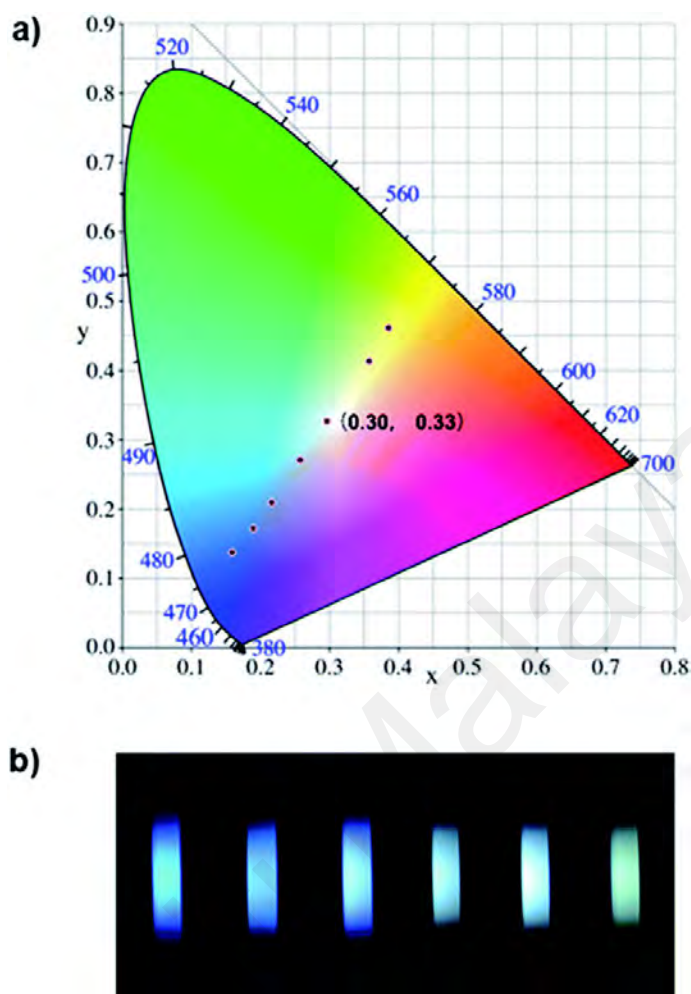
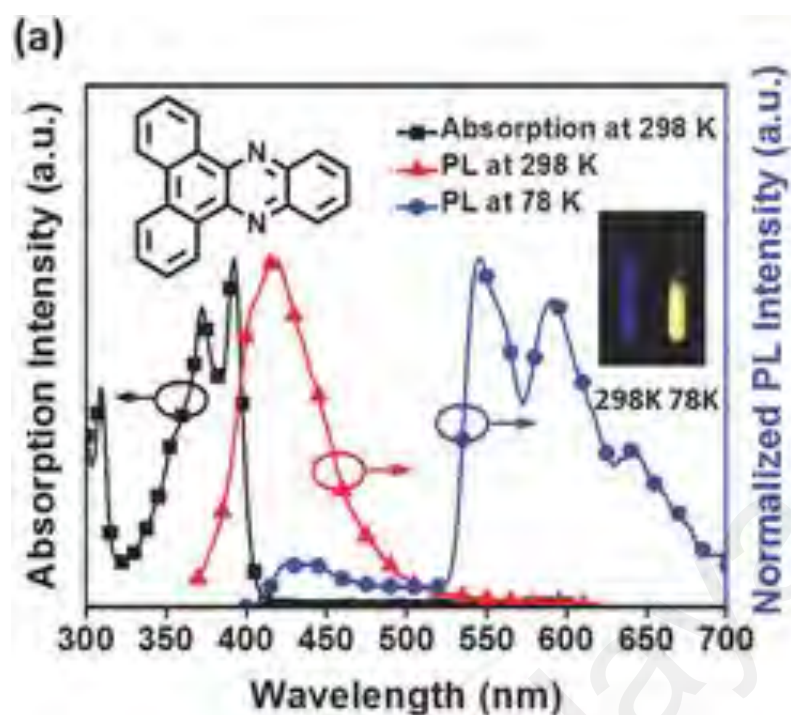


Figure 2.32: (a) Some emission colour coordinates for **NP4C** plotted in the CIE 1931 chromaticity diagram consistent to the PL emission for multifarious control strategies. (b) Several fluorescence photographs of **NP4C** solutions in combination with several conditions including temperature, solvent polarity and host-guest interaction, at concentration 25  $\mu\text{M}$  (D. Li et al., 2018).

In 2018, another new single molecule white light: aza-aromatic compound dibenzo[a,c]phenazine, **DPPZ** (Figure 2.33) has been produced (C. Zhou et al., 2018). Interestingly, it consists of ternary emission of fluorescence including simultaneous fluorescence ( $S_1$ ) and dual room-temperature phosphorescence ( $T_1$  and  $T_n$ ) that exhibits pure powder white light emission with CIE coordinates (0.28, 0.33). However, the lifetime of the **DPPZ** was too short (0.072 ns).



**Figure 2.33: Chemical structure, absorption and emission spectra of a) DPPZ in THF solution under 298 and 78 K. The inset is the photo of the steady-state emission of DPPZ. The excitation wavelength for DPPZ is 390 nm (C. Zhou et al., 2018).**

Hernando et al., (2019) established a dye encapsulation within liquid-filled capsules by new fabrication methods, hence allowing direct transfer of the luminescent properties from solution to the solid form (Vázquez-Mera et al., 2019). Figure 2.34 illustrates the development of the white light emitter dye liquid-filled capsules by presenting a thermally responsive chromophore into the capsule. These materials are capable of colour tuning, which does not only allow abundant modulation of the emitted colour but also enables external fine control of the system allowing precise recognition of white light at the desired temperature and excitation wavelength.

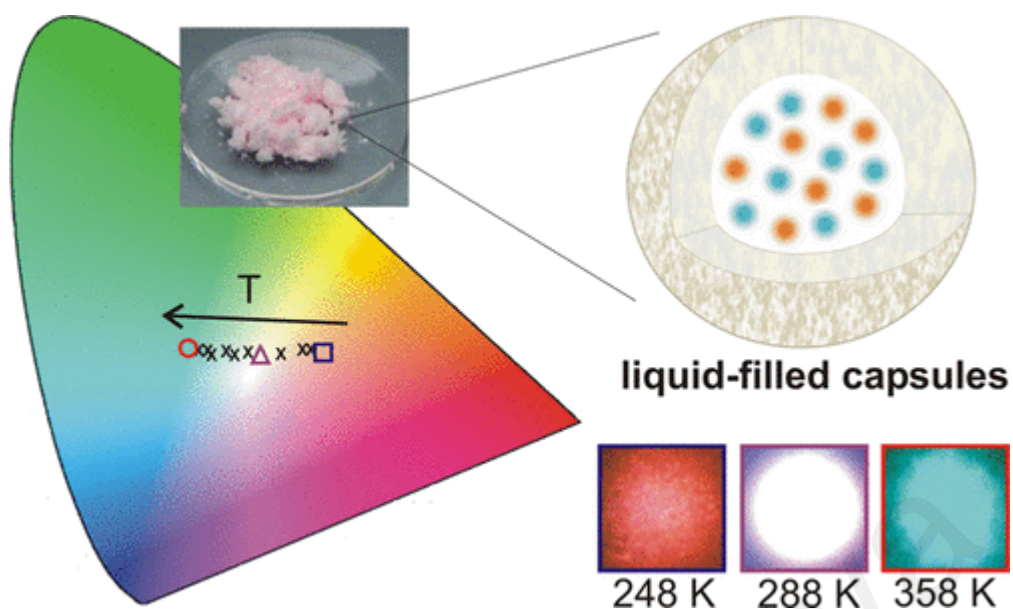


**Figure 2.34:** Schematic illustrations of encapsulated dye liquid-filled capsules plotted in the CIE 1931 chromaticity diagram consistent to different thermal responses (Vázquez-Mera et al., 2019).

Recently, in 2019, Ghosh and co-workers discovered a solid bright white light emission namely, 1-(1H-phenanthro[9,10-d]imidazol-2-yl)naphthalen-2-ol, **1H** (chemical structure in Figure 2.35) (Sinha, Chowdhury, Ghorai, & Ghosh, 2019). The solid **1H** shows bright white colour emission under UV light irradiation at 365 nm, while, upon excitation at 375 nm by UV-Vis spectrometer (Figure 2.36 (a)) it displays a broad emission band covering the visible spectrum with two emission maxima appear at 475 nm and 580 nm with CIE coordinates (0.35, 0.36), as shown in Figure 2.36.

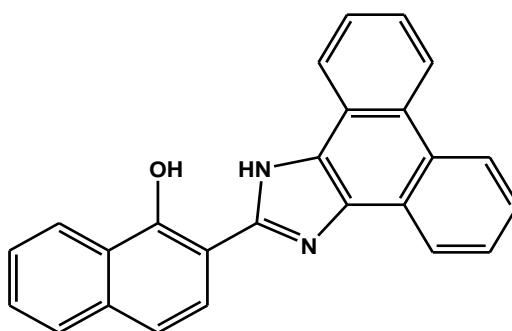


**Figure 2.35:** Chemical Structure of **1H**.

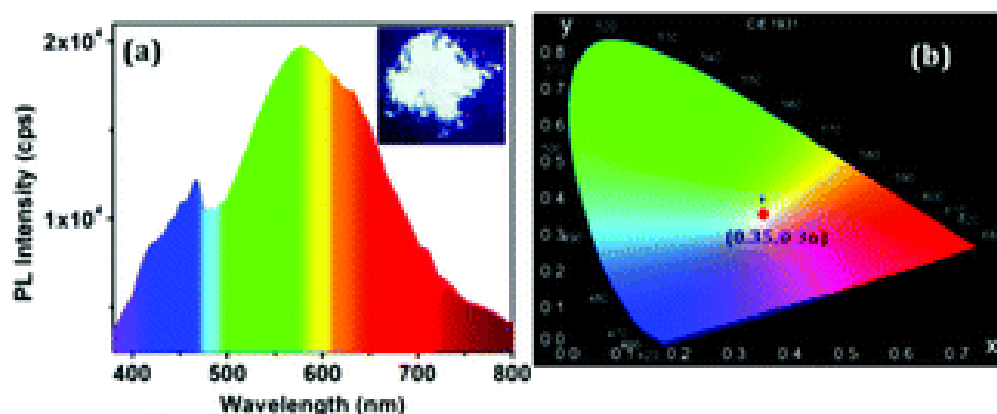


**Figure 2.36: Solid state emission spectra with the CIE coordinates of 1H in its normal form. Inset pictures indicate the colours under irradiation at 365 nm (Sinha et al., 2019).**

### 2.3 White Light Emission from a Simple Mixture of Fluorescent Organic Compounds

The novel approach is to target a mixture of simple organic compounds that share a similar range of excitation wavelengths in the UVA region (340-375 nm) yet emit at different wavelengths in the visible range (400-700 nm). It is hypothesised that a mixture of three such components should emit white light, and this can be combined with a suitable, commercially available UV LED. Three compounds were identified for this strategy: furocoumarin (FC), dansyl aniline (DA), and 7-hydroxycoumarin-3-carboxylic acid (CC) as shown in Figure 2.37, respectively. These compounds yield distinct emission colours yet are all excited in the UVA region (340 to 375 nm). 7-hydroxycoumarin-3-carboxylic acid is commercially available and was used as purchased. The synthesis of furo[3,2-c]coumarin was reported by Nair and co-workers and involves a [4+1] cycloaddition with in-situ generated heterocyclic coumarin methides and isocyanides (V. Nair, R. S. Menon, A. Vinod, & S. Viji, 2002a). The synthesis of dansyl aniline was adapted from a procedure reported by Xiao et al. (see Section 2.42) (Xiao et al., 2017).

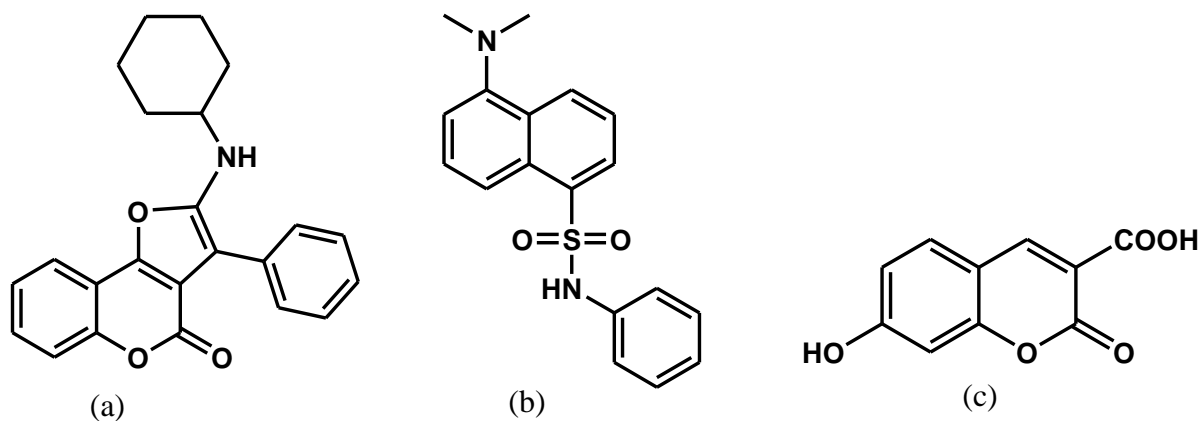


**Figure 2.37 Chemical structures of (a) FC, (b) DA and (c) CC.**

## 2.4 Materials and Methods

All starting materials and reagents were purchased from Sigma Aldrich (UK). They were used without further purification. Hydrophilic aerogel was obtained from Cabot Corporation (USA) for white light emission solid preparation.  $^1\text{H}$  NMR (400 MHz) spectra were measured on a Bruker Biospin DRX-600 spectrometer using TMS as an internal standard. 7-hydroxy-3-carboxylic acid coumarin (CC) (Mw = 206.15 g/mol, Sigma Aldrich) was used as a blue-purple emitting material. UV-vis absorption and fluorescence spectra in solution were recorded on a Cary 5000 UV-Vis-NIR Spectrophotometer from Agilent Technologies and FLS 1000 Spectrometer from Edinburgh Instruments, respectively. Excitation and emission monochromator band pass were kept at 1 nm using a quartz cell cuvette (1x1 cm). CIE colour coordinates have been calculated using freely available Osram Sylvania software.

### 2.4.1 Synthesis of Furo[3,2-c]coumarin (FC)

4-hydroxycoumarin (4.86 g, 30 mmol, 1 eq.) and benzaldehyde (3.18 g, 30 mmol, 1 eq.) were dissolved in benzene (150 mL) and heated to reflux. After 30 minutes, cyclohexyl isocyanide (3.27 g, 30 mmol, 1 eq.) was added to the reaction mixture, which was heated to reflux for a further 24 h. The pure compound was obtained by recrystallization from diethyl ether (100 mL) to yield a light yellow powder (9.70 g, 92%

yield). Analysis were in agreement with the literature (Nair et al., 2002a). Figure 2.38 shows the schematic of the reaction. Light yellow powder, m.p. = 110-112°C, FTIR ( $\text{cm}^{-1}$ ) = 3250 (NH), 2925-2850 (C=C of cyclohexane), 1720 (C=O of pyrone), 1570 (C=C of pyrone),  $^1\text{H}$  NMR (400 MHz,  $\text{CDCl}_3$ ) =  $\delta$  1.18-2.08(m, 10H), 3.55-3.58 (m, 1H), 4.29 (d,  $J = 8.32\text{Hz}$ , 1H), 7.27-7.31 (m, 2H), 7.39 (d,  $J = 4.00\text{ Hz}$ , 1H), 7.43 (t,  $J = 8.00\text{ Hz}$ , 3H), 7.52 (d,  $J = 8.00\text{ Hz}$ , 2H), 7.77 (d,  $J = 8.00\text{ Hz}$ , 1H),  $^{13}\text{C}$  NMR:  $\delta$  24.19, 25.54, 34.15, 53.69, 77.05, 97.47, 110.94, 112.87, 117.29, 119.49, 123.95, 124.89, 127.01, 128.66, 129.19, 130.73, 132.87, 149.81, 151.32, 154.89, 157.95. UV-Vis = 374 nm in ethanol. MS (ESI) =  $m/z$  360.

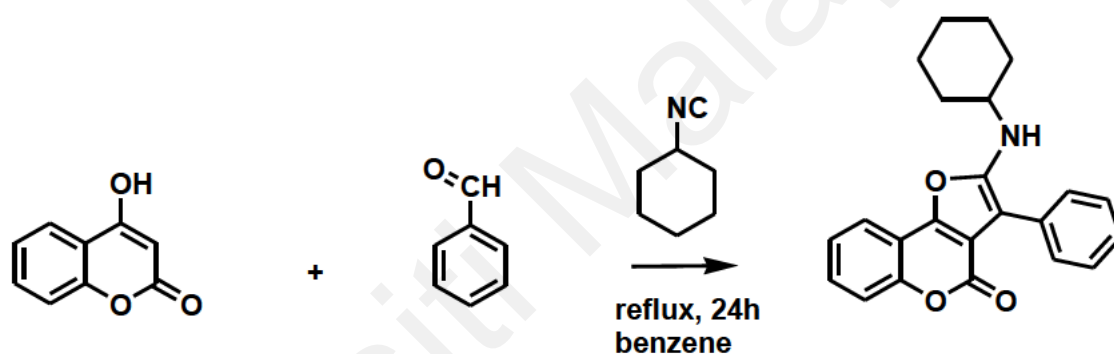


**Figure 2.38: Synthesis of furo[3,2-c]coumarin derivatives.**

#### 2.4.2 Synthesis of dansyl aniline (DA)

Dansyl chloride (2.69 g, 10 mmol, 1 eq.) and aniline (9.30 g, 10 mmol, 1 eq.) were dissolved and stirred in acetonitrile (50 mL) overnight. The pure compound was obtained by recrystallization from distilled water and ethanol to produce up to 65% yield (2.12 g). Analysis were in agreement with the literature (Xiao et al., 2017). Figure 2.39 shows the schematic of the reaction. Yellow powder, m.p. = 131-133°C, FTIR ( $\text{cm}^{-1}$ ) = 3270 (NH), 2833 (N- $\text{CH}_3$ ), 1601 (NH-aromatic), 1349 ( $\text{SO}_2$ -NH), 1159 ( $\text{SO}_2$  stretching).  $^1\text{H}$  NMR (400 MHz,  $\text{CDCl}_3$ ):  $\delta$  2.90 ppm (s, 6H,  $\text{N}(\text{CH}_3)_2$ ), 6.68 (s, 1H), 6.95-6.93 (d, 2H,  $J = 8\text{ Hz}$ , Ar), 7.07-7.05 (m, 1H, Ar), 7.17-7.13 (m, 2H, Ar), 7.22-7.20 (d, 1H,  $J = 8.00\text{ Hz}$ , Ar), 7.45 (t, 1H,  $J = 7.20\text{ Hz}$ , Ar), 7.61 (t, 1H,  $J = 7.60\text{ Hz}$ , Ar), 8.16 (d, 1H,  $J = 8.00\text{ Hz}$ , Ar), 8.35 (d, 1H,  $J = 8.80\text{ Hz}$ , Ar), 8.52 (d, 1H,  $J = 8.40\text{ Hz}$ , Ar).  $^{13}\text{C}$  NMR:

$\delta$  162.96, 152.18, 138.79, 133.17, 132.29, 132.11, 130.83, 130.39, 129.16, 128.61, 125.40, 121.80, 117.88, 115.22, 77.33, 77.02, 76.70, 45.41. UV-Vis = 339 nm in ethanol. MS (ESI) =  $m/z$  327.

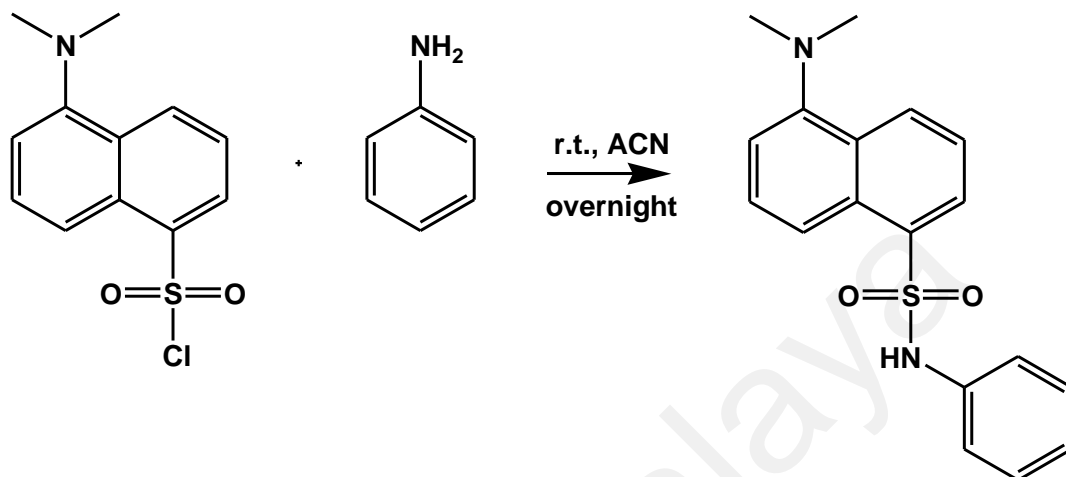


**Figure 2.39: Synthesis of dansyl aniline.**

## 2.5 Results and Discussion

Each of the three organic fluorophores was prepared in requisite proportions (CC =  $2.2 \times 10^{-3}$  M, FC =  $1.6 \times 10^{-3}$  M and DA =  $1.6 \times 10^{-3}$  M) in ethanol and subjected to UV-Vis absorption and fluorescence spectral studies. UV-Vis absorption and fluorescence spectra for all the fluorophores are shown in Figure 2.40 (a) and (b), respectively. Each of the fluorophores has a broad characteristic absorption band of around 300–420 nm with varying maxima; 339 nm for DA, 355 nm for CC, and 375 nm for FC. Fluorescence emission maxima occur at 450 nm, 512 nm, and 530 nm for DA, CC, and FC, respectively. Under UV light excitation at 390 nm, CC, FC, and DA show blue, cyan and yellow emission, respectively (inset photograph, Figure 2.40 (b)). The CIE chromaticity coordinate for CC appears in the blue-violet region (0.16, 0.11); the coordinate for FC appears in the cyan region (0.27, 0.46); for DA it appears in the green-yellow region (0.33, 0.53) of the CIE diagram (Figure 2.41). It is observed that the points for CC, FC and DA appear on the opposite side of the white region in the CIE diagram. From this observation

it was hypothesised that it should be possible to obtain white light emission by mixing the three fluorescent compounds.

Accordingly, a series of solutions were prepared by varying the ratio of DA with a fixed ratio of CC and FC at 1.375:1 (Table 2.1). Solutions were prepared containing varying ratios of CC:FC:DA (1.375:1:3, 1.375:1:4, 1.375:1:5, 1.375:1:6 and 1.375:1:7) and were analysed by UV-Vis absorption and fluorescence spectral studies as shown at Appendices (Figure A1 and Figure A2 a-c).

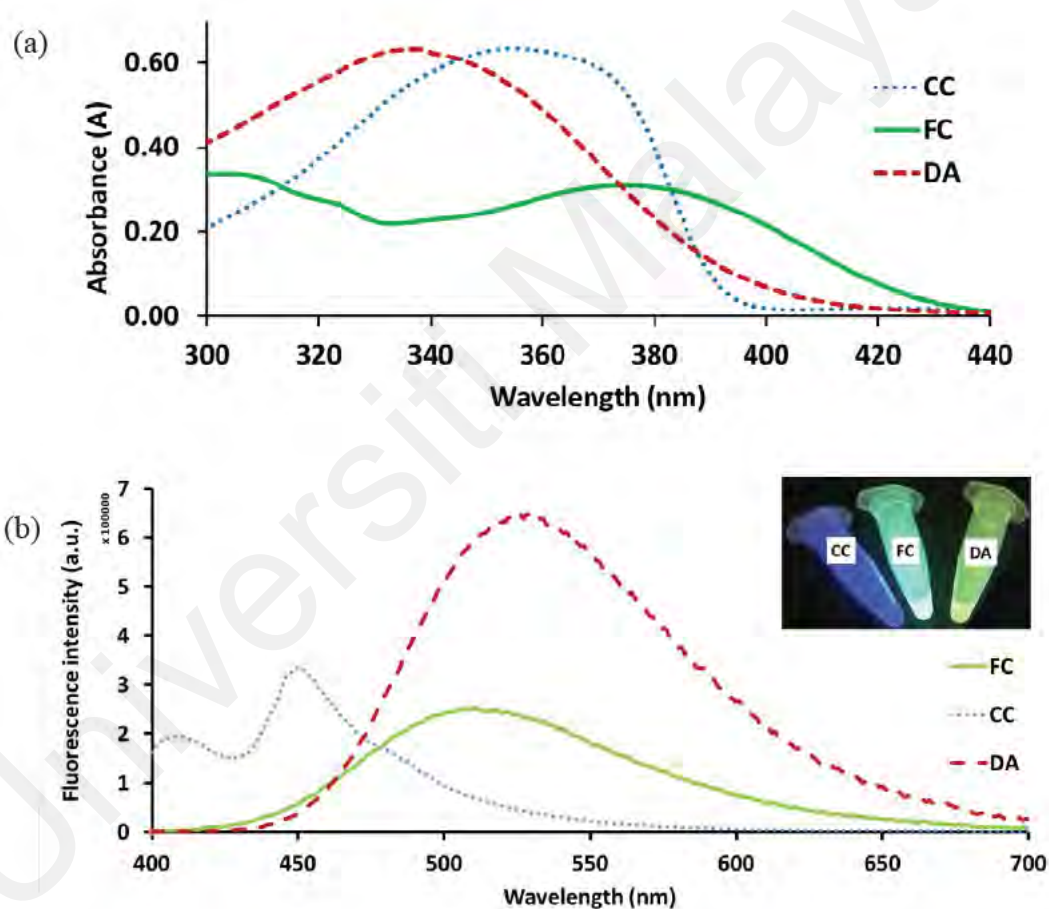


**Figure 2.40:** (a) Absorption spectra for each of the compounds (CC =  $2.2 \times 10^{-3}$  M, FC =  $1.6 \times 10^{-3}$  M and DA =  $1.6 \times 10^{-3}$  M) in ethanol. (b) Fluorescence spectra for each of the compounds (CC =  $2.2 \times 10^{-3}$  M, FC =  $1.6 \times 10^{-3}$  M and DA =  $1.6 \times 10^{-3}$  M) in ethanol. Inset: Photograph taken under UV light (390 nm) for each of the compounds (CC, FC and DA) in ethanol.

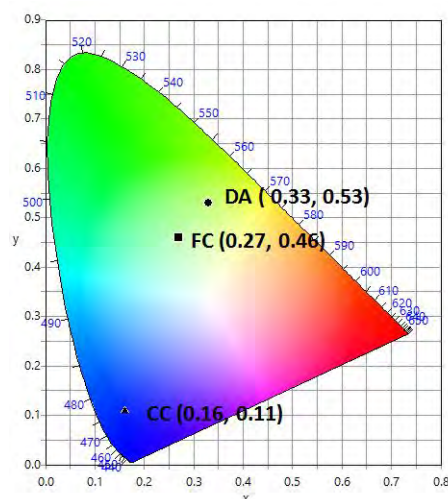


**Figure 2.41: CIE-1931 diagram. Chromaticity plot for colour coordinates of CC (▲), FC (■) and DA (●).**

**Table 2.1 Various ratio combinations of dansyl aniline (DA) with furocoumarin (FC) and carboxylic coumarin (CC).**

No	CC ( $2.2 \times 10^{-3} \text{M}$ )	FC ( $1.6 \times 10^{-3} \text{M}$ )	DA ( $1.6 \times 10^{-3} \text{M}$ )	Excitation wavelength (nm)	CIE (x,y)	CCT (K)	Photograph under UV lamp (390 nm)
A	1.375	1	3	340	(0.21,0.25)	34558	
				350	(0.21,0.25)	34558	
				375	(0.21,0.24)	49898	
				380	(0.22,0.26)	25581	
				390	(0.23,0.27)	22043	
B	1.375	1	4	340	(0.21,0.26)	28475	
				350	(0.21,0.25)	34558	
				375	(0.21,0.25)	34558	
				380	(0.22,0.28)	19499	
				390	(0.24,0.29)	14638	
C	1.375	1	5	340	(0.22,0.28)	19499	
				350	(0.22,0.27)	22043	
				375	(0.22,0.27)	22043	
				380	(0.23,0.27)	19890	
				390	(0.24,0.30)	14638	
D	1.375	1	6	340	(0.23,0.30)	14638	
				350	(0.23,0.30)	14638	
				375	(0.23,0.28)	13610	
				380	(0.23,0.28)	13610	
				390	(0.25,0.31)	11315	
E	1.375	1	7	350	(0.24,0.30)	13610	
				375	(0.24,0.29)	14683	
				380	(0.24,0.33)	11474	
				390	(0.27,0.33)	9167	

Based on the UV-Vis spectra, all the ratios show similar excitation wavelength, within the range of 350 to 355 nm. The mixture of the fluorescent solution was excited at various wavelengths (340, 350, 360, 370, 375, 380, and 390 nm). Further increases in concentrations up to 1.375:1:8 and 1.375:1:9 were also tried but led to an increasingly yellow coloured emission profile, therefore no further fluorescence analysis was conducted at these increased ratios as it was deemed to be beyond the scope of the present research objective (to produce white light emission). Each of the fluorescence spectra shows almost similar bands of emission and fluorescence intensity except at 390 nm. From these, 390 nm exhibits the best fluorescence intensity with a broadband emission profile. By varying the excitation wavelength it is expected that for a mixture of different fluorophores the emission profile should vary (Youjun Yang, Lowry, Schowalter, Fakayode, Escobedo, Xu, Zhang, Jensen, Fronczek, & Warner, 2006). Figure 2.42 shows the colour coordinates for these solutions in the CIE diagram. It is seen that the point CFD (0.27, 0.33), corresponding to the composition concentration of CC =  $2.2 \times 10^{-3}$  M, FC =  $1.6 \times 10^{-3}$  M and DA =  $1.6 \times 10^{-3}$  M, with ratio of 1.375:1:7; CC:FC:DA, is extremely close to that of pure white light, coordinate O (0.33, 0.33).

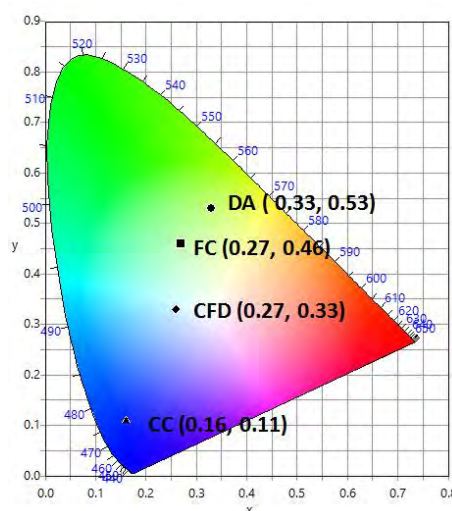


**Figure 2.42: CIE-1931 diagram. Chromaticity plot for colour coordinates of CC (▲), FC (■), DA (●) and for the mixture, CFD (◆) corresponding to a ratio of 1.375:1:7 CC:FC:DA, in ethanol solution.**

The emission spectrum corresponding to point CFD covered the entire visible region (400–700 nm) (Figure 2.43), with three emission maxima at 430, 450 and 525 nm. These bands appear to be similar to the individual CC, FC and DA emissions, indicating that the emission spectra are due to the simultaneous emission from all of the fluorescents. The fluorescence analysis from the mixture clearly shows that excitation at 390 nm results in emission that broadly covers the entire visible range up to about 700 nm. The absorption and emission spectra of the fluorescents do not exhibit any significant overlap (CC, FC and DA: absorption band (300-400 nm), emission band (400-700 nm)). Furthermore, by comparing the emission spectrum of the mixture CFD with the spectrum from each individual compound (Figure 2.43 (b)), there is very little/no peak shifting which indicates that simultaneous emission occurs which results in white light generation. Examining the individual emission responses of FC and CC (Figure 2.43 (b)) there is also the possibility that self-absorption may be occurring, and it is expected that this may become more apparent at higher concentrations (Oliva et al., 2013; J. Wang et al., 2013). Observations from a complementary experiment in which the amount of DA was increased 7-fold and added to a fixed CC:FC (1.375:1) ratio, given in (Table 2.1), show the production of white light emission at 390 nm. Furthermore, the CIE coordinates, correlated colour temperature (CCT) and photograph under UV lamp illumination (390 nm) are given for various ratio combinations of the fluorescents in ethanol. As is seen in Table 2.1, simple variations in relative composition of the components modify the CIE indices and the corresponding colour temperatures in a facile manner.

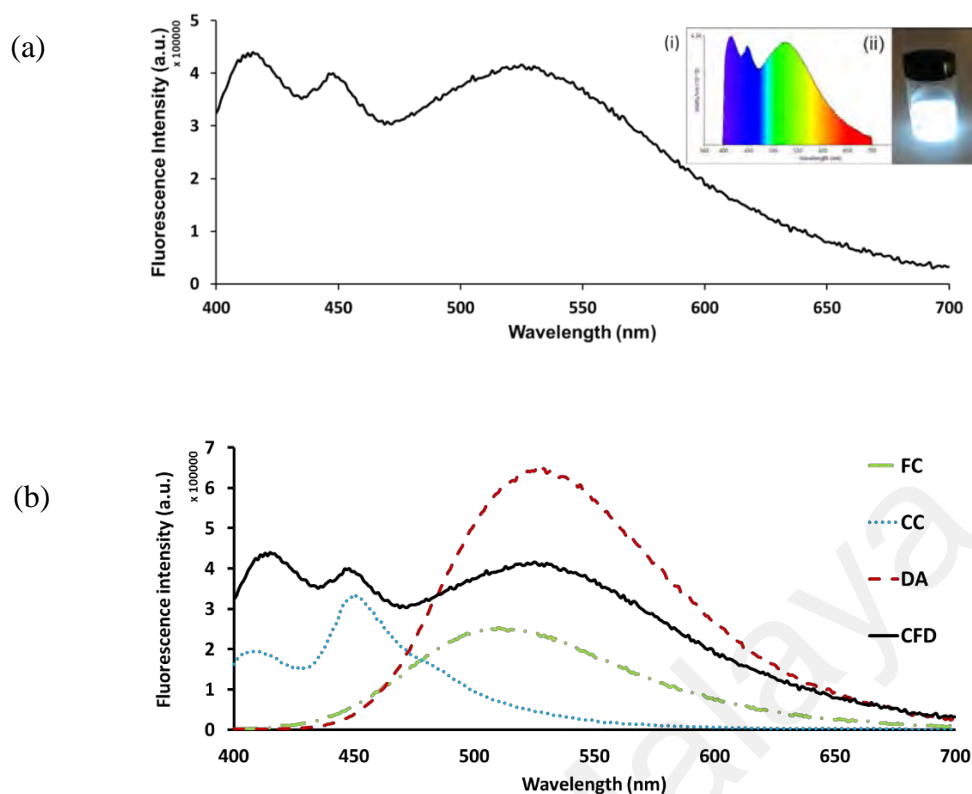


**Figure 2.43: (a) Fluorescence spectrum for a mixture, CFD, of CC:FC:DA (1.375:1:7) in ethanol at 390 nm. Inset: (i) Colour spectrum and (ii) photograph of the CFD solution in ethanol under UV light (390 nm). (b) Shows overlay of both fluorescence spectrum from a mixture (CFD, where CC:FC:DA = 1.375:1:7) and the fluorescence spectra of the three components individually (FC, CC, DA) in ethanol at 390 nm.**

The possibility of producing white light emission with this simple mixture from a solid media has also been explored. Aerogels offer high porosity (nanometer-scale pore sizes), they are lightweight materials with low densities ( $0.003\text{--}0.15\text{ kg/m}^3$ ) and large surface areas ( $500\text{--}1000\text{ m}^2/\text{g}$ ). (Karaaslan, Kadla, & Ko, 2016; Smirnova & Gurikov, 2018) Such properties mean that aerogel has great potential for use in a wide range of applications, including thermal insulation (Mishra, Kotresh, Militky, & Jamshaid, 2016), electrochemical applications (e.g., super capacitors) (Araby et al., 2016), materials for tissue engineering (Maleki et al., 2016), bio-sensors (Wen, Liu, Herrmann, & Eychmüller, 2014) and amongst several others. In this work, two commercially available aerogel variants: dry hydrophilic and dry hydrophobic silica aerogel has been tested. The hydrophilic aerogel produces white light upon excitation after soaking in the white light

emission mixture, whilst the hydrophobic aerogel produced a blue light emission. The aerogel was soaked in the white light emission mixture in ethanol for 3 days in a fume hood. Subsequently, the gel was filtered and allowed to dry. The dried aerogel then exhibits white light emission when excited under UV light illumination. The fluorescence emission spectrum of the mixture incorporated into aerogel is shown in Figure 2.44(a), which covered the visible region from 400 to 650 nm. The aerogel shows good white light emission under UV light (inset, Figure 2.44(i)). A good CIE coordinate value of (0.27, 0.33) was obtained for the white light emission aerogel from the corresponding emission spectrum, excited at 390 nm (Figure 2.44(b)). Finally, as an exemplar application to demonstrate the potential of this approach, the white light emission aerogel was applied in an ad-hoc fashion as a coating for a commercial UV LED. Side by side images of the regular UV LED and the modified aerogel white light emission LED are shown in Figure 2.45. As can be observed, the modified LED produces a uniform white light emission.

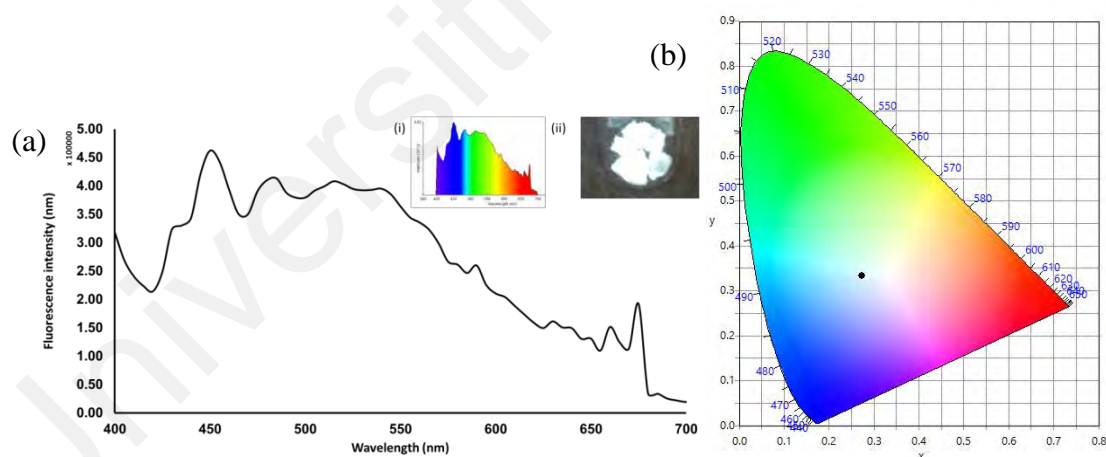


**Figure 2.44 White light emission aerogel. (a) Emission spectrum of mixture incorporated into aerogel for white light emission. Inset (i) Colour spectrum of the modified aerogel and (ii) photograph of the modified aerogel under UV illumination (390 nm). (b) CIE plot for colour coordinate of white light emitting aerogel (0.27,0.33).**

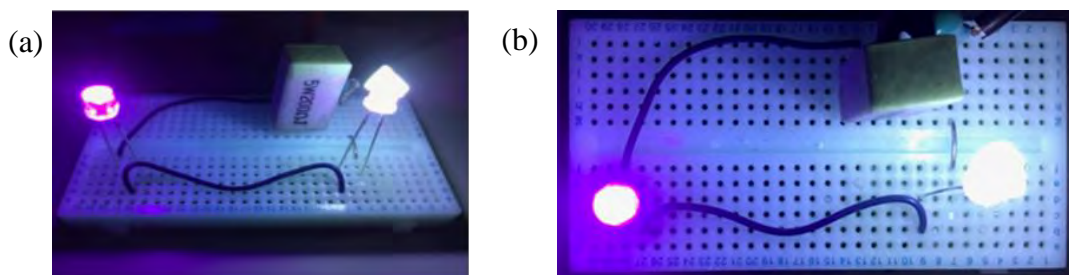


**Figure 2.45: Side-by-side image for the same UV LED. In each image the left-hand side is the uncoated UV LED and the right-hand side LED is coated with aerogel to produce white light emission. Both images are taken of the same experimental setup: (a) is a side view and (b) is a top view.**

## 2.6 Conclusion

This chapter highlights the production of white light emission from organic molecules as an effort to achieve a ‘green’ and sustainable emitter material. Current development of white organic light emission materials throughout the years have been discussed in section 2.2. Most of the organic compounds utilised were oligomers and macromolecules, which are labour-intensive and tedious to synthesise. This research (Section 2.3) has led to a novel production of white light emission from a mixture of simple and small molecules by mixing three fluorescent organic compounds; furocoumarin (FC), dansyl aniline (DA), and 7-hydroxycoumarin-3-carboxylic acid (CC). It was observed that a broadband and simultaneous emission involving coumarin carboxylic acid, furocoumarin and dansyl aniline play a vital role in obtaining a CIE index close to that of pure white light. These results offer promising white light emission results for two conditions, either as a solution (in ethanol) or a solid (silica aerogel). When the mixture is either in ethanol solution or immobilised in silica aerogel, it exhibits a CIE chromaticity index of (0.27, 0.33). The silica aerogel is applied as a coating to a UV LED to demonstrate its applicability as a low-cost, organic coating for white light emission via simultaneous emission. Due to the unique thermal insulation properties of aerogel, future work can consider novel strategies for mixing the organic compounds with aerogel to determine

whether a long-term white light emission can be obtained that is able to withstand the localised heat generated during prolonged usage.

Universiti Malaya

## CHAPTER 3: COUMARINS AS FLUORESCENT CHEMOSENSORS

The first part of this chapter will introduce coumarin as a fluorescent chemosensor. This will be followed by examples where coumarins have been used as sensing materials for metallic ions in a broad sense. Next, this chapter will review the use of fluorescence-based coumarin sensors specifically for the metallic ion,  $\text{Fe}^{3+}$ . Finally, a new furocoumarin-derived sensor has been developed for the sensitive and selective detection of  $\text{Fe}^{3+}$ . The results from this chapter have been published in a peer-reviewed article (Sarih, Ciupa, et al., 2020). Note that, furo[3,2-c]coumarin was previously used (Chapter 2) as for a key component of the mixture contributing to white light emission.

### 3.1 Introduction

Coumarin is an aromatic heterocyclic compound made up of two fused six-member aromatic rings, between benzene and pyrone, to form as a benzopyrone. The academic literature contains an abundance of information regarding the synthesis and bioactivities of coumarin derivatives (Kinza Aslam, Khosa, Jahan, & Nosheen, 2010; Medina et al., 2015; Narayanaswamy et al., 2014). Research involving this ring system has been applied to a wide range of areas including pharmaceuticals (P. Jain & Joshi, 2012), optical brighteners (Tiki, Amin, & Kanwal, 2010), fluorescents (X. Cao, Lin, & Yu, 2011; X. Cao, Lin, Yu, & Wang, 2011; Dong et al., 2016; He et al., 2015; Hongqi Li, Cai, & Chen, 2012; Hongqi Li et al., 2011; Xie et al., 2012; Yuan, Lin, Xie, Chen, & Zhu, 2012; Yuan, Lin, Zhao, et al., 2012) and laser dyes. Coumarin-derived fluorescent chemosensors are commonly created by combining coumarin with other functional receptors. The aromatic structure and acetyl group of coumarin as shown in Figure 3.1, are usually used to represent the fluorophore scaffold. This is because of the presence of enhanced charge transfer carriers as a result of the substitution reaction. Due to quenching effects, namely the photoinduced electron transfer (PET) process, isomerisation and other effects, some chemosensors are considered to be weak fluorophores. However, a strong fluorescence

can be recovered through the interactions with certain analytes, which cause the aforementioned quenching effects to be restrained. Furthermore, other chemosensors such as those under the chemodosimeter subclass, depend on chemical bond cleavage; hence they either release a strong fluorescent compound or create novel chemical bonds. (D. Cao et al., 2019b) Consequently, this produces changes in wavelength. These mechanisms are further discussed in the following sections of this chapter.

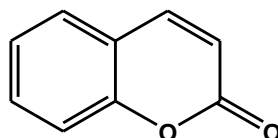


**Figure 3.1: Structural formula of coumarin.**

Furocoumarins which are one of the coumarin derivatives that can be classified into two groups, i. furan fused benzene ring (psoralen and angelicin) and ii. furan fused lactone ring (furo[3,2-c]coumarin, furo[2,3-c]coumarin and furo[3,4-c]coumarins) (Y.-J. Jang, Syu, Chen, Yang, & Lin, 2012). Both psoralen and angelicin compounds are commonly studied because of their abundance in nature compared to the fused furan on the lactone ring (Y.-J. Jang et al., 2012). In this study, furo[3,2-c]coumarin has been chosen as a suitable fluorescent heterocyclic candidate as it gives an excellent yield based on published reports (Nair et al., 2002a; Shaabani, Teimouri, & Bijanzadeh, 2004; J. Wu, 2005). Furthermore, the synthesis method for furo[3,2-c]coumarin is both efficient and straightforward (one-pot). It is found in natural products, for example, rhizome of *Salvia miltiorrhiza* Bunge exhibits potent biological activities (antitumor, antioxidant, anticoagulant, antifungal, anticancer) with several therapeutic applications (Melough, Cho, & Chun, 2018). Nair and co-workers reported their preparative procedure which involves *in-situ* [4+1] cycloaddition of heterocyclic coumarin methides and isocyanides (Nair et al., 2002a). Since coumarins typically show excellent spectroscopic properties, high stability and low toxicity (Sethna & Shah, 1945), so the hypothesis is furo[3,2-c]coumarin derivatives could have potential as fluorescent sensor probes.

The study of fluorescent probes for metal ion detection is a vibrant research field, attracting great interest due to both the importance of detecting heavy metals but also because this sensing approach can offer high sensitivity and fast response times with relatively simple instrumentation requirements (Carter, Young, & Palmer, 2014; S. Maher et al., 2016; Yuming Yang, Zhao, Feng, & Li, 2013). Due to the low concentrations at which metal ions are present, for example in biosystems and in the environment, high-sensitivity probes are essential for practical applications (García-Beltrán et al., 2014; J. Zhang, Cheng, Li, Zhu, & Lu, 2016). In recent years, a large number of fluorescent sensors from coumarin derivatives have been reported for metal ion detection (D. Cao et al., 2019a), such as  $\text{Cu}^{2+}$  (H.-Q. Chang, Zhao, Wu, Jia, & Wang, 2017; Ş. N. K. Elmas et al., 2017; Karaoglu, Yilmaz, & Menteşe, 2017; Ye et al., 2017),  $\text{Zn}^{2+}$  (Aich, Goswami, Das, & Mukhopadhyay, 2015; An, Yan, Yang, Li, & Zhou, 2013; Lim et al., 2005; L. Wang et al., 2018; M.-h. Yan, Li, & Yang, 2011),  $\text{Al}^{3+}$  (Hossain, Singh, Lakma, Pradhan, & Singh, 2017; Qin, Li, Wang, Yang, & Fan, 2014),  $\text{Mg}^{2+}$  (G. F. Chen, Zhang, Li, & Chen, 2015; Gharami et al., 2017; Ray & Bharadwaj, 2008) and  $\text{Fe}^{3+}$  (G. F. Chen et al., 2013; Ruiping Wang, Wan, Feng, & Bai, 2014; W. Wang et al., 2018; Yao, Dou, Qin, & Liu, 2009; Zhao et al., 2016a). Reference (Z. Yan, Hu, & You, 2016) gives an excellent overview of some of the sensing materials used for  $\text{Fe}^{3+}$  detection.

Among the metal ions, iron is an essential trace element found in living organisms, and both its deficiency and excess are associated with various disorders, such as Alzheimer's, Parkinson's disease (Burdo & Connor, 2003; Dietrich et al., 2017; Sui, Tang, Liu, Kim, & Belfield, 2014) and anemia (Skalnaya & Skalny, 2018). An excessive amount of iron in the human body can cause toxic damage to various organs including the heart and liver (Skalnaya & Skalny, 2018), whilst a lack of iron is related to weakened cognitive growth and decreases the capacity for physical work (Lal, 2019). In severe excess it is known to be lethal and death has occurred following human ingestion of  $\sim 40$  mg/kg

(Council). The major source of daily iron intake for humans is from food (e.g., green vegetables contain 20 -150 mg/kg (Organization)) with drinking water (assuming an average concentration of 0.3 mg/L) accounting for ~0.6 mg of daily intake. Iron concentration in surface waters is usually  $< \sim 1$  mg/L but much higher concentrations are encountered in groundwater (e.g.,  $> 50$  mg/L). Excess iron in the environment can also arise due to chemical treatment processes (e.g., coagulation) and from corrosion of ferrous materials. In the USA, the environmental protection agency (EPA) guidelines state that the maximum level of  $\text{Fe}^{3+}$  in drinking water is  $5.37 \mu\text{M}$  (EPA, 2013), and in the UK, the drinking water inspectorate (DWI) has set a maximum concentration limit for total iron at  $200 \mu\text{g/L}$  (Inspectorate, 2010).

The analysis of  $\text{Fe}^{3+}$  is of great importance for various application areas including biomedical (Ullah et al., 2018), environmental (Machado et al., 2013) and aquatic (Thamdrup, 2000). In previous work successful attempts have been reported for the detection of  $\text{Fe}^{3+}$  (G. F. Chen et al., 2013; Ruiping Wang et al., 2014; W. Wang et al., 2018; Yao et al., 2009; Zhao et al., 2016a). However, in each case, selectivity is not demonstrated for some heavy metals (that exhibit properties similar to those of  $\text{Fe}^{3+}$ ) which could interfere with detection (X. Liu et al., 2018). For example,  $\text{Ru}^{3+}$ , which amongst the variety of transition metal ions, theoretically, has the greatest similarity to  $\text{Fe}^{3+}$ , is not tested for potential interference. Ruthenium is mainly used in the electronics (Busana, Prudenziati, & Hormadaly, 2006; Rane, Prudenziati, & Morten, 2007; Sahu et al., 2018) and chemical industries (Rezayee, Huff, & Sanford, 2015; Schutz, 1996), but it also used for biomedical purposes such as anti-cancer drugs (Gupta et al., 2013; Valente & Garcia, 2014). Therefore, for any  $\text{Fe}^{3+}$  fluorescent probe, it is important to extensively demonstrate selectivity, testing with other heavy metals including ruthenium, as it can be presented in the environment (Masson et al., 2019), biological systems (Szczepaniak et al., 2019) and water (Sato, Kudo, & Tsuda, 2011) samples.

### 3.2 Coumarin Derivatives as Chemosensors for Fe<sup>3+</sup>

This section critiques relevant studies from the scientific literature related to the topic of coumarin derivatives as chemosensors for Fe<sup>3+</sup>. Some of them are highly selective to Fe<sup>3+</sup> while some were also responsive to other metal ions too. In 2013, a “turn-on” fluorescence sensor to detect two heavy metals (Fe<sup>3+</sup> and Al<sup>3+</sup>) using a simple coumarin-based Schiff base with high selectivity was designed and synthesised from 4-(diethylamino)salicylaldehyde and 6-amino-7-hydroxycoumarin (**L**). (L. Wang, Li, & Cao, 2013) The fluorescence enhancements of **L** at 488 nm are 7-fold and 4-fold upon the addition of equivalent mounts of Fe<sup>3+</sup> and Al<sup>3+</sup>; respectively as shown in Figure 3.2. Interestingly, after a rapid photo-response by fluorescence “turn-on” signalling of **L** via the intramolecular OH...NCH interaction in a photo-isomerised product, **L'** was pronounced, displaying a 130-fold and 65-fold fluorescence enhancement at 488 and 516 nm, respectively, as depicted in Figure 3.3.

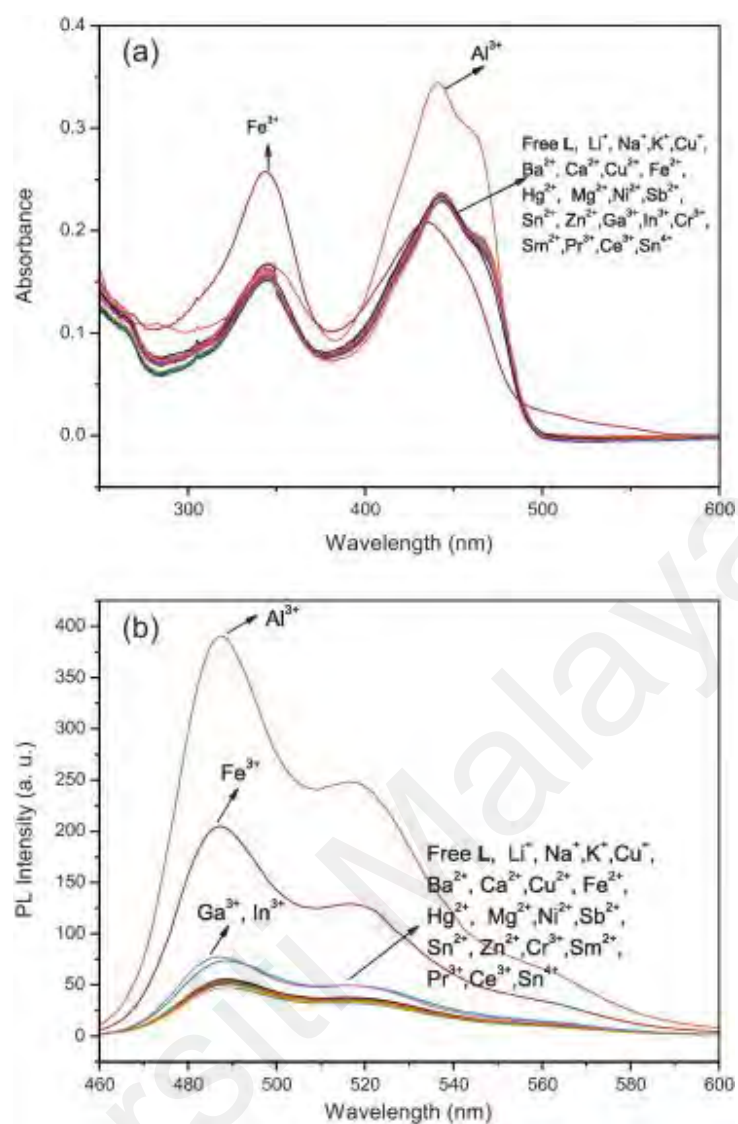


Figure 3.2: (a) UV-Vis and (b) Fluorescence spectra of L (10  $\mu\text{M}$ ) in the absence and presence of 1 eq. of different metal ions in methanol (L. Wang et al., 2013).

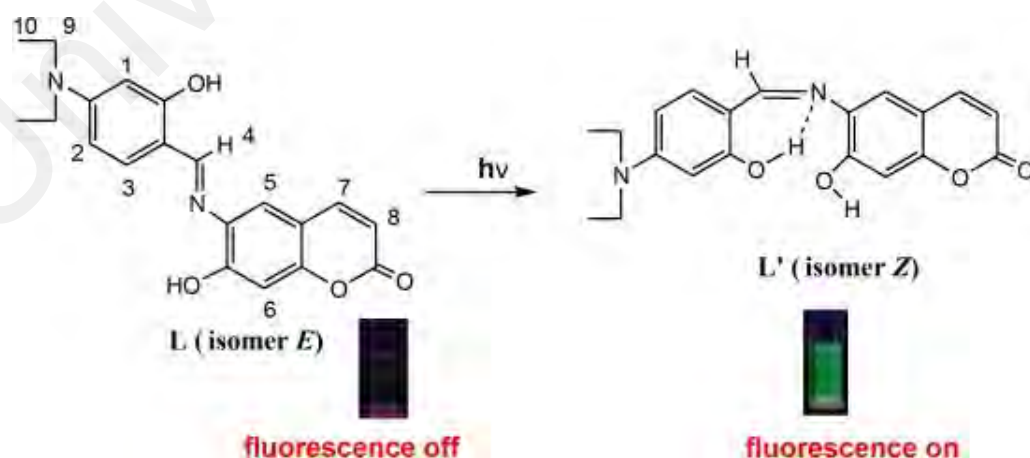
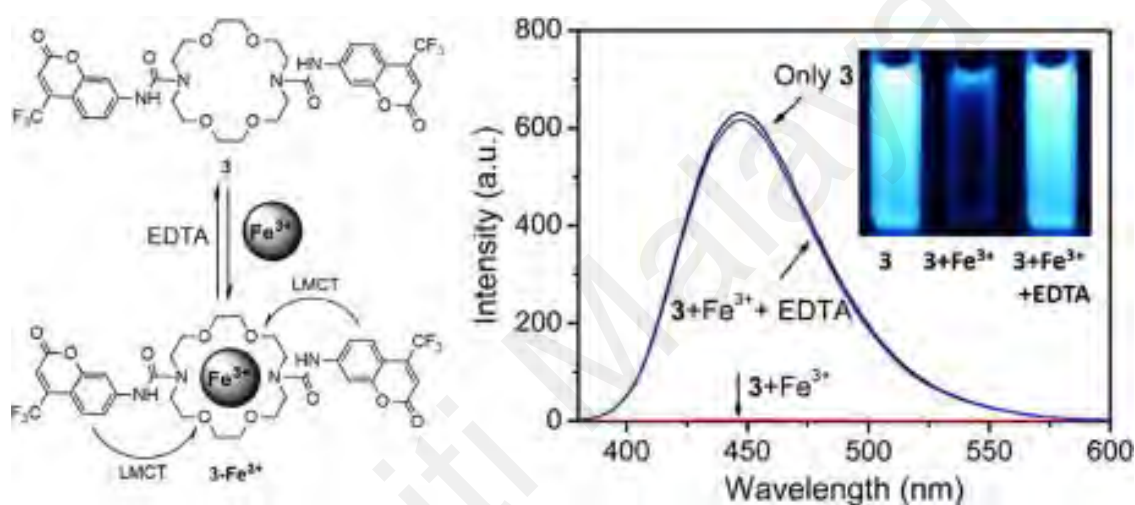


Figure 3.3: Structures of L and L' and approach of metal ions toward the coordination sites of both isomers (L. Wang et al., 2013).

Yin et al., synthesised diaza-18-crown-6 ether, which was joined with dual coumarin (7-amino-4-trifluoromethylcoumarins) compounds, **DC**, that exhibited a highly selective fluorescent chemosensor for  $\text{Fe}^{3+}$  over other environmentally and biologically relevant metal cations (Hongda Li, Li, & Yin, 2014). The sensor was able to detect  $\text{Fe}^{3+}$  through the complexation of  $\text{Fe}^{3+}$  ions with the chemosensor by a ligand-metal charge transfer (LMCT) as illustrated in Figure 3.4. Interestingly, the sensor to  $\text{Fe}^{3+}$  exhibits a low detection limit ( $0.31 \mu\text{M}$ ), and fast response which is less than 10 s.



**Figure 3.4: Proposed mechanism and binding of DC- $\text{Fe}^{3+}$  (H. Li et al., 2014).**

According to Guo et al., coumarin derivatives could be used for efficient fluorophores because they demonstrate some advantages such as large Stokes shifts, good photostability and high quantum yields (determined to be 0.75) (En, Guo, Chen, Dong, & Peng, 2014). They produced a new fluorescent coumarin based chemosensor, **DAT-1** as shown in Figure 3.5 (a), for  $\text{Fe}^{3+}$  using 2-amino-2-(hydroxymethyl)-1,3-propanediol (tris) as the metal-binding receptor that can produce blue fluorescence emission at 448 nm in an acidic aqueous medium ( $\text{pH} = 4.8$ ) solution. After adding  $\text{Fe}^{3+}$ , the fluorescence intensity showed significant decrease and it could be used for the detection of  $\text{Fe}^{3+}$  by the naked eye, as shown in Figure 3.2 (b). They also mentioned that due to the specific structure of **DAT-1**, the recognition unit of the sensor could selectively complex with  $\text{Fe}^{3+}$ . The PET effect on the N atom causes fluorescence quenching of **DAT-1** so it cannot

complex with other ions except  $\text{Fe}^{3+}$  due to its specific recognition. Hence, the sensor cannot be quenched by other ions without PET effect. Interestingly, **DAT-1** not only has good photophysical properties and water solubility, but it also shows excellent membrane permeability and is not toxic, so it could be used as an effective chemosensor for sensing  $\text{Fe}^{3+}$  in living cells.

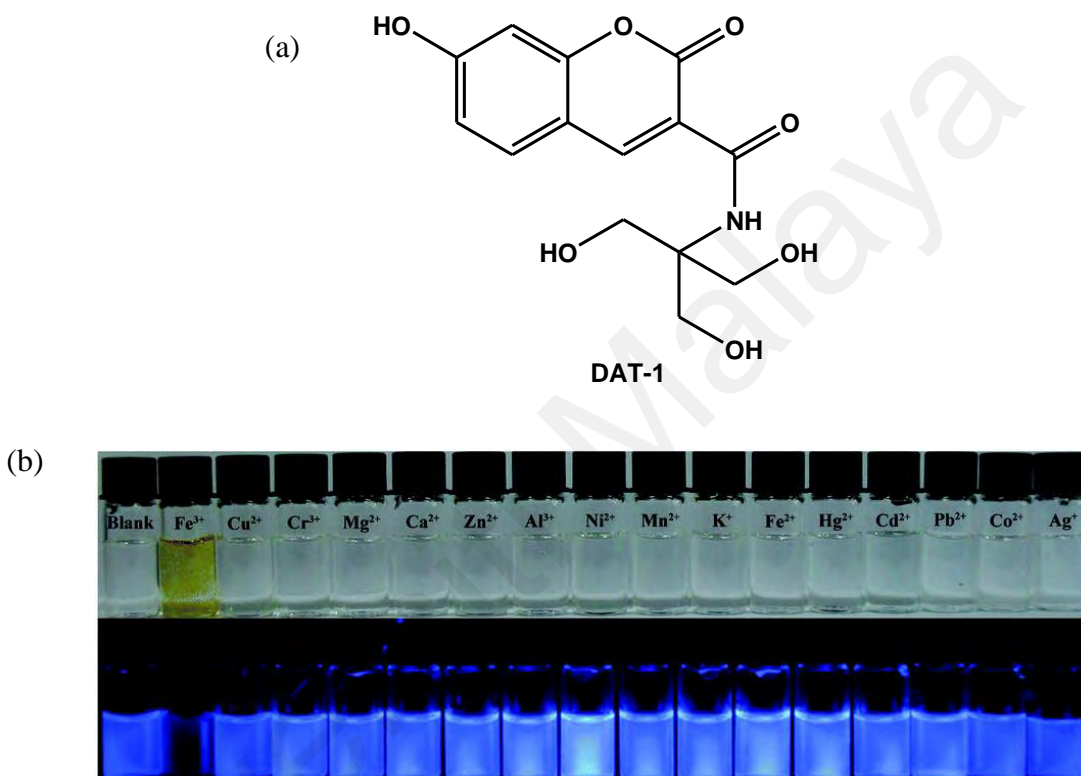


**Figure 3.5:** (a) Chemical structure **DAT-1**. (b) Fluorescent (bottom) and color (top) responses of **DAT-1** (20  $\mu\text{M}$ ) in  $\text{Na}_2\text{HPO}_4$ -citric acid buffer solutions (0.2 M) upon the addition of (100 equiv.) metal ions in water (En et al., 2014).

Additionally, a novel coumarin-naphthalimide conjugate (**CN**) “turn-on” chemosensor for  $\text{Fe}^{3+}$  was designed and synthesised. This chemosensor displays a high selectivity for  $\text{Fe}^{3+}$  among other ions with fluorescence enhancement in aqueous THF solution (Z. Li et al., 2014). The binding ratio of the **CN**- $\text{Fe}^{3+}$  complex was determined to be 1:1 with a low detection limit of 0.388  $\mu\text{M}$ , according to the Job’s plot method. Figure 3.6 shows the proposed binding mode between **CN** with  $\text{Fe}^{3+}$ .

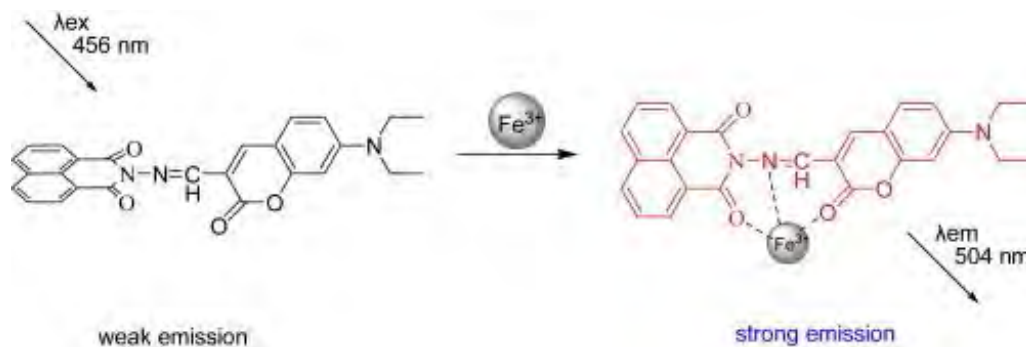


**Figure 3.6: Possible binding mode of CN with Fe<sup>3+</sup> (Z. Li et al., 2014).**

A novel 7-oxy-3-(3,4,5-trimethoxyphenyl)coumarin substituted phthalonitrile derivative, **OCP**, (Figure 3.7) has been synthesised and the chemosensor behaviours of these compounds to metal ions have also been analysed by fluorescence spectroscopy, revealing that these compounds act as fluorescence chemosensors for the determination of Fe<sup>3+</sup> ions in a solution (Kaya, Yuksel, Özpınar, Bulut, & Durmuş, 2014). Fe<sup>3+</sup> complex structures of mono-coumarin ring substituted derivatives have been investigated by using DFT computations. The competitive experiment, as illustrated in Figure 3.8, show the selectivity of **OCP** towards Fe<sup>3+</sup>. However, no stoichiometry confirmation was given in the article.

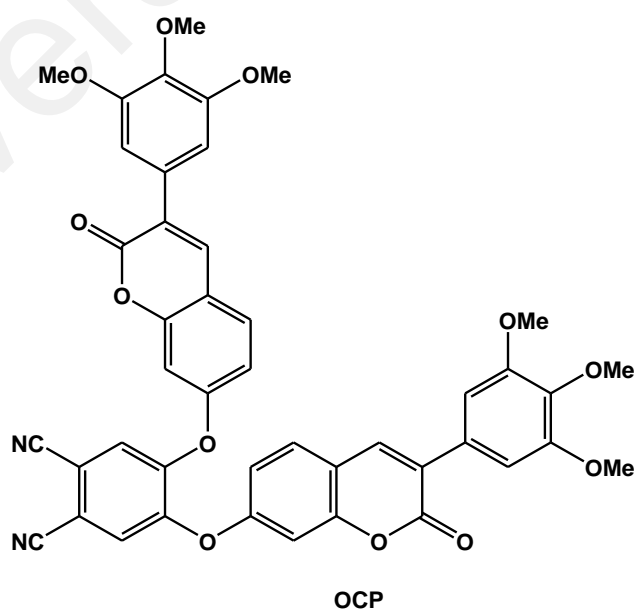


**Figure 3.7: The chemical structure of 7-oxy-3-(3,4,5-trimethoxyphenyl)coumarin substituted phthalonitrile derivative (OCP).**

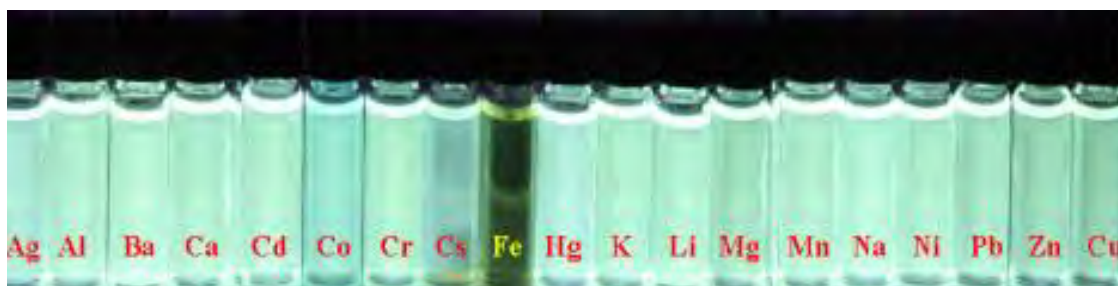


**Figure 3.8: The fluorescence emission responses of the OCP to different metal ions under UV lamp (Kaya et al., 2014).**

According to Joshi et al., two fluorescents conjugated to a protected phenylalanine amino acid through a triazole containing spacer coumarins (**A** and **B**), as chemical structures shown in Figure 3.9, have been used to produce a fluorescence-based  $\text{Fe}^{3+}$  sensor (Joshi et al., 2015). For  $\text{Fe}^{3+}$  in DMF or DMF/water (3/2 v/v), the fluorescence of compounds **A** and **B** was almost entirely quenched. The proposed binding mode, as predicted by density functional theory (DFT) calculations with supporting IR analysis, suggests that a 1:1 complex is formed between  $\text{Fe}^{3+}$  and the sensor. Figure 3.10 shows that the suggested binding mode is occupied by the Fe–N interaction. Both the synthesised compounds act as selective and sensitive sensors for the micromolar detection of  $\text{Fe}^{3+}$  ions.

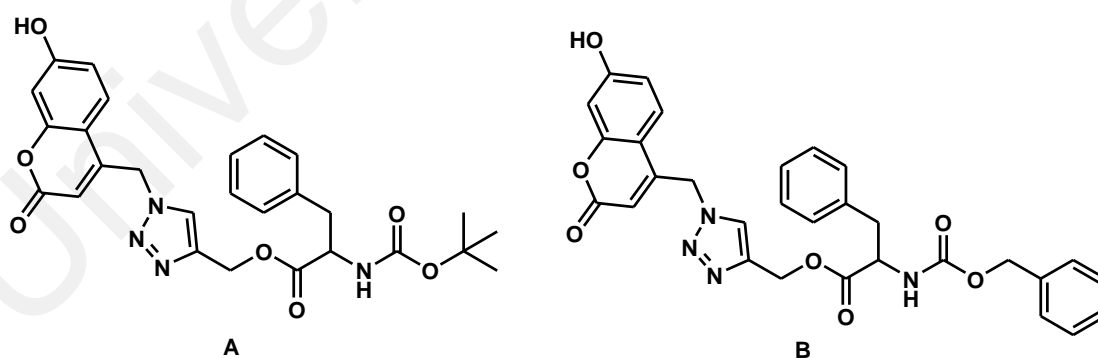


**Figure 3.9: Molecular structures of (S)-1-((7-hydroxy-2-oxo-2H-chromen-4-yl)methyl)-1H-1,2,3-triazol-4-yl methyl 2-(tert-butoxycarbonylamino)-3-phenylpropanoate, A and (S)-1-((7-hydroxy-2-oxo-2H-chromen-4-yl)methyl)-1H-1,2,3-triazol-4-yl methyl 2-(benzyloxycarbonylamino)-3-phenylpropanoate, B.**

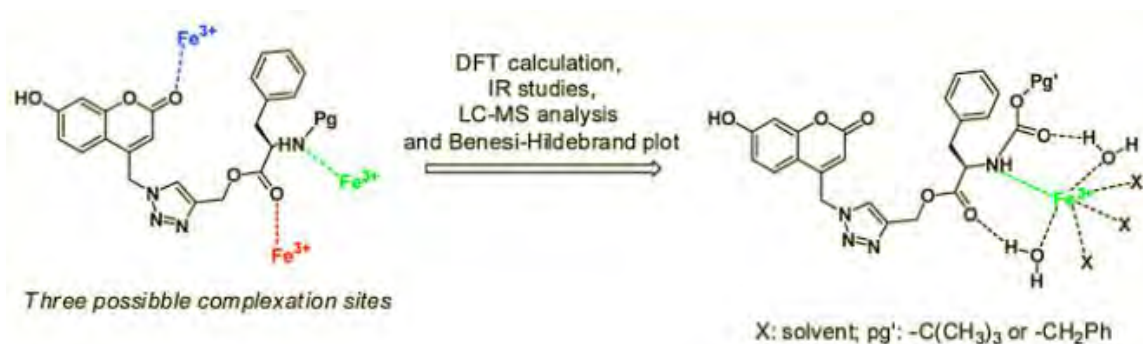


**Figure 3.10: Proposed structure of A-Fe<sup>3+</sup> and B-Fe<sup>3+</sup> complexes (Joshi et al., 2015).**

Qin, J. C. et al. provide another interesting example, a fluorescent sensor (**RC**) for Fe<sup>3+</sup> based on rhodamine 6G and coumarin conjugate (Qin et al., 2015). **RC** displays a significant fluorescence enhancement at 550 nm due to an intramolecular FRET mechanism from coumarin to rhodamine 6G (Figure 3.11). It gives a low detection limit for Fe<sup>3+</sup>, reaching the  $4.05 \times 10^{-6}$  M level which is sufficiently low to allow the detection of Fe<sup>3+</sup> concentrations in many chemical and biological systems.

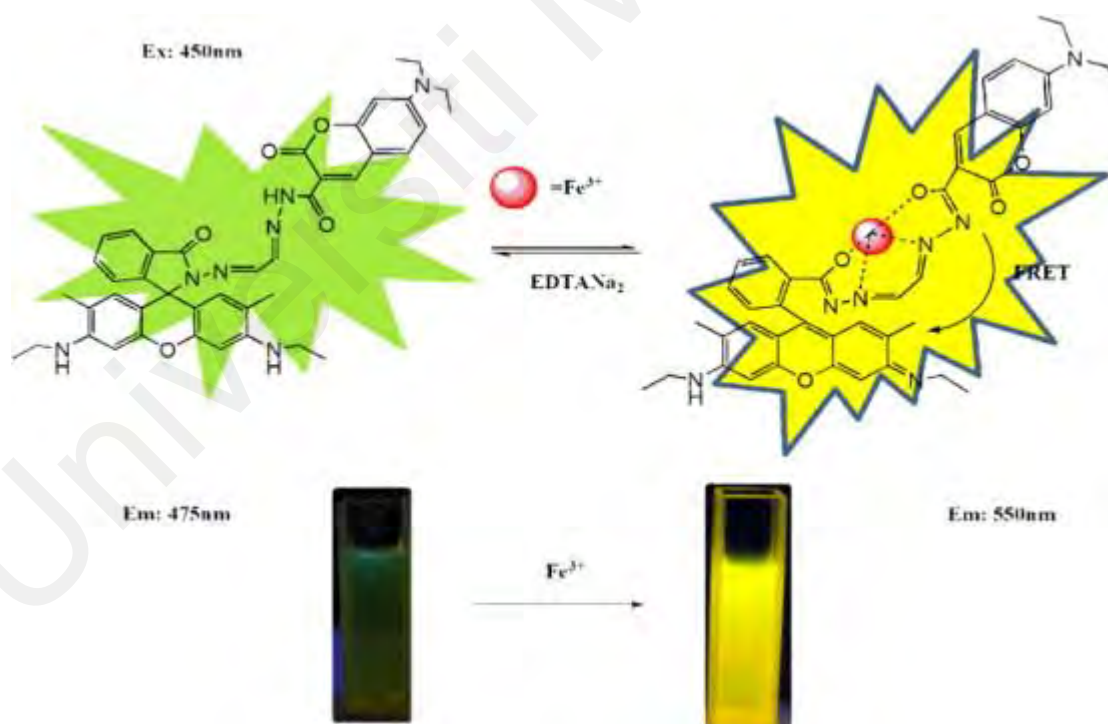


**Figure 3.11: Proposed mechanism for detection of Fe<sup>3+</sup> and inset photograph under UV irradiation at ex. 475 nm (Qin et al., 2015).**

The conjugation of the coumarin-rhodamine compound (**CR**) can exhibit a blue fluorescence emission at 465 nm in methanol (Hu, Wang, Long, & Xiao, 2016). Moreover, additional  $\text{Fe}^{3+}$  induces a slight fluorescence enhancement at 465 nm and causes the appearance of a new fluorescence emission at 573 nm with a 75-fold ratiometric fluorescence enhancement. Figure 3.12 illustrates the possibility of PET quenching that is limiting the coumarin and rhodamine undergoing a spiro-ring opening from the binding of  $\text{Fe}^{3+}$ . As a result, this generates an efficient FRET coupling between coumarin and rhodamine, resulting in the new fluorescence band. Notably, **CR** has been demonstrated to be highly selective and is not liable to interference with other metal cations.

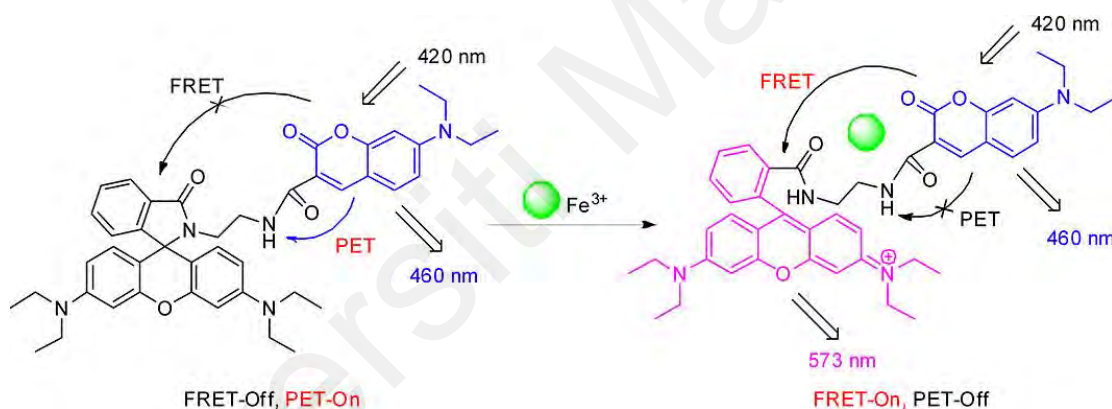


**Figure 3.12:  $\text{Fe}^{3+}$ -induced FRET OFF–ON and PET ON–OFF (Hu et al., 2016).**

Kumari et al. reported a coumarin derivative, (S)-4-((4-((3-amino-2-oxo-4-phenylbutoxy)methyl)-1H-1,2,3-triazol-1-yl)methyl)-7-hydroxy-2H-chromen-2-one, (**APC**) as a “turn-on” fluorescence chemosensor for  $\text{Fe}^{3+}$  and  $\text{Cu}^{2+}$  over other metal cations with detection limits of 143 nM and 71.31  $\mu\text{M}$ , respectively (Joshi, Kumari, Sarmah, Sakhuja, & Pant, 2016). Their report indicates that a 1:1 complex was formed between  $\text{Fe}^{3+}/\text{Cu}^{2+}$ ; this has been confirmed by the results acquired from LC–MS, IR studies and DFT calculations. The proposed binding is demonstrated in Figure 3.13. The compound acts as a significantly sensitive chemosensor for nanomolar detection of  $\text{Fe}^{3+}$

and micromolar detection of  $\text{Cu}^{2+}$ . This is in agreement with their competitive experiment results (Figure 3.14).

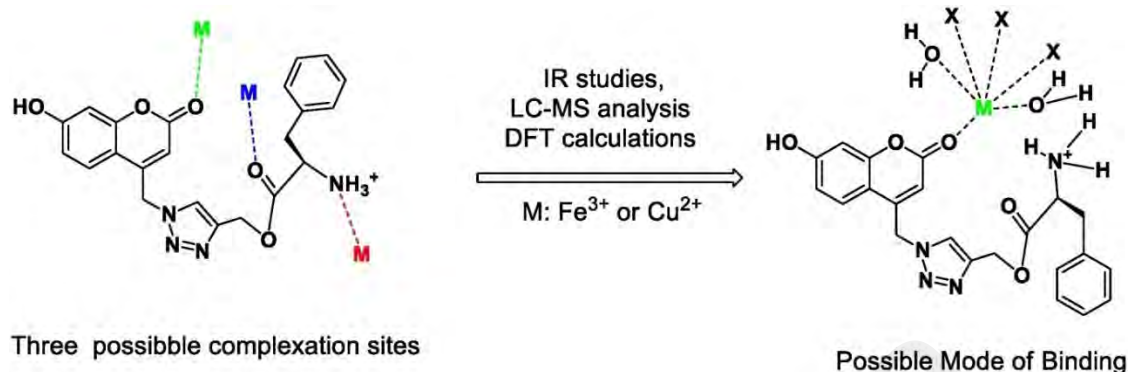


**Figure 3.13:** Proposed binding site for APC- $\text{Fe}^{3+}$  and APC - $\text{Cu}^{2+}$  complexes (Joshi et al., 2016).

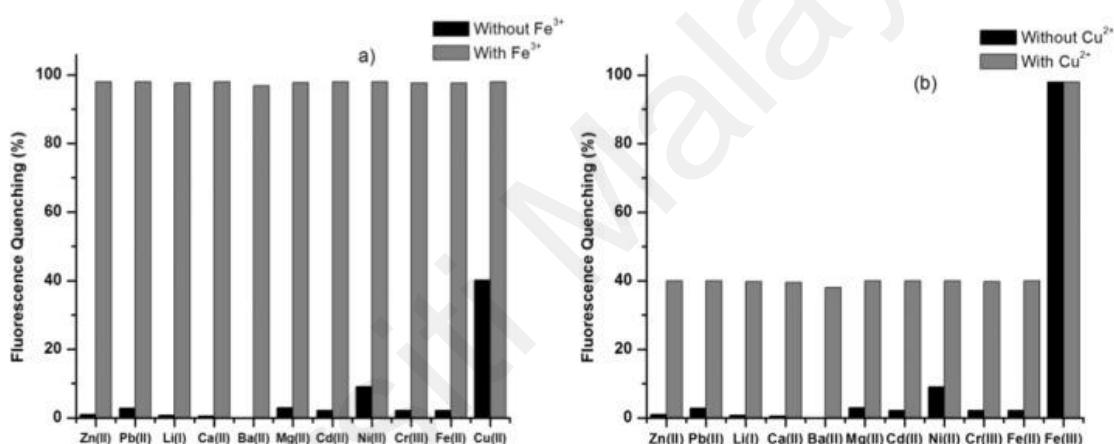


**Figure 3.14:** Column diagrams of the relative fluorescence intensity of APC with different, metal ions at 480 nm. Black bars represent the addition of various metal ions to the blank solution and grey bars represent the subsequent addition of (a)  $\text{Fe}^{3+}$  (5 eq.) and (B)  $\text{Cu}^{2+}$  (5 eq.) into the solutions (Joshi et al., 2016).

Figure 3.15 shows the phenanthro[9,10-d]imidazole-coumarin Schiff based compounds **PC1** and **PC2** can recognise  $\text{Fe}^{3+}$  in an aqueous solution containing 70% DMF, which produces quenched fluorescence upon binding  $\text{Fe}^{3+}$  for both sensors (Zhao et al., 2016b). This finding showed the selective “turn-off” fluorescence phenomenon due to the paramagnetic quenching effect of  $\text{Fe}^{3+}$  with the formation of a 1:1 sensor- $\text{Fe}$  complex in DMF/HEPES aqueous buffer (7:3, v/v, 10 mM, pH = 7.4). Although there is a stronger binding constant for **PC1**, **PC2** exhibits a lower detection limit of 0.83  $\mu\text{M}$  for  $\text{Fe}^{3+}$  than the limit for **PC1** which is 4.28  $\mu\text{M}$ . Moreover, **PC2** was sensitive to pH changes

because the addition of  $\text{Fe}^{3+}$  into **PC2** showed distinct fluorescence quenching across the pH range (4.0–8.0) at which the maximum response to  $\text{Fe}^{3+}$  sensing was observed. Therefore, the results implied that **PC2** could be applicable as a sensor in most biological systems. This is indeed an interesting finding from the analysis.

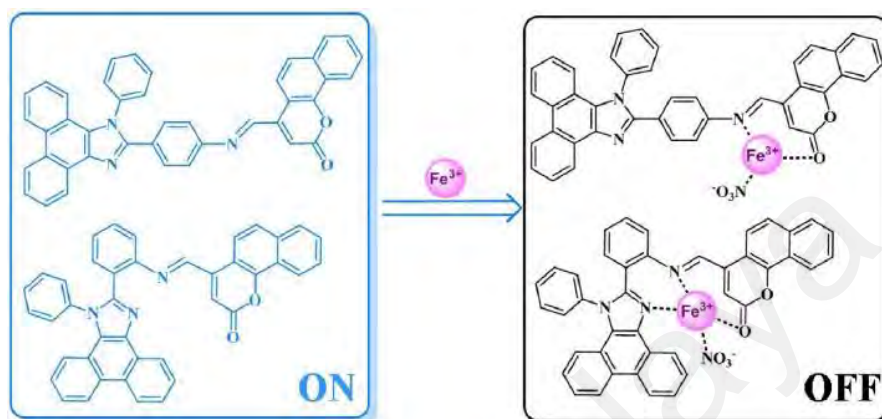


**Figure 3.15: The proposed binding modes for compound PC1 and PC2 with  $\text{Fe}^{3+}$  (Zhao et al., 2016b).**

In 2017, Zhou et al. synthesised another derivative of the phenanthro[9,10-d]imidazole-coumarin fluorescence sensor, **PICA** and successfully sensing  $\text{Fe}^{3+}$  as a “turn-off” chemosensor in the DMF/HEPES aqueous buffer (1:1, v/v, 10 mM, pH = 7.4) with a LOD of 4.8  $\mu\text{M}$ .(Zhao et al., 2017) **PICA** has been applied for the determination of  $\text{Fe}^{3+}$  concentration in real water samples. The fluorescence quenching of the 1:1 **PICA**– $\text{Fe}^{3+}$  complex was initiated to further act as a selective “turn-on” fluorescence sensor for phosphate anions over common anions and cations in the same condition with a dislocation process. The proposed mechanism of the “on-off-on” fluorescence response is illustrated in Figure 3.16.

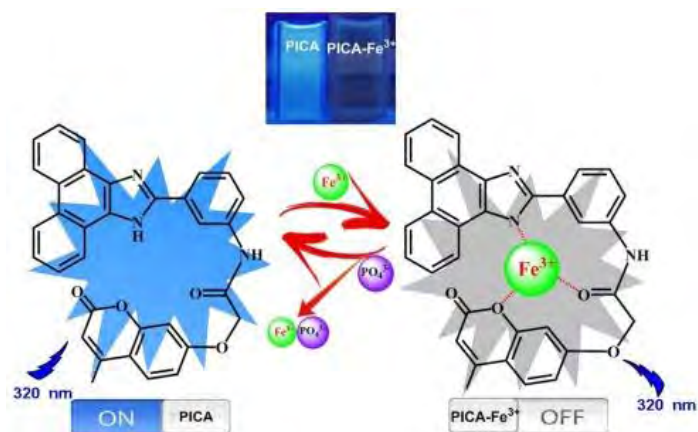


**Figure 3.16: The proposed mechanism for  $\text{PO}_4^{3-}$  detection by  $\text{PICA-Fe}^{3+}$  complex (Zhao et al., 2017).**

A highly selective chemosensor towards  $\text{Fe}^{3+}$  and  $\text{Ca}^{2+}$  ions has been produced by utilising a click chemistry procedure by producing two different coumarin derivatives (**TC**) connected via a triazole linkage (Puthiyedath & Bahulayan, 2018b). Based on Figure 3.17, **TC** shows enhanced fluorescence upon complexation with  $\text{Ca}^{2+}$ , whereas quenching of fluorescence occurs in the presence of  $\text{Fe}^{3+}$ . The fluorescence enhancement/quenching in the sensor happens due to a PET process in which the energy level ordering of the excited states is changed by the formation of the 1:1 complex of  $\text{Ca}^{2+}$  or  $\text{Fe}^{3+}$  with the coumarin derivatives.

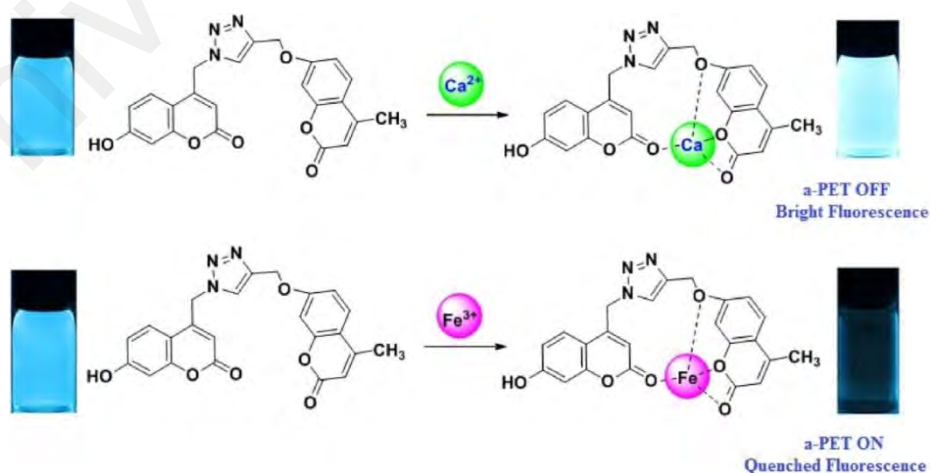


**Figure 3.17: Proposed complexation mechanism for sensing of  $\text{Ca}^{2+}$  and  $\text{Fe}^{3+}$  ions by **TC** (Puthiyedath & Bahulayan, 2018b).**

A coumarin chemosensor, 7-hydroxy-2-oxo-*N*-(pyridin-2-ylmethyl)chromene-3-carboxamide (**Probe 1**), exhibited a high fluorescence emission profile at 447 nm and demonstrated significant selectivity towards Fe<sup>3+</sup> ions (Warrier & Kharkar, 2018). The probe showed approximately 30-fold decrease in fluorescence intensity upon complexation with Fe<sup>3+</sup> and exhibited a low detection limit of 0.76 μM and also showed promise as an intracellular chemosensor for Fe<sup>3+</sup> (Figure 3.18).

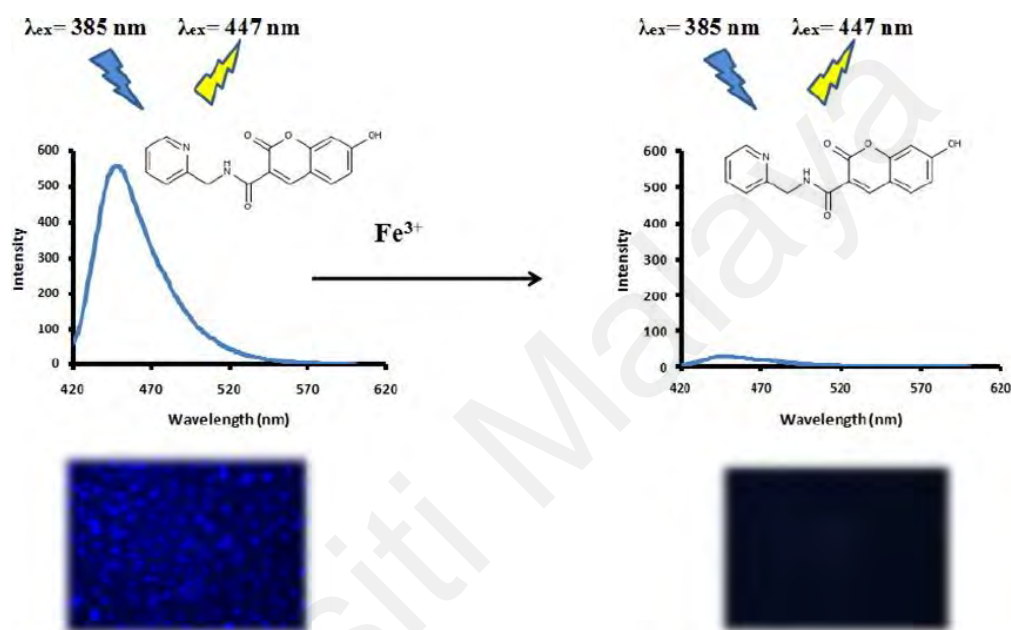


**Figure 3.18: Probe 1 showed a decrease in fluorescence intensity upon complexation with Fe<sup>3+</sup> and shows potential to be used as an intracellular chemosensor for Fe<sup>3+</sup> (Warrier & Kharkar, 2018).**

Wang et al., have developed a new fluorescent chemosensor (**FB**) based on coumarin for the detection of Fe<sup>3+</sup> with specific binding that causes strong fluorescence quenching through a 1:1 complex formation (W. Wang et al., 2018). Figure 3.19 shows that **FB** has high selectivity to Fe<sup>3+</sup> in the presence of other competing cations. Moreover, the *in situ* generated non-fluorescent **FB-Fe<sup>3+</sup>** complex was employed for the specific recognition of pyrophosphate (PPi) by a displacement process and causes the fluorescence to “turn-on” as illustrated in Figure 3.20. The process of **FB** and PPi recognition are rapid and reversible, thus **FB** allows for the investigation of fluorescent response for Fe<sup>3+</sup> and PPi in living cells by use of a confocal microscope.

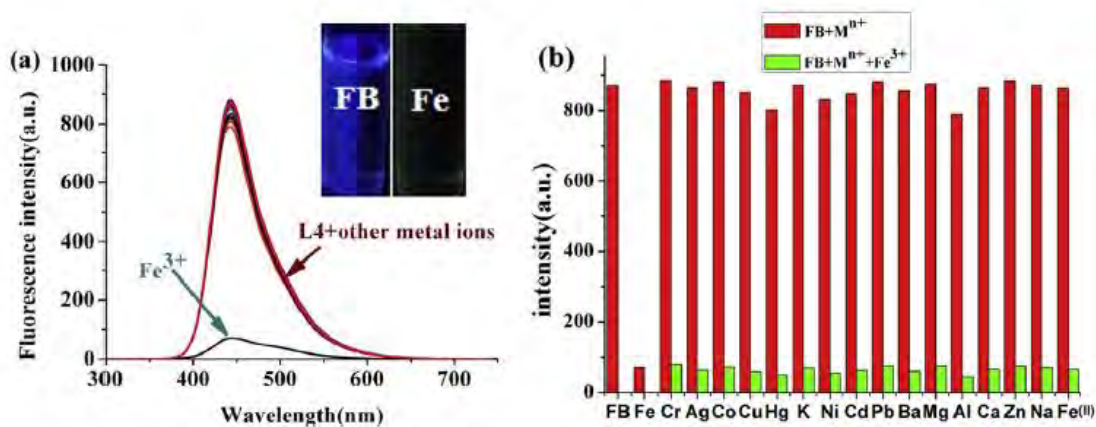


**Figure 3.19** (a) Changes in the emission spectra of FB in the presence of different metal ions in HEPES buffer (DMSO:H<sub>2</sub>O = 3:7, 20 mM, pH = 7.2); (b) Fluorescence response of FB to Fe<sup>3+</sup> in the presence of other common metal ions (W. Wang et al., 2018).

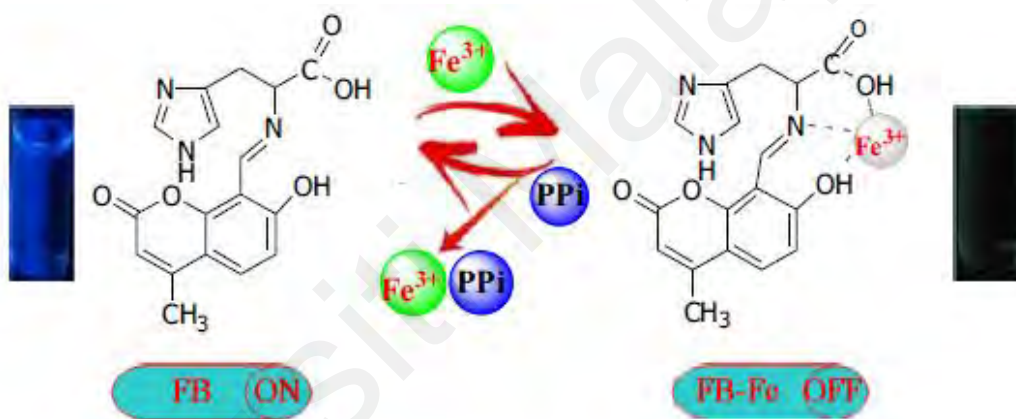


**Figure 3.20:** The proposed mechanism for PPI detection by FB-Fe<sup>3+</sup> complex (W. Wang et al., 2018).

Figure 3.21 shows a fluorescent probe based on isocoumarin, 2-amino-4-phenyl-6-(isocoumarin-3-yl)-3-cyanopyridine (**APICP**) for determining Fe<sup>3+</sup> and Hg<sup>2+</sup> ions in the DMSO/HEPES buffer solution (9/1 v/v, 5 μM, pH 7.0) with the detection limits of the probe calculated at 5.51 nM and 8.12 nM for Fe<sup>3+</sup> and Hg<sup>2+</sup> ions, respectively (S. N. K. Elmas et al., 2020). Based on the Job's plot result, the stoichiometry of the **APICP**-Fe<sup>3+</sup>/Hg<sup>2+</sup> complexes at a ratio of 2:1. This was confirmed by both FTIR and ESI-MS results. **APICP** can potentially be used as a promising candidate for sensing Fe<sup>3+</sup> and Hg<sup>2+</sup> in biological cells as it was shown to have relatively low cytotoxicity in the Hep G2 cell.

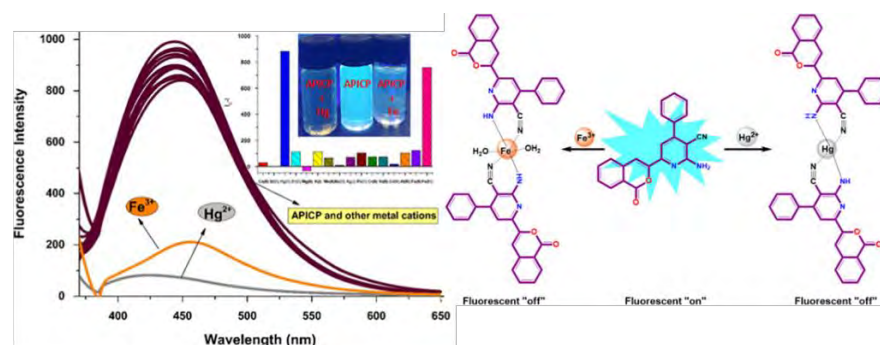


**Figure 3.21: The fluorescence emission responses of the APICP to different metal ions and proposed binding mechanism of APICP-Fe<sup>3+</sup>/Hg<sup>2+</sup> complexes (S. N. K. Elmas et al., 2020).**

All the findings discussed in this section are from recent studies (from 2014-2020) regarding coumarin derivative-based chemosensors for selective Fe<sup>3+</sup> detection, on its own or together with other metal ions. There are a variety of coumarin derivatives that have been synthesised that can selectively recognise Fe<sup>3+</sup>, via “turn-on” or “turn-off” fluorescence. A summary of the literature surveyed is given in table 3.1.

Based on the literature review conducted (2013 – 2020) none of the studies have been tested together with Ru<sup>3+</sup>, which exhibits properties very similar to that of Fe<sup>3+</sup>. In the next section (Section 3.3) will discuss about a chemosensor based on a coumarin derivative has been tested with Ru<sup>3+</sup> (amongst a variety of other metal ions) and showed selectively to Fe<sup>3+</sup>, which is unique compared to the other reports on coumarin-based chemosensors for Fe<sup>3+</sup>. For any Fe<sup>3+</sup> fluorescent probe, it is important to extensively demonstrate selectivity, testing with other heavy metals including ruthenium, as it can be presented in the environment (Masson et al., 2019), biological systems (Szczepaniak et al., 2019) and water (Sato et al., 2011) samples. Furthermore, furo[3,2-c]coumarin showed good photophysical properties and yet there has been no application of this compound as a sensor reported in the literature. Thus, this research has expanded the application of furo[3,2-c]coumarin as a chemosensor for Fe<sup>3+</sup>. The subsequent part of this chapter will discuss further in detail (methodology, results, and discussions) regarding the development of this novel Fe<sup>3+</sup> Fluorescence sensor.

**Table 3.1: Summary of the literature surveyed that selectively recognise Fe<sup>3+</sup> only and other metals.**

COMPOUND	DETECTION	SIGNALLING MECHANISM	LOD	REF.
6-amino-7-hydroxycoumarin, ( <b>L</b> )	“Turn-on” fluorescence (Fe <sup>3+</sup> and Al <sup>3+</sup> )	metal complexes inhibit the C=N isomerisation	Fe <sup>3+</sup> =4.3 μM Al <sup>3+</sup> =2.4 μM	(L. Wang et al., 2013)
diaza-18-crown-6 ether joined with dual coumarin (7-amino-4-trifluoromethylcoumarins) compounds, ( <b>DC</b> )	“Turn-off” fluorescence (Fe <sup>3+</sup> )	LMCT	0.31 μM	(H. Li et al., 2014)
2-amino-2-(hydroxymethyl)-1,3-propanediol (tris), ( <b>DAT</b> )	“Turn-off” fluorescence (Fe <sup>3+</sup> )	PET	0.3 μM	(En et al., 2014)
coumarin-naphthalimide conjugate, ( <b>CN</b> )	“Turn-on” fluorescence (Fe <sup>3+</sup> )	metal complexes inhibit the C=N isomerization	0.388 μM	(Z. Li et al., 2014)
7-oxy-3-(3,4,5-trimethoxyphenyl)coumarin substituted phthalonitrile derivative, ( <b>OCP</b> )	“Turn-off” fluorescence (Fe <sup>3+</sup> )	-	nd	(Kaya et al., 2014)
(S)-(1-((7-hydroxy-2-oxo-2H-chromen-4-yl) methyl)-1H-1,2,3-triazol-4-yl)methyl 2-(tert-butoxycarbonylamino)-3-phenylpropanoate, ( <b>A</b> ) and (S)-(1-((7-hydroxy-2-oxo-2H-chromen-4-yl)methyl)-1H-1,2,3-triazol-4-yl) methyl 2-(benzyloxycarbonylamino)-3-phenylpropanoate, ( <b>B</b> )	“Turn-off” fluorescence (Fe <sup>3+</sup> )	LMCT	A=7.65 μM B=10.2 μM	(Joshi et al., 2015)
rhodamine 6G and coumarin conjugate, ( <b>RC</b> )	Fluorescence enhancement (Fe <sup>3+</sup> )	Intramolecular FRET mechanism from coumarin to rhodamine 6G	4.05 μM	(Qin et al., 2015)
conjugation of the coumarin-rhodamine compound, ( <b>CR</b> )	Fluorescence enhancement (Fe <sup>3+</sup> )	Fe <sup>3+</sup> -induced FRET OFF-ON and PET ON-OFF	nd	(Hu et al., 2016)
(S)-4-((4-((3-amino-2-oxo-4-phenylbutoxy)methyl)-1H-1,2,3-triazol-1-yl)methyl)-7-hydroxy-2H-chromen-2-one, ( <b>APC</b> )	“Turn-on” fluorescence (Fe <sup>3+</sup> and Cu <sup>2+</sup> )	LMCT	Fe <sup>3+</sup> =143 nM, Cu <sup>2+</sup> =71.31 μM	(Joshi et al., 2016)
phenanthro[9,10-d]imidazole-coumarin Schiff based compounds ( <b>PC1</b> and <b>PC2</b> )	“Turn-off” fluorescence (Fe <sup>3+</sup> )	LMCT	<b>PC1</b> =4.28 μM, <b>PC2</b> =0.83 μM	(Zhao et al., 2016b)
phenanthro[9,10-d]imidazole-coumarin derivative, ( <b>PICA</b> )	“Turn-off” fluorescence (Fe <sup>3+</sup> )	LMCT	4.8 μM	(Zhao et al., 2017)
coumarin derivatives ( <b>TC</b> ) connected via a triazole linkage	“Turn-off” fluorescence (Fe <sup>3+</sup> )Fluorescence enhancement (Ca <sup>2+</sup> )	PET	Fe <sup>3+</sup> =3.81 μM Ca <sup>2+</sup> =2.61 μM	(Puthiyedath & Bahulayan, 2018a)
7-hydroxy-2-oxo-N-(pyridin-2-ylmethyl)chromene-3-carboxamide ( <b>Probe 1</b> )	“Turn-off” fluorescence (Fe <sup>3+</sup> )	LMCT	0.76 μM	(Warrier & Kharkar, 2018)
Coumarin derivative ( <b>FB</b> )	“Turn-off” fluorescence (Fe <sup>3+</sup> )	LMCT	8.73 × 10 <sup>-8</sup> M	(W. Wang et al., 2018)
isocoumarin, 2-amino-4-phenyl-6- (isocoumarin-3-yl) -3-cyanopyridine ( <b>APICP</b> )	“Turn-off” fluorescence (Fe <sup>3+</sup> and Hg <sup>2+</sup> )	LMCT	Fe <sup>3+</sup> =5.51 nM, Hg <sup>2+</sup> =8.12 nM	(S. N. K. Elmas et al., 2020)

### 3.3 Furo[3,2-c]coumarin-derived Fe<sup>3+</sup> Selective Fluorescence Sensor: Synthesis, Fluorescence Study and Application to Water Analysis

#### 3.3.1 Materials and Methods

##### 3.3.1.1 Materials and Instrumentation

All reagents were purchased from commercial suppliers and used without further purification. The salts used in stock solutions of metal ions were Al(NO<sub>3</sub>)<sub>3</sub>·9H<sub>2</sub>O, CaCl<sub>2</sub>, CoCl<sub>2</sub>·6H<sub>2</sub>O, Cu(NO<sub>3</sub>)<sub>2</sub>·4H<sub>2</sub>O, FeCl<sub>2</sub>·4H<sub>2</sub>O, Fe(NO<sub>3</sub>)<sub>3</sub>·9H<sub>2</sub>O, KOH, MgCl<sub>2</sub>, MnCl<sub>2</sub>, NaOH, NiCl<sub>2</sub>·6H<sub>2</sub>O, Pb(NO<sub>3</sub>)<sub>2</sub>, RuCl<sub>3</sub>·H<sub>2</sub>O, Zn(NO<sub>3</sub>)<sub>2</sub>·6H<sub>2</sub>O.

<sup>1</sup>H NMR (400 MHz) spectra were acquired on a Bruker AVANCE 400 MHz NMR Spectrometer using TMS (tetramethylsilane) as internal standard. All stock solutions of the samples for both UV-Vis and Fluorescence studies were prepared at 0.1 mM in different solvents (ethanol, chloroform and ethyl acetate) and diluted in 10 mL with appropriate concentrations. UV-vis absorption and fluorescence spectra of the furocoumarin derivatives (in solution) were recorded on a CARY 60 UV-Vis spectrophotometer and CARY Eclipse Fluorescence Spectrometer, respectively. Excitation and emission monochromator band pass were kept at 5 nm using a quartz cell cuvette (1x1 cm). The absolute quantum yields were calculated using quinine sulfate in 0.1M H<sub>2</sub>SO<sub>4</sub> as a standard. Fluorescence lifetime measurements were performed with the use of an FLS 1000 Spectrometer (Edinburgh Instruments, Livingston, UK) at room temperature. In these experiments the fluorescence lifetimes of the furocoumarin derivatives in methanol were measured using the photon counting technique (requiring at least 10,000 photons per second to be counted because the signal-to noise ratio becomes unsatisfactory at lower count rates (Leback, 1997)) with an excitation wavelength set to 374 nm in all the cases. UV-vis absorption and fluorescence spectra of **FH** and all metal ions were performed with the use of a Cary 5000 UV-Vis-NIR Spectrophotometer (Agilent Technologies) and FLS 1000 Spectrometer (Edinburgh Instruments), respectively. Paper spray ionisation mass spectrometry (PSI-MS) (Deidre E Damon et al.,

2016; F. P. Jjunju et al., 2016; Simon Maher, Fred PM Jjunju, et al., 2016) was performed on a Waters Xevo TQ-MS (Waters, Wilmslow, UK).

### 3.3.1.2 Synthesis of furo [3,2-c] coumarin derivatives (Figure 3.22).

Equimolar amounts of 4-hydroxycoumarin and benzaldehyde derivatives were dissolved in benzene (0.2 M) and heated under reflux. After 30 minutes, cyclohexyl isocyanide (1 eq.) was added to the reaction mixture and further refluxed for 24 h. The pure compound was obtained by recrystallization from diethyl ether to produce up to 85% yield. These compounds have been reported and the characterization data agreed with previous studies (Nair et al., 2002a; Shaabani et al., 2004).

2-(Cyclohexylamino)-3-phenyl-4H-furo[3,2-c]chromen-4-one. **FH**, 92% yield, light yellow powder, m.p. = 110-112°C, FTIR ( $\text{cm}^{-1}$ ) = 3250 (NH), 2925-2850 (C=C of cyclohexane), 1720 (C=O of pyrone), 1570 (C=C of pyrone),  $^1\text{H NMR}$  (400 MHz,  $\text{CDCl}_3$ ) =  $\delta$  1.18-2.08(m, 10H), 3.55-3.58 (m, 1H), 4.29 (d, J = 8.32Hz, 1H), 7.27-7.31 (m, 2H), 7.39 (d, J = 4.00 Hz, 1H), 7.43 (t, J = 8.00 Hz, 3H), 7.52 (d, J = 8.00 Hz, 2H), 7.77 (d, J = 8.00 Hz, 1H),  $^1\text{H NMR}$  spectrum of **FH** as shown in Figure A11. UV-Vis = 375 nm (in ethanol).

2-(Cyclohexylamino)-3-(4-chlorophenyl)-4H-furo[3,2-c]chromen-4-one. **FCI**, 90% yield, bright crystalline yellow, m.p. = 120-122°C, FTIR ( $\text{cm}^{-1}$ ) = 3289 (NH), 2930-2857 (C=C of cyclohexane), 1707 (C=O of pyrone), 1593 (C=C of pyrone),  $^1\text{H NMR}$  (400 MHz,  $\text{CDCl}_3$ ) =  $\delta$  1.16 - 2.07 (m, 10H), 3.57 (br, 1H), 4.21 (s, 1H), 7.33 - 7.28 (m, 1H), 7.41 - 7.39 (m, 4H), 7.47 (d, J = 6.40 Hz, 2H), 7.77 (d, J = 7.60 Hz, 1H),  $^1\text{H NMR}$  spectrum of **FCI** as shown in Figure A12 UV-Vis = 375 nm (in ethanol).

2-(Cyclohexylamino)-3-(4-nitrophenyl)-4H-furo[3,2-c]chromen-4-one. **FNO<sub>2</sub>**, 85% yield, reddish orange powder, m.p. = 145-147°C, FTIR ( $\text{cm}^{-1}$ ) = 3389 (NH), 2929 - 2851 (C=C of cyclohexane), 1736 (C=O of pyrone), 1574 (C=C of pyrone),  $^1\text{H NMR}$  (400

MHz, CDCl<sub>3</sub>) = δ 1.19 - 2.11 (m, 10H), 3.67 (m, 1H), 4.60 (d, J = 7.96Hz, 1H), 7.34 (t, J = 6.80 Hz, 1H), 7.45-7.40 (m, 2H) 7.69 (d, J = 8.72Hz, 2H), 7.77 (d, J = 7.64Hz, 1H), 8.22(d, J = 8.64 Hz, 2H), <sup>1</sup>H NMR spectrum of **FNO<sub>2</sub>** as shown in Figure A13. UV-Vis = 380 nm (in ethanol).

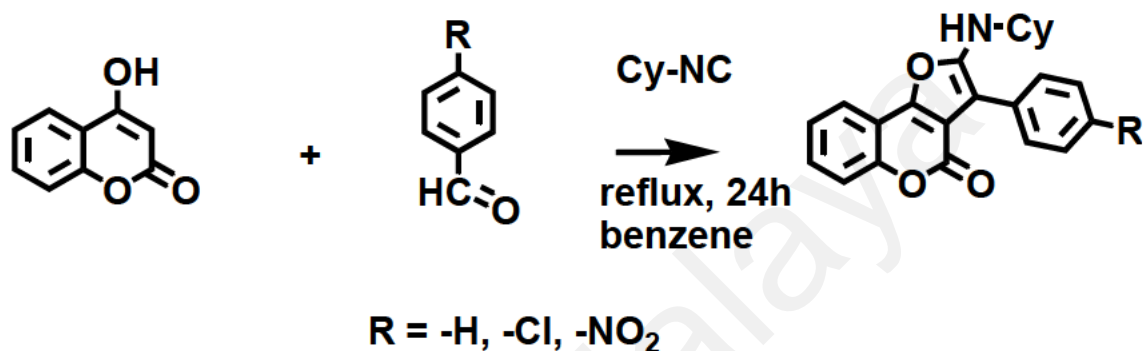


**Figure 3.22: Synthesis of furo[3,2-c]coumarin derivative.**

### 3.3.1.3 Fluorescence spectral responses of **FH** to metal ions.

The analysis was conducted for two different solvent systems: pure methanol and a water/methanol mixture (9:1, v/v). All stock solutions of the furocoumarin (**FC**) and various metal ions ( $\text{Mg}^{2+}$ ,  $\text{Ca}^{2+}$ ,  $\text{Mn}^{2+}$ ,  $\text{Fe}^{2+}$ ,  $\text{Fe}^{3+}$ ,  $\text{Al}^{3+}$ ,  $\text{Ni}^{2+}$ ,  $\text{Cu}^{2+}$ ,  $\text{Zn}^{2+}$ ,  $\text{Co}^{2+}$ ,  $\text{Pb}^{2+}$  and  $\text{Ru}^{3+}$ ) were analysed at a concentration of 0.001 M, except  $\text{Na}^+$  and  $\text{K}^+$  at 0.2 M in methanol. Then, each of the metal ions were diluted to 50  $\mu\text{M}$ , while **FH** was diluted to 0.5  $\mu\text{M}$  in methanol. For the water/methanol solvent system, **FH** was diluted to 5  $\mu\text{M}$ .

For testing, **FH** was mixed with each of the metal ions for up to 1 minute (by stirring until no layers could be visually observed) after which UV-Vis and fluorescence analysis were carried out. The fluorescence emission spectra were recorded from 430 to 700 nm with an excitation wavelength at 374 nm. Both excitation and emission slit widths were set at 1 nm. For the competing analysis, the fluorescence changes of **FH** in methanol were measured by the treatment of 50  $\mu\text{M}$   $\text{Fe}^{3+}$  ion in the presence of 50  $\mu\text{M}$  other interfering

metal ions. All of the background metal ions tested showed no interference with the detection of  $\text{Fe}^{3+}$  by competitive experiment.

### 3.3.2 Results and discussion

The structures of the furocoumarin derivatives (**FH**, **FCI**, and **FNO<sub>2</sub>**) were characterized by  $^1\text{H}$  NMR and FTIR. These results are in good agreement with the chemical structures for furocoumarin from the literature (Nair et al., 2002a; Shaabani et al., 2004). Table 3.2 summarizes the UV-Vis and fluorescence spectroscopy data of **FH**, **FCI** and **FNO<sub>2</sub>**. Figure A3, shows the UV-Vis spectra of **FH**, **FCI** and **FNO<sub>2</sub>** in ethanol. In Figure 3.23, the fluorescence spectra of **FH** and **FCI** show higher intensity than **FNO<sub>2</sub>**. The main contributing factor responsible for the high fluorescence intensity of furocoumarin is related to its planar and rigid structure (Levitus, 2011). Fluorescence of **FNO<sub>2</sub>** was severely quenched, contrary to the responses for **FH** and **FCI**. Chloro- in **FCI** is a weaker electron withdrawing group (EWG) than  $-\text{NO}_2$  in **FNO<sub>2</sub>**, however, the chloro-substituent can also donate through the aromatic ring, which has a high electron density, as the atom is enriched with non-bonding electrons. Therefore, it can be through a  $\pi$ -electron delocalization promoter rather than a nitro group, which acts as a relatively strong EWG as illustrated in Figure 3.24. In this case, chlorophenyl would be a donor group to the furocoumarin moiety. It has been reported that the EWG decreases electron density of the aromatic ring with the exception of the halogen substituent group (Lawrence & Frei, 2000). The EWG of the nitro group in the benzene ring (nitroaromatic) has empty  $\pi^*$  orbitals of low energy, which are good acceptors of electrons. Therefore electron-rich fluorescent molecules can potentially undergo strong quenching via a PET (B. Bag & Bharadwaj, 2004), fluorescence resonance energy transfer (FRET) or electron exchange energy transfer with nitroaromatics (Yingxin Ma, Wang, & Wang, 2015; Martelo, Marques, Burrows, & Berberan-Santos, 2019; S. Wang, Li, Pan, & Tang, 2012).

Hence, based on the result clearly showed that the chloro- substituent is higher fluorescence intensity than the nitro- substituent.

**Table 3.2: Concentration [M], Absorbance (Abs), fluorescence lifetimes ( $\tau$ ) and quantum yield ( $\Phi_f$ ) for fluorescence properties of furocoumarin derivatives in ethanol solution. nd = not determined.**

Compounds	[M]	Abs	Molar Abs	$\lambda_{ex}$ (nm)	$\lambda_{em}$ (nm)	$\Phi_f$	Stokes shift (cm <sup>-1</sup> )	$\tau$ (ns)
<b>FH</b>	$1.00 \times 10^{-6}$	0.20	$2.00 \times 10^5$	375	492	0.48	127	5.61
<b>FCI</b>	$1.00 \times 10^{-6}$	0.37	$3.70 \times 10^5$	375	491	1.00	126	4.17
<b>FNO<sub>2</sub></b>	$1.00 \times 10^{-5}$	0.22	$5.70 \times 10^4$	380	440	nd	60	nd

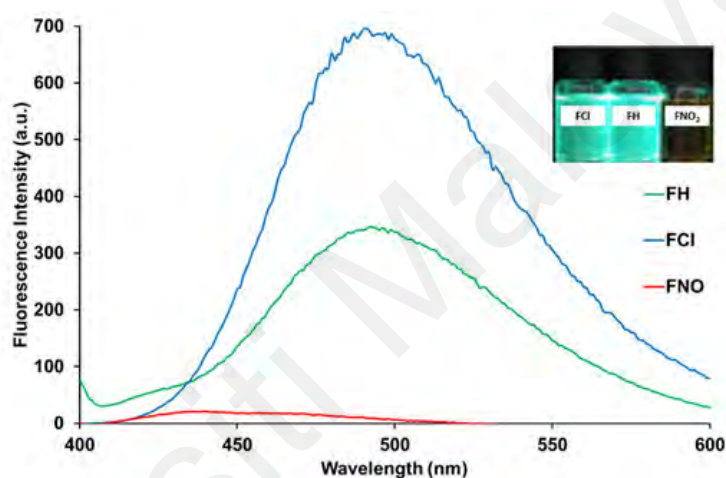


**Figure 3.23: Fluorescence Spectra of Furocoumarin derivatives (FCI, FH, FNO<sub>2</sub>) in ethanol. Inset: Photograph image of furocoumarin in ethanol under UV lamp illumination. Both FCI and FH are similar in concentration,  $1.00 \times 10^{-6}$  M, while FNO<sub>2</sub> is  $1.00 \times 10^{-5}$  M, at excitation wavelength 375 nm.**



**Figure 3.24: Possible mechanisms whereby chloro- substituent (R=Cl) donates electron density through aromatic ring compared with nitro- substituent (R=NO<sub>2</sub>).**

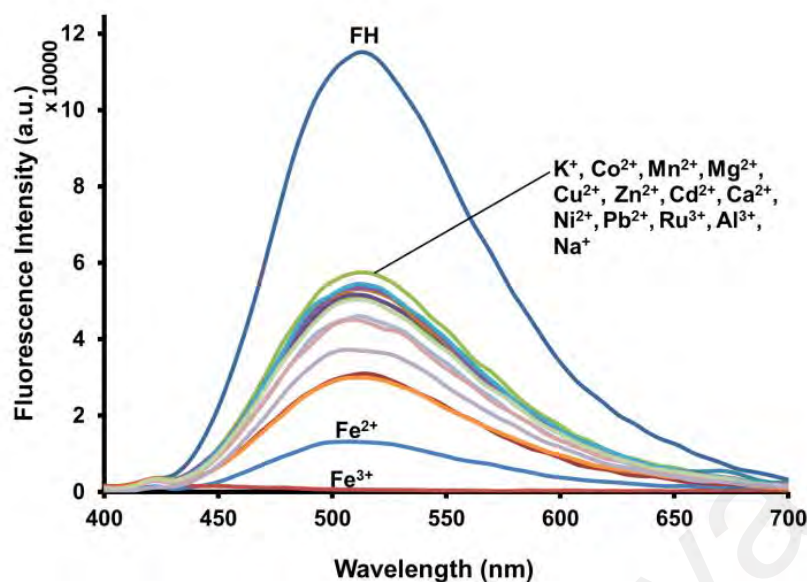


**Figure 3.25: Fluorescence spectra of FH (0.5  $\mu\text{M}$ ) in the presence of different metal ions (100 equiv.) in methanol, at excitation wavelength 374 nm.**

### 3.3.2.1 Fluorescence and UV–Vis titration studies of FH with other metal ions.

The photophysical complexation studies of **FH** with an extensive series of metal salts including  $\text{Na}^+$ ,  $\text{K}^+$ ,  $\text{Mg}^{2+}$ ,  $\text{Ca}^{2+}$ ,  $\text{Mn}^{2+}$ ,  $\text{Fe}^{2+}$ ,  $\text{Fe}^{3+}$ ,  $\text{Al}^{3+}$ ,  $\text{Ni}^{2+}$ ,  $\text{Cu}^{2+}$ ,  $\text{Zn}^{2+}$ ,  $\text{Co}^{2+}$ ,  $\text{Pb}^{2+}$  and  $\text{Ru}^{3+}$  in methanol, was performed using fluorescence spectroscopy. As shown in Figure 3.25, the mixture of **FH** with  $\text{Fe}^{3+}$  was the only test sample that exhibited no fluorescence emission (i.e., “turn-off”) in the wavelength range from 430 to 700 nm. Remarkably, in the presence of 50  $\mu\text{M}$  of various metal ions, fluorescence spectra of **FH** exhibited an appreciable fluorescence emission except in the case of  $\text{Fe}^{3+}$ , which resulted in a noticeable “turn-off” fluorescence response. This fluorescence spectral change was also observed visually when examined with a UV transilluminator (380 nm) as illustrated in Figure A4. The interaction of **FH** with  $\text{Fe}^{3+}$  leads to an immediate fluorescence “turn-off”, while for the other metal ions, a slight fluorescence quenching is observed by the naked eye. As mentioned, the planar and rigid structure of the **FH** molecule makes it a highly fluorescent compound. However, when chelation occurs, there is a transfer of charges within the fluorescent ligand-metal system which then causes the fluorescence quenching (Yongmin Ma, Luo, Quinn, Liu, & Hider, 2004; Nudelman et al., 1998). Therefore, it can

be inferred that the fluorescence quenching of **FH** in the presence of  $\text{Fe}^{3+}$  is due to a ligand-metal charge transfer (LMCT) mechanism. This suggestion is supported by considering the paramagnetic nature of  $\text{Fe}^{3+}$  with an unfilled d shell, this would take part in the energy and/or electron transfer processes leading to quenching of the fluorescence (Xu, Hou, Ma, Wu, & Wei, 2013; L. Yang, Yang, Xu, Zhang, & Liu, 2013). When  $\text{Fe}^{3+}$  binds with **FH**, the fluorescent opens a non-radiative deactivation channel induced by the unfilled d shell, resulting in fluorescence quenching due to electron transfer (Warrier & Kharkar, 2018). Thus, the mechanism of LMCT could happen promptly due to the strong paramagnetic quenching property of  $\text{Fe}^{3+}$ , leading to a severe fluorescence quenching effect (i.e., “turn-off”) to coordinate between **FH** and  $\text{Fe}^{3+}$ .

To gain a quantitative evaluation of the relation between the change in emission intensity of **FH** and the amount of  $\text{Fe}^{3+}$  interaction, a fluorescence titration experiment was carried out with varying concentrations of  $\text{Fe}^{3+}$ , as shown in Figure 3.26). The emission intensity of the peak at 511 nm was systematically quenched by increasing the concentration of  $\text{Fe}^{3+}$  from 5 to 50  $\mu\text{M}$ . Moreover, the emission intensity at 511 nm was linearly proportional (correlation coefficient,  $R^2 > 0.99$ ) to the concentration of  $\text{Fe}^{3+}$  over the range of 0–30  $\mu\text{M}$ , with a limit of detection of 1.93  $\mu\text{M}$  (Figure 3.27). These observations revealed that **FH** is suitable for use as a sensor for the quantitative measurement of  $\text{Fe}^{3+}$ . To investigate the binding stoichiometry between **FH** and  $\text{Fe}^{3+}$ , a Job’s plot experiment was carried out by keeping the total concentration of **FH** and  $\text{Fe}^{3+}$  ions at 20  $\mu\text{M}$  and changing the molar ratio of  $\text{Fe}^{3+}$  from 0 to 1. As shown in Figure 3.28 the result indicates a maximum molar fraction of 0.7, indicating the formation of 1:2 complex of **FH** and  $\text{Fe}^{3+}$ . This agrees with complexes previously reported (J. Chen et al., 2009; P. Singh, Singh, Bhargava, & Kumar, 2015). On the basis of changes in emission intensity at 511 nm, the stoichiometric ratio and apparent binding constant of **FH** with  $\text{Fe}^{3+}$  was determined using Benesi–Hildebrand (B-H) linear regression analysis. From the

B–H plot, a 1:2 stoichiometry between **FH** with  $\text{Fe}^{3+}$  was confirmed with an association constant of  $5.25 \times 10^3 \text{ M}^{-1}$  (Figure 3.30).

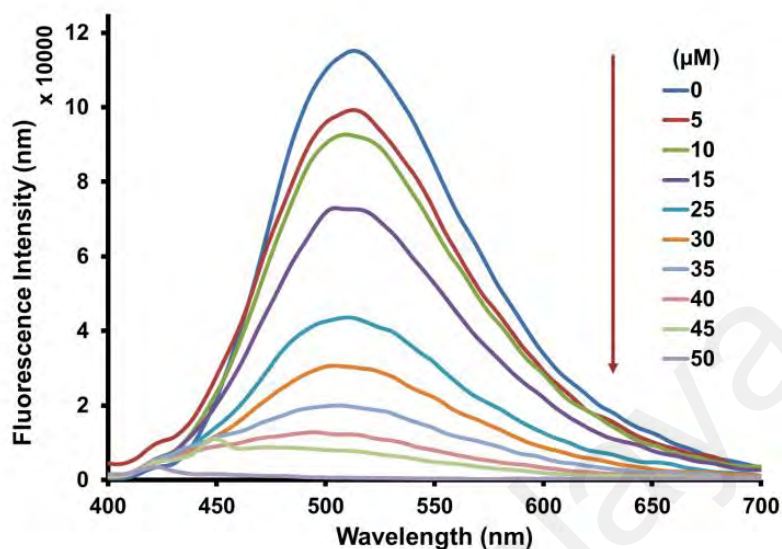


**Figure 3.26:** Fluorescence emission spectra of **FH** ( $0.5 \mu\text{M}$ ) was titrated with  $\text{Fe}^{3+}$  ( $0 - 100$  equiv.) in methanol, at excited at  $374 \text{ nm}$ .

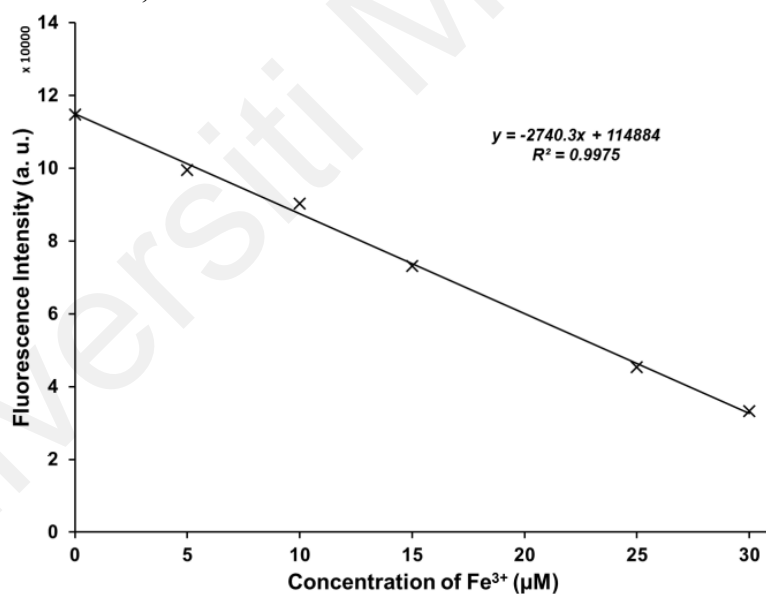


**Figure 3.27:** Calibration curve based on **FH** titration with  $\text{Fe}^{3+}$  in methanol.

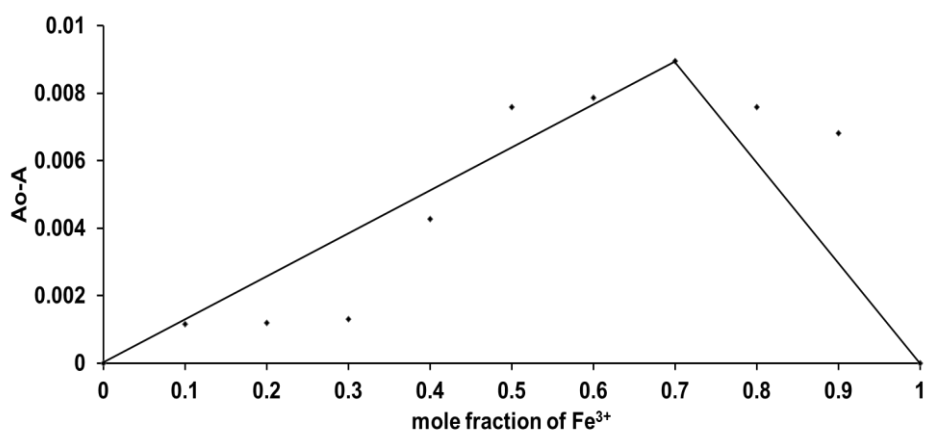


**Figure 3.28: Job's plot for determining the stoichiometry for FH and Fe<sup>3+</sup> in methanol. Total concentration=  $2 \times 10^{-5}$  M.**

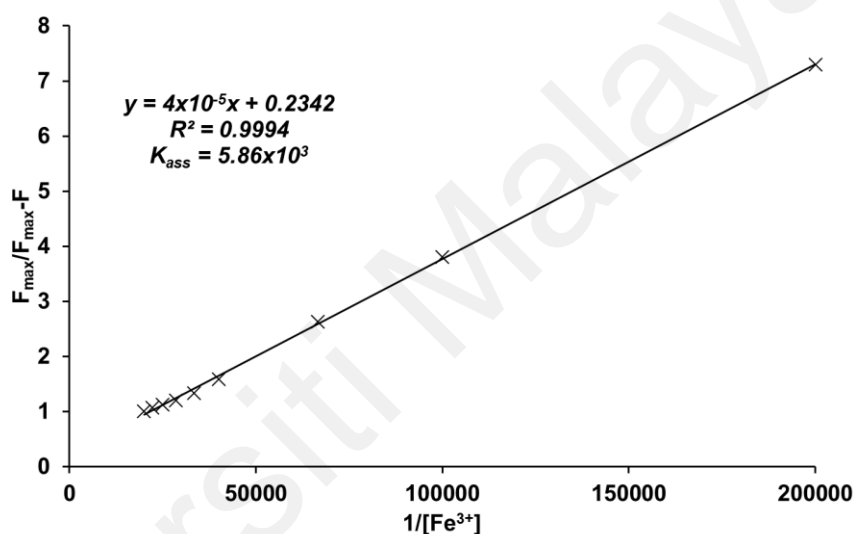


**Figure 3.29: Benesi-Hildebrand plot of FH sensor with Fe<sup>3+</sup>.**

### 3.3.2.2 Competition experiment using fluorescence spectroscopy.

To further investigate the practical applicability of **FH** as a selective sensor for Fe<sup>3+</sup>, a competition experiment was carried out for **FH** in the presence of Fe<sup>3+</sup> mixed with other metal ions (Na<sup>+</sup>, K<sup>+</sup>, Mg<sup>2+</sup>, Ca<sup>2+</sup>, Fe<sup>2+</sup>, Mn<sup>2+</sup>, Al<sup>3+</sup>, Ni<sup>2+</sup>, Cu<sup>2+</sup>, Zn<sup>2+</sup>, Co<sup>2+</sup>, Pb<sup>2+</sup>, Ru<sup>3+</sup>). Interestingly, the fluorescence emission intensity was quenched in every case after mixing Fe<sup>3+</sup> with each of the candidate metal ions (Figure 3.30). Thus, **FH** shows great promise as a highly selective and sensitive fluorescence “turn-off” sensor for the detection of Fe<sup>3+</sup> even in the presence of other analogous ions (in particular, Fe<sup>2+</sup> and Ru<sup>3+</sup>). Furthermore, based on the general trend in Figure 3.30, it is apparent that 3+ cations tend to exhibit stronger binding that effects fluorescence quenching of **FH**. This may be due to

stabilization of the binding with an anion ( $\text{NO}_3^-$ ); 2 bonds at **FH** and one bond with anion. Consider, for example  $\text{Al}^{3+}$ , where the cation can bind in a similar way. This tridentate binding is certainly more stable than the other 2+ cations with bidentate binding. It is also apparent that  $\text{Fe}^{3+}$  shows better binding with **FH** than  $\text{Fe}^{2+}$  which can be attributed to the cationic radii, since  $\text{Fe}^{3+}$  is much smaller than  $\text{Fe}^{2+}$  about half the size of the  $\text{Fe}^{3+}$  radius (Sánchez, Sabio, Gálvez, Capdevila, & Dominguez-Vera, 2017). When considering 1+ cations it is interesting that  $\text{Na}^+$  also quenches **FH** but with  $\text{K}^+$  to a lesser extent. This is probably related to the single bond with **FH** that is not very stable. Moreover,  $\text{Na}^+$  has better electronegativity compared to  $\text{K}^+$ , which one expects promotes better binding with **FH**.

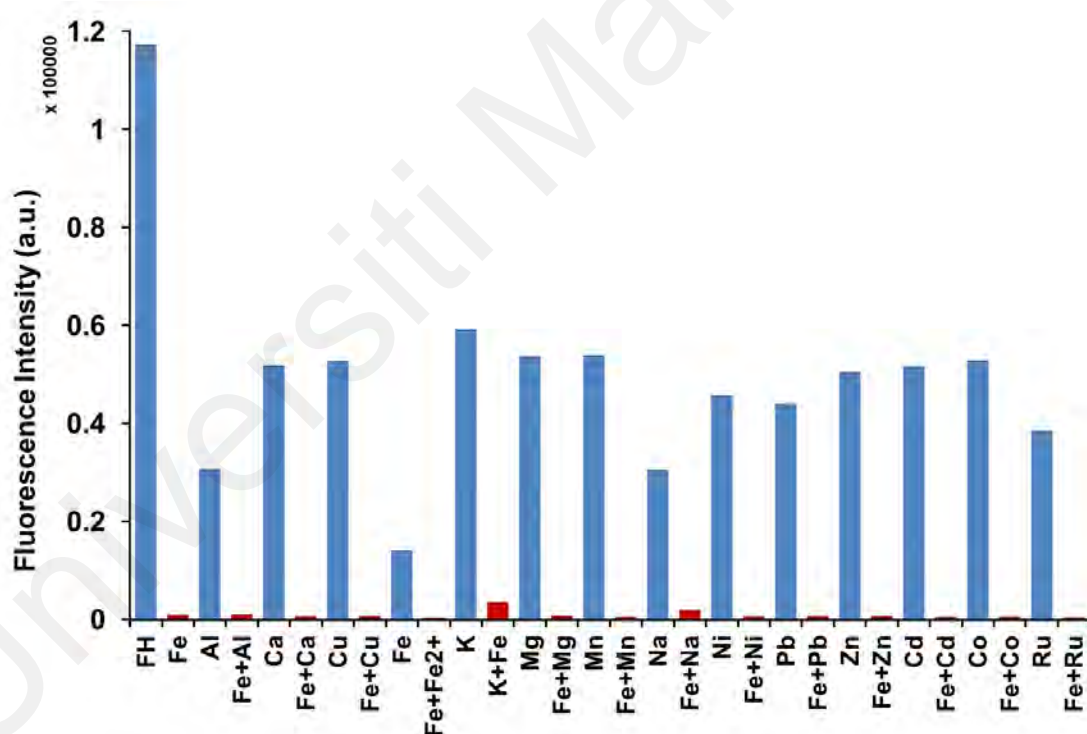


**Figure 3.30: Competitive experiments in the FH +  $\text{Fe}^{3+}$  system with potential interfering metal ions. FH (0.5  $\mu\text{M}$ ),  $\text{Fe}^{3+}$  (50  $\mu\text{M}$ ), and other metals (50  $\mu\text{M}$ ). Excited at 374 nm and emission measured at 511 nm.**

### 3.3.2.3 Proposed sensing mechanism.

To study the reasonable binding mode of **FH** and  $\text{Fe}^{3+}$ , mass spectrometry analysis has been carried out and supports the formation of a 1:2 **FH**- $\text{Fe}^{3+}$  complex. As illustrated in Figure A5, **FH** exhibits an intense protonated peak at  $m/z$  360.21, while in the presence of  $\text{Fe}^{3+}$ , a peak at  $m/z$  595.55 is observed, which is attributed to the formation of a protonated  $\text{FH}:(\text{Fe}^{3+}\text{NO}_3)_2$  complex. For the mentioned results above, as well as the Job's plot (Figure A6), and suspected that the sensing mechanism for the 1:2 binding modes of the **FH**- $\text{Fe}^{3+}$  complex is as suggested in Figure 3.31. IR spectroscopy was used to elucidate the coordination mode between **FH** and  $\text{Fe}^{3+}$  (Figure A7), showing the FTIR spectra of **FH** before and after the addition of  $\text{Fe}^{3+}$ . A shift in the characteristic absorption band in the FTIR spectra confirmed the coordination behaviour for **FH**- $\text{Fe}^{3+}$ . Upon the introduction of  $\text{Fe}^{3+}$ , an extremely broad peak appeared between 3665 and 3125  $\text{cm}^{-1}$ , which is attributed to the involvement of nitrogen from the primary amine (NH) and oxygen from furan in the binding of  $\text{Fe}^{3+}$ . Furthermore, the stretching vibration frequency of the pyrone carbonyl ( $\text{C}=\text{O}$ ) at 1720  $\text{cm}^{-1}$  is shifted to 1605  $\text{cm}^{-1}$ .

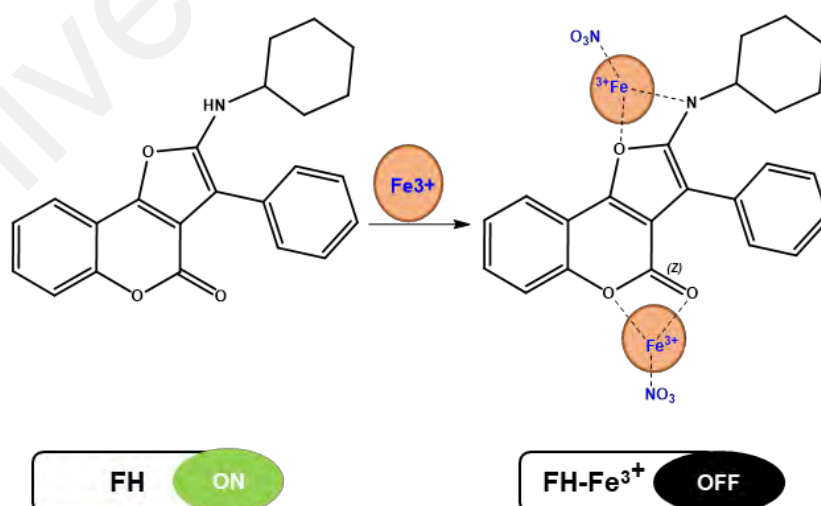


Figure 3.31: Proposed binding mode of FH with  $\text{Fe}^{3+}$ .

#### 3.3.2.4 Fluorescence and UV–vis titration studies of FH with other metal ions (in water/methanol (9:1, v/v)).

Fluorescence quenching in protic solvents is a common problem with previously reported fluorescence sensors (Anderson, Nagirimadugu, & Abelt, 2019), in order to confirm FH is not susceptible to this issue and to demonstrate a real-world sample application, the photophysical properties of sensor **FH** were examined in a predominantly aqueous environment, water/methanol (9:1, v/v) at 5  $\mu\text{M}$ . This composition of 9:1 v/v water / methanol was at the maximum solubility of **FH** in water. Changes to the fluorescence properties of **FH** caused by various metal ions are shown in Figure 3.32. The result shows  $\text{Fe}^{3+}$  also produces significant quenching in the fluorescent emission of **FH**. The other tested metals only show relatively insignificant changes, except  $\text{Co}^{2+}$ ,  $\text{Na}^+$  and  $\text{K}^+$ . So, it can be concluded that **FH** also has high selectivity for recognition of  $\text{Fe}^{3+}$  in a predominantly aqueous solution. The fluorescence spectra of **FH** (5  $\mu\text{M}$ ) in water/methanol (9:1, v/v), in the presence of various concentrations of  $\text{Fe}^{3+}$  ion (0.2–8 equivalent), are shown in Figure 3.33, which shows quenching in the fluorescent emission of **FH** when the concentration of  $\text{Fe}^{3+}$  is increased. A Job's plot of **FH** with  $\text{Fe}^{3+}$  also indicates the formation of a 1:2 complex (Figure A10). A competitive assay (Figure 3.34) confirms that **FH** can still detect  $\text{Fe}^{3+}$  even in the presence of other heavy metals. Thus, in a predominantly aqueous solution, **FH** exhibits high selectivity for  $\text{Fe}^{3+}$  over the other tested metal ions except  $\text{Co}^{2+}$ ,  $\text{Na}^+$  and  $\text{K}^+$ .

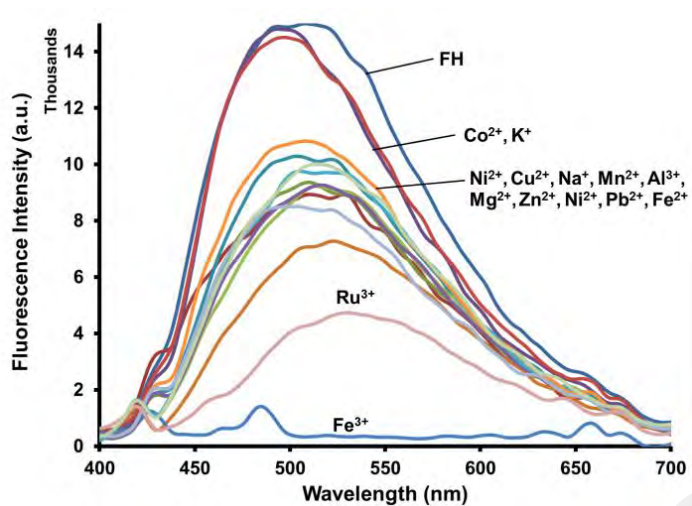


Figure 3.32: Fluorescence spectra of FH (5  $\mu\text{M}$ ) in the presence of different metal ions (10 equiv.) in water/methanol (9:1, v/v). Excited at 374 nm.

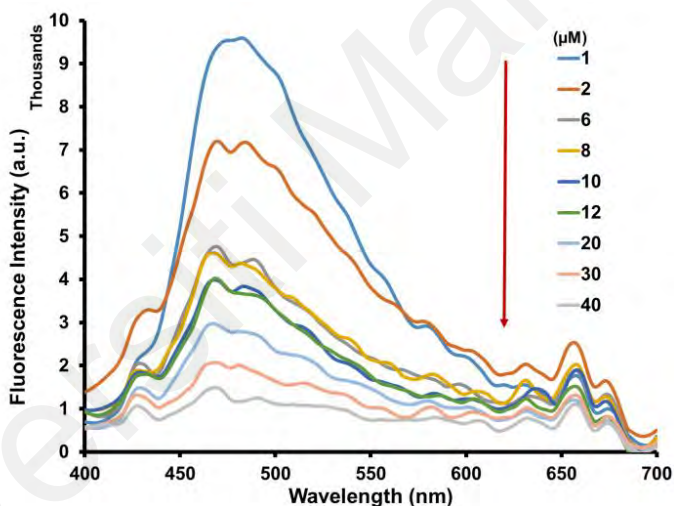
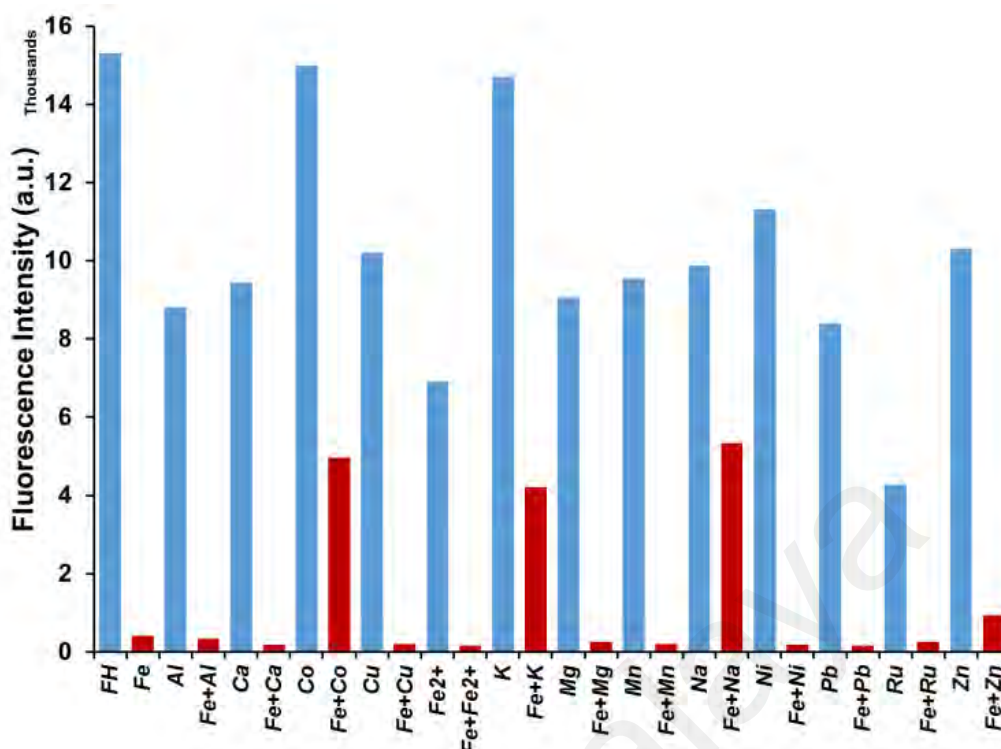


Figure 3.33: Fluorescence emission spectra of FH (5  $\mu\text{M}$ ) was titrated with  $\text{Fe}^{3+}$  (0.2–equiv.) in water/methanol (9:1, v/v). Excited at 374 nm.



**Figure 3.34: Competitive experiments in the FH + Fe<sup>3+</sup> system with interfering metal ions. FH (5 μM), Fe<sup>3+</sup> (50 μM) and other metals (50 μM) in water/methanol (9:1, v/v). Excited at 374 nm and emission measured at 511 nm.**

### 3.3.2.5 Determination of Fe<sup>3+</sup> in real water samples.

To investigate the applicability of the FH sensor in realistic environmental samples, recovery studies were carried out in mineral drinking water and tap water samples doped with Fe<sup>3+</sup>, using fluorescence emission spectroscopy. Mineral water samples were directly purchased from a local supermarket (Brand: Volvic, Source: Clairvic Spring, Auvergne Regional Park, at the North of the Puy de Dôme in France) and tap water samples were obtained from our laboratory. The fluorescence intensities of samples were analysed after being spiked with a standard solution of Fe<sup>3+</sup>. Testing on these water samples was performed without any sample pre-treatment except for the addition of **FH**, Fe<sup>3+</sup> and allowing 1 minute for mixing. From Table 3.3, it showed that the recoveries of Fe<sup>3+</sup> were from 91.5% to 125%. These data indicate that **FH** as a sensor has significant potential for the practical detection of Fe<sup>3+</sup> in various aqueous samples where other potentially competing species are present.

**Table 3.3: Analytical results of FH-Fe<sup>3+</sup> in water samples.**

Water samples	Added ( $\mu\text{M}$ )	Found ( $\mu\text{M}$ )	Recovery (%)	RSD (%)
Mineral water	2.0	2.1	105	0.71
	10.0	10.0	100	5.71
	20.0	19.3	96.5	9.60
Tap water	2.0	2.5	125	0.5
	10.0	9.8	98	6.9
	20.0	18.3	91.5	4.2

### 3.4 Conclusion

Initially, this chapter discussed the introduction and previous reports of coumarin derivatives applications as a fluorescence-based sensor, especially for Fe<sup>3+</sup> sensing. The main work in this application has been focused on utilising the furo[3,2-coumarin] compound which has been synthesised in a one-pot synthesis reaction with high yield (82-92%), to study its fluorescence properties for the first time. Subsequently, one of the furo[3,2-c]coumarin derivatives (**FH**), was tested further for application as a novel fluorescent chemosensor for Fe<sup>3+</sup>. Based on the fluorescence data, **FH** is the most promising furocoumarin derivative as it exhibits strong fluorescence ( $\Phi_f = 0.48$ ) with a long fluorescence lifetime (5.6 ns) and a large Stokes' shift. **FH** exhibits a highly selective, sensitive, and instant “turn-off” fluorescence response to Fe<sup>3+</sup> over other metal ions. This was attributed to a charge transfer mechanism. Selectivity was demonstrated against 13 other competing metal ions (Na<sup>+</sup>, K<sup>+</sup>, Mg<sup>2+</sup>, Ca<sup>2+</sup>, Mn<sup>2+</sup>, Fe<sup>2+</sup>, Al<sup>3+</sup>, Ni<sup>2+</sup>, Cu<sup>2+</sup>, Zn<sup>2+</sup>, Co<sup>2+</sup>, Pb<sup>2+</sup> and Ru<sup>3+</sup>) and aqueous compatibility was demonstrated in a 10% MeOH-H<sub>2</sub>O solution. As an indicative application, this finding demonstrated the potential of this sensor for the quick measurement of Fe<sup>3+</sup> in mineral and tap water samples highlighting the real-world application of **FH** as a turn-off fluorescence sensor.

## CHAPTER 4: RAPID SCREENING AND REACTION MONITORING VIA DUAL-TIP PAPER SPRAY IONISATION

In this chapter a rapid screening technique is explored for the synthesis of dansyl aniline, which is a key component of the white light emission LED coating from chapter 2. The synthesis of dansyl aniline has been screened rapidly and monitored by using reactive paper spray ionisation (PSI) via a novel design of the paper substrate denoted as dual-tip. The first part of this chapter deliberates the fundamentals of reactive PSI, an ambient ionisation technique commonly used with mass spectrometry (MS). This is examined further by focusing on reaction monitoring via PS-MS. Then the methodology is described for the novel research conducted as part of this chapter (as it relates to the new dual-tip design). Significant parts of this chapter have been published (Sarih, Romero-Perez, et al., 2020).

### 4.1 Introduction

It is well known that chemical synthesis can be achieved using charged microdroplets (Girod, Moyano, Campbell, & Cooks, 2011) whereby the product(s) can be collected by spraying a reaction mixture toward a target/collector surface under ambient conditions (Müller, Badu-Tawiah, & Cooks, 2012). Moreover, the reaction mixture can be monitored online by spraying directly into a mass spectrometer for analysis (Bain et al., 2014; Maher, Jjunju, & Taylor, 2015). This is sometimes known as direct ionisation. Amongst the plethora of available ionisation methods, there is a distinct class known as ambient ionisation (AI) that specifically refers to ionisation conducted within the ambient environment, outside the mass spectrometer, and with minimal sample preparation (Bain et al., 2014; Cooks, Ouyang, Takats, & Wiseman, 2006; Harris, Galhena, & Fernández, 2011; Jjunju et al., 2015; Monge, Harris, Dwivedi, & Fernández, 2013; Barry L. Smith et al., 2019; B. L. Smith, Jjunju, Taylor, Young, & Maher, 2016). Spray-based AI methods create a localised-environment for charged microdroplets that is conducive for reactions

to occur between constituents of the droplet solution (Ryan D Espy, Wleklinski, Yan, & Cooks, 2014; Laskin et al., 2012; Moolayil et al., 2006). AI methods can be defined by three distinguishing features; firstly, sampling and ionisation is done externally from the mass spectrometer to allow full access and control of the sample during analysis; secondly, analysis is performed in the innate state of the sample, meaning that less preparation steps are required compared to traditional analytical methods; and last but not least, the analyte of interest is directly transferred into the mass spectrometer, thus lessening matrix effects during ionisation (Frey, Damon, & Badu-Tawiah, 2019).

Paper spray, also known as paper spray ionisation (PSI), sits firmly in the ambient ionisation family (da Silva et al., 2019; Manicke, Bills, & Zhang, 2016). Paper spray is a popular AI method as it can enable effective ionisation and transport of charged droplets in the open air environment external to the mass spectrometer, with no pneumatic assistance needed as well as minimal requirement for prior sample preparation (J. Liu et al., 2010; H. Wang, Liu, Cooks, & Ouyang, 2010a; X. Yan, Augusti, Li, & Cooks, 2013). Paper spray is a relatively new ambient ionisation method which continues to increase in popularity. Wang et al., first reported PS-MS for the analysis of therapeutic drugs in dried blood samples (DBSs) (H. Wang, Liu, Cooks, & Ouyang, 2010b). Paper spray is performed by applying a solvent to a paper triangle that holds the dried sample (Figure 4.1). Paper spray depends on sample collection performed directly on the paper substrate followed by elution of the target analyte with a spray solvent. The solvent performs an online solid or liquid extraction by applying a direct current (DC) voltage (typically 3–5 kV) to the back end of the paper by a conductive material (e.g., an alligator clip acting as an electrode). Electric charge accumulates at the sharp tip of the paper triangle since the paper substrate is positioned facing the MS inlet held at ground (or other lower potential) level. Charged droplets are generated from the applied solvent via Taylor cone formation. Based on this process of electrospray, molecules are extracted from the sample on the

paper and are then ionised. Consequently, they are characterised by the MS. Paper is also appropriate for distant sampling due to its distinctive characteristics, firstly, the sample is easily collected; secondly, it is cheap and widely available, which makes it suitable for use in supply-limited situations; thirdly, its ability to stabilise samples in dry conditions which lessens shipping and biohazard necessities; fourthly, the dried samples are easily stored; and lastly, it is easy to dispose of (e.g., by burning or biodegradation) (Frey et al., 2019).

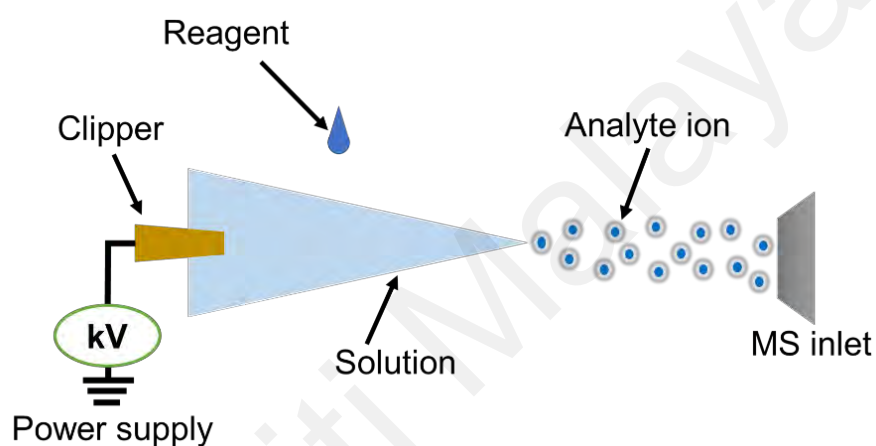


**Figure 4.1: Schematic diagrams of the PS-MS.**

In a conventional sense, PS-MS has been widely utilised for many types of sample analysis including biomedical and clinical studies (Bills & Manicke, 2016; Carmany et al., 2018; Chamberlain, Rubio, & Garrett, 2019; L. Fan & Lee, 2012; Y.-C. Huang et al., 2020; Shi, El Gierari, Faix, & Manicke, 2016; Shi, El Gierari, Manicke, & Faix, 2015; H. Wang et al., 2011; Yannell, Kesely, Chien, Kissinger, & Cooks, 2017), therapeutics (Ryan D. Espy, Manicke, Ouyang, & Cooks, 2012; Y. Liu et al., 2018; Suraritdechachai et al., 2019; Vandergrift & Gill, 2019) illegal drugs analysis (de Paula, Jurisch, Piccin, & Augusti, 2018; Ryan D. Espy et al., 2014; Jurisch, de Paula, & Augusti; McKenna, Jett, Shanks, & Manicke, 2018), environmental monitoring (Jjunju et al., 2013; F. P. M. Jjunju et al., 2016; H. Liu et al., 2019; Simon Maher, Fred Jjunju, et al., 2016; Moura et al.,

2020), detection of chemical warfare agents (CWAs) (Dhummakupt et al., 2017; Dowling, McBride, McKenna, Glaros, & Manicke, 2020; McKenna et al., 2017), and also for screening chemical reactions and reaction monitoring studies (S. Bag, Hendricks, Reynolds, & Cooks, 2015; Bain, Pulliam, Raab, & Cooks, 2016; Bain et al., 2014; Banerjee, Basheer, & Zare, 2016; Choi & Cha, 2020; Davis & Badu-Tawiah, 2017; Resende et al., 2017; Rindelaub, Wiley, Cooper, & Shepson, 2016; X. Yan et al., 2013; X. Zhou, Pei, & Huang, 2015; Zhu et al., 2019a). In the paper spray experiment, reactions are carried out by using small amounts of reagents with subsequent mass spectrometric assessment providing insight regarding certain aspects of the chemical reactivity. Recently, several classical reactions have been carried out using reactive AI-based methods, including: Katritzky reaction (X. Yan et al., 2013), Claisen–Schmidt base-catalyzed condensations (Bain et al., 2014), haloform reactions (Bain, Pulliam, Raab, & Cooks, 2015) and synthesis of carboxylic acids from alcohols (Zhu et al., 2019b).

In the next section (Section 4.2) the peer-reviewed academic literature is critiqued in regard to reactions performed using PS-MS.

#### **4.2 Chemical reaction and reaction monitoring by Reactive PS-MS**

A reactive PS-MS experiment is typically carried out under ambient conditions. Firstly, reagents are placed on the paper surface by drop-casting. Next, the sample is eluted from the paper as charged droplets released by field evaporation. Finally, the result can be analysed/monitored by a mass spectrometer.

Reactive PS-MS has been used for an increasing number of reactions. Recently, Yan et al., performed a classical Katritzky reaction using PS-MS. In this case, the authors were able to perform a Katritzky reaction using 2,4,6-triphenyl pyrylium cation and mono-, di- amines, as shown in Figure 4.2 and applying them to the paper substrate (X. Yan et al., 2013). Based on their investigation related to the Katritzky reaction that compared between reactive PS-MS and bulk solution phase, the rate of product formation is

increased observed in reactive paper spray mode compared with the bulk solution phase reaction. It could be due to solvent evaporation on the paper before microdroplet formation or evaporation of solvent from the droplets. Both of the evaporation processes would cause an enhanced concentration of the reagent and increased intermolecular interactions. However, the product formation increases with extended dwell time on the paper (Figure 4.3) indicating that the reaction acceleration is considerable as influenced by solvent evaporation before droplet formation. Performing a Katritzky reaction in this manner can be advantageous for similar reaction schemes whereby investigators are scoping possible mechanisms. Since the PS-MS reaction happens within a few seconds it can improve screening capability, but the approach is not suitable for material collection. Despite low yields, the total amounts are not necessarily purified without further intervention and the amounts obtained are in the nanaogram to microgram region. The finding also concludes that PSI-MS offers an effective way to investigate organic reactions that permits effective reaction optimisation and activity screening including fast product detection and/or characterisation.

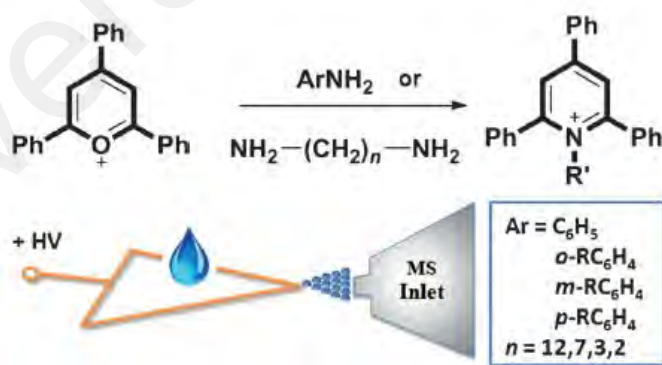


**Figure 4.2: Katritzky reaction monitoring between 2,4,6-triphenyl pyrylium cation and mono-, di-amines monitored by reactive Paper spray mass spectrometry (X. Yan et al., 2013).**

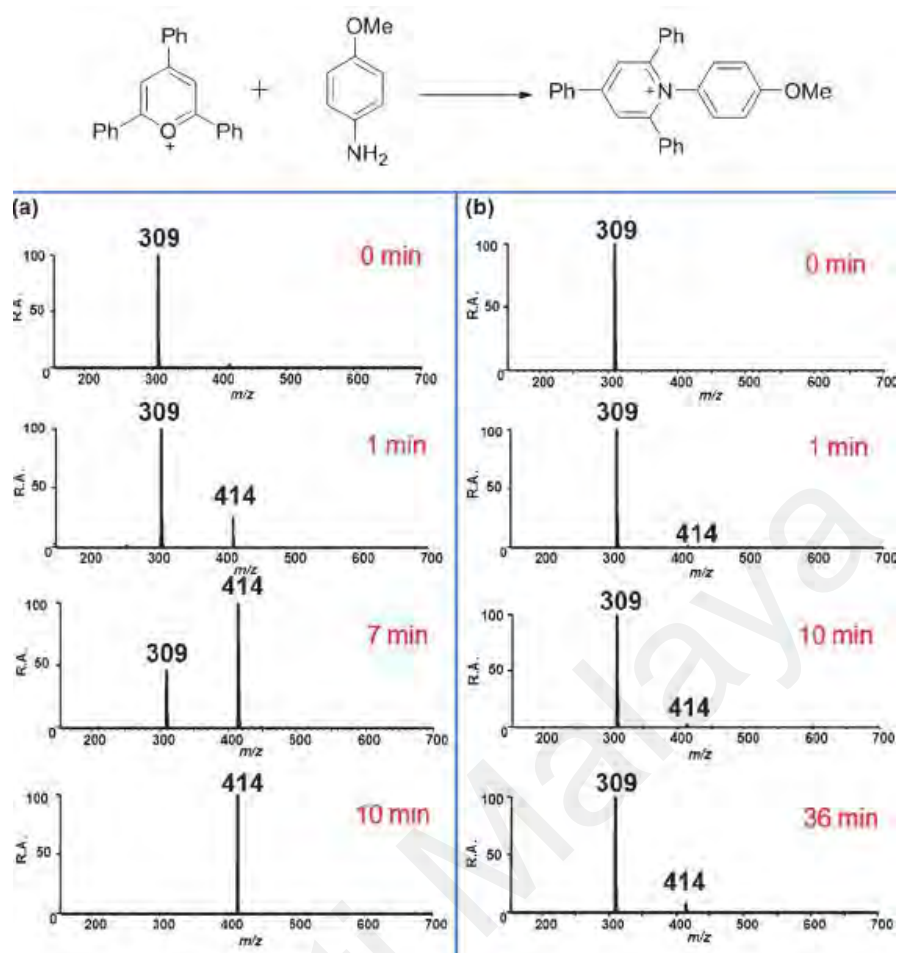


**Figure 4.3: Time-resolved mass spectra displaying the Katritzky reaction between the pyrylium cation ( $m/z$  309) and p-methoxyaniline to produce the pyridinium cation ( $m/z$  414). a) using reactive PS-MS (as dwell time shown in each spectrum) and b) under bulk solution-phase conditions. R.A. = relative abundance (X. Yan et al., 2013).**

An interesting reactive PS-MS experiment was carried out which made distinct changes to the paper substrate. In this work, an oxidation reaction between 1,2,3,4-tetrahydroquinoline (THQ, MW 133) and 6-methoxy-1,2,3,4-tetrahydroquinoline (6-methoxy-THQ, MW 163) was carried out and this was performed using a plasma-induced dehydrogenation method, assisted with hydrophobic paper at atmospheric pressure and temperature (Davis & Badu-Tawiah, 2017). The outcomes of the experiment are shown in Figure 4.4, where the resultant quinolines were detected at  $m/z$  130 and 160 as protonated species for quinoline and 6-methoxy quinoline, respectively. The accelerated dehydrogenation reactions happened on the surface of a low energy hydrophobic paper which acted both as a container for the reacting liquid drop and as a medium for the paper

spray ionisation of reaction products. Consequently, characterisation by ambient mass spectrometry was performed. The dehydrogenation reaction rate, which increased more than three times, was perceived in the presence of graphite particles in order to increase conductivity and surface effects during reaction. Based on this finding, it was concluded that corona discharge appears to be an efficient source to generate highly reactive species in ambient air for dehydrogenation. Through the combination with hydrophobic paper, direct analysis of the reaction mixture is allowed without further sample workup.

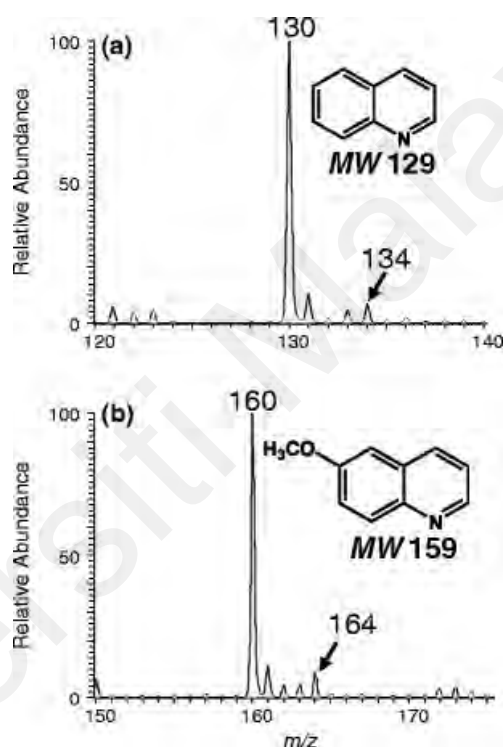


**Figure 4.4: Paper spray mass spectra recorded after 2 minute plasma-based dehydrogenation reaction involving (a) THQ (MW 133) and (b) 6-methoxy-THQ (MW 163) to produce the corresponding quinolines at  $m/z$  130 and 160, respectively (Davis & Badu-Tawiah, 2017).**

Bain et al. had reported regarding Claisen–Schmidt base-catalysed condensation and MS analysis (Bain et al., 2014). In these experiments, PSI of a reaction mixture (6-hydroxy-1-indanone and para-substituted benzaldehyde) being sprayed and produced, 6-Hydroxy-2-(para substituted-benzylidene)-indan-1-one, within a millisecond timeframe before mass analysis (Figure 4.5). It was mentioned that the condensation reaction by paper spray can accelerate the reaction rates and this can be controlled by varying the pH

and concentrations of the reagents. The PSI method was coupled with online analysis (by mass spectrometry) and off-line analysis (e.g., thin layer chromatography, TLC), as illustrated in Figure 4.6. Figure 4.6 (right) also shows the reaction completeness for both the traditional bulk synthesis and the paper spray reaction, where interestingly the spot of the product appeared at 30 s spray time for online paper spray reaction but 1 hr from the traditional bulk phase reaction.

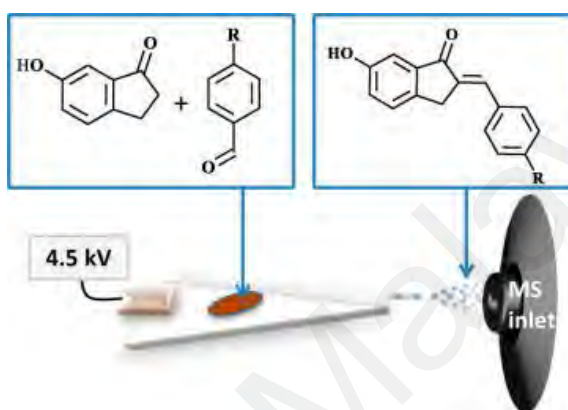


**Figure 4.5: PSI of a reaction mixture (6-hydroxy-1-indanone and para-substituted benzaldehyde) being sprayed from a paper spray substrate toward the MS inlet (Bain et al., 2014).**



**Figure 4.6: Online paper spray reaction (from spotted starting reagents) collected on a TLC plate (left); Chromatographic separation on TLC plate (right) (Bain et al., 2014).**

In a similar fashion Bain et al. compared a synthetic reaction of haloform oxidation by traditional bulk-phase methods and reactive PSI (Ryan M. Bain et al., 2016). The reaction between 2-acetonaphthone and sodium hypochlorite produces naphthalene-2-carboxylate and chloroform. In this experiment, the authors mainly focused on the result from PSI-

MS that sprayed with 2 modes that they defined. Spray mode 1 (high solvent) was spraying with a wetted substrate with an increased amount of solvent. In this case the droplets changed through the transition region as described in ion chronogram in Figure 4.7. For mode 2 (low solvent), when the paper was dried, smaller droplets were produced compared to mode 1. Figure 4.7 shows spray mode 1 which mainly exhibited chlorate ions at  $m/z$  83 and 85, while spray mode 2 had the prominent addition of ions due to the reaction product at  $m/z$  171. Therefore, spray mode 2 showed an accelerated reaction rate compared to spray mode 1, which only displayed the constituents of the reaction mixture. Furthermore, they also mentioned that PSI method (less than 2 min.) is significantly faster than bulk-phase synthesis (45 min.).

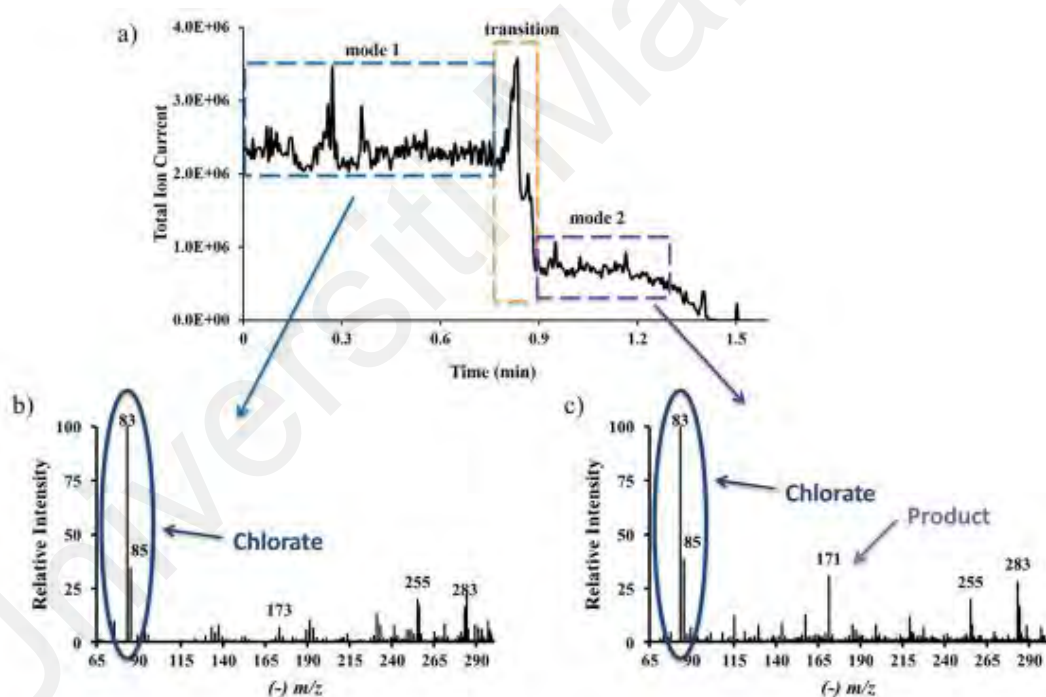


**Figure 4.7:** (a) Ion chronogram produced when paper spray ionisation is performed on the reaction mixture. Negative ion mass spectra are shown in (b) spray mode 1 and (c) spray mode 2 (Ryan M. Bain et al., 2016).

Another method using reactive paper spray in reaction monitoring has been reported by Banerjee and co-workers. The method adopted embedded the paper spray substrate with nanoparticles (Banerjee et al., 2016). They developed the nanoparticle-embedded paper-spray mass spectrometry to investigate three types of heterogeneously catalysed

reactions, firstly a palladium-nanoparticle-catalysed Suzuki cross-coupling reaction, secondly a palladium- or silver-nanoparticle-catalysed 4-nitrophenol reduction, and thirdly, a gold-nanoparticle-catalysed glucose oxidation. These reactions were practically rapid within 30 s, on the nanocatalyst-embedded paper, which then transported the transient intermediates and products to a mass spectrometer for reaction characterisation and detection, as shown in Figure 4.8. Based on the results, the reaction yields from the nanoparticle-embedded paper under the spray conditions are much faster (42% yield within 30 s) than conventional reactions in the bulk phase, which needs several minutes to hours.



**Figure 4.8: Schematic illustration of the nanocatalyst-embedded paper for the reactive paper spray methods (Banerjee et al., 2016).**

A similar approach was attempted by Resende et al.. They coated the paper substrate with a photocatalyst for performing photocatalytic degradation with Methylene Blue dye, which also functioned to monitor the dye's activity. Initially,  $\text{TiO}_2$  as a photocatalyst was immobilised on the paper surface, before cutting it into a triangular shape (Resende et al., 2017). Then, a small amount of the Methylene Blue dye (in aqueous solution), was dropped onto the paper, before exposing to UV-C radiation, as shown in Figure 4.9. Based on the results, photocatalysis exhibited a significant performance to degrade Methylene Blue when compared to the photolysis process since the absorption of UV-C radiation by  $\text{TiO}_2$  perhaps made reactive species on the paper substrate cause quicker dye degradation.

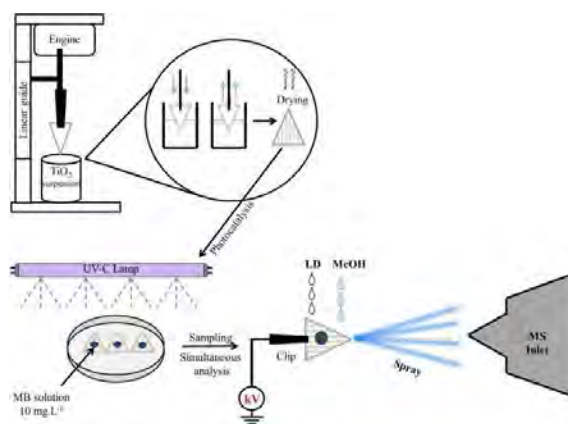


**Figure 4.9: Schematic diagrams of the steps for photocatalysis degradation process of the Methylene Blue dye with photolytic reactions and subsequent PS-MS analysis (Resende et al., 2017).**

In 2019, Zhu, X. et al., reported a fast synthesis of carboxylic acids directly from alcohols (Figure 4.10) in microdroplets by PSI under UV irradiation (Zhu et al., 2019a). The acceleration of the oxidation reaction happened because a paper substrate was cut into a thin film format, resulting in microdroplets of smaller sizes by PSI, as depicted in Figure 4.11. Based on these results, the product yields can reach up to 100% for all tested alcohols except 4-nitrobenzene alcohol (39%) in microdroplets compared to bulk phase. paper spray based synthesis requires no phase transfer catalysts, making it easy for salt deposition, which normally occurs at the capillary tips for completion.

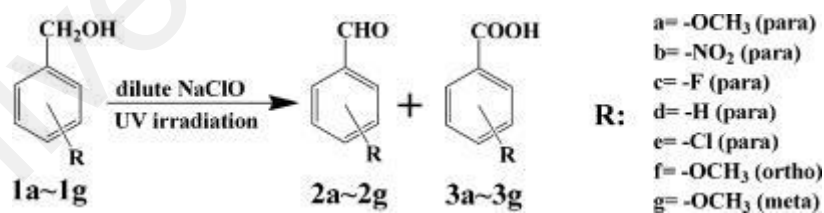


**Figure 4.10: Synthesis of Carboxylic Acids from Alcohols in Microdroplets (Zhu et al., 2019a).**

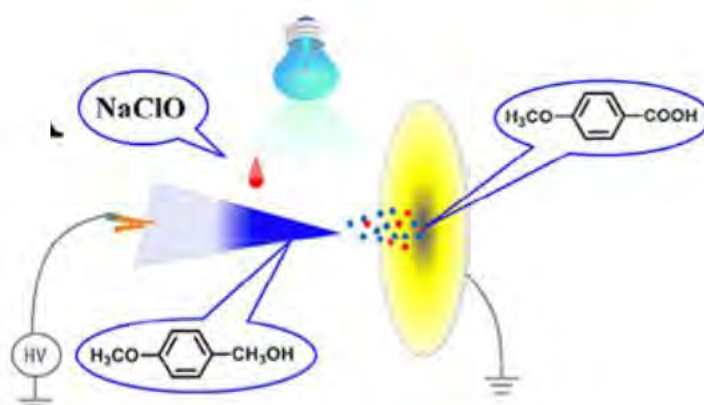


**Figure 4.11: Setup of single-tip paper spray for microdroplet oxidation of 4-methoxybenzyl alcohol with NaOCl (Zhu et al., 2019a).**

There is another ambient ionisation technique which combines paper spray with laser illumination, called laser assisted paper spray ionisation mass spectrometry (LAPSI-MS) (Basuri, Sarkar, Paramasivam, & Pradeep, 2018). A laser pointer is shined on a triangularly cut paper together with high voltage applied for ionisation, as illustrated in Figure 4.12. The analyte solution is continuously pumped via a syringe pump containing a fused silica capillary at a chosen infusion rate. The authors reported that LAPSI-MS promises enhanced ionisation with high signal intensity for polycyclic aromatic hydrocarbons (PAHs) (Figure 4.13), which are usually not ionisable with similar ionisation methods involving solvent sprays. This method can also be used for monitoring in situ photo-assisted reactions.

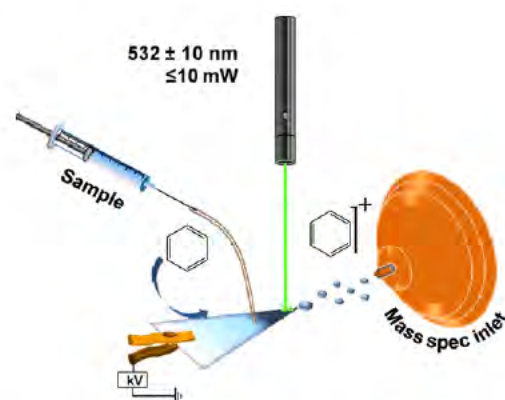


**Figure 4.12: Schematic of the experimental setup of LAPSI-MS. A green diode laser was pointed at the tip of the paper with a continuous supply of analyte through a syringe with fused silica capillary (Basuri et al., 2018).**

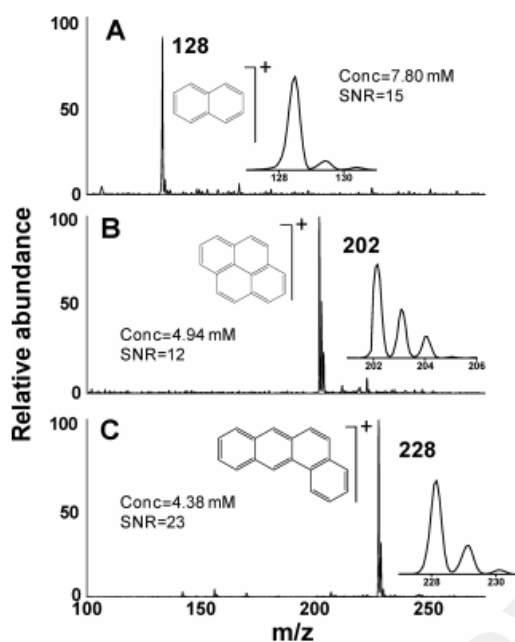


**Figure 4.13: LAPSI-MS spectra of PAHs: (A) naphthalene, (B) pyrene, and (C) benzantracene in positive ion mode. Isotope distributions of the species are shown (Basuri et al., 2018).**

Based on above literature reviews discussed, it is clear that PS-MS can accelerate the reaction rates and also (with a mass spectrometer) monitor the reaction process for a variety of chemical reactions. To the best of my knowledge there does not appear to be any report in the literature regarding nucleophilic substitution reactions studied using PS-MS. Thus, a new approach for paper spray reaction monitoring is introduced in the next section (Section 4.3) by performing nucleophilic substitution reactions of dansyl chloride with aniline under ambient conditions by reactive PSI and monitored with mass spectrometry. The method was used to accelerate and monitor the time course of the reaction of dansyl chloride with aniline, in acetonitrile, to produce the product of dansyl aniline. Three distinct PSI arrangements were explored as representing three types of sample loading and interaction; conventional single tip as well as two novel setups, a dual-tip and a co-axial arrangement, so as to limit on-paper interaction between reagents. The effect on product abundance was investigated using these different paper configurations as it relates to the time course and distance of microdroplet travel. The methodology and results of this research is discussed in the following section.

### **4.3 Accelerated Nucleophilic Substitution Reactions of Dansyl Chloride with Aniline under Ambient Conditions via Dual-tip Reactive Paper Spray**

Dansyl derivatives are known for their small available fluorophore with good photo-physical properties, including a large Stokes' shift and absorbance in the near UV region (J. Fan et al., 2013; J. Huang et al., 2014), one such example is dansyl aniline. Dansyl aniline is a fluorescently labelled aniline that is used in the manufacture of dyes, medicinals, resins, varnishes, perfumes, as a vulcanising rubber and even as a solvent. As mentioned in chapter 2, dansyl aniline was combined into a simple mixture of fluorescent organics, to produce almost pure white light emission (WLE) from a narrow band UV LED (Muhamad Sarih et al., 2019). The fluorescent property of dansyl aniline also enables us to monitor various aspects of the reaction optically (before, during and after the reaction) on both the paper spray and target/collector substrates. Section 4.4 will explain this research works including the time course of the reaction for the nucleophilic substitution reaction of dansyl chloride with aniline to yield dansyl aniline (Figure 4.14). This was investigated with PSI-MS and compared with the bulk solution-phase reaction, as monitored by ESI-MS. As mentioned earlier, PSI-MS is usually performed in a standard configuration, with a single macroscopic triangular tip (isosceles triangle) cut from chromatography paper (X. Yan et al., 2013). In this research, three different substrate configurations, including: a traditional single tip and two novel arrangements: dual-tip and a co-axial paper setup (Figure 4.15), as representing three types of sample loading and interaction. The idea regarding the two proposed novel arrangements is to limit (or entirely negate) the solution phase (i.e., on paper) interactions between the reagents. The effect on product ion abundance was investigated from the different types of paper tip configuration including distance of droplet travel and droplet distribution for each of the 3 techniques. Furthermore, this work also consider to monitor silyl-alkylated dansyl aniline synthesis by reactive paper spray with dual-tip configuration.

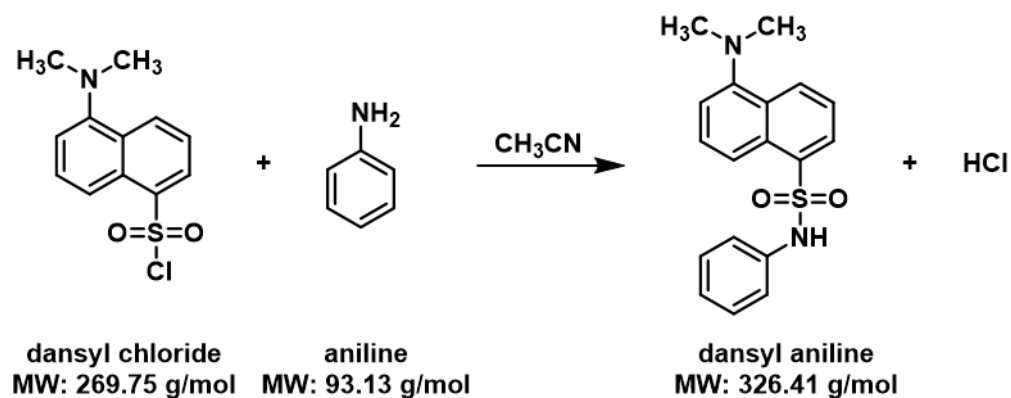


Figure 4.14: Synthesis of dansyl aniline.

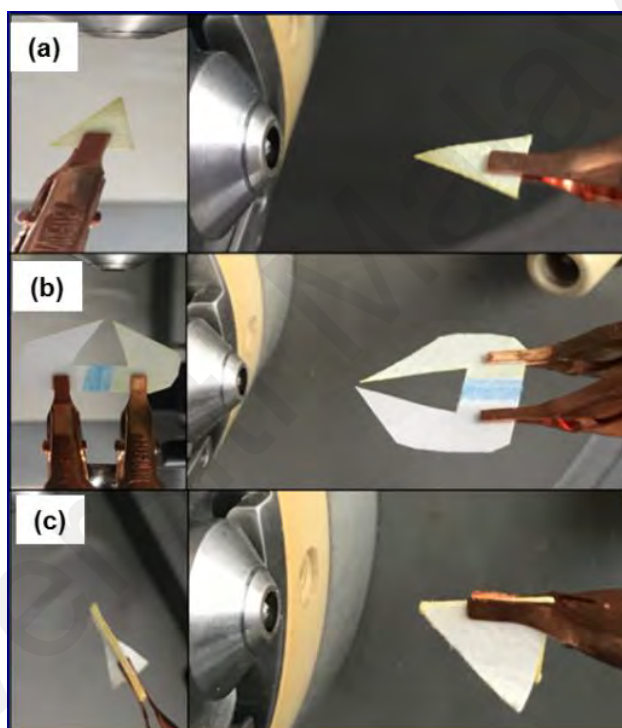


Figure 4.15: Photograph of the three PS arrangements: (a) single tip, (b) dual tip, and (c) co-axial.

#### 4.4 Materials and Methods

All reagents and solvents were of analytical grade or higher and were used directly without further purification. Dansyl chloride, aniline, (3-Bromopropyl)trimethoxysilane and HPLC-grade acetonitrile were purchased from Sigma–Aldrich (UK). The filter paper used for paper spray ionisation was Whatman grade I, from Whatman International Ltd (Maidstone, UK).



#### **4.4.2 The procedure for the dansyl aniline synthesis by ESI-MS.**

For ESI analysis, 10  $\mu\text{L}$  of 100  $\mu\text{M}$  dansyl chloride and 10  $\mu\text{L}$  of 100  $\mu\text{M}$  aniline (in acetonitrile) were mixed together in a syringe vessel before ESI-MS analysis using a Waters Xevo TQ-MS (Waters, Wilmslow, UK).

#### **4.4.3 The procedure for the dansyl aniline synthesis under reactive paper spray conditions.**

The reagents were drop-cast onto paper: 5  $\mu\text{L}$  of 100  $\mu\text{M}$  dansyl chloride and 5  $\mu\text{L}$  of 100  $\mu\text{M}$  aniline (in acetonitrile). The experiment was carried out and compared for each of the paper tip configurations, whilst varying the spray distance (1, 1.5, 2, 2.5, 3, 4 & 5 cm) from the apex of the tip to the source inlet of the mass spectrometer (Waters Xevo TQ-MS), with +6 kV applied.

#### **4.4.4 The procedure for the silyl-alkylated dansyl aniline synthesis by reactive paper spray with dual-tip configuration.**

The reagents were drop-cast onto paper: 5  $\mu\text{L}$  of 100  $\mu\text{M}$  dansyl aniline and 10  $\mu\text{L}$  of 100  $\mu\text{M}$  (3-bromopropyl)trimethoxysilane (in acetonitrile). The experiment was carried out at 2 cm spray distance from the apex of the tip of the paper to the inlet of the mass spectrometer (Waters Xevo TQ-MS), with +8 kV applied.

#### **4.4.5 Observations of reactive paper spray for the fluorescent product using UV-light.**

The experiment is carried out for each of the paper tips by spraying each of the reagents (25  $\mu\text{L}$  of 0.1  $\mu\text{M}$ ), at  $\sim$ +6 kV (at a distance = 2 cm), onto a paper substrate (acting as a collection surface). Both the paper spray and paper target substrates were observed *in-situ* under UV-light illumination (at  $\lambda_{\text{ex}} = 340 \text{ nm}$ ), in a dark room. Paper substrate is used as a collector because to enable for capturing the product during the course of the experiment with minimal evaporative losses.

#### 4.4.6 Characterising the droplet distribution.

The droplet distribution experiment (Figure 4.17 (a) and (b)) is carried out for each of the paper configurations by spraying onto an ITO coated glass slide using 2 pulses, each 50 ms in duration, at  $\sim +6$  kV (at distance = 5 mm) for each distribution. The glass was examined under a microscope (x40 lens) and images were captured from the central region of the glass slide. The images were then processed using ImageJ software to determine the droplet counts for each configuration.

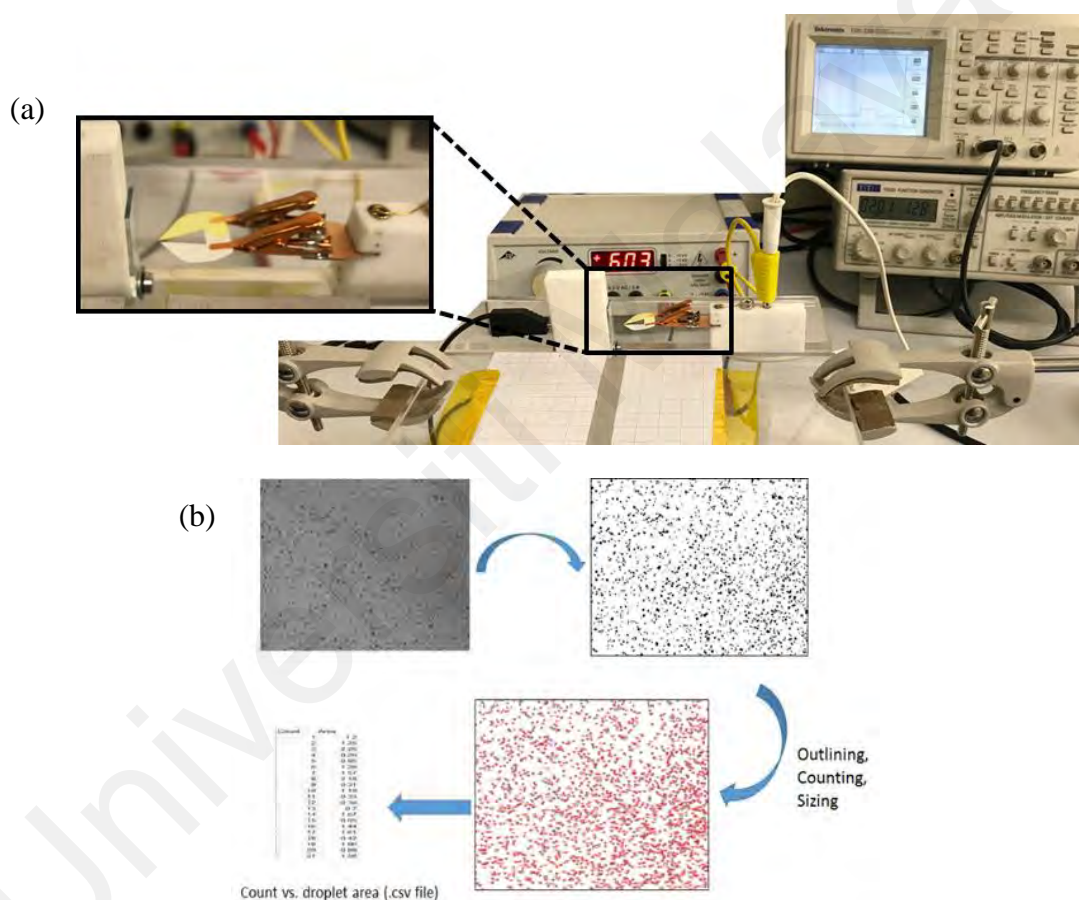


**Figure 4.17: (a) Experimental set-up for the droplet distribution (e.g., dual tips). (b) Typical Image Processing steps.**

#### 4.5 Results and Discussion

A nucleophilic substitution reaction between dansyl chloride and aniline, conducted under reactive paper spray conditions, yielded dansyl aniline as expected. Mass spectra of the product ions, as well as reactant ions, recorded as a function of the dwell time of

the solution on the single tip paper substrate, are shown in Figure 4.18a. Here, the reagents were pre-mixed before drop-casting onto the paper triangle. The aniline reagent (*MW* 93) reacts with dansyl chloride (*MW* 269) to yield the corresponding dansyl aniline product detected at *m/z* 327. The unreacted reagents, aniline and dansyl chloride were also detected at *m/z* 94 and 270 as protonated species, respectively. Product formation was fast with the dansyl chloride peak at *m/z* 270 disappearing in just 10 minutes dwell time (Figure 4.18a,iii). In comparison with the bulk solution reaction from the control experiment, using the same equimolar concentration of reagents, a high abundance of unreacted dansyl chloride was observed, even after 27 minutes of reaction time (Figure 4.18b). Further inspection reveals that the 27 minute bulk-phase reaction shows a strong resemblance with the on-paper reaction after only 1 minute (i.e., Figure 4.18a,i versus Figure 4.18b,iii). An enhancement factor more than ~27 times in favour of the paper-based reaction can be estimated assuming comparable product yield for both reaction conditions were used in the experiment. It was suspected that because dansyl chloride is a moisture sensitive compound, in an ambient environment (Hallen, 1986) is it susceptible to hydrolysis by water and hydroxyl ions (Gray, 1972). Therefore, an excess amount of dansyl chloride is required (Gray, 1972) in synthesis reactions to get a better yield of the product. In future, this method can be optimised by consuming excess amount of the dansyl chloride.

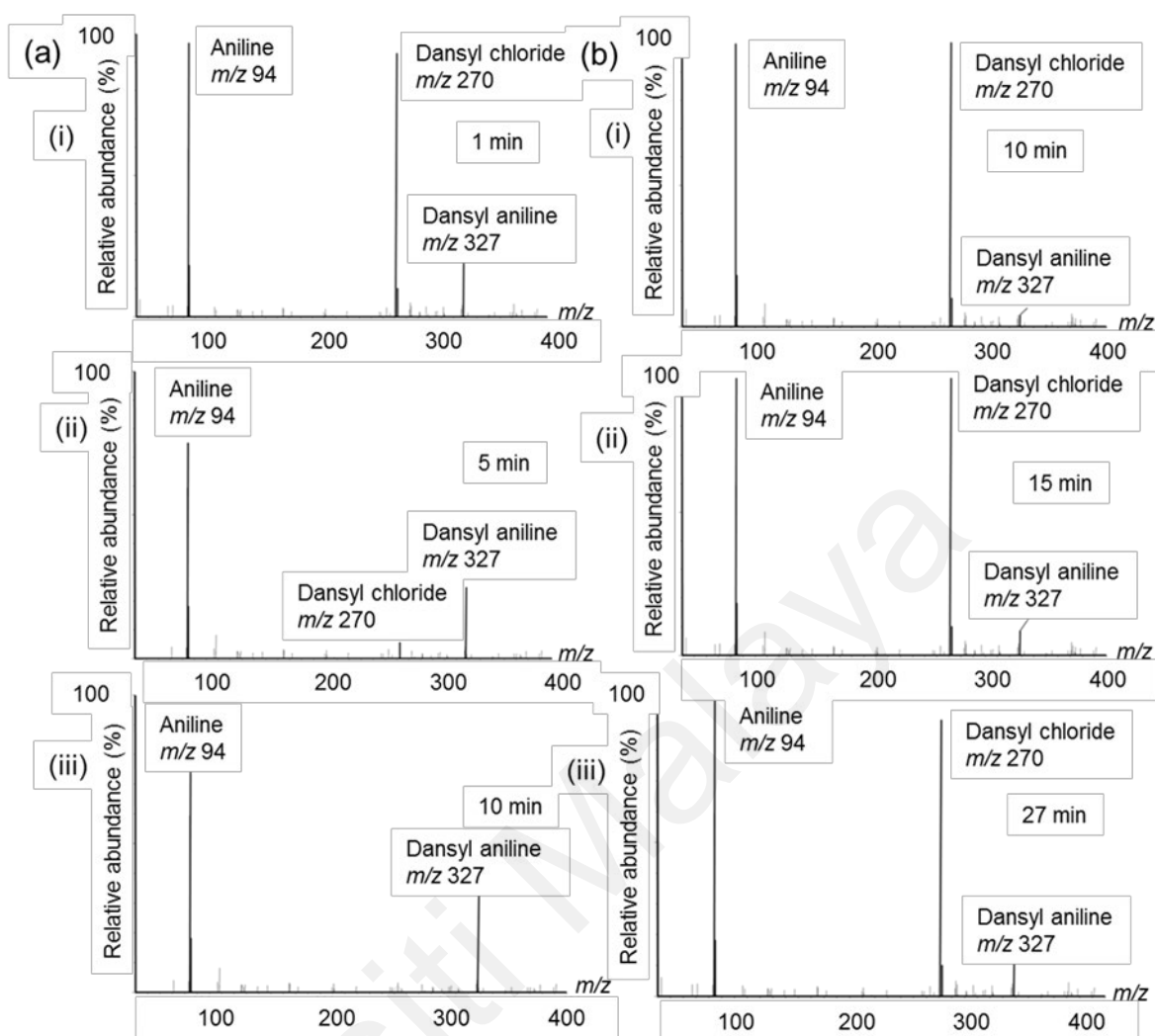


**Figure 4.18: Time-resolved mass spectra showing the synthesis of dansyl aniline (protonated molecular product ion at  $m/z$  327), from the reaction between  $[\text{aniline}+\text{H}]^+$  at  $m/z$  94 and  $[\text{dansyl chloride}+\text{H}]^+$  at  $m/z$  270. (a) Using single tip (conventional) PSI-MS and (b) by ESI-MS.**

The three different paper spray configurations, as representing three different types of sample loading and interaction were investigated for this reaction. The co-axial and dual-tip arrangements should minimise any on-paper interaction compared to a classical paper spray approach (using a single, macroscopic tip), with the reaction occurring predominantly in the desolvating droplets. To shed light on this hypothesis, the effect of distance was examined for the various paper configurations to explore the effect of droplet travel on the reaction progression. The distance from the paper tip to the MS inlet was systematically increased from 1 cm up to 5 cm. As can be seen in Figure 4.19, the dual-

tip paper arrangement consistently gave the highest product ion yield. The distance from the paper tip to the MS inlet was systematically increased up to 5 cm. The rise and then fall of the product signal confirms the absence of any major effect on product formation, except the distance of droplet travel on the timescale of the experiment. The decrease in droplet size caused by solvent evaporation over longer distances increases the reaction rate by concentrating charged species at the surface, albeit at the expense of some signal loss (due to spray divergence). (Cech & Enke, 2001; X. Yan, Bain, & Cooks, 2016) Bain et al., suggest that the faster reaction rate of molecules at surfaces is a result of the partial desolvated nature of surface-active species contributing to reaction acceleration. (Bain, Pulliam, Ayrton, Bain, & Cooks, 2016) The fact that the dual-tip consistently gave the highest product ion abundance at each distance investigated is attributed to effective reagent mixing at the Taylor cone, followed by reaction acceleration in the droplet-phase where solvent evaporation is most effective and leads to a more efficient reaction.

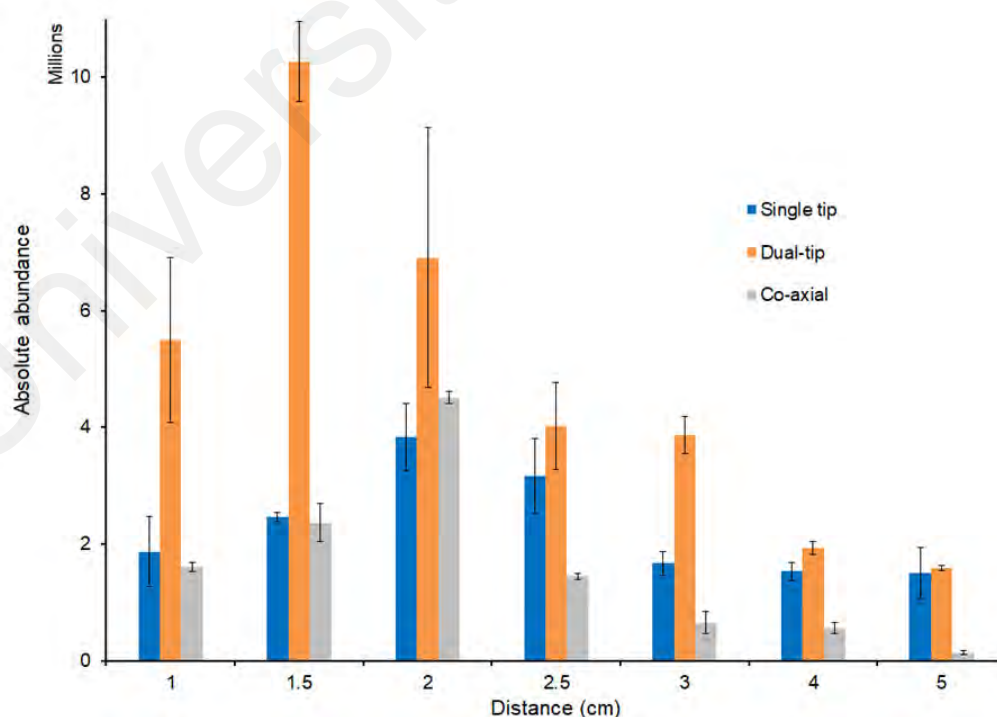


**Figure 4.19: Absolute abundance of product ion ( $m/z$  327) from each paper arrangement loaded at different distances. The error bars indicate the standard deviation from 3 replicas.**

The distance effect suggests that the ambient interactions of the droplets is an important feature. In this regard the product material was collected from spraying the reagents for each of the paper tip arrangements, as shown in Figure 4.20, which clearly shows that the dual-tip gives the brightest yellow emission light (indicating dansyl aniline formation). Another observation is that the conventional single tip leads to the majority of product being formed in an outer ring. It is suspected that this is likely due to the fact that smaller droplets are more likely to be found in the outer regions of the Taylor cone formation, as is common for electrospray-type events (Murphy, Johnson, & Rainville, 2014). Interestingly, for the dual-tip arrangement the fluorescent product is located predominantly at the centre of the target collection surface, where the individual plumes from the two spray tips interact, which this spraying interaction is described as photo shown in Figure 4.21. Moreover, in Figure 4.22, the dual-tip clearly shows highest amount of droplet distribution than amongst others sample loading methods, which consistently showed the highest yield of product and also the highest density of droplet counts per given area Figure A15. Figure 4.23 shows droplet size distribution for each arrangement. Dual-tip gives highest droplet frequency compared to co-axial and single tip. The results showed that the dual-tip sprayed the reagents more effectively to the substrate compare with the others.

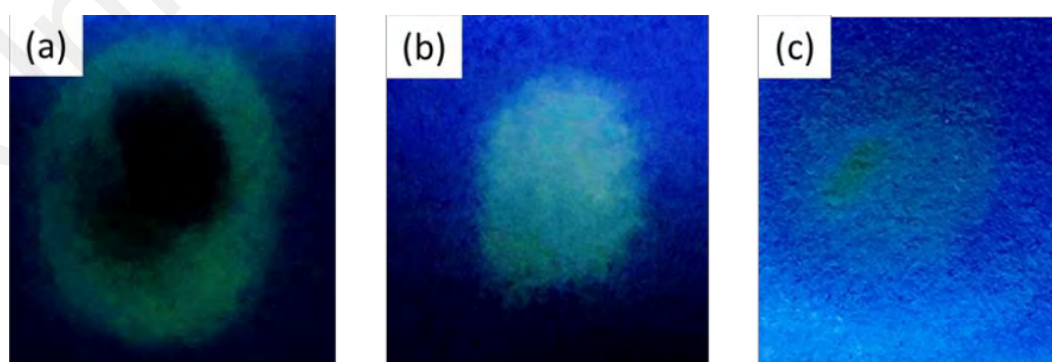


**Figure 4.20: Image of paper substrate collection surface (i.e., target) whereby 0.1 M of dansyl chloride and 0.1 M aniline solution were sprayed from: single tip, dual tip and co-axial tip arrangements at a distance of 2 cm (as labelled in the image).**

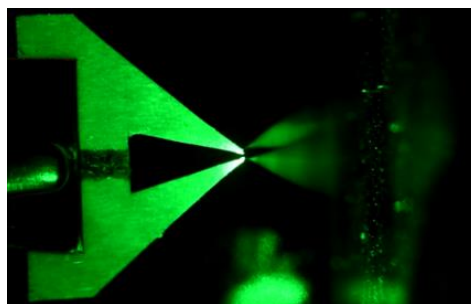


**Figure 4.21:** Reactive paper showed reagents were spraying by dual tip paper arrangement.

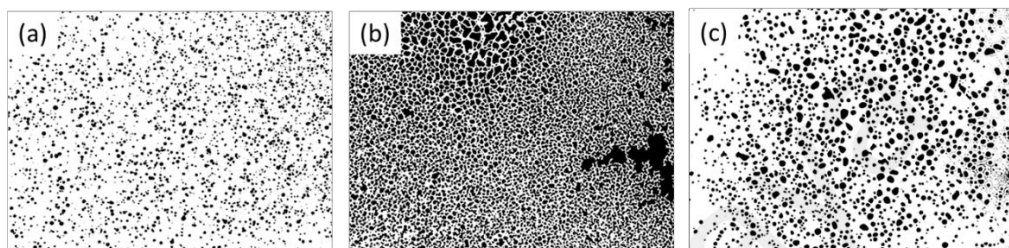


**Figure 4.22:** Droplet distribution analysis by spraying 0.001 mM of dansyl chloride and aniline solution from: (a) single tip, (b) dual-tips and (c) co-axial tip arrangement at a distance of 5 mm to an ITO glass slide (as the target/collection surface). Imaging area: 18.13 mm x 13.60 mm (horizontal x vertical), with microscope magnification (x40 lens).

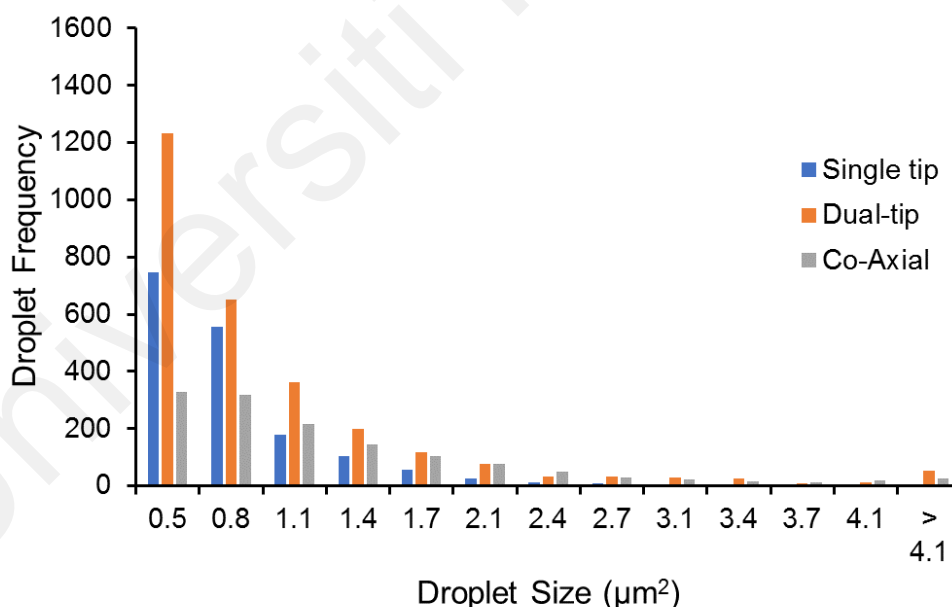


**Figure 4.23:** Droplet size for the three paper loading types. Each was sprayed on to an ITO coated glass slide at a distance of 5 mm and the central region of the slide was examined in each case to obtain the droplet distribution.

In the dual-tip arrangement, the two reactants are deposited in close proximity to the respective paper tips. On the paper spray substrate, the two sides of the single substrate are separated by a hydrophobic (wax) barrier at the centre that is deposited to isolate the

two regions (see wax barrier, blue colour, in Figure 4.15b). This significantly inhibits the possibility of any interaction on the paper and thus any interaction between the two reactants is predominantly in the microdroplet/gas phase. To confirm this, the reaction progression was also examined under UV-light illumination for each of the paper tips. Still images were captured at distinct instances: i) reagents loading, ii) when high voltage is first applied, iii) after 30 s of spraying, iv) after 1 min of spraying and v) after spraying had completed (Figure 4.24). It is shown that the fluorescence of dansyl aniline (a yellow emission light) starts to appear for single tip and co-axial on the paper substrate during spraying but not for the dual-tip arrangement. Therefore, as expected, for the dual-tip arrangement there is little/no interaction of reagents on the paper and therefore no on-surface product formation.

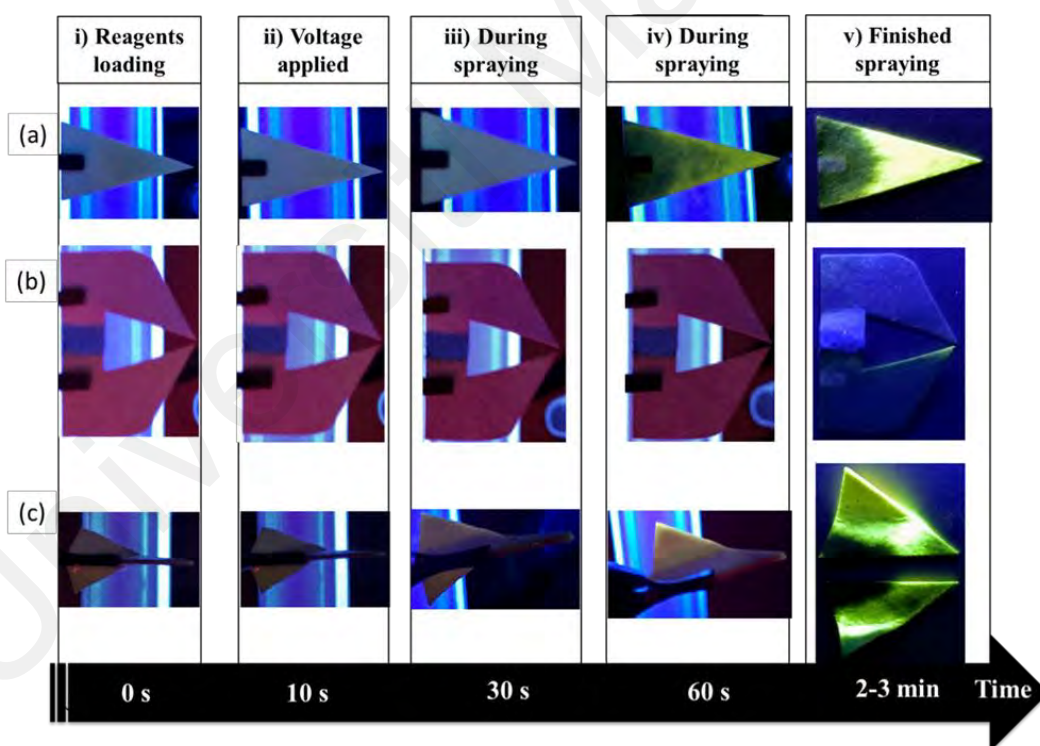


**Figure 4.24: Flow of spraying observation under UV light from each of the paper tips: single tip (ST), dual-tip (DT) and coaxial (CA).**

Reaction monitoring of nucleophilic substitution has been further demonstrated by using dual-tip reactive paper spray for the synthesis of silyl-alkylated dansyl aniline (Figure 4.25). The reaction between dansyl aniline and (3-bromopropyl)trimethoxysilane

was selected to investigate steric effects due to the bulky dansyl aniline nucleophile and also to study the reaction mechanism. The results demonstrate the formation of the protonated product ion ( $m/z$  489) when dansyl aniline and (3-bromopropyl)trimethoxysilane were introduced in 1:2 (v/v) ratio. The intensity of product was greatly increased when the experiment was conducted using increased amount of (3-bromopropyl)trimethoxysilane (Figure 4.26). The potential of PSI-MS for preliminary screening in this way is highly advantageous since it is fast, straightforward and informative, particularly for reactions that are difficult or hard to synthesise by conventional means.

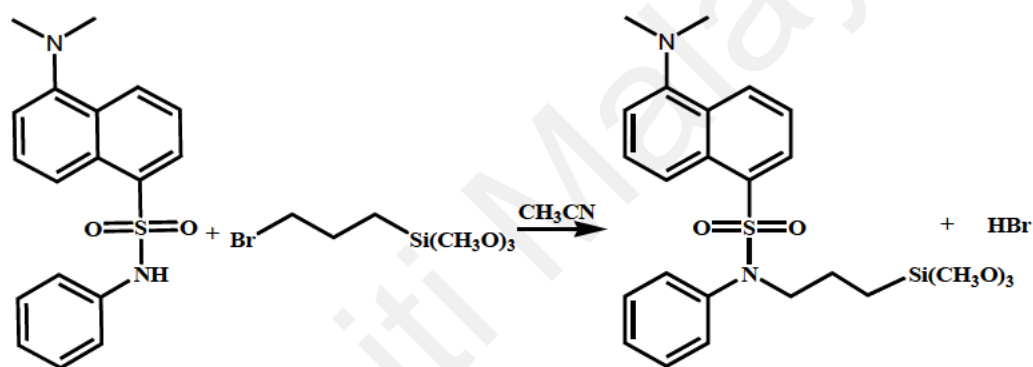


**Figure 4.25: Synthesis of silyl-functionalized dansyl aniline.**

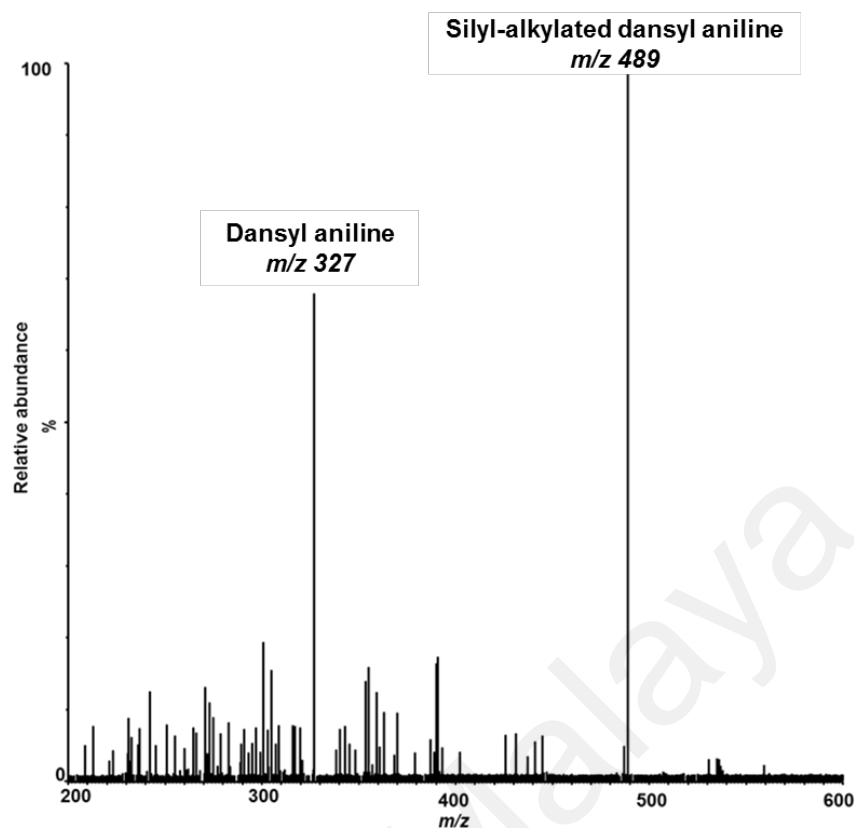


**Figure 4.26:** Mass spectrum showing the synthesis of silyl alkylated dansyl aniline (protonated molecular product ion at  $m/z$  489), from the reaction between [dansyl aniline+H]<sup>+</sup> at  $m/z$  327 and [(3-bromopropyl)trimethoxysilane +H]<sup>+</sup> at  $m/z$  244 (very little appearance in the full spectrum) in 1:2 ratio (v/v) by using dual tip PSI-MS.

#### 4.6 Conclusion

In this chapter, PSI is introduced and discussed in the context of reaction acceleration and monitoring. The discussion continued with a presentation of a novel synthesis monitoring technique of dansyl aniline using PSI-MS. To my knowledge, the nucleophilic substitution synthesis reaction between dansyl chloride and aniline by PSI-MS is the first to be reported. The results showed that PSI could be used to accelerate and, when coupled with MS, monitor the time course of the reaction of dansyl chloride with aniline in acetonitrile, to produce dansyl aniline. Three distinct PSI arrangements were investigated in this study, representing three types of sample loading and interaction. These are: a conventional single tip setup, as well as two novel setups, namely dual tip, and a co-axial setup. The effect on product yield was investigated using these different types of paper

tips for a range of geometric considerations, which includes the distance of microdroplet travel. Based on the results, the product yield of dansyl aniline increases at a given distance and decreases thereafter for all PSI configurations. Amongst the variety of sample loading methods, the novel dual tip arrangement showed increased product yield, while also exhibiting the largest microdroplet density. In future work, the PS-MS method using dual tip arrangement will be further investigated for similar reactions. It can be extremely useful and insightful for other nucleophilic substitution reactions and preliminary reaction screening. Moreover, as previous chapters have discussed regarding the application of synthesised organic fluorophores for white emission light materials and chemosensor, the PS-MS method could be also useful in the future for screening and monitoring the synthesis reaction of the other compounds (e.g., furocoumarin).

## CHAPTER 5: CONCLUSIONS AND FUTURE WORK

This final chapter will evaluate the work from the preceding chapters, draw some conclusions and looks towards future research prospects.

The first result in this thesis (Chapter 2) relates to the production of WLE from organic fluorophores. The literature related to this work are based on WLE from organic compounds and most of them utilised a mixture of macromolecules like, oligomers and polymers to produce the WLE properties. However, in this thesis, WLE is produced from three simple organic compounds, two of which were synthesised using a simple procedure. The optimised mixture of furocoumarin, dansyl aniline and 7-hydroxycoumarin-3-carboxylic acid at a ratio 1.375:1:7 in ethanol, generates almost pure white light, with identical CIE values in the solution and when immobilised in solid silica aerogel, (0.27, 0.33). The WLE from simple organic materials offers significant potential for applications in the global lighting industry. When immobilised in aerogel and applied to a commercial UV LED, it was demonstrated how this approach can produce effective WLE. Following this approach, further research avenues utilising aerogels to provide thermal insulation for solid state lighting applications can be explored, for long term and robust white light generation. Furthermore, it would be interesting to see if such a system can be used as a dye for tuneable a dye laser. Other than that, by utilising these fluorophores as adsorbates for producing a monolayer is another future research plan, thus a white organic light emission monolayer will be produced.

The next finding in this research (Chapter 3) is the development of a novel chemosensor from furocoumarin derivatives, known as furo[3,2-c]coumarin for selective sensing of  $\text{Fe}^{3+}$ . At the first step, the furo[3,2-c]coumarin derivatives (**FH**, **FCI** and **FNO2**), were synthesised and characterised, and their fluorescence properties analysed for the first time. These were successfully synthesised by mixing 4-hydrocoumarin, benzaldehyde derivatives, and cyclohexyl isocyanide under reflux conditions within 24 h

using single step produced high yield (82-92% yield) of products. All compounds were purified by recrystallisation, preventing the need for time consuming column chromatography and showing that this chemistry is amenable to automated high throughout synthesis and screening technologies. Both **FH** and **FCI** produced strong fluorescence intensity whilst **FNO<sub>2</sub>** does not, because of a strong electron withdrawing from -NO<sub>2</sub>, causing fluorescence quenching of furocoumarin. Furthermore, the fluorescence study has led to a successful demonstration of a novel coumarin-based fluorescent (**FH**) ratiometric chemosensor, with an LMCT mechanism attributed to the recognition of Fe<sup>3+</sup> in methanol and also in water/methanol (9:1, v/v). **FH** formed 1:2 complexes with Fe<sup>3+</sup> and exhibited a fluorescence turn-off response to Fe<sup>3+</sup>. Extensive competitive selectivity experiments in methanol were performed for Na<sup>+</sup>, K<sup>+</sup>, Mg<sup>2+</sup>, Ca<sup>2+</sup>, Mn<sup>2+</sup>, Fe<sup>2+</sup>, Al<sup>3+</sup>, Ni<sup>2+</sup>, Cu<sup>2+</sup>, Zn<sup>2+</sup>, Co<sup>2+</sup>, Pb<sup>2+</sup> and Ru<sup>3+</sup>, demonstrating that **FH** has higher selectivity towards Fe<sup>3+</sup> (fluorescence turn-off) than other analogous ions and other previously reported Fe<sup>3+</sup> sensors. The emission intensity at 511 nm of the sensor was linearly proportional (correlation coefficient, R<sup>2</sup> > 0.99) to the concentration of Fe<sup>3+</sup> over the range of 0–30 μM, with a limit of detection of 1.93 μM. These observations revealed that **FH** is suitable for use as a sensor for the quantitative measurement of Fe<sup>3+</sup>. Furthermore, in an aqueous environment the sensor selectivity reduces but the “turn off” effect is still operational, confirming that water does not fully quench fluorescence. The potential of this sensor has been further highlighted by testing with untreated mineral and tap water samples. These results set the foundation for a second generation of sensors with improved sensing properties and water solubilising groups with the real potential of developing a fully aqueous furocoumarin based sensor, which is the subject of future work.

Then, the final research effort involved a new method for dansyl aniline synthesis, a key component of the WLE mixture in chapter 2, which has been accelerated and

monitored under ambient conditions via reactive paper spray using a novel substrate arrangement. In this finding, three PS tip configurations were investigated, and it is shown that a novel dual-tip arrangement leads to improvement in product ion yield. Since dansyl aniline is a fluorophore, fluorescence observation can be made throughout the PS reaction. The reaction progression was examined under UV-light illumination for each of the paper tips and showed the yellow emission light of dansyl aniline starts to appear for single tip and co-axial on the paper substrate during and after spraying except for the dual-tip arrangement. This confirms that for the dual tip arrangement there is no interaction between the reagents on the paper. Product formation occurs exclusively in the microdroplet in ambient air. The droplet distribution was also examined and showed that the dual tip arrangement had the largest droplet density. Furthermore, the optimal dual tip arrangement was also used to synthesise silyl-alkylated dansyl aniline and showed promising reaction screening and monitoring. This further demonstrates that this approach can be extremely useful and insightful for other nucleophilic substitution reactions for preliminary reaction screening.

Overall, the research works presented in this dissertation specifically relate to the fluorescence-based applications from the synthesised organic fluorophores; furo[3,2-c]coumarin and dansyl aniline. Most importantly, the reported discoveries provide exciting and beneficial fluorescence-based applications using the simple organic fluorophores that have been highlighted in this thesis. Future work may extend to the other types of organic fluorophores or may can use the synthesised compounds for the other applications.

## REFERENCES:

- Abbel, R., van der Weegen, R., Pisula, W., Surin, M., Leclère, P., Lazzaroni, R., . . . Schenning, A. P. (2009). Multicolour self-assembled fluorene co-oligomers: from molecules to the solid state via white-light-emitting organogels. *Chemistry—A European Journal*, 15(38), 9737-9746.
- Achelle, S., Rodríguez-López, J., Katan, C., & Robin-le Guen, F. (2016). Luminescence behavior of protonated methoxy-substituted diazine derivatives: toward white light emission. *The Journal of Physical Chemistry C*, 120(47), 26986-26995.
- Aich, K., Goswami, S., Das, S., & Mukhopadhyay, C. D. (2015). A new ICT and CHEF based visible light excitable fluorescent probe easily detects in vivo Zn<sup>2+</sup>. *RSC Advances*, 5(39), 31189-31194.
- An, J.-m., Yan, M.-h., Yang, Z.-y., Li, T.-r., & Zhou, Q.-x. (2013). A turn-on fluorescent sensor for Zn (II) based on fluorescein-coumarin conjugate. *Dyes and Pigments*, 99(1), 1-5.
- Anderson, R. S., Nagirimadugu, N. V., & Abelt, C. J. (2019). Fluorescence quenching of carbonyl-twisted 5-acyl-1-dimethylaminonaphthalenes by alcohols. *ACS Omega*, 4(9), 14067-14073.
- Araby, S., Qiu, A., Wang, R., Zhao, Z., Wang, C.-H., & Ma, J. (2016). Aerogels based on carbon nanomaterials. *Journal of Materials Science*, 51(20), 9157-9189.
- Atilgan, S., Ozdemir, T., & Akkaya, E. (2010). Selective Hg(II) sensing with improved Stokes shift by coupling the internal charge transfer process to excitation energy transfer. *Organic Letters*, 12(21), 4792-4795.
- Ayranci, R., Kirbay, F. O., Demirkol, D. O., Ak, M., & Timur, S. (2018). Copolymer based multifunctional conducting polymer film for fluorescence sensing of glucose. *Methods and Applications in Fluorescence*, 6(3), 35012.
- Bag, B., & Bharadwaj, P. K. (2004). Attachment of an electron-withdrawing fluorophore to a cryptand for modulation of fluorescence signaling. *Inorganic Chemistry*, 43(15), 4626-4630.
- Bag, S., Hendricks, P. I., Reynolds, J. C., & Cooks, R. G. (2015). Biogenic aldehyde determination by reactive paper spray ionization mass spectrometry. *Analytica Chimica Acta*, 860, 37-42.

- Bain, R. M., Pulliam, C. J., Ayrton, S. T., Bain, K., & Cooks, R. G. (2016). Accelerated hydrazone formation in charged microdroplets. *Rapid Communications in Mass Spectrometry*, 30(16), 1875-1878.
- Bain, R. M., Pulliam, C. J., Raab, S. A., & Cooks, R. G. (2015). Chemical synthesis accelerated by paper spray: The Haloform reaction. *Journal of Chemical Education*, 93(2), 340-344.
- Bain, R. M., Pulliam, C. J., Yan, X., Moore, K. F., Müller, T., & Cooks, R. G. (2014). Mass spectrometry in organic synthesis: Claisen–Schmidt Base-catalyzed condensation and Hammett. *Journal of Chemical Education*, 91(11), 1985-1989.
- Bairi, P., Roy, B., Chakraborty, P., & Nandi, A. K. (2013). Co-assembled white-light-emitting hydrogel of melamine. *ACS Applied Materials & Interfaces*, 5(12), 5478-5485.
- Balan, B., Vijayakumar, C., Ogi, S., & Takeuchi, M. (2012). Oligofluorene-based nanoparticles in aqueous medium: hydrogen bond assisted modulation of functional properties and color tunable FRET emission. *Journal of Materials Chemistry*, 22(22), 11224-11234.
- Banerjee, S., Basheer, C., & Zare, R. N. (2016). A study of heterogeneous catalysis by nanoparticle-embedded Paper-Spray Ionization Mass Spectrometry. *Angewandte Chemie International Edition*, 55(41), 12807-12811.
- Basuri, P., Sarkar, D., Paramasivam, G., & Pradeep, T. (2018). Detection of hydrocarbons by laser assisted Paper Spray Ionization Mass Spectrometry (LAPSI MS). *Analytical Chemistry*, 90(7), 4663-4668.
- Benelhadj, K., Muzuzu, W., Massue, J., Retailleau, P., Charaf-Eddin, A., Laurent, A. D., . . . Ziessel, R. (2014). White emitters by tuning the excited-state intramolecular proton-transfer fluorescence emission in 2-(2'-hydroxybenzofuran) benzoxazole dyes. *Chemistry—A European Journal*, 20(40), 12843-12857.
- Bills, B., & Manicke, N. (2016). Development of a prototype blood fractionation cartridge for plasma analysis by Paper Spray Mass Spectrometry. *Clinical Mass Spectrometry*, 2, 18-24.
- Bozdemir, O. A., Guliyev, R., Buyukcakir, O., Selcuk, S., Kolemen, S., Gulseren, G., . . . Akkaya, E. U. (2010). Selective manipulation of ICT and PET processes in Styryl-Bodipy derivatives: applications in molecular logic and fluorescence sensing of metal ions. *Journal of the American Chemical Society*, 132(23), 8029-8036.

- Burdo, J. R., & Connor, J. R. (2003). Brain iron uptake and homeostatic mechanisms: An overview. *Biometals*, 16(1), 63-75.
- Busana, M. G., Prudenziati, M., & Hormadaly, J. (2006). Microstructure development and electrical properties of RuO<sub>2</sub>-based lead-free thick film resistors. *Journal of Materials Science: Materials in Electronics*, 17(11), 951-962.
- Cao, D., Liu, Z., Verwilt, P., Koo, S., Jangjili, P., Kim, J. S., & Lin, W. (2019a). Coumarin-based small-molecule fluorescent chemosensors. *Chemical Reviews*, 119(18), 10403-10519.
- Cao, D., Liu, Z., Verwilt, P., Koo, S., Jangjili, P., Kim, J. S., & Lin, W. (2019b). Coumarin-based small-molecule fluorescent chemosensors. *Chemical Reviews*, 119(18), 10403-10519.
- Cao, X., Lin, W., & Yu, Q. (2011). A ratiometric fluorescent probe for thiols based on a tetrakis(4-hydroxyphenyl)porphyrin-coumarin Scaffold. *The Journal of Organic Chemistry*, 76(18), 7423-7430.
- Cao, X., Lin, W., Yu, Q., & Wang, J. (2011). Ratiometric sensing of fluoride anions based on a BODIPY-coumarin platform. *Organic Letters*, 13(22), 6098-6101.
- Carmany, D. O., Mach, P. M., Rizzo, G. M., Dhummakupt, E. S., McBride, E. M., Sekowski, J. W., . . . Glaros, T. (2018). On-substrate enzymatic reaction to determine acetylcholinesterase activity in whole blood by Paper Spray Mass Spectrometry. *Journal of the American Society for Mass Spectrometry*, 29(12), 2436-2442.
- Carter, K. P., Young, A. M., & Palmer, A. E. (2014). Fluorescent sensors for measuring metal ions in living systems. *Chemical Reviews*, 114(8), 4564-4601.
- Cech, N. B., & Enke, C. G. (2001). Practical implications of some recent studies in electrospray ionization fundamentals. *Mass Spectrometry Reviews*, 20(6), 362-387.
- Chamberlain, C. A., Rubio, V. Y., & Garrett, T. J. (2019). Strain-level differentiation of bacteria by Paper Spray Ionization Mass Spectrometry. *Analytical Chemistry*, 91(8), 4964-4968.
- Chang, H.-Q., Zhao, X.-L., Wu, W.-N., Jia, L., & Wang, Y. (2017). A highly sensitive on-off fluorescent chemosensor for Cu<sup>2+</sup> based on coumarin. *Journal of Luminescence*, 182, 268-273.

- Chang, Y. L., Song, Y., Wang, Z., Helander, M. G., Qiu, J., Chai, L., . . . Lu, Z. (2013). Highly efficient warm white organic light-emitting diodes by triplet exciton conversion. *Advanced Functional Materials*, 23(6), 705-712.
- Chapter 1 - Tools of the Cell Biologist. (2008). In S. R. Goodman (Ed.), *Medical Cell Biology (Third Edition)* (pp. 1-26). San Diego: Academic Press.
- Chen, G. F., Jia, H. M., Zhang, L. Y., Hu, J., Chen, B. H., Song, Y. L., . . . Bai, G. Y. (2013). A highly selective fluorescent sensor for Fe<sup>3+</sup> ion based on coumarin derivatives. *Research on Chemical Intermediates*, 39(9), 4081-4090.
- Chen, G. F., Zhang, L. Y., Li, H. Y., & Chen, B. H. (2015). Synthesis of coumarin derivatives containing 2-aminothiazole moiety and their recognition of metal ions. *Research on Chemical Intermediates*, 41(7), 4273-4281.
- Chen, J., Cao, S., Wang, D., Wu, S., & Wang, X. (2009). A phenol-based compartmental ligand as a potential chemosensor for Zinc(ii) cations. *Journal of the Brazilian Chemical Society*, 20, 13-18.
- Choi, S., & Cha, S. (2020). Investigation of reactions between Isothiazolinones and Cysteamine by reactive Paper Spray Ionization Mass Spectrometry (Reactive PSI MS). *Bulletin of the Korean Chemical Society*, 41(1), 48-53.
- Cie, C. (1932). Commission internationale de l'eclairage proceedings, 1931. *Cambridge University, Cambridge*.
- Cooks, R. G., Ouyang, Z., Takats, Z., & Wiseman, J. M. (2006). Ambient Mass Spectrometry. *Science*, 311(5767), 1566-1570.
- Coskun, A., Deniz, E., & Akkaya, E. (2007). A sensitive fluorescent chemosensor for anions based on a styryl–boradiazaindacene framework. *Tetrahedron Letters*, 48(31), 5359-5361.
- Council, N. R. National Academy of Science. (1989). Recommended Dietary Allowances (10th Ed), *Trace elements: Iron* (pp.195-203), Baltimore, MD: University Park Press.
- Courtis, A. M., Santos, S. A., Guan, Y., Hendricks, J. A., Ghosh, B., Szantai-Kis, D. M., . . . Mazitschek, R. (2014). Monoalkoxy BODIPYs—A fluorophore class for bioimaging. *Bioconjugate Chemistry*, 25(6), 1043-1051.
- D'Andrade, B. W., & Forrest, S. R. (2004). White organic light-emitting devices for solid-state lighting. *Advanced Materials*, 16(18), 1585-1595.

- da Silva, L. C., Pereira, I., de Carvalho, T. C., Allochio Filho, J. F., Romão, W., & Vaz, B. G. (2019). Paper spray ionization and portable mass spectrometers: A review. *Analytical Methods*, 11(8), 999-1013.
- Damon, D. E., Maher, Y. S., Yin, M., Jjunju, F. P., Young, I. S., Taylor, S., . . . Badu-Tawiah, A. K. (2016). 2D wax-printed paper substrates with extended solvent supply capabilities allow enhanced ion signal in paper spray ionization. *Analyst*, 141(12), 3866-3873.
- Damon, D. E., Maher, Y. S., Yin, M., Jjunju, F. P. M., Young, I. S., Taylor, S., . . . Badu-Tawiah, A. K. (2016). 2D wax-printed paper substrates with extended solvent supply capabilities allow enhanced ion signal in paper spray ionization. *Analyst*, 141(12), 3866-3873.
- Davis, K. M., & Badu-Tawiah, A. K. (2017). Direct and efficient dehydrogenation of tetrahydroquinolines and primary amines using corona discharge generated on ambient hydrophobic Paper Substrate. *Journal of the American Society for Mass Spectrometry*, 28(4), 647-654.
- de Paula, C., Jurisch, M., Piccin, E., & Augusti, R. (2018). Recognizing drug-facilitated crimes: Detection and quantification of benzodiazepines in beverages using fast liquid–liquid extraction with low temperature partitioning and paper spray mass spectrometry. *Drug Testing and Analysis*, 10(9), 1348-1357.
- Dhummakupt, E. S., Mach, P. M., Carmany, D., Demond, P. S., Moran, T. S., Connell, T., . . . Glaros, T. (2017). Direct analysis of aerosolized chemical warfare simulants captured on a modified glass-based substrate by “Paper-Spray” Ionization. *Analytical Chemistry*, 89(20), 10866-10872.
- Dietrich, O., Levin, J., Ahmadi, S.-A., Plate, A., Reiser, M. F., Bötzel, K., . . . Ertl-Wagner, B. (2017). MR imaging differentiation of Fe<sup>2+</sup> and Fe<sup>3+</sup> based on relaxation and magnetic susceptibility properties. *Neuroradiology*, 59(4), 403-409.
- Dong, B., Song, X., Wang, C., Kong, X., Tang, Y., & Lin, W. (2016). Dual site-controlled and lysosome-targeted Intramolecular Charge Transfer–Photoinduced Electron Transfer–Fluorescence Resonance Energy Transfer fluorescent probe for monitoring pH changes in living cells. *Analytical Chemistry*, 88(7), 4085-4091.
- Dowling, S., McBride, E. M., McKenna, J., Glaros, T., & Manicke, N. E. (2020). Direct soil analysis by paper spray mass spectrometry: Detection of drugs and chemical warfare agent hydrolysis products. *Forensic Chemistry*, 17, 100206.

- Elmas, S. N. K., Dincer, Z. E., Erturk, A. S., Bostanci, A., Karagoz, A., Koca, M., . . . Yilmaz, I. (2020). A novel fluorescent probe based on isocoumarin for Hg<sup>2+</sup> and Fe<sup>3+</sup> ions and its application in live-cell imaging. *Spectrochimica Acta Part A: Molecular and Biomolecular Spectroscopy*, 224, 117402.
- Elmas, Ş. N. K., Ozen, F., Koran, K., Yilmaz, I., Gorgulu, A. O., & Erdemir, S. (2017). Coumarin based highly selective “off-on-off” type novel fluorescent sensor for Cu<sup>2+</sup> and S<sup>2-</sup> in Aqueous Solution. *Journal of Fluorescence*, 27(2), 463-471.
- En, D., Guo, Y., Chen, B.-T., Dong, B., & Peng, M.-J. (2014). Coumarin-derived Fe<sup>3+</sup>-selective fluorescent turn-off chemosensors: synthesis, properties, and applications in living cells. *RSC Advances*, 4(1), 248-253.
- Environmental Protection Agency, USA. (2013). *Secondary drinking water regulations: Guidance for nuisance chemicals*. Washington, DC. Retrieved from: <https://www.epa.gov/sdwa/secondary-drinking-water-standards-guidance- nuisance-chemicals>
- Espy, R. D., Manicke, N. E., Ouyang, Z., & Cooks, R. G. (2012). Rapid analysis of whole blood by Paper Spray Mass Spectrometry for point-of-care therapeutic drug monitoring. *Analyst*, 137(10), 2344-2349.
- Espy, R. D., Teunissen, S. F., Manicke, N. E., Ren, Y., Ouyang, Z., van Asten, A., & Cooks, R. G. (2014). Paper Spray and Extraction Spray Mass Spectrometry for the direct and simultaneous quantification of eight drugs of abuse in whole blood. *Analytical Chemistry*, 86(15), 7712-7718.
- Espy, R. D., Wleklinski, M., Yan, X., & Cooks, R. G. (2014). Beyond the flask: reactions on the fly in ambient mass spectrometry. *TrAC Trends in Analytical Chemistry*, 57, 135-146.
- Fan, J., Hu, M., Zhan, P., & Peng, X. (2013). Energy transfer cassettes based on organic fluorophores: construction and applications in ratiometric sensing. *Chemical Society Reviews*, 42(1), 29-43.
- Fan, L., & Lee, J. A. (2012). Managing the effect of hematocrit on DBS analysis in a regulated environment. *Bioanalysis*, 4(4), 345-347.
- Feng, X., Qi, C., Feng, H.-T., Zhao, Z., Sung, H. H., Williams, I. D., . . . Tang, B. Z. (2018). Dual fluorescence of tetraphenylethylene-substituted pyrenes with aggregation-induced emission characteristics for white-light emission. *Chemical Science*, 9(25), 5679-5687.

- Frey, B. S., Damon, D. E., & Badu-Tawiah, A. K. (2020). Emerging trends in paper spray mass spectrometry: Microsampling, storage, direct analysis, and applications. *Mass Spectrometry Reviews*, 39(4), 336-370.
- Gabe, Y., Urano, Y., Kikuchi, K., Kojima, H., & Nagano, T. (2004). Highly sensitive fluorescence probes for nitric oxide based on boron dipyrromethene chromophore: rational design of potentially useful bioimaging fluorescence probe. *Journal of the American Chemical Society*, 126(10), 3357-3367.
- Galas, L., Gallavardin, T., Bénard, M., Lehner, A., Schapman, D., Lebon, A., . . . Franck, X. (2018). "Probe, Sample, and Instrument (PSI)": The hat-trick for fluorescence live cell imaging. *Chemosensors*, 6(3), 40.
- García-Beltrán, O., Cassels, K. B., Pérez, C., Mena, N., Núñez, T. M., Martínez, P. N., . . . Aliaga, E. M. (2014). Coumarin-based fluorescent probes for dual recognition of Copper(II) and Iron(III) ions and their application in bio-imaging. *Sensors*, 14(1).
- Gaynor, W., Hofmann, S., Christoforo, M. G., Sachse, C., Mehra, S., Salleo, A., . . . Müller-Meskamp, L. (2013). Color in the corners: ITO-free white OLEDs with angular color stability. *Advanced Materials*, 25(29), 4006-4013.
- Gharami, S., Sarkar, D., Ghosh, P., Acharyya, S., Aich, K., Murmu, N., & Mondal, T. K. (2017). A coumarin based azo-phenol ligand as efficient fluorescent "OFF-ON-OFF" chemosensor for sequential detection of Mg<sup>2+</sup> and F<sup>-</sup>: Application in live cell imaging and as molecular logic gate. *Sensors and Actuators B: Chemical*, 253, 317-325.
- Giansante, C., Raffy, G., Schäfer, C., Rahma, H., Kao, M.-T., Olive, A. G. L., & Del Guerzo, A. (2011). White-light-emitting self-assembled nanofibers and their evidence by microspectroscopy of individual objects. *Journal of the American Chemical Society*, 133(2), 316-325.
- Giansante, C., Schäfer, C., Raffy, G., & Del Guerzo, A. (2012). Exploiting direct and cascade energy transfer for color-tunable and white-light emission in three-component self-assembled nanofibers. *The Journal of Physical Chemistry C*, 116(41), 21706-21716.
- Giansante, C., Schäfer, C., Raffy, G., & Del Guerzo, A. (2012). Exploiting direct and cascade energy transfer for color-tunable and white-light emission in three-component self-assembled nanofibers. *The Journal of Physical Chemistry C*, 116(41), 21706-21716.

- Girod, M., Moyano, E., Campbell, D. I., & Cooks, R. G. (2011). Accelerated bimolecular reactions in microdroplets studied by desorption electrospray ionization mass spectrometry. *Chemical Science*, 2(3), 501-510.
- Gray, W. R. (1972). End-group analysis using dansyl chloride *Methods in Enzymology* (Vol. 25, pp. 121-138): Academic Press.
- Gupta, G., Sharma, G., Koch, B., Park, S., Lee, S. S., & Kim, J. (2013). Syntheses, characterization and molecular structures of novel Ru(II), Rh(III) and Ir(III) complexes and their possible roles as antitumour and cytotoxic agents. *New Journal of Chemistry*, 37, 2573-2581.
- Hallen, C. P. (1986). An investigation into the analytical utility of changes in polarization accompanying analytical derivatization reactions (fluorescence). (Doctoral thesis, University of New Hampshire, Durham, UK). Retrieved from <https://scholars.unh.edu/dissertation/1494>.
- Han, Y., Li, M., Qiu, F., Zhang, M., & Zhang, Y.-H. (2017). Cell-permeable organic fluorescent probes for live-cell long-term super-resolution imaging reveal lysosome-mitochondrion interactions. *Nature Communications*, 8(1), 1307.
- Harris, G. A., Galhena, A. S., & Fernández, F. M. (2011). Ambient sampling/ionization Mass Spectrometry: Applications and current trends. *Analytical Chemistry*, 83(12), 4508-4538.
- Hawken, P., Lovins, A. B., & Lovins, L. H. (2013). *Natural capitalism: The next industrial revolution* (2nd ed.). London, England: Routledge.
- He, L., Xu, Q., Liu, Y., Wei, H., Tang, Y., & Lin, W. (2015). Coumarin-Based Turn-On Fluorescence Probe for Specific Detection of Glutathione over Cysteine and Homocysteine. *ACS Applied Materials & Interfaces*, 7(23), 12809-12813.
- Hossain, S. M., Singh, K., Lakma, A., Pradhan, R. N., & Singh, A. K. (2017). A schiff base ligand of coumarin derivative as an ICT-Based fluorescence chemosensor for Al<sup>3+</sup>. *Sensors and Actuators B: Chemical*, 239, 1109-1117.
- Hsu, C.-Y., & Liu, Y.-L. (2010). Rhodamine B-anchored silica nanoparticles displaying white-light photoluminescence and their uses in preparations of photoluminescent polymeric films and nanofibers. *Journal of Colloid and Interface Science*, 350(1), 75-82.
- Hu, Y., Wang, J., Long, L., & Xiao, X. (2016). A ratiometric fluorescence sensor for Fe<sup>3+</sup> based on FRET and PET processes. *Luminescence*, 31(1), 16-21.

- Huang, J., Liu, M., Ma, X., Dong, Q., Ye, B., Wang, W., & Zeng, W. (2014). A highly selective turn-off fluorescent probe for Cu(ii) based on a dansyl derivative and its application in living cell imaging. *RSC Advances*, 4(44), 22964-22970.
- Huang, Y.-C., Chung, H.-H., Dutkiewicz, E. P., Chen, C.-L., Hsieh, H.-Y., Chen, B.-R., . . . Hsu, C.-C. (2020). Predicting breast cancer by Paper Spray Ion Mobility Spectrometry Mass Spectrometry and machine learning. *Analytical Chemistry*, 92(2), 1653-1657.
- Inspectorate, D. W. (2010). What are the drinking water standards. *Drinking Water Inspectorate, London*.
- Jain, A., Blum, C., & Subramaniam, V. (2009). Fluorescence lifetime spectroscopy and imaging of visible fluorescent proteins *Advances in Biomedical Engineering* (pp. 147-176): Elsevier.
- Jain, P., & Joshi, H. (2012). Coumarin: chemical and pharmacological profile. *Journal of Applied Pharmaceutical Science*, 2(6), 236-240.
- Jang, E., Jun, S., Jang, H., Lim, J., Kim, B., & Kim, Y. (2010). White-light-emitting diodes with quantum dot color converters for display backlights. *Advanced Materials*, 22(28), 3076-3080.
- Jang, Y.-J., Syu, S.-e., Chen, Y.-J., Yang, M.-C., & Lin, W. (2012). Syntheses of furo [3, 4-c] coumarins and related furyl coumarin derivatives via intramolecular Wittig reactions. *Organic & Biomolecular Chemistry*, 10(4), 843-847.
- Jiao, Y., Zhu, B., Chen, J.-H., & Duan, X. (2015). Fluorescent Sensing of Fluoride in Cellular System. *Theranostics*, 5, 173-187.
- Jjunju, F. P., Maher, S., Damon, D. E., Barrett, R. M., Syed, S., Heeren, R. M., . . . Badu-Tawiah, A. K. (2016). Screening and quantification of aliphatic primary alkyl corrosion inhibitor amines in water samples by paper spray mass spectrometry. *Analytical Chemistry*, 88(2), 1391-1400.
- Jjunju, F. P. M., Li, A., Badu-Tawiah, A., Wei, P., Li, L., Ouyang, Z., . . . Cooks, R. G. (2013). In situ analysis of corrosion inhibitors using a portable mass spectrometer with paper spray ionization. *Analyst*, 138(13), 3740-3748.
- Jjunju, F. P. M., Maher, S., Damon, D. E., Barrett, R. M., Syed, S. U., Heeren, R. M. A., . . . Badu-Tawiah, A. K. (2016). Screening and quantification of aliphatic primary alkyl corrosion inhibitor amines in water samples by Paper Spray Mass Spectrometry. *Analytical Chemistry*, 88(2), 1391-1400.

- Jjunju, F. P. M., Maher, S., Li, A., Badu-Tawiah, A. K., Taylor, S., & Graham Cooks, R. (2015). Analysis of polycyclic aromatic hydrocarbons using desorption atmospheric pressure chemical ionization coupled to a portable mass spectrometer. *Journal of the American Society for Mass Spectrometry*, 26(2), 271-280.
- Joshi, S., Kumari, S., Bhattacharjee, R., Sarmah, A., Sakhuja, R., & Pant, D. D. (2015). Experimental and theoretical study: Determination of dipole moment of synthesized coumarin–triazole derivatives and application as turn off fluorescence sensor: High sensitivity for iron (III) ions. *Sensors and Actuators B: Chemical*, 220, 1266-1278.
- Joshi, S., Kumari, S., Sarmah, A., Sakhuja, R., & Pant, D. D. (2016). Solvatochromic shift and estimation of dipole moment of synthesized coumarin derivative: Application as sensor for fluorogenic recognition of Fe<sup>3+</sup> and Cu<sup>2+</sup> ions in aqueous solution. *Journal of Molecular Liquids*, 222, 253-262.
- Jurisch, M., de Paula, C. C. A., & Augusti, R. Distinguishing legal and illegal cigarettes by applying paper spray mass spectrometry and chemometric tools. *Rapid Communications in Mass Spectrometry*, 34(9), 8752.
- Kamtekar, K. T., Monkman, A. P., & Bryce, M. R. (2010). Recent advances in white organic light-emitting materials and devices (WOLEDs). *Advanced Materials*, 22(5), 572-582.
- Karaaslan, M. A., Kadla, J. F., & Ko, F. K. (2016). 5 - lignin-based aerogels. In O. Faruk & M. Sain (Eds.), *Lignin in Polymer Composites* (pp. 67-93): William Andrew Publishing.
- Karaoglu, K., Yilmaz, F., & Menteşe, E. (2017). A new fluorescent “turn-off” coumarin-based chemosensor: synthesis, structure and Cu-selective fluorescent sensing in water samples. *Journal of fluorescence*, 27(4), 1293-1298.
- Kaya, E. N., Yuksel, F., Özpınar, G. A., Bulut, M., & Durmuş, M. (2014). 7-Oxy-3-(3, 4, 5-trimethoxyphenyl) coumarin substituted phthalonitrile derivatives as fluorescent sensors for detection of Fe<sup>3+</sup> ions: Experimental and theoretical study. *Sensors and Actuators B: Chemical*, 194, 377-388.
- Kinza Aslam, K., Khosa, M. K., Jahan, N., & Nosheen, S. (2010). Short communication: synthesis and applications of Coumarin. *Pakistan Journal of Pharmaceutical Sciences*, 23(4), 449-454.
- Klaauk, H. (2006). *Organic electronics: materials, manufacturing, and applications*: John Wiley & Sons.

- Kolemen, S., & Akkaya, E. (2018). Reaction-based BODIPY probes for selective bio-imaging. *Coordination Chemistry Reviews*, 354, 121-134.
- l'Éclairage, C. I. d. (1924). Commission Internationale de l'Éclairage Proceedings. *Commission Internationale de l'Éclairage Proceedings*.
- Lal, A. (2020). Iron in health and disease: An update. *The Indian Journal of Pediatrics*. 87(1), 58-65.
- Laskin, J., Eckert, P. A., Roach, P. J., Heath, B. S., Nizkorodov, S. A., & Laskin, A. (2012). Chemical analysis of complex organic mixtures using reactive nanospray Desorption Electrospray Ionization Mass Spectrometry. *Analytical Chemistry*, 84(16), 7179-7187.
- Lavis, L. D., & Raines, R. T. (2008). Bright ideas for chemical biology. *ACS Chemical Biology*, 3(3), 142-155.
- Lawrence, J. F., & Frei, R. W. (2000). *Chemical derivatization in liquid chromatography* (Vol. 7): New York, NY: Elsevier Science .
- Leaback, D. H. (1997). Extended theory and improved practice for the quantitative measurement of fluorescence. *Journal of Fluorescence*, 7(1), 55-57.
- Ledemi, Y., Trudel, A.-A., Rivera, V. A., Chenu, S., Véron, E., Nunes, L. A., . . . Messaddeq, Y. (2014). White light and multicolor emission tuning in triply doped Yb 3+/Tm 3+/Er 3+ novel fluoro-phosphate transparent glass-ceramics. *Journal of Materials Chemistry C*, 2(25), 5046-5056.
- Levitus, M. (2011). Handbook of fluorescence spectroscopy and imaging. From ensemble to single molecules. Edited by Markus Sauer, Johan Hofkens and Jörg Enderlein. *Angewandte Chemie International Edition*, 50(39), 9017-9018.
- Li, D., Hu, W., Wang, J., Zhang, Q., Cao, X.-M., Ma, X., & Tian, H. (2018). White-light emission from a single organic compound with unique self-folded conformation and multistimuli responsiveness. *Chemical Science*, 9(26), 5709-5715.
- Li, H., Cai, L., & Chen, Z. (2012). Coumarin-Derived Fluorescent Chemosensors, *Advances in Chemical Sensors*, Wen Wang, IntechOpen. Retrieved from: <https://www.intechopen.com/books/advances-in-chemical-sensors/coumarin-derived-fluorescent-chemosensors>
- Li, H., Cai, L., Li, J., Hu, Y., Zhou, P., & Zhang, J. (2011). Novel coumarin fluorescent dyes: synthesis, structural characterization and recognition behavior towards Cu (II) and Ni (II). *Dyes and Pigments*, 91(3), 309-316.

- Li, H., Li, L., & Yin, B. (2014). Highly selective fluorescent chemosensor for Fe<sup>3+</sup> detection based on diaza-18-crown-6 ether appended with dual coumarins. *Inorganic Chemistry Communications*, 42, 1-4.
- Li, Z., Zhou, Y., Yin, K., Yu, Z., Li, Y., & Ren, J. (2014). A new fluorescence “turn-on” type chemosensor for Fe<sup>3+</sup> based on naphthalimide and coumarin. *Dyes and Pigments*, 105, 7-11.
- Lim, N. C., Schuster, J. V., Porto, M. C., Tanudra, M. A., Yao, L., Freake, H. C., & Brückner, C. (2005). Coumarin-based chemosensors for Zinc(ii): toward the determination of the design algorithm for CHEF-type and ratiometric probes. *Inorganic Chemistry*, 44(6), 2018-2030.
- Liu, E., Vega, S., Treiser, M. D., Sung, H. J., & Moghe, P. V. (2011). 3.317 - Fluorescence imaging of cell–biomaterial interactions. In P. Ducheyne (Ed.), *Comprehensive Biomaterials* (pp. 291-303). Oxford: Elsevier.
- Liu, H., Gao, W., Tian, Y., Liu, A., Wang, Z., Cai, Y., & Zhao, Z. (2019). Rapidly detecting tetrabromobisphenol A in soils and sediments by paper spray ionization mass spectrometry combined with isotopic internal standard. *Talanta*, 191, 272-276.
- Liu, J., Fraire, J. C., De Smedt, S. C., Xiong, R., & Braeckmans, K. (2020). Intracellular labeling with extrinsic probes: delivery strategies and applications. *Small*, 16(22), 2000146.
- Liu, J., Wang, H., Manicke, N. E., Lin, J.-M., Cooks, R. G., & Ouyang, Z. (2010). Development, characterization, and application of paper spray ionization. *Analytical Chemistry*, 82(6), 2463-2471.
- Liu, S., Li, F., Diao, Q., & Ma, Y. (2010). Aggregation-induced enhanced emission materials for efficient white organic light-emitting devices. *Organic Electronics*, 11(4), 613-617.
- Liu, X., Li, N., Xu, M.-M., Wang, J., Jiang, C., Song, G., & Wang, Y. (2018). Specific colorimetric detection of Fe<sup>3+</sup> ions in aqueous solution by squaraine-based chemosensor. *RSC Advances*, 8(61), 34860-34866.
- Liu, Y., Nishiura, M., Wang, Y., & Hou, Z. (2006).  $\pi$ -conjugated aromatic enynes as a single-emitting component for white electroluminescence. *Journal of the American Chemical Society*, 128(17), 5592-5593.

- Liu, Y., Su, Q., Chen, M., Dong, Y., Shi, Y., Feng, W., . . . Li, F. (2016). Near-Infrared upconversion chemodosimeter for in vivo detection of Cu<sup>2+</sup> in Wilson disease. *Advanced Materials*, 28(31), 6625-6630.
- Liu, Y., Zhou, Y., Dai, Y., Zhao, Z., He, L., & Zhang, Q. (2018). Quantitative analysis of finasteride tablets dissolution content with non-isotopically labeled internal standard by paper spray ionization mass spectrometry. *Journal of Separation Science*, 41(21), 4083-4089.
- Luo, D., Liu, S. G., Li, N. B., & Luo, H. Q. (2018). Water-soluble polymer dots formed from polyethylenimine and glutathione as a fluorescent probe for Mercury(II). *Microchimica Acta*, 185(6), 284.
- Ma, Y., Luo, W., Quinn, P. J., Liu, Z., & Hider, R. C. (2004). Design, synthesis, physicochemical properties, and evaluation of novel iron chelators with fluorescent sensors. *Journal of Medicinal Chemistry*, 47(25), 6349-6362.
- Ma, Y., Wang, S., & Wang, L. (2015). Nanomaterials for luminescence detection of nitroaromatic explosives. *TrAC Trends in Analytical Chemistry*, 65, 13-21.
- Machado, S., Stawiński, W., Slonina, P., Pinto, A., Grosso, J., Nouws, H., . . . Delerue-Matos, C. (2013). Application of green zero-valent iron nanoparticles to the remediation of soils contaminated with ibuprofen. *Science of the Total Environment*, 461, 323-329.
- Maher, S., Bastani, B., Smith, B., Jjunju, F., Taylor, S., & Young, I. S. (2016, 30 Oct.-3 Nov. 2016). *Portable fluorescent sensing array for monitoring heavy metals in water*. Paper presented at the 2016 IEEE SENSORS.
- Maher, S., Jjunju, F., Damon, D., Gorton, H., Maher, Y., Syed, S., . . . Badu-Twaihah, A. (2016). Direct analysis and quantification of metaldehyde in water using reactive paper spray mass spectrometry. *Scientific Reports*, 6, 35643.
- Maher, S., Jjunju, F. P., Damon, D. E., Gorton, H., Maher, Y. S., Syed, S. U., . . . Badu-Tawiah, A. K. (2016). Direct analysis and quantification of metaldehyde in water using reactive paper spray mass spectrometry. *Scientific Reports*, 6, 35643.
- Maher, S., Jjunju, F. P. M., & Taylor, S. (2015). Colloquium: 100 years of mass spectrometry: Perspectives and future trends. *Reviews of Modern Physics*, 87(1), 113-135.
- Maiti, D. K., & Banerjee, A. (2013). A peptide based two component white light emitting system. *Chemical Communications*, 49(61), 6909-6911.

- Maiti, D. K., Bhattacharjee, R., Datta, A., & Banerjee, A. (2013). Modulation of fluorescence resonance energy transfer efficiency for white light emission from a series of stilbene-erythrin based donor-acceptor pair. *The Journal of Physical Chemistry C*, 117(44), 23178-23189.
- Maity, A., Ali, F., Agarwalla, H., Anothumakkool, B., & Das, A. (2015). Tuning of multiple luminescence outputs and white-light emission from a single gelator molecule through an ESIPT coupled AIEE process. *Chemical Communications*, 51(11), 2130-2133.
- Maleki, H., Durães, L., García-González, C. A., del Gaudio, P., Portugal, A., & Mahmoudi, M. (2016). Synthesis and biomedical applications of aerogels: Possibilities and challenges. *Advances in Colloid and Interface Science*, 236, 1-27.
- Manicke, N. E., Bills, B. J., & Zhang, C. (2016). Analysis of biofluids by paper spray MS: advances and challenges. *Bioanalysis*, 8(6), 589-606.
- Martelo, L. M., Marques, L. F., Burrows, H. D., & Berberan-Santos, M. N. (2019). Explosives detection: from sensing to response. In B. Pedras (Ed.), *Fluorescence in Industry* (pp. 293-320). Cham: Springer International Publishing.
- Masson, O., Steinhäuser, G., Zok, D., Saunier, O., Angelov, H., Babić, D., . . . Burbidge, C. (2019). Airborne concentrations and chemical considerations of radioactive ruthenium from an undeclared major nuclear release in 2017. *Proceedings of the National Academy of Sciences*, 116(34), 16750-16759.
- McCann, T. E., Kosaka, N., Koide, Y., Mitsunaga, M., Choyke, P. L., Nagano, T., . . . Kobayashi, H. (2011). Activatable Optical Imaging with a Silica-Rhodamine Based Near Infrared (SiR700) Fluorophore: A comparison with cyanine based dyes. *Bioconjugate Chemistry*, 22(12), 2531-2538.
- McKenna, J., Dhummakupt, E. S., Connell, T., Demond, P. S., Miller, D. B., Michael Nilles, J., . . . Glaros, T. (2017). Detection of chemical warfare agent simulants and hydrolysis products in biological samples by paper spray mass spectrometry. *Analyst*, 142(9), 1442-1451.
- McKenna, J., Jett, R., Shanks, K., & Manicke, N. (2018). Toxicological drug screening using Paper Spray High-Resolution Tandem Mass Spectrometry (HR-MS/MS). *Journal of Analytical Toxicology*, 42(5), 300-310.
- Medina, F. G., Marrero, J. G., Macías-Alonso, M., González, M. C., Córdova-Guerrero, I., Teissier García, A. G., & Osegueda-Robles, S. (2015). Coumarin heterocyclic

derivatives: chemical synthesis and biological activity. *Natural Product Reports*, 32(10), 1472-1507.

Melough, M. M., Cho, E., & Chun, O. K. (2018). Furocoumarins: A review of biochemical activities, dietary sources and intake, and potential health risks. *Food and Chemical Toxicology*, 113, 99-107.

Melucci, M., Zambianchi, M., Barbarella, G., Manet, I., Montalti, M., Bonacchi, S., . . . Reschiglian, P. (2010). Facile tuning from blue to white emission in silica nanoparticles doped with oligothiophene fluorophores. *Journal of Materials Chemistry*, 20(44), 9903-9909.

Ming, W., Wang, X., Lu, W., Zhang, Z., Song, X., Li, J., & Chen, L. (2017). Magnetic molecularly imprinted polymers for the fluorescent detection of trace 17 $\beta$ -estradiol in environmental water. *Sensors and Actuators B: Chemical*, 238, 1309-1315.

Mishra, R., Kotresh, T. M., Militky, J., & Jamshaid, H. (2016). Aerogels for thermal insulation in high-performance textiles AU - Venkataraman, M. *Textile Progress*, 48(2), 55-118.

Molla, M. R., & Ghosh, S. (2012). Hydrogen-bonding-mediated J-aggregation and white-light emission from a remarkably simple, single-component, naphthalenediimide chromophore. *Chemistry—A European Journal*, 18(5), 1290-1294.

Monge, M. E., Harris, G. A., Dwivedi, P., & Fernández, F. M. (2013). Mass spectrometry: Recent advances in direct open air surface sampling/ionization. *Chemical Reviews*, 113(4), 2269-2308.

Moolayil, J. T., George, M., Srinivas, R., Swamy, N., Russell, A. L., Giblin, D. E., & Gross, M. L. (2006). The mass spectrometry-induced cyclization of protonated N-[2-(benzoyloxy) phenyl]-benzamide: A gas-phase analog of a solution reaction. *International Journal of Mass Spectrometry*, 249, 21-30.

Moura, A. C. M., Lago, I. N., Cardoso, C. F., dos Reis Nascimento, A., Pereira, I., & Vaz, B. G. (2020). Rapid monitoring of pesticides in tomatoes (*Solanum lycopersicum* L.) during pre-harvest intervals by paper spray ionization mass spectrometry. *Food Chemistry*, 310, 125938.

Muhamad Sarih, N., Myers, P., Slater, A., Slater, B., Abdullah, Z., Tajuddin, H. A., & Maher, S. (2019). White light emission from a simple mixture of fluorescent organic compounds. *Scientific Reports*, 9(1), 11834.

- Mukherjee, S., & Thilagar, P. (2014). Organic white-light emitting materials. *Dyes and Pigments*, 110, 2-27.
- Müller, T., Badu-Tawiah, A., & Cooks, R. G. (2012). Accelerated carbon-carbon bond-forming reactions in preparative electrospray. *Angewandte Chemie International Edition*, 51(47), 11832-11835.
- Murphy, J. P., Johnson, J., & Rainville, P. D. (2014). *Enhancing mass spectrometry sensitivity by reducing chromatographic flow rates with ionKey/MS*. Millford, USA: Waters Corporations.
- Nair, V., Menon, R. S., Vinod, A. U., & Viji, S. (2002b). A facile three-component reaction involving [4+1] cycloaddition leading to furan annulated heterocycles. *Tetrahedron Letters*, 43(12), 2293-2295.
- Nandhikonda, P., & Heagy, M. D. (2010). An organic white light-emitting dye: very small molecular architecture displays panchromatic emission. *Chemical Communications*, 46(42), 8002-8004.
- Narayanaswamy, V. K., Gleiser, R. M., Kasumbwe, K., Aldhubiab, B. E., Attimarad, M. V., & Odhav, B. (2014). Evaluation of halogenated coumarins for antimosquito properties. *The Scientific World Journal*, 2014.
- Nicolai, H. T., Hof, A., & Blom, P. W. (2012). Device physics of white polymer light-emitting diodes. *Advanced Functional Materials*, 22(10), 2040-2047.
- Nudelman, R., Ardon, O., Hadar, Y., Chen, Y., Libman, J., & Shanzer, A. (1998). Modular fluorescent-labeled siderophore analogues. *Journal of Medicinal Chemistry*, 41(10), 1671-1678.
- Oliva, J., Mayen, L. P., De la Rosa, E., Diaz-Torres, L. A., Castro, A. T., & Salas, P. (2013). Tunable white light from photo-and electroluminescence of ZnO nanoparticles. *Journal of Physics D: Applied Physics*, 47(1), 015104.
- Park, Y., Postupna, O., Zhugayevych, A., Shin, H., Park, Y.-S., Kim, B., . . . Park, J. (2015). A new pH sensitive fluorescent and white light emissive material through controlled intermolecular charge transfer. *Chemical Science*, 6(1), 789-797.
- Pati, A. K., Jana, R., Gharpure, S. J., & Mishra, A. K. (2016). Photophysics of diphenylbutadiynes in water, acetonitrile-water, and acetonitrile solvent systems: Application to single component white light emission. *The Journal of Physical Chemistry A*, 120(29), 5826-5837.

- Puthiyedath, T., & Bahulayan, D. (2018a). A click derived triazole-coumarin derivative as fluorescence on-off PET based sensor for Ca<sup>2+</sup> and Fe<sup>3+</sup> ions. *Sensors and Actuators B: Chemical*, 272, 110-117.
- Puthiyedath, T., & Bahulayan, D. (2018b). A click derived triazole-coumarin derivative as fluorescence on-off PET based sensor for Ca<sup>2+</sup> and Fe<sup>3+</sup> ions. *Sensors and Actuators B: Chemical*, 272, 110-117.
- Qin, J.-c., Li, T.-r., Wang, B.-d., Yang, Z.-y., & Fan, L. (2014). Fluorescent sensor for selective detection of Al<sup>3+</sup> based on quinoline-coumarin conjugate. *Spectrochimica Acta Part A: Molecular and Biomolecular Spectroscopy*, 133, 38-43.
- Qin, J.-c., Yang, Z.-y., Wang, G.-q., & Li, C.-r. (2015). FRET-based rhodamine-coumarin conjugate as a Fe<sup>3+</sup> selective ratiometric fluorescent sensor in aqueous media. *Tetrahedron Letters*, 56(35), 5024-5029.
- Rane, S., Prudenziati, M., & Morten, B. (2007). Environment friendly perovskite ruthenate based thick film resistors. *Materials Letters*, 61(2), 595-599.
- Ray, D., & Bharadwaj, P. K. (2008). A Coumarin-Derived Fluorescence Probe Selective for Magnesium. *Inorganic Chemistry*, 47(7), 2252-2254.
- Resende, S., Teodoro, J., Binatti, I., Gouveia, R., Oliveira, B., & Augusti, R. (2017). On-surface photocatalytic degradation of methylene blue: In situ monitoring by paper spray ionization mass spectrometry. *International Journal of Mass Spectrometry*, 418, 107-111.
- Rezayee, N. M., Huff, C. A., & Sanford, M. S. (2015). Tandem Amine and Ruthenium-Catalyzed Hydrogenation of CO<sub>2</sub> to Methanol. *Journal of the American Chemical Society*, 137(3), 1028-1031.
- Rindelaub, J. D., Wiley, J. S., Cooper, B. R., & Shepson, P. B. (2016). Chemical characterization of  $\alpha$ -pinene secondary organic aerosol constituents using gas chromatography, liquid chromatography, and paper spray-based mass spectrometry techniques. *Rapid Communications in Mass Spectrometry*, 30(13), 1627-1638.
- Sahraei, R., Pordel, M., Behmadi, H., & Razavi, B. (2013). Synthesis of a new class of strongly fluorescent heterocyclic compounds: 3H-imidazo [4, 5-a] acridine-11-carbonitriles. *Journal of Luminescence*, 136, 334-338.

- Sahu, A., Dash, D., Mishra, K., Mishra, S., Yadav, R., & Kashyap, P. (2018). Properties and applications of ruthenium. IntechOpen. Retrieved from: <https://www.intechopen.com/books/noble-and-precious-metals-properties-nanoscale-effects-and-applications/properties-and-applications-of-ruthenium>.
- Sánchez, M., Sabio, L., Gálvez, N., Capdevila, M., & Dominguez-Vera, J. M. (2017). Iron chemistry at the service of life. *IUBMB Life*, 69(6), 382-388.
- Sanju, K. S., Neelakandan, P. P., & Ramaiah, D. (2011). DNA-assisted white light emission through FRET. *Chemical Communications*, 47(4), 1288-1290.
- Sanju, K. S., & Ramaiah, D. (2013). White photoluminescence and electroluminescence from a ternary system in solution and a polymer matrix. *Chemical Communications*, 49(99), 11626-11628.
- Santhosh Babu, S., Aimi, J., Ozawa, H., Shirahata, N., Saeki, A., Seki, S., . . . Nakanishi, T. (2012). Solvent-free luminescent organic liquids. *Angewandte Chemie International Edition*, 51(14), 3391-3395.
- Santra, S., Zhang, P., Wang, K., Tapeç, R., & Tan, W. (2001). Conjugation of biomolecules with luminophore-doped silica nanoparticles for photostable biomarkers. *Analytical Chemistry*, 73(20), 4988-4993.
- Sarih, N. M., Ciupa, A., Moss, S., Myers, P., Slater, A. G., Abdullah, Z., . . . Maher, S. (2020). Furo[3,2-c]coumarin-derived Fe<sup>3+</sup> selective fluorescence sensor: synthesis, fluorescence study and application to water analysis. *Scientific Reports*, 10(1), 7421.
- Sarih, N. M., Romero-Perez, D., Bastani, B., Rauytanapanit, M., Boisdon, C., Praneenararat, T., . . . Maher, S. (2020). Accelerated nucleophilic substitution reactions of dansyl chloride with aniline under ambient conditions via dual-tip reactive paper spray. *Scientific Reports*, 10(1), 21504.
- Sato, I., Kudo, H., & Tsuda, S. (2011). Removal efficiency of water purifier and adsorbent for iodine, cesium, strontium, barium and zirconium in drinking water. *The Journal of Toxicological Sciences*, 36(6), 829-834.
- Schutz, R. W. (1996). Ruthenium enhanced titanium alloys. *Platinum Metals Review*, 40(2), 54-61.
- Sessolo, M., Tordera, D., & Bolink, H. J. (2013). Ionic iridium complex and conjugated polymer used to solution-process a bilayer white light-emitting diode. *ACS Applied Materials & Interfaces*, 5(3), 630-634.

- Sethna, S. M., & Shah, N. M. (1945). The chemistry of coumarins. *Chemical Reviews*, 36(1), 1-62.
- Shaabani, A., Teimouri, M. B., & Bijanzadeh, H. R. (2004). One-pot three-component condensation reactions in water. An efficient and improved procedure for the synthesis of furan annulated heterocycles. *Monatshefte für Chemie / Chemical Monthly*, 135(5), 589-593.
- Shaikh, T., Patil, J., Gaikwad, D., Hegade, P., Patil, P., Undale, K., . . . Pore, D. (2014). Catalyst-free access to pseudo multi-component synthesis of benzopyranopyrimidines. *Indian Journal of Chemistry*, 53B(10) 1288-1294.
- Shang, M., Li, C., & Lin, J. (2014). How to produce white light in a single-phase host? *Chemical Society Reviews*, 43(5), 1372-1386.
- Shi, R.-Z., El Gierari, E. T. M., Faix, J. D., & Manicke, N. E. (2016). Rapid measurement of cyclosporine and sirolimus in whole blood by Paper Spray–Tandem Mass Spectrometry. *Clinical Chemistry*, 62(1), 295-297.
- Shi, R.-Z., El Gierari, E. T. M., Manicke, N. E., & Faix, J. D. (2015). Rapid measurement of tacrolimus in whole blood by paper spray-tandem mass spectrometry (PS-MS/MS). *Clinica Chimica Acta*, 441, 99-104.
- Singh, P., Singh, H., Bhargava, G., & Kumar, S. (2015). Triple-signaling mechanisms-based three-in-one multi-channel chemosensor for discriminating Cu<sup>2+</sup>, acetate and ion pair mimicking AND, NOR, INH and IMP logic functions. *Journal of Materials Chemistry C*, 3(21), 5524-5532.
- Singh, V., & Mishra, A. K. (2015). White light emission from vegetable extracts. *Scientific Reports*, 5, 11118.
- Singh, V., & Mishra, A. K. (2016a). White light emission from a mixture of pomegranate extract and carbon nanoparticles obtained from the extract. *Journal of Materials Chemistry C*, 4(15), 3131-3137.
- Singh, V., & Mishra, A. K. (2016b). White light emission from an aqueous vegetable cocktail: Application towards pH sensing. *Dyes and Pigments*, 125, 362-366.
- Sinha, S., Chowdhury, B., Ghorai, U. K., & Ghosh, P. (2019). Multitasking behaviour of a small organic compound: solid state bright white-light emission, mechanochromism and ratiometric sensing of Al(iii) and pyrophosphate. *Chemical Communications*, 55(35), 5127-5130.

- Skalnaya, M. G., & Skalny, A. V. (2018). Essential trace elements in human health: a physician's view. *Publishing House of Tomsk State University, Tomsk*.
- Smirnova, I., & Gurikov, P. (2018). Aerogel production: Current status, research directions, and future opportunities. *The Journal of Supercritical Fluids*, 134, 228-233.
- Smith, B. L., Hughes, D. M., Badu-Tawiah, A. K., Eccles, R., Goodall, I., & Maher, S. (2019). Rapid scotch whisky analysis and authentication using desorption atmospheric pressure chemical ionisation Mass Spectrometry. *Scientific Reports*, 9(1), 7994.
- Smith, B. L., Jjunju, F. P. M., Taylor, S., Young, I. S., & Maher, S. (2016, 30 Oct.-3 Nov. 2016). *Development of a portable, low cost, plasma ionization source coupled to a mass spectrometer for surface analysis*. Paper presented at the 2016 IEEE SENSORS, Orlando, FL, USA.
- Sozmen, F., Kolemen, S., Kumada, H.-O., Ono, M., Saji, H., & Akkaya, E. (2014). Designing BODIPY-based probes for fluorescence imaging of  $\beta$ -amyloid plaques *RSC Advances*, 4(92), 51032-51037.
- Süel, G. (2011). Chapter thirteen - Use of fluorescence microscopy to analyze genetic circuit dynamics. In C. Voigt (Ed.), *Methods in Enzymology* (Vol. 497, pp 275-293): Academic Press.
- Sui, B., Tang, S., Liu, T., Kim, B., & Belfield, K. D. (2014). Novel BODIPY-based fluorescence turn-on sensor for  $Fe^{3+}$  and its bioimaging application in living cells. *ACS Applied Materials & Interfaces*, 6(21), 18408-18412.
- Sun, C.-Y., Wang, X.-L., Zhang, X., Qin, C., Li, P., Su, Z.-M., . . . Wu, H. (2013). Efficient and tunable white-light emission of metal-organic frameworks by iridium-complex encapsulation. *Nature Communications*, 4, 2717.
- Sun, Y.-F., Huang, W., Lu, C.-G., & Cui, Y.-P. (2009). The synthesis, two-photon absorption and blue upconversion fluorescence of novel, nitrogen-containing heterocyclic chromophores. *Dyes and Pigments*, 81(1), 10-17.
- Suraritdechachai, S., Charoenpakdee, C., Young, I., Maher, S., Vilaivan, T., & Praneenararat, T. (2019). Rapid detection of the antibiotic sulfamethazine in pig body fluids by paper spray mass spectrometry. *Journal of Agricultural and Food Chemistry*, 67(10), 3055-3061.

- Szczepaniak, G., Nogaś, W., Piątkowski, J., Ruszczyńska, A., Bulska, E., & Grela, K. (2019). Semiheterogeneous purification protocol for the removal of ruthenium impurities from olefin metathesis reaction products using an isocyanide scavenger. *Organic Process Research & Development*, 23(5), 836-844.
- Tang, C., Liu, X. D., Liu, F., Wang, X. L., Xu, H., & Huang, W. (2013). Recent progress in polymer white light-emitting materials and devices. *Macromolecular Chemistry and Physics*, 214(3), 314-342.
- Täuscher, E., Weiß, D., Beckert, R., Fabian, J., Assumpção, A., & Görls, H. (2011). Classical heterocycles with surprising properties: the 4-hydroxy-1,3-thiazoles. *Tetrahedron Letters*, 52(18), 2292-2294.
- Thamdrup, B. (2000). Bacterial manganese and iron reduction in aquatic sediments *Advances in Microbial Ecology* (pp. 41-84): Springer.
- Tiki, A., Amin, A., & Kanwal, A. (2010). Chemistry of optical brighteners and uses in textile industries. *Pakistan Textile Journal*, 59(7), 42.
- Udayan, A., Arumugam, M., & Pandey, A. (2017). Chapter 4 - Nutraceuticals from algae and cyanobacteria. In R. P. Rastogi, D. Madamwar, & A. Pandey (Eds.), *Algal Green Chemistry* (65-89). Amsterdam: Elsevier.
- Ullah, I., Li, W., Lei, S., Zhang, Y., Zhang, W., Farooq, U., . . . Zhang, X. (2018). Simultaneous co-substitution of Sr<sup>2+</sup>/Fe<sup>3+</sup> in hydroxyapatite nanoparticles for potential biomedical applications. *Ceramics International*, 44(17), 21338-21348.
- Valente, A., & Garcia, M. (2014). Syntheses of macromolecular ruthenium compounds: A new approach for the search of anticancer drugs. *Inorganics*, 2(1), 96-114.
- Vandergrift, G. W., & Gill, C. G. (2019). Paper spray mass spectrometry: A new drug checking tool for harm reduction in the opioid overdose crisis. *Journal of Mass Spectrometry*, 54(9), 729-737.
- Vázquez-Mera, N. A., Otaegui, J. R., Sánchez, R. S., Prats, G., Guirado, G., Ruiz-Molina, D., . . . Hernando, J. (2019). Color-tunable white-light-emitting materials based on liquid-filled capsules and thermally responsive dyes. *ACS Applied Materials & Interfaces*, 11(19), 17751-17758.
- Vijayakumar, C., Praveen, V. K., & Ajayaghosh, A. (2009). RGB emission through controlled donor self-assembly and modulation of excitation energy transfer: A novel strategy to white-light-emitting organogels. *Advanced Materials*, 21(20), 2059-2063.

- Vijayakumar, C., Sugiyasu, K., & Takeuchi, M. (2011). Oligofluorene-based electrophoretic nanoparticles in aqueous medium as a donor scaffold for fluorescence resonance energy transfer and white-light emission. *Chemical Science*, 2(2), 291-294.
- Wang, H., Liu, J., Cooks, R. G., & Ouyang, Z. (2010a). Paper spray for direct analysis of complex mixtures using mass spectrometry. *Angewandte Chemie*, 122(5), 889-892.
- Wang, H., Liu, J., Cooks, R. G., & Ouyang, Z. (2010b). Paper spray for direct analysis of complex mixtures using mass spectrometry. *Angewandte Chemie International Edition*, 49(5), 877-880.
- Wang, H., Manicke, N. E., Yang, Q., Zheng, L., Shi, R., Cooks, R. G., & Ouyang, Z. (2011). Direct analysis of biological tissue by paper spray mass spectrometry. *Analytical Chemistry*, 83(4), 1197-1201.
- Wang, J., Zhang, F., Zhang, J., Tang, W., Tang, A., Peng, H., . . . Wang, Y. (2013). Key issues and recent progress of high efficient organic light-emitting diodes. *Journal of Photochemistry and Photobiology C: Photochemistry Reviews*, 17, 69-104.
- Wang, L., Li, H., & Cao, D. (2013). A new photoresponsive coumarin-derived Schiff base: Chemosensor selectively for Al<sup>3+</sup> and Fe<sup>3+</sup> and fluorescence “turn-on” under room light. *Sensors and Actuators B: Chemical*, 181, 749-755.
- Wang, L., Li, W., Zhi, W., Huang, Y., Han, J., Wang, Y., . . . Ni, L. (2018). A new coumarin schiff based fluorescent-colorimetric chemosensor for dual monitoring of Zn<sup>2+</sup> and Fe<sup>3+</sup> in different solutions: An application to bio-imaging. *Sensors and Actuators B: Chemical*, 260, 243-254.
- Wang, R., Peng, J., Qiu, F., & Yang, Y. (2011). Enhanced white-light emission from multiple fluorophores encapsulated in a single layer of diblock copolymer micelles. *Chemical Communications*, 47(10), 2787-2789.
- Wang, R., Peng, J., Qiu, F., Yang, Y., & Xie, Z. (2009). Simultaneous blue, green, and red emission from diblock copolymer micellar films: A new approach to white-light emission. *Chemical Communications*(44), 6723-6725.
- Wang, R., Wan, Q., Feng, F., & Bai, Y. (2014). A novel coumarin-based fluorescence chemosensor for Fe<sup>3+</sup>. *Chemical Research in Chinese Universities*, 30(4), 560-565.

- Wang, S., Li, N., Pan, W., & Tang, B. (2012). Advances in functional fluorescent and luminescent probes for imaging intracellular small-molecule reactive species. *TrAC Trends in Analytical Chemistry*, 39, 3-37.
- Wang, W., Wu, J., Liu, Q., Gao, Y., Liu, H., & Zhao, B. (2018). A highly selective coumarin-based chemosensor for the sequential detection of Fe<sup>3+</sup> and pyrophosphate and its application in living cell imaging. *Tetrahedron Letters*, 59(19), 1860-1865.
- Wang, X., Yan, J., Zhou, Y., & Pei, J. (2010). Surface modification of self-assembled one-dimensional organic structures: white-light emission and beyond. *Journal of the American Chemical Society*, 132(45), 15872-15874.
- Warrier, S., & Kharkar, P. S. (2018). Highly selective on-off fluorescence recognition of Fe<sup>3+</sup> based on a coumarin derivative and its application in live-cell imaging. *Spectrochimica Acta Part A: Molecular and Biomolecular Spectroscopy*, 188, 659-665.
- Wen, D., Liu, W., Herrmann, A. K., & Eychmüller, A. (2014). A membraneless glucose/O<sub>2</sub> biofuel cell based on Pd aerogels. *Chemistry—A European Journal*, 20(15), 4380-4385.
- World Health Organization. (2003) *Iron in Drinking Water: Background Document for Development of WHO Guidelines for Drinking Water Quality*. Geneva, Switzerland: WHO Press.
- Wu, D., Sedgwick, A. C., Gunnlaugsson, T., Akkaya, E. U., Yoon, J., & James, T. D. (2017). Fluorescent chemosensors: the past, present and future. *Chemical Society Reviews*, 46(23), 7105-7123.
- Wu, J. (2005). General microwave-assisted protocols for the expedient synthesis of furo [3, 2-c] chromen-4-ones. *Chemistry Letters*, 35(1), 118-119.
- Wyszecki, G., & Stiles, W. S. (1982). *Color science* (Vol. 8): Wiley New York.
- Xiao, Y., Guo, Y., Dang, R., Yan, X., Xu, P., & Jiang, P. (2017). A dansyl-based fluorescent probe for the highly selective detection of cysteine based on a d-PeT switching mechanism. *RSC Advances*, 7(34), 21050-21053.
- Xie, L., Chen, Y., Wu, W., Guo, H., Zhao, J., & Yu, X. (2012). Fluorescent coumarin derivatives with large stokes shift, dual emission and solid state luminescent properties: An experimental and theoretical study. *Dyes and Pigments*, 92(3), 1361-1369.

- Xu, J.-H., Hou, Y.-M., Ma, Q.-J., Wu, X.-F., & Wei, X.-J. (2013). A highly selective fluorescent sensor for Fe<sup>3+</sup> based on covalently immobilized derivative of naphthalimide. *Spectrochimica Acta Part A: Molecular and Biomolecular Spectroscopy*, 112, 116-124.
- Yamaguchi, K., Murai, T., Guo, J.-D., Sasamori, T., & Tokitoh, N. (2016). Acid-responsive absorption and emission of 5-n-arylaminothiazoles: emission of white light from a single fluorescent dye and a lewis acid. *ChemistryOpen*, 5(5), 434-438.
- Yan, M.-h., Li, T.-r., & Yang, Z.-y. (2011). A novel coumarin Schiff-base as a Zn (II) ion fluorescent sensor. *Inorganic Chemistry Communications*, 14(3), 463-465.
- Yan, X., Augusti, R., Li, X., & Cooks, R. G. (2013). Chemical reactivity assessment using reactive paper spray ionization mass spectrometry: the Katritzky reaction. *ChemPlusChem*, 78(9), 1142-1148.
- Yan, X., Bain, R. M., & Cooks, R. G. (2016). Organic reactions in microdroplets: Reaction acceleration revealed by mass spectrometry. *Angewandte Chemie International Edition*, 55(42), 12960-12972.
- Yan, Z., Hu, L., & You, J. (2016). Sensing materials developed and applied for bio-active Fe<sup>3+</sup> recognition in water environment. *Analytical Methods*, 8(29), 5738-5754.
- Yang, L., Yang, W., Xu, D., Zhang, Z., & Liu, A. (2013). A highly selective and sensitive Fe<sup>3+</sup> fluorescent sensor by assembling three 1,8-naphthalimide fluorophores with a tris(aminoethylamine) ligand. *Dyes and Pigments*, 97(1), 168-174.
- Yang, Q.-Y., Wu, K., Jiang, J.-J., Hsu, C.-W., Pan, M., Lehn, J.-M., & Su, C.-Y. (2014). Pure white-light and yellow-to-blue emission tuning in single crystals of Dy (III) metal-organic frameworks. *Chemical Communications*, 50(57), 7702-7704.
- Yang, Y., Lowry, M., Schowalter, C. M., Fakayode, S. O., Escobedo, J. O., Xu, X., . . . Warner, I. M. (2006). An organic white light-emitting fluorophore. *Journal of the American Chemical Society*, 128(43), 14081-14092.
- Yang, Y., Zhao, Q., Feng, W., & Li, F. (2013). Luminescent Chemodosimeters for Bioimaging. *Chemical Reviews*, 113(1), 192-270.
- Yannell, K. E., Kesely, K. R., Chien, H. D., Kissinger, C. B., & Cooks, R. G. (2017). Comparison of paper spray mass spectrometry analysis of dried blood spots from devices used for in-field collection of clinical samples. *Analytical and Bioanalytical Chemistry*, 409(1), 121-131.

- Yao, J., Dou, W., Qin, W., & Liu, W. (2009). A new coumarin-based chemosensor for Fe<sup>3+</sup> in water. *Inorganic Chemistry Communications*, 12(2), 116-118.
- Ye, F., Chai, Q., Liang, X.-M., Li, M.-Q., Wang, Z.-Q., & Fu, Y. (2017). A highly selective and sensitive fluorescent turn-off probe for Cu<sup>2+</sup> based on a guanidine derivative. *Molecules*, 22(10), 1741.
- Yuan, L., Lin, W., Xie, Y., Chen, B., & Zhu, S. (2012). Single fluorescent probe responds to h<sub>2</sub>o<sub>2</sub>, no, and h<sub>2</sub>o<sub>2</sub>/no with three different sets of fluorescence signals. *Journal of the American Chemical Society*, 134(2), 1305-1315.
- Yuan, L., Lin, W., Zhao, S., Gao, W., Chen, B., He, L., & Zhu, S. (2012). A unique approach to development of near-infrared fluorescent sensors for in vivo imaging. *Journal of the American Chemical Society*, 134(32), 13510-13523.
- Zhang, J., Cheng, F., Li, J., Zhu, J.-J., & Lu, Y. (2016). Fluorescent nanoprobe for sensing and imaging of metal ions: recent advances and future perspectives. *Nano Today*, 11(3), 309-329.
- Zhang, N.-N., Sun, C., Jiang, X.-M., Xing, X.-S., Yan, Y., Cai, L.-Z., . . . Guo, G.-C. (2017). Single-component small-molecule white light organic phosphors. *Chemical Communications*, 53(66), 9269-9272.
- Zhang, P., Li, L., Zhao, Y., Tian, Z., Qin, Y., & Lu, J. (2016). 8-Anilino-1-naphthalenesulfonate/layered double hydroxide ultrathin films: small anion assembly and its potential application as a fluorescent biosensor. *Langmuir*, 32(35), 9015-9022.
- Zhao, B., Liu, T., Fang, Y., Wang, L., Kan, W., Deng, Q., & Song, B. (2017). A new selective chemosensor based on phenanthro [9, 10-d] imidazole-coumarin with sequential “on-off-on” fluorescence response to Fe<sup>3+</sup> and phosphate anions and its application in live cell. *Sensors and Actuators B: Chemical*, 246, 370-379.
- Zhao, B., Liu, T., Fang, Y., Wang, L., Song, B., & Deng, Q. (2016a). Two ‘turn-off’ Schiff base fluorescence sensors based on phenanthro[9,10-d]imidazole-coumarin derivatives for Fe<sup>3+</sup> in aqueous solution. *Tetrahedron Letters*, 57(39), 4417-4423.
- Zhao, B., Liu, T., Fang, Y., Wang, L., Song, B., & Deng, Q. (2016b). Two ‘turn-off’ Schiff base fluorescence sensors based on phenanthro [9, 10-d] imidazole-coumarin derivatives for Fe<sup>3+</sup> in aqueous solution. *Tetrahedron Letters*, 57(39), 4417-4423.
- Zhou, C., Zhang, S., Gao, Y., Liu, H., Shan, T., Liang, X., . . . Ma, Y. (2018). Ternary emission of fluorescence and dual phosphorescence at room temperature: a single-

molecule white light emitter based on pure organic aza-aromatic material. *Advanced Functional Materials*, 28(32), 1802407.

Zhou, X., Pei, J., & Huang, G. (2015). Reactive paper spray mass spectrometry for in situ identification of quinones. *Rapid Communications in Mass Spectrometry*, 29(1), 100-106.

Zhu, X., Zhang, W., Lin, Q., Ye, M., Xue, L., Liu, J., . . . Cheng, H. (2019b). Direct microdroplet synthesis of carboxylic acids from alcohols by preparative paper spray ionization without phase transfer catalysts. *ACS Sustainable Chemistry & Engineering*, 7(7), 6486-6491.

Universiti Malaya